Heat Transfer Coefficient and Adiabatic Effectiveness Measurements for an Internal Turbine Vane Cooling Feature

Jeffrey N. Prausa

Thesis submitted to the Faculty
of the Virginia Polytechnic Institute and State University
in partial fulfillment of the requirements for the degree of

Master of Science
in
Mechanical Engineering

Dr. K. A. Thole, Chair
Dr. W. F. O'Brien
Dr. B. Vick

May 21, 2004
Blacksburg, VA

Keywords: gas turbines, film cooling, internal cooling,
microcircuit, heat transfer augmentation, friction augmentation

© 2004, Jeffrey N. Prausa

Heat Transfer Coefficient and Adiabatic Effectiveness Measurements for an Internal Turbine Airfoil Cooling Feature

Jeffrey N. Prausa

Abstract

Aircraft engine manufacturers strive for greater performance and efficiency by continually increasing the turbine inlet temperature. High turbine inlet temperatures significantly degrade the lifetime of components in the turbine. Modern gas turbines operate with turbine inlet temperatures well above the melting temperature of key turbine components. Without active cooling schemes, modern turbines would fail catastrophically. This study will evaluate a novel cooling scheme for turbine airfoils, called microcircuit cooling, in which small cooling channels are located extremely close to the surface of a turbine airfoil. Coolant bled from the compressor passes through the microcircuits and exits through film cooling slots. On further cooling benefit is that the microcircuit passages are filled with irregular pin fin features that serve to increase convective cooling through the channels.

Results from this study indicate a strong interaction between the internal microcircuit features and the external film-cooling from the slot exit. Asymmetric cooling patterns downstream of the slot resulted from the asymmetric pin fin design within the microcircuit. Adiabatic effectiveness levels were found to be optimum for the slot design at a blowing ratio of 0.37. The pin fin arrangement along with the impingement cooling at the microcircuit entrance increased the area-averaged heat transfer by a factor of three, relative to an obstructed channel, over a Reynolds range of 5,000 to 15,000.

Acknowledgments

First and foremost, I have to thank the most important person in my life, my wife Tricia. Without your unconditional support, love and occasional kick in the pants, I never would have achieved as much as I have. I hope you were able to take something positive away from your long hours at the cement (cEEEEment) plant, but I owe you more than I could ever repay for sticking with me these past two years.

I have to thank my family as well, there's no way to explain how much they have influenced my life. Dad, you've got more practical knowledge about any subject under the sun than anyone I know. When I picture myself as a husband, father and professional, you are the mold I hope to fill; thank you. Mom, you have given me the gift of ambition. Your overachievement has instilled in me a drive for perfection. You've set the example of leadership and achievement that I can only hope to match in my life. Thank you for everything. The two of you helped make me the person I am today, and I'm proud of where I'm from. Beth, you have the biggest heart of anyone I've ever met. You're generous to a fault and give until you have nothing, I wish I were as open-minded and giving as you. The only advice I will ever give you is this; save something for yourself, you deserve it.

I have to mention VMI as well. While I was there I spent a lot of time telling people how awful it was. Unfortunately, it took leaving to realize what 'the I' really did for me. I owe my work ethic, my ability to work under pressure, and, most importantly, my honor to VMI.

What would an Acknowledgments page be without everyone's nickname? You guys have made these two years fly by. I wish I had room to say something about everyone, but I don't have much page left. Arkie, Couchy, JEChris, Big D, Fratty, the Rickster, Chris, Brown, S2H, Peyton, Will Pocket Will, Scritto (aka JOOOOOOOOe), Angela, and, of course, Paul; I couldn't have done it without you. Well maybe I could have, but it might have been done much faster and with better quality. Special thanks go out to Erin and Nick. Nick, without your construction help and tutelage, I would have surely put an eye out by now. Erin, we have achieved a lot, despite our amazing inability to communicate anything to each other. You've been a great partner, best of luck.

Finally, I have to thank Karen. Thanks for keeping me right there in the middle, not too up, not too down. You led me like a general and treated me like a colleague, and I thank you. You've been the best boss I've ever had.

Contents

Nomenclature

A	= area
B	= blue
d	= streamwise slot length, standard pin fin diameter
D_h	= hydraulic diameter;
f	= friction factor
F_M	= PinFin predicted Friction Multiplier
G	= green
h	= heat transfer coefficient
I	= momentum flux ratio;
k	= thermal conductivity
L	= fin efficiency channel height
M	= mass flux ratio; blowing ratio;
NHFR	= net heat flux reduction;
Nu	= Nusselt Number;
P	= pressure or spanwise slot spacing
p	= perimeter
q''	= heat flux
Q	= heat transfer
R	= red
Re	= Reynolds Number;
s	= cooling feature geometry normalization factor
s_n	= streamwise pin fin spacing
s_p	= pitchwise pin fin spacing
t	= thickness
T	= temperature
TC	= thermocouple
u	= uncertainty
U	= Velocity

w	= spanwise slot width
X	= streamwise distance
Y	= spanwise distance
Z	= pitchwise distance

Greek:

δ	= partial derivative
ΔP	= static pressure differential
ε	= surface emissivity
η	= adiabatic effectiveness;
η_f	= fin efficiency;
η_{GT}	= Brayton Cycle gas turbine efficiency;
Ω	= electrical resistance in Ohms
ρ	= density
σ	= Boltzman Constant;

Subscripts:

$\overline{\text{variable}}$	= spanwise averaged value
$\overline{\overline{\text{variable}}}$	= area averaged value
o, ∞	= upstream with no blowing
∞	= mainstream
∞,corrected	= mainstream adjusted for boundary layer cooling
1	= engine air inlet
2	= compressor exit
3	= turbine inlet
4	= turbine exit
avg	= average
AW	= adiabatic wall

bg	= background
bulk	= unobstructed channel
c	= coolant
conduction	= due to conduction heat transfer
const	= constant
convection	= due to convection heat transfer
cs	= cross section
dynamic	= due to fluid motion
e	= effective
exit	= evaluated at the exit plane
f	= fin
freeconv	= natural convection
heater	= describing the inconel strip heater
inlet	= inlet location
j	= jet
line	= along a specified line
m	= mean
max	= maximum possible value
MC	= microcircuit
o	= unobstructed baseline (with film cooling for NHFR)
PW	= Pratt & Whitney
removed	= taken away
static	= fluid at rest
surf	= surface
surr	= ambient
total	= sum of all portions
TS	= mainstream test section
VT	= Virginia Tech (current study)
w	= wall

List of Tables

List of Figures

Chapter 1

Introduction

Since their first trip through the sky in 1939, gas turbine engines have taken man to the edge of the atmosphere and across the globe. We have used them to propel vehicles of war and to travel around the world. Gas turbine engines are vital components of aircraft that carry everything from passengers and commerce to bombs and air superiority. Since that first flight in 1939, gas turbine technology has thrust forward at a staggering pace. Airlines demand cheaper, quieter and more efficient engines, while global militaries push the boundaries of performance with the most technologically advanced engines produced in the world. While their end goals are completely different, these two groups agree that raising turbine inlet temperature is the best way to improve the performance of their engines.

Some analogies are in order to convey the magnitude of the gas turbine engines' power. The best military engines can produce over 175 kN of thrust [www.pratt-whitney.com]. That's enough thrust to suspend ten full size sport-utility vehicles in mid-air. That fact is even more impressive when we consider that the engines weigh less than one tenth of their thrust capacity. The aircraft they propel can accelerate from a standstill to 300 km per second in just 11 seconds [www.f-16.net]. Commercial engines can carry over 500 passengers 8,000 miles across the globe before filling the fuel tanks [www.boeing.com]. As incredible as these performance specifications are, they are for yesterday's engines. The engines of the future will fly faster, further, and more efficiently than ever. As mentioned, the key to improving all of these goals is to raise the temperature of the hot gas entering the turbine, the portion that produces the engine's mechanical power.

All gas turbine engines operate on a theoretical cycle invented by George Brayton in 1870, the cycle is aptly named the Brayton Cycle. The cycle efficiency is described by the following:

$$\eta_{GT} = 1 - \frac{T_4 - T_1}{T_3 - T_2} \tag{1.1}$$

where T_1 is the temperature of air entering the engine, T_2 is the temperature of air exiting the compressor, T_3 is the turbine inlet temperature, and T_4 is the temperature of gas exiting the turbine. Clearly, increasing the turbine inlet temperature will result in greater cycle efficiency. The thrust output of the engine is also directly related to the turbine inlet temperature [Çengel and Boles, 1998]. Engineers have steadily increased the turbine inlet temperature to fit their performance needs. In the first engine designs, turbine temperatures were not a problem, but just another design point to be varied. About 30 years ago, technology caught up with material limits.

1.1 Turbine Cooling Technology

Today's turbines operate well above the melting temperatures of their structural components. The material of a typical turbine vane will melt at 1315°C, while the temperature of the gas exiting the combustor is well over 1650°C. The turbine inlet is one of the harshest thermal environments in modern engineering. Engine failure is the most obvious danger in such an environment. Perhaps even more costly to engine manufacturers, the thermal environment can seriously degrade the life of turbine parts. Figure 1-1 gives an idea of the life savings for a given reduction in metal temperature experienced by a first stage turbine vane. Not to be discouraged, engineers have kept engines in the air with several ingenious cooling methods.

Internal Cooling. The most tested method of turbine component cooling is to pass cool air from the compressor through the turbine parts to remove some of the heat imparted by the mainstream gas flow. Engineers called this internal cooling. This was first proposed in the 1960's, and is still used today. Engineers were able to significantly raise the turbine inlet temperatures while still using the same materials for their components. Hot mainstream combustion gasses heat the turbine components. Instead of

allowing the temperature of these components to keep rising (until they melt), active internal cooling schemes give the heat a place to go, into the cooling fluid. Cool air bled from the compressor is circulated through turbine components, where it removes some of the heat imparted from the mainstream gas. The heat removed from the component is defined by Equation 1.2:

$$Q_{removed} = h \cdot A_{surf} \cdot (T_w - T_c) \tag{1.2}$$

where $Q_{removed}$ is the amount of heat removed from the blade or vane, T_w is the metal wall temperature, T_c is the cool air temperature, A_{surf} is the heat transfer surface area inside the blade, and h is the convection heat transfer coefficient.

The keys to maximizing the amount of heat removed are the convective heat transfer coefficients and surface area. Clearly, a greater convection coefficient will result in greater heat transfer, as will increased surface area. Heat transfer coefficient is a function of many things including surface geometry, fluid motion (turbulence), fluid properties, and bulk fluid velocity [Çengel and Boles, 1998]. Often times, fluid properties and bulk fluid velocity are variables that cannot be controlled. Engineers are forced to manipulate surface geometry and fluid turbulence levels to increase their heat transfer coefficients. Engineers have used several methods to augment heat transfer in turbine component cooling channels. Many designers place ribs along their channel walls, normal to the flow, to increase heat transfer surface area and turbulence levels. Some engineers try to increase turbulence levels and delay boundary layer separation by placing small dimples on the walls of the heat transfer areas, much like the dimples on a golf ball [Bunker et al., 2003]. Still others put cylindrical posts, pin fins, in the path of the flow to both increase surface area and turbulence levels. Currently, most cooling configurations use some combination of all the above cooling schemes. Figure 1-2 shows an example of an internal cooling configuration. This study uses a modified method of pin-fin cooling, which will be discussed later.

External Cooling. When it became evident that internal cooling could not adequately cool turbine components alone, engineers decided to concentrate their efforts

closer to the source of the crippling heat. The mainstream gas transfers heat to the turbine components through the same heat transfer mode, convection. In contrast with internal cooling, engineers try to reduce the heat transfer coefficient outside the vane. Lowering heat transfer coefficient can be difficult. The aerodynamics of turbine flows are complex, highly turbulent, and can be difficult to predict. Even when predicted accurately, some flow structures that increase heat transfer are characteristic to turbine passages and cannot be changed. Engineers realized that the coolant air circulated through the internal passages of the turbine components, even after being heated by the metal, was still cooler than the external metal temperatures. They determined that a thin film of cool air on the external airfoil surfaces would serve to insulate the metal from the hot mainstream gas. Thus film cooling was born, Figure 1-3 shows an example of a film cooled turbine blade. Air bled from the compressor is injected through discrete cooling holes in the airfoil skin and forms a thin layer of cool gas that adheres to the metal surfaces and, ideally, prevents high heat transfer to the metal.

In practice, engineers work very hard to keep the cool film on the walls. Too much coolant forced through the small cooling holes will separate from the wall (called blow-off, or jet detachment). Separated coolant completely fails to protect the metal. Additionally, strong pressure gradients in the turbine can sweep coolant from needed locations, resulting in hot-spots on the airfoils and endwalls. Cooling effectiveness is measured with a dimensionless variable called adiabatic effectiveness, defined in Equation 1.3:

$$\eta_{AW} = \frac{T_\infty - T_{AW}}{T_\infty - T_c} \tag{1.3}$$

where T_∞ is the mainstream gas temperature, T_c is the coolant temperature, and T_{AW} is the temperature of the metal if it were an adiabatic surface (allows no heat transfer). The adiabatic wall temperature is the same temperature as the fluid directly adjacent to the wall. Higher adiabatic effectiveness indicates a cooler surface, while a lower effectiveness indicates a hotter surface. In addition to internal cooling performance, this study will assess the external film cooling adiabatic effectiveness of a new cooling

design. In addition, this study will actually study the effects of the internal cooling arrangement on the external effectiveness.

1.2 Microcircuit Cooling

Pratt and Whitney, the sponsor of this work, has developed a new turbine component cooling scheme known as microcircuit cooling. Microcircuit cooling aims to provide both internal and external cooling by both raising the internal heat transfer coefficient and providing film cooling to the external metal. While this concept is not new to turbine engineering, the application of the concept is entirely unique. The microcircuit is named as such because the internal flow passages are extremely small and intricate. Previous internal cooling schemes use internal channels that complete their circuit through the vane or blade in two to four passes. Pratt & Whitney's design still uses these large cooling channels, but additionally employs micro channels through the skin of the airfoil, between the internal channel and the external surface. Figure 1-4 is a cross section schematic of the microcircuit channel through the skin of the airfoil. These channels are necessarily small; the metal between the internal channel and the airfoil's external surface is only as thick as four standard post cards. The microcircuits fit in that space.

Putting the microcircuit channels close to the airfoil surface is desirable for two major reasons. First, the smaller channels result in greater velocities for the air blown through them. As discussed above, this increases turbulence levels, and therefore, heat transfer—an advantageous feature for internal cooling schemes. Second, the closer the channels are to the surface, the more heat they can remove from the external wall. This is due to the nature of conduction heat transfer. So far, the only method of heat transfer discussed has been convection, but the heat from the external gas path must pass through solid metal before being convected away by the internal cooling flow. This necessitates an understanding of the conduction heat transfer through the metal. Conduction heat transfer is strongly dependent upon the thermal conductivity and thickness of the material in question. While most metals offer relatively low resistance to heat transfer (through

their high thermal conductivities), between two cross sections of identical material, a thinner sample will always allow greater heat transfer. Clearly, the closer the microcircuit channels are to the surface, the more heat they can remove.

Another aspect of the microcircuits that was alluded to earlier is the heat transfer augmenting features within the channels. While an unobstructed channel provides good heat transfer characteristics, the addition of pin fin features can increase the turbulence levels of the cooling air, increase the surface area from which to transfer heat, and provide areas of locally high velocity (also increasing turbulence). The focus of this study is to evaluate a microcircuit cooling design developed by Pratt and Whitney, for use in their cutting edge military aircraft engines. The design not only incorporates the micro-cooling channels, but a varied pin fin array with discreet, rectangular cooling slots to provide film cooling on the external airfoil surface. Part of the unique design of the microcircuit is the variation of the pin fin cross sections. Most designs use standard cylindrical pin fins, while the Pratt and Whitney microcircuit design uses widely varying cross sections throughout the pin fin array. In addition to increasing heat transfer augmentation, the pin fins create a large pressure drop as well. This is the detrimental aspect of the microcircuit design. Along with the heat transfer results, this study will analyze the pressure drop characteristics of the microcircuit design and compare the results to the frictional losses associated with flow through a straight channel.

1.3 Research Objectives

This study has three distinct objectives. We will quantify both internal and external cooling performance for the specific microcircuit design provided by our sponsors, Pratt and Whitney. Additionally, the third objective is to describe the effects that the internal cooling scheme has on the distribution of the external film cooling flow. External adiabatic effectiveness results will be compared to film cooling data taken by other researchers here at Virginia Tech, as well as elsewhere. Internal heat transfer coefficient results will be compared to standard pin fin analyses, dimpled channel studies, and ribbed channel results.

The second chapter of this document will summarize the pertinent literature on the topics of external film cooling and internal convective cooling. The third chapter will discuss the design and construction of the testing facility. Our data reduction methodology will be discussed in the fourth chapter. The fifth chapter will discuss our results, while the sixth will draw conclusions and make recommendations for future work.

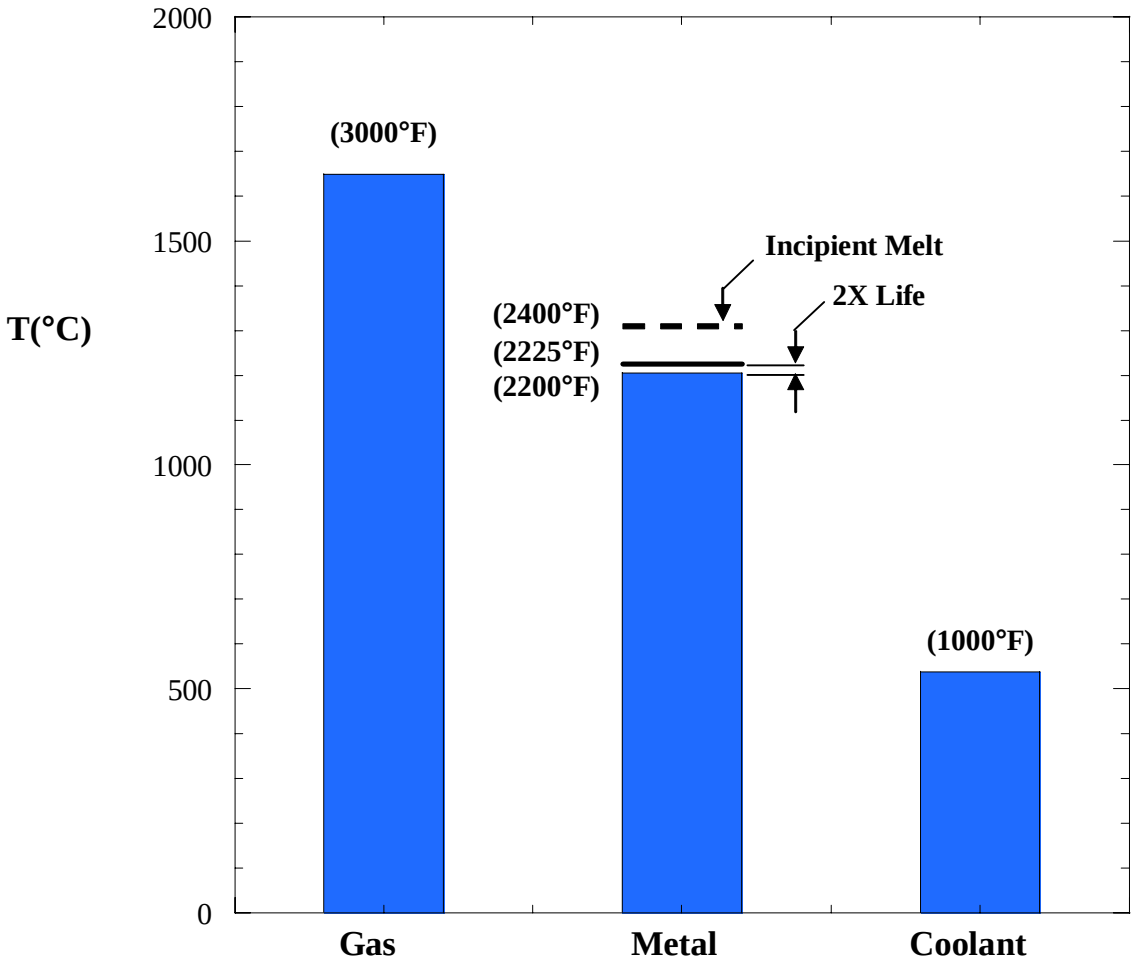

Figure 1-1 Typical first stage turbine vane temperatures. Note the increased life for a small drop in metal temperature.

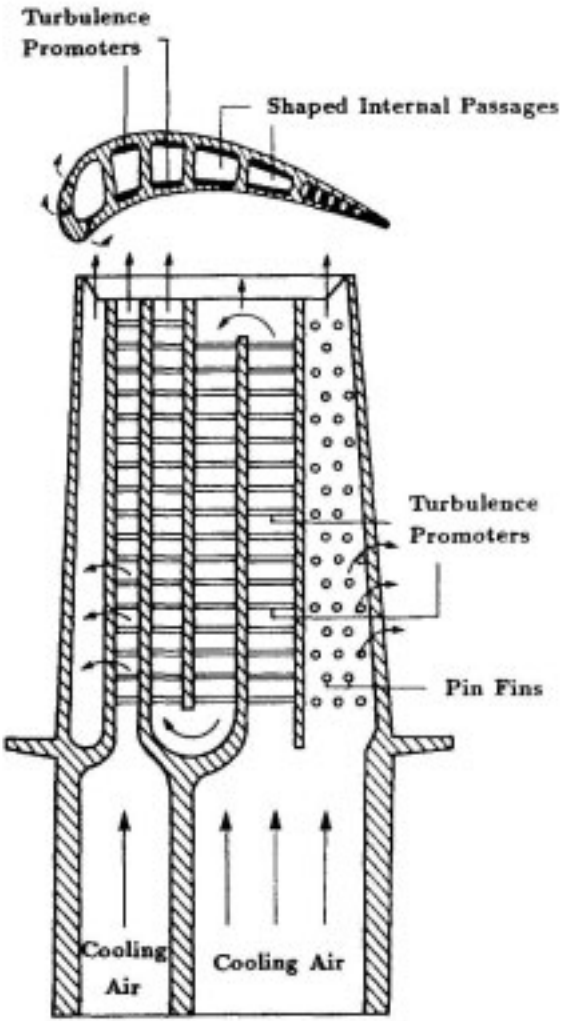

Figure 1-2 Internal cooling passages. The ribbed channels promote turbulence and increase heat transfer surface area, while the pin fins cool the trailing edge [Han et al., 1984].

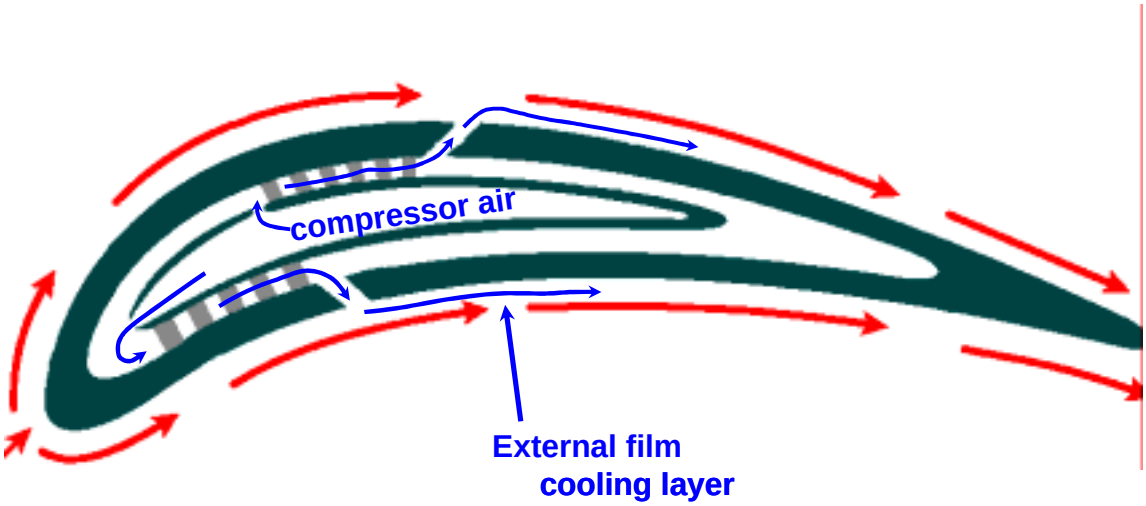

Figure 1-3 Film cooled airfoil. Coolant stays near the metal and forms an insulating barrier between the hot combustion gas and the airfoil skin.

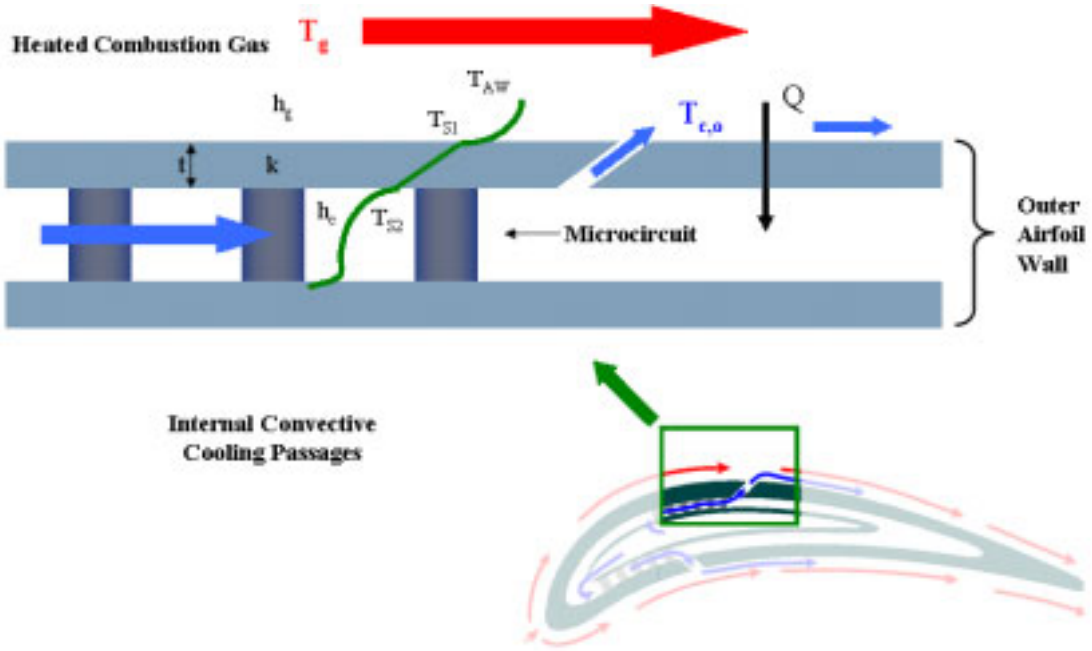

Figure 1-4 Microcircuit cross section. The pedestal features increase internal heat transfer and exhaust coolant through film cooling features.

Chapter 2

Review of Relevant Literature

Turbine heat transfer is a highly specialized area of research. General heat transfer is difficult enough, but the special constraints of the gas turbine require the very best researchers. The field of turbine heat transfer has seen hundreds of contributors over its half century life span. Each has provided valuable insight into the extremely complicated turbine environment, although very few have established themselves as true experts in the field. However, the schemes discussed in this paper, internal convective cooling and external film cooling, each have several researchers that have consistently set the standards for the rest of the field. The first two sections of this chapter will discuss the seminal studies associated with the two cooling methods evaluated by the current research. Additionally, they will discuss the studies that are most recent in the field and closely related to the current research. External cooling studies will be summarized in Section 1, while internal cooling studies will be discussed in Section 2. In addition, the third section will evaluate the uniqueness of the research with regard to both geometry and objective.

2.1 External Film Cooling Studies

Researchers have studied film cooling for over 35 years. Many film cooling studies were performed in the early 1960's. Goldstein [1971] describes the state of the art at that time. Many studies at the time looked at tangential coolant injection, although the earliest examination of injection physics did not have to do with turbine components at all. Wieghardt [1946] described the physics of injection heat transfer, although his study concerned the injection of hot fluid over aircraft wings to prevent icing. A major contribution of his work was the correlation of adiabatic effectiveness with the parameter X/Ms, which normalized an observed cooling flow's benefit by its mass flow and cooling

feature shape. That normalization, which will be discussed in detail in Chapter 5, allowed comparison between different film cooing mass flux ratios and geometries. The ability to make comparisons across vastly different experimental conditions set the stage for the explosion of film cooling research to follow. Some time later, Scesa [1954] first investigated the effects of coolant ejected through slots normal to the mainstream flow while Papell [1960] was the first to investigate the effects of coolant slots and holes inclined at varying streamwise angles.

Since those first studies, film cooling research has come a long way. Researchers vary countless experimental parameters in the ultimate search for the optimum film cooling scheme. As mentioned, many of the earliest studies investigated tangential coolant injection. Figure 2-1 is an example of a tangential coolant injection feature (also known as a backward facing step [Goldstein, 1971]. However, Metzger et al. [1972] found that tangential slot injection caused a measurable increase in heat transfer coefficient along the wall. In response to this phenomenon, they concluded that a proper heat transfer analysis must account for the increase in heat transfer coefficient as an evaluation parameter. Wittig et al. [1994] continued this work, evaluating both adiabatic effectiveness levels and heat transfer coefficients for a backward facing step over a wide range of blowing ratios. That study found that, depending upon geometry and coolant flow rate, peak heat transfer coefficients can be 200 percent higher than the heat transfer coefficients with no coolant blowing. Recall from Chapter 1, high heat transfer coefficient outside the turbine component increases metal temperature and degrades the part's life. Even in 1972, results like these prompted researchers to evaluate alternate methods of film cooling.

In general, engineers can always expect an increase in heat transfer coefficient as a result of film cooling injection. The turbulent mixing of the jet with the mainstream causes the increase in heat transfer. However, the increase in heat transfer coefficient is only detrimental when it outweighs the increase in adiabatic effectiveness provided by the coolant flow. The relation between these two competing phenomena is called the heat load ratio, or net heat flux reduction (NHFR). NHFR is defined as follows [Sen et al., 1996]:

$$NHFR = \frac{q''}{q_o''} = \frac{h}{h_o}\left(1 - \eta \frac{T_\infty - T_c}{T_\infty - T_w}\right) \tag{2.1}$$

where q'' is the heat flux to the airfoil wall without film cooling, q_o'' is the heat flux to the wall with film cooling present, h is the heat transfer coefficient corresponding to no blowing, h_o is the heat transfer coefficient with blowing, T_∞ is the mainstream gas temperature, T_c is the coolant temperature, T_w is the wall temperature and η is the local adiabatic effectiveness. NHFR values less than unity indicate beneficial component cooling. Above NHFR levels of one, a cooling scheme does no cooling at all; it actually causes a greater heat flux to the component. The current study will only evaluate the adiabatic effectiveness levels of our coolant configuration.

The research described above was extremely important in advancing the knowledge base of film cooling studies. Since those studies, researchers have focused on refining film cooling configurations within the NHFR bound. Goldstein et al. [1974] examined lateral expansion through the cross section of a film cooling hole. Thole et al. [1996b] presented results for film cooling holes with both lateral and streamwise expansion angles. Figure 2-2 is a cross section of the cooling geometry evaluated by Thole et al. [1996b]. Both studies showed adiabatic effectiveness levels downstream of an expanded hole are consistently higher than those measured downstream of a hole with constant cross section. Increased levels were due to both decreased exit momentum (caused by the increased exit area) allowing less chance for coolant jet lift-off, and increased coolant spreading on the external surface. Figure 2-3 is a schematic of the test facility used for the Thole et al. [1996b] study. Incidentally, that study provided the inspiration for the two channel test facility constructed for the current study.

Countless other researchers have done film cooling *hole* studies, but very few coolant *slot* studies have been performed since the inception of film cooling. Most of the studies that have been undertaken use a continuous cooling slot, such as may be found at the combustor-turbine interface. Such configurations provide film cooling to a turbine's endwall only, they cannot cool the airfoil surface. Liburdy et al. [1997] considered continuous slots with both straight and shaped cross sections. Figure 2-4 is a detailed cross section of the slot geometry tested for that study. Liburdy et al. [1997] found

results similar to Goldstein [1974] and Thole et al. [1996b]. The shaped slot mitigated a separation region at the slot inlet, thereby reducing the slot injection angle with respect to the mainstream. This ensures greater cooling, resulting in higher effectiveness levels, especially downstream. Encouragingly, Liburdy et al. [1997] also found reduced heat transfer coefficients downstream of the shaped cooling slot. The reduction in heat transfer coefficient was attributed to the attenuation of the separation region downstream of the slot exit by using the shaped slot configuration. However, as mentioned, this continuous slot geometry is more applicable to the endwall region of a turbine component. Structural concerns prevent engineers from employing a continuous slot along large portions of a blade or vane's span.

Rhee et al. [2002] completed a study that came slightly closer to matching the geometry of the current study. They compared circular film cooling holes to ones of square cross section. In addition, they investigated a square hole with an expanded exit, making the breakout area resemble the current study's two-dimensional discreet slot. However, like most studies, their film cooling injection took place at an angle of 35° from the mainstream. Figure 2-5 is as schematic of the configurations tested by Rhee et al. [2002]. While Section 2.3 is dedicated to the uniqueness of the current study, there is a clear gap in the literature when investigating slot cooling for application on the mainbody airfoil. The fact that the current study uses a normal injection angle serves to distinguish itself even further.

Smith et al. [2004] studied slot geometry matching the current study and collected adiabatic effectiveness measurements, both on a flat plate and a blade. However, Smith's geometry did not include a microcircuit between the coolant plenum and slot exit.

2.2 Internal Convective Cooling Studies

In addition to film cooling, turbine durability engineers realized that the passages feeding the injection features could provide significant convective cooling on the internal side of the turbine component. Engineers have long studied heat transfer augmentation through increased flow turbulence. Heat transfer in channels with relative wall roughness

characteristics were completed in the early 1960's, although they were not specifically aimed at turbine cooling [Hall, 1962]. Burggraf [1970] applied the technology to the cooling channels in a turbine blade. These studies cemented the knowledge base for future studies in internal cooling.

The majority of recent studies can be split into two categories, ribbed channel studies and pin fin studies. There are other cooling methods as well; Bunker and Donnellan [2003] and Mahmood et al. [2001] studied the heat transfer augmentation provided by adding shallow concavities to a channel's walls. However, most studies focus on the more conventional cooling methods. Researchers in the 1980's produced a flood of research regarding heat transfer through channels with turbulence promoters. Some of the papers on the subject include Boyle [1984], Han [1984], Han et al. [1985], Metzger and Vedula [1987], and Taslim and Spring [1987]. All of these studies characterized heat transfer augmentation and/or friction factor augmentation through cooling channels with various rib geometries.

In parallel with the ribbed channel studies, researchers have studied the heat transfer benefits and friction penalties associated with pin finned arrays. The earliest studies did not directly apply to the turbine industry. Zukauskas [1972] collected the seminal results for heat transfer from a cylinder in cross flow completed at the time. The length-to-diameter ratios in those studies were too large for consideration in a turbine application, however. Brown et al. [1980] was the first to specifically apply the heat transfer analysis of short pin fin arrays to the cooling of a turbine airfoil's trailing edge. Several researchers significantly advanced the state of the art in the early 1980's. Metzger and Haley [1982a] performed heat transfer and flow visualization experiments for pin fin arrays with both high and low fin efficiencies and concluded that the results for the two different pin types matched very closely. However, Nusselt numbers for the different pin materials demonstrated differing Reynolds number dependence. Metzger et al. [1982b] characterized the developing heat transfer through staggered pin fin arrays and varied the spacing of the array. Metzger et al. [1982b] found that the peak heat transfer region occurred earlier in the array with larger streamwise spacing. VanFossen and Simoneau [1984] investigated the effects of varying the number of pin fin rows in an array on the overall heat transfer. That study found that the addition of pin-fins upstream

of a staggered array could produce higher Nusselt numbers than additional rows upstream of an inline array. Metzger et al. [1986] investigated the effects of non-uniform pin fin arrays. The net result of that study was the determination of a process to combine the row by row effects of uniform arrays by superposition to determine the behavior of non-uniform arrays. Armstrong and Winstanley [1988] investigated the effects of varying pin fin spacing and height-to-diameter ratio and determined correlations for array averaged heat transfer and Reynolds number.

The 1990's saw further refinement of pin fin array research. Chyu [1990] investigated heat transfer and pressure drop between inline and staggered pin fin arrays, both with and without a pin-endwall fillet. Figure 2-6 is a schematic of the different pin fin arrangements tested by Chyu [1990]. They found the fillet to be detrimental to heat transfer augmentation. Interestingly, Thole and Zess [2001] produced reductions in near-wall mainstream turbulence levels at the junction of a vane and endwall by attaching a fillet structure. Decreased turbulence levels would result in decreased heat transfer coefficient, as observed by Chyu [1990]. Clearly, however, results were perceived as positive by Thole and Zess [2001], since a reduction in turbulence on the external side helps cool the vane.

Chyu et al. [1998] investigated the heat transfer from pin fin arrays of varying cross section for application in the trailing edge region. Among the geometries tested, Chyu et al. [1998] evaluated cubic and diamond pin fin arrays and compared them to standard, circular pin fins; again for the trailing edge. The study found that cubic pin fins produce heat transfer rates significantly higher than diamond or pin fin arrays with only moderate friction augmentation. As was shown in Chyu [1990], the staggered array always produced greater heat transfer augmentation, but greater pressure loss as well. Chyu et al. [1999] studies short pin fin arrays in the trailing edge, but attempts to characterize the heat transfer from both the pin fin surfaces and the endwall surfaces. Previous studies investigating pin fin heat transfer heated either the pin fins, or the endwall, but not both. Chyu et al. [1999] used a mass transfer technique that effectively rendered the entire wetted surface thermally active, as opposed to the pin fins or endwall alone. The net result of the study was that the heat transfer coefficients around the pin fins are consistently higher than those found on the endwalls. However, despite the

increased heat transfer coefficient, the pin fins still contribute little to the overall heat transfer to the cooling fluid. Chyu et al. [1999] found this discrepancy to be due to the larger heat transfer area of the endwall compared to the area of the pins, especially in arrays that optimize pin spacing for minimal pressure loss.

As mentioned, all of the above studies applied the pin fin technology to the trailing edge of the turbine airfoil. As described in Section 1.2, Pratt & Whitney has developed a new method of cooling to be used throughout the airfoil. Microcircuit cooling places pin fins, and other irregularly shaped turbulators, throughout a narrow channel located in the airfoil skin. Since the microcircuits are so small, their placement is not limited to the trailing edge. Several studies done at Virginia Tech have investigated microcircuit cooling applied throughout turbine components. Couch [2003], Christophel et al. [2003], and Hohlfeld [2003] investigated the use of a microcircuit cooling feature on the tip of a turbine blade. Ranson [2004] studied the use of microcircuits to cool the blade hub. Couch [2003] and Christophel et al. [2003] studied microcircuit performance with experimental validation in a large scale, non-rotating, low-speed wind tunnel located in the Virginia Tech Experimental and Computational Convection Laboratory (VTExCCL). Hohlfeld [2003] also worked in the VTExCCL, but performed a vast computational study used to predict tip behavior and verify experiments done by Couch [2003] and Christophel et al. [2003]. Ranson [2004] used the same wind tunnel as the other researchers, but he constructed another test section to shift the measurement plane from the tip to the endwall.

2.3 Uniqueness of Research

The current study is unique for several reasons. First, with regard to film cooling, literature for the specific cooling feature geometry is extremely sparse. Figure 2-7 is a cross section of the current study's injection feature. The fact that the cooling slots inject normal to the mainstream flow alone makes them unique, but the radiused transitions from microcircuit passage to the film cooling exit plane are unparalleled in the literature. As far as internal cooling, the microcircuit design is not only unique in the body of

internal cooling literature, but unique among microcircuits as well. The tip microcircuit discussed in the previous section did not make use of any turbulators, it was simply an air passage located near the surface of the tip. Figure 2-8 is a graphic of the tip microcircuit. The endwall microcircuits, specifically one located beneath the suction side passage endwall, used pin fins to augment heat transfer. Figure 2-9 is a schematic of the endwall microcircuits investigated by Ranson [2004].

The microcircuit studied for this investigation was unique both in placement and design. Intended for placement in the airfoil skin, the periodic microcircuit array studied here would be replicated hundreds of times over in the production airfoil. The cooling pattern, composed of several rows of irregularly shaped pin fins, is peerless in design. In addition, microcircuit designs employed in the mainbody skin of an airfoil are absent in the literature, even among microcircuit studies.

Despite the unparalleled geometry and the novelty of the microcircuit concept, one of this study's goals is unique even among non-proprietary work. A main goal of this research is to evaluate the effects that the internal cooling features have on the external film. Couch [2003], Christophel et al. [2003], and Hohlfeld [2003] certainly documented the effects of coolant exiting their microcircuit design, but they did not attempt to draw conclusions as to the effects due to specific aspects of the design they examined. This study will do just that. We will evaluate the magnitude of the cooling benefit due to both internal convective cooling and external film cooling, and further explain the effects that our specific microcircuit geometry has on both internal and external performance.

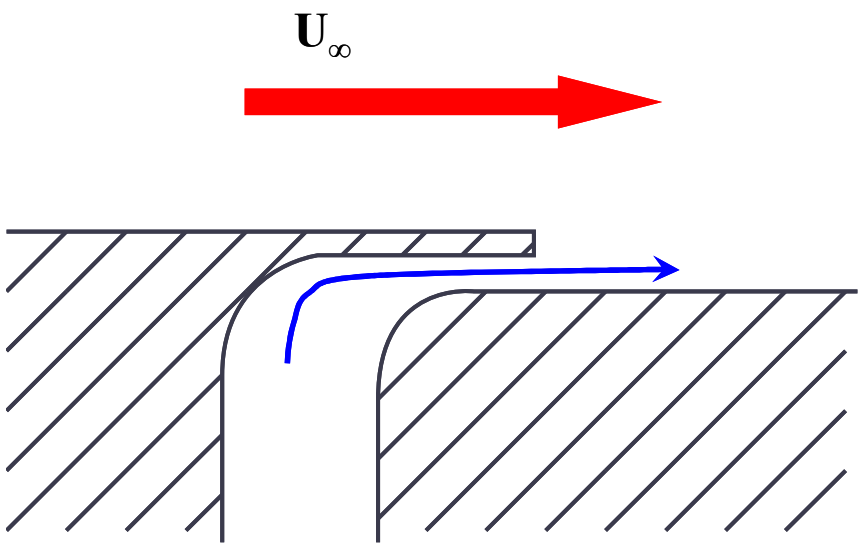

Figure 2-1 Tangential film cooling feature [Goldstein, 1971].

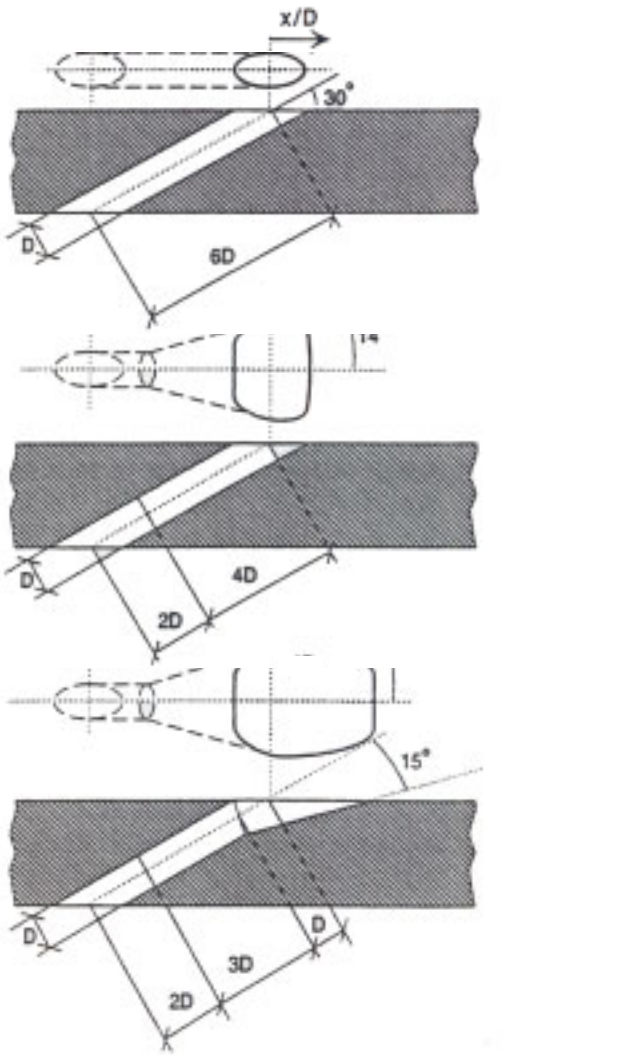

Cylindrical, fanshaped, and laidback fanshaped hole geometries

Figure 2-2 Cross section of film cooling designs studied by Thole et al. [1996b].

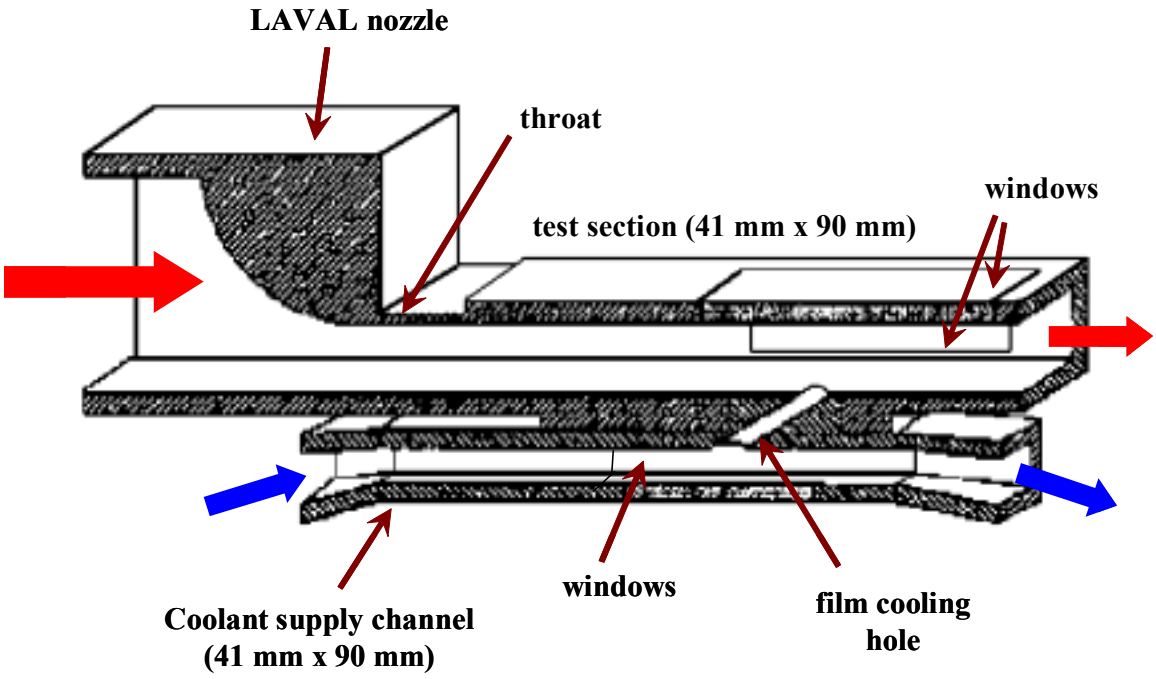

Figure 2-3 Two channel test facility to evaluate a film cooling design. This facility provided the inspiration for the facility constructed for the current study [Thole et al., 1996b].

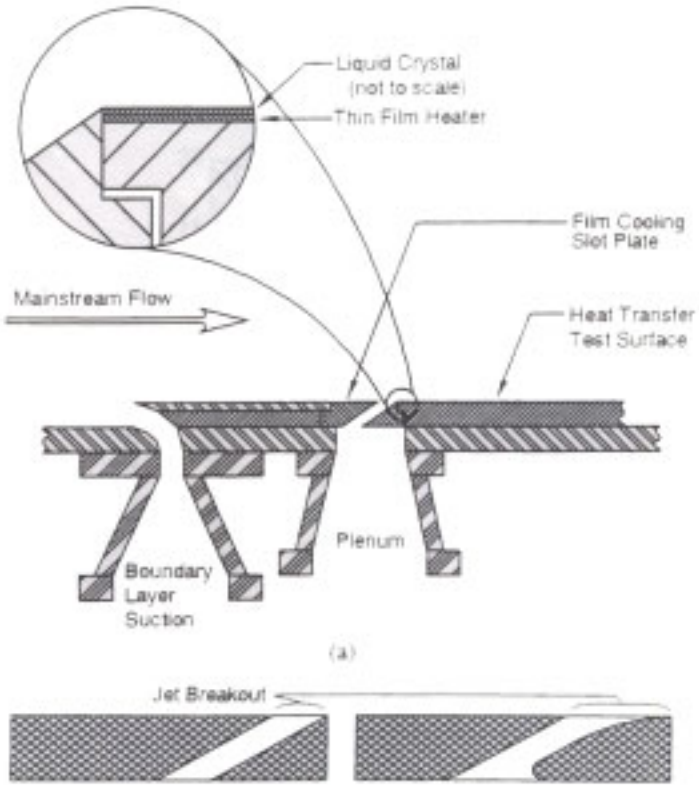

Figure 2-4 Cross section of film cooling slot studied by Liburdy et al. [1997].

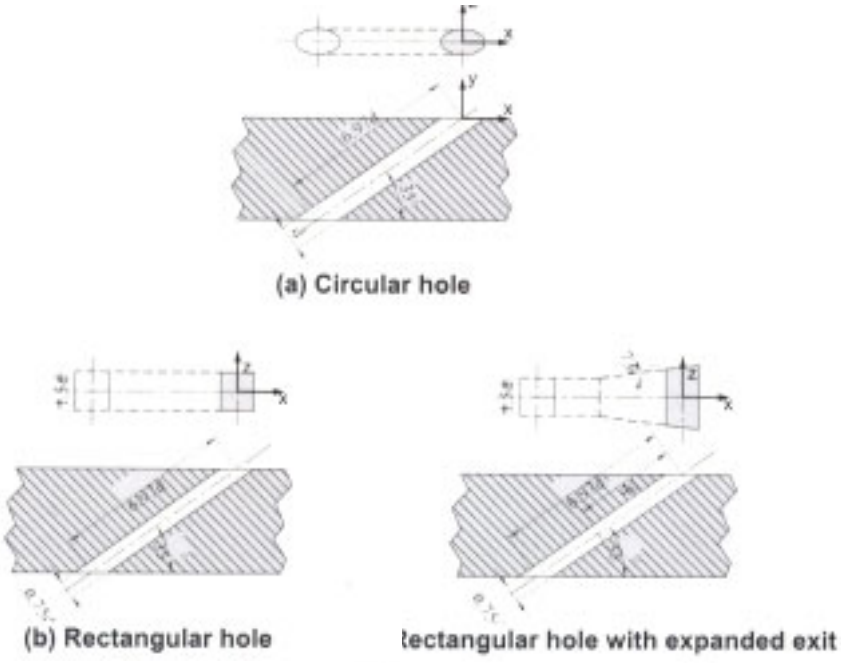

Figure 2-5 Schematic of the cooling configurations tested by Rhee et al. [2002].

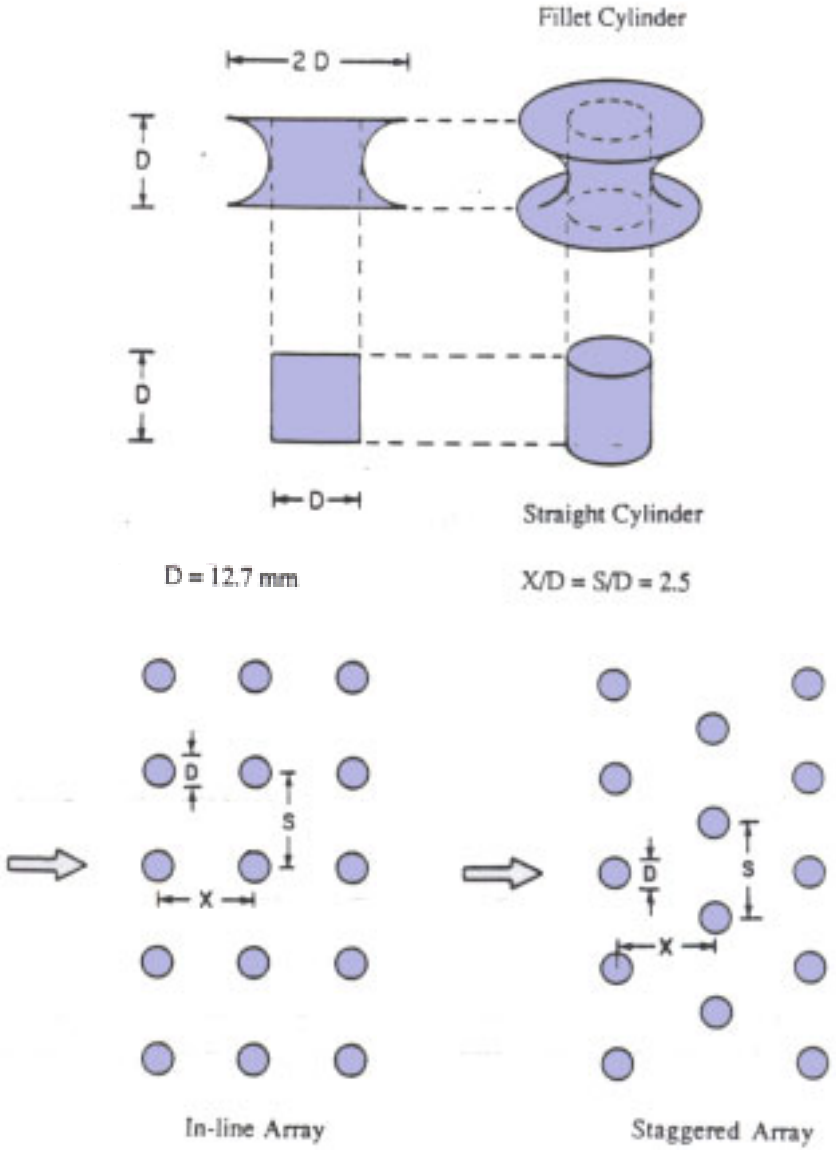

Figure 2-6 Pin fin configurations examined by Chyu [1990].

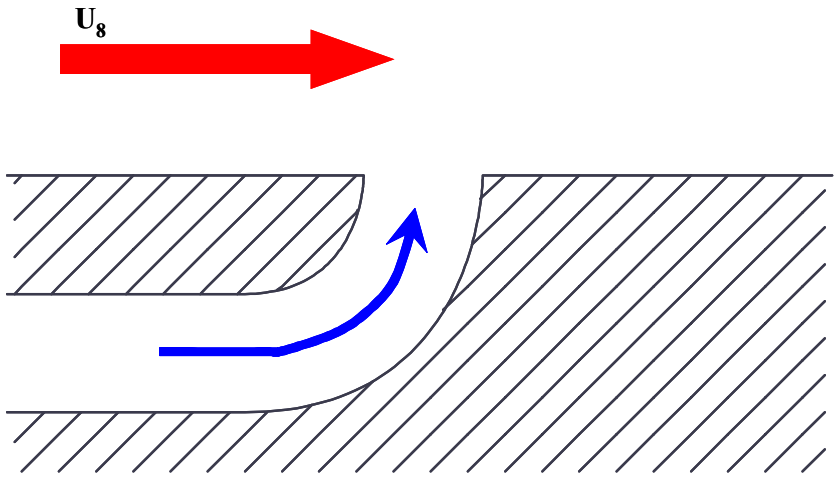

Figure 2-7 Slot injection feature cross section for current study.

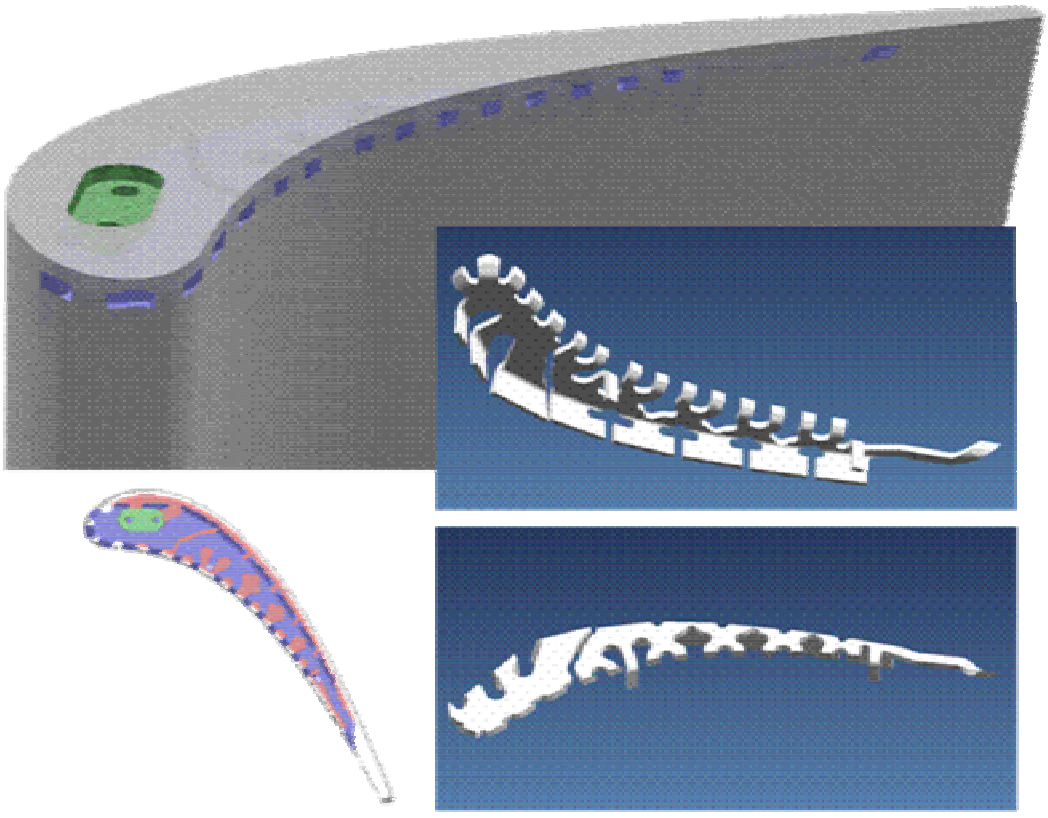

Figure 2-8 Tip microcircuit cooling configuration. The bottom left image is a top view of the tip microcircuit. The images on the right are isometric views of the microcircuit from the top and bottom. The image in the background is the microcircuit (semi-transparent in blue) as positioned in the tip [Hohlfeld,2003].

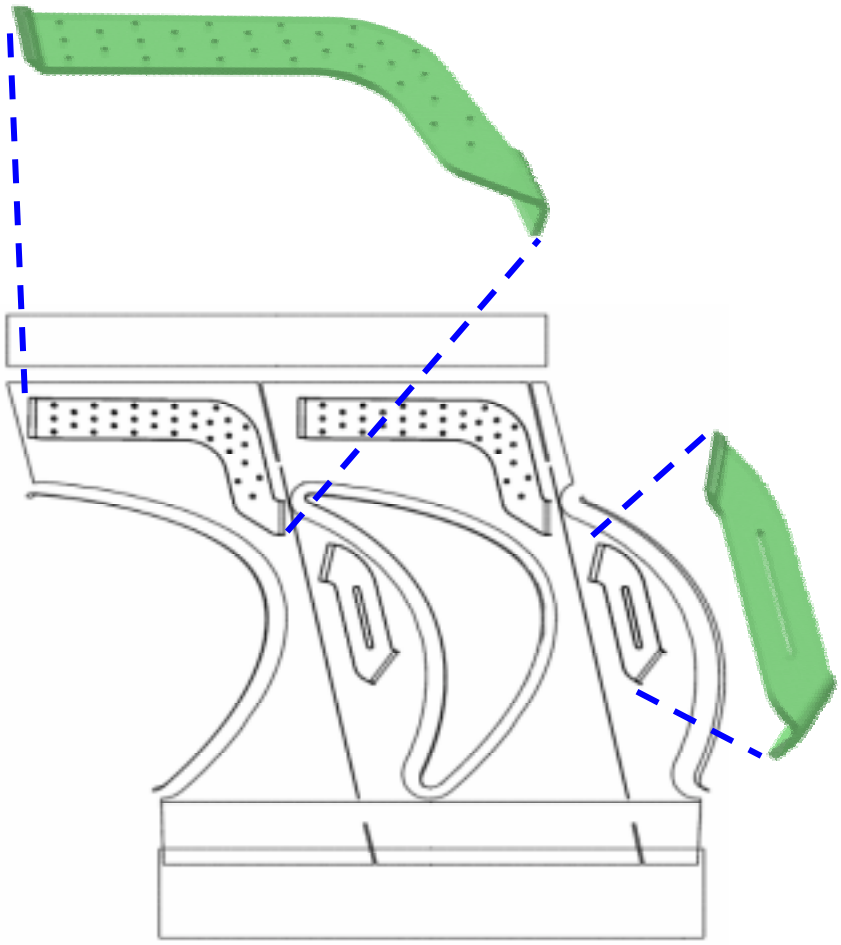

Figure 2-9 Schematic of endwall microcircuit cooling configuration evaluated by Ranson [2004]. The schematic is a top-view of the vane passage endwall. The green exploded views are isometric views of the platform microcircuits.

Chapter 3

Design and Construction of Experimental Facility

The microcircuit designs presented in this study are extremely small at actual engine scale; the airflow channel height would only accommodate four human hairs stacked atop one another. This size constraint does not easily lend itself to laboratory testing. Often, experimentalists do large scale testing of their geometry to improve the spatial resolution offered by their measurement collection media. That is the case for this study as well.

This chapter will discuss the design and construction of a new test facility specifically modeled to test a scaled up microcircuit design. The first section of this chapter will describe the design, construction, instrumentation, data acquisition procedure, and benchmarking of the primary flow loop. The primary loop represents the mainstream flow through a first stage vane passage and will be known as the mainstream loop throughout this document. The second section will discuss the design, construction, geometric specifications, instrumentation, data acquisition procedure and benchmarking of the coolant supply channels. The coolant supply channels correspond to the high pressure cooling air bled from the compressor. The third section of the chapter will discuss the experimental uncertainty of the measured values for both external and internal testing.

3.1 External Mainstream Loop

Because of the novelty of the microcircuit, none of the wind tunnels in the laboratory could accommodate the complex internal and external flow paths required to characterize the desired heat transfer environment. Rather than undertaking an extensive rework of the current wind tunnels, we constructed a new facility. The new facility was a closed-loop, two-channel, recirculating wind tunnel specifically designed to allow

measurements from both sides of the injection cooling feature. Figure 3-1 is a general schematic of the flow paths around the measurement planes. The larger of the two channels simulated the hot, combusted mainstream flow through a turbine airfoil's passage. To move air through the mainstream loop, a blower was placed upstream of the measurement locations. Thermal flow conditioning took place in a heat exchanger upstream of the test section. The blower, heat exchanger, and other mainstream loop components will be discussed in this section. The smaller of the two channels replicates the cooling flow bled from the compressor. Bypassing the combustor, this air is used for film cooling in an actual engine. This coolant loop is fed by an outside compressed air source and will be discussed in detail in the following section of this chapter.

Mainstream Design and Construction. Determining an appropriate scale for the test facility was the first step in the wind tunnel design. Spatial resolution is one of the most attractive aspects of large scale testing, but care must be taken to ensure that all aspects of the experiment can properly scale back to the original operating conditions. It is often impossible to scale or recreate actual engine conditions in the laboratory, as was the case with this study. However, excellent results can still be achieved by matching key non-dimensional parameters. Mass flux ratio—also called blowing ratio—matches engine conditions on the external wall, and we report our results as non-dimensional adiabatic effectiveness. The internal portion of this study matches engine flow conditions with regard to Reynolds number and reports heat transfer results as Nusselt numbers in the microcircuit. Because of our inability to match engine realistic density ratios, external and internal experiments were not performed simultaneously.

As mentioned above, the actual microcircuit was exceptionally small and required significant scaling to achieve reasonable spatial resolution with available measurement techniques. An extensive study was completed comparing several parameters relevant to the microcircuit scale. If the scale was too small, measurements collected would not have fully realized the benefits of large scale testing. If the scale was too large, however, the flow conditions required to match the non-dimensional parameters listed above could not have been achieved practically. Ultimately, the microcircuit was scaled up twenty-five times. This scaling ensured attainable flow conditions, but still allowed detailed

observation of the flow and thermal environments occurring in the microcircuit passages. For the detailed calculations completed for the scaling study see Appendix A.

Once the microcircuit scale was decided, sizing of the remaining components took place. The cornerstone of the mainstream flow loop was the blower, manufactured by Cincinnati Fan. This piece of equipment, briefly mentioned above, was a 13.75 horsepower, high pressure blower driven by three-phase alternating current at 460 volts. A variable frequency drive allowed us to vary the frequency of the supplied power, thereby allowing differing rotational speeds. The blower was chosen so that the expected operating point would be achieved with supply power oscillating at approximately 30 Hz. Since 30 Hz was the midpoint of the operational capability, as the blower was capable of using power from 0-60 Hz. Choosing the 30 Hz design point allowed for maximum variability of mainstream test conditions. See Appendix B for the corresponding blower curves and variable frequency drive programming information. Isolation mounts protected the wind tunnel from any vibrations produced by the rotating machinery of the blower. Additionally, the diffuser section at the blower exit and return duct at the blower inlet were attached with flexible rubber ducting to resist the transmission of blower movement.

Immediately downstream of the blower, the mainstream air entered the diffuser section. Design of this section was critical for good experimental results. Flow irregularities in the diffuser section could have propagated downstream and had adverse effects on the delicate flow-field of the test section. The diffuser section had to impose flow and thermal uniformity before it could allow air to enter the test section. Uniformity was achieved through a dramatic slowing of the flow in the diffuser section. As the flow slowed, dynamic pressure converted to static pressure, which became uniform when the flow effectively stopped, as in a plenum. Standard wind tunnels achieve this slowing through a long duct with a slight expansion angle, usually less than 15 degrees. Unfortunately, geometric constraints eliminated the long expansion section option for our tunnel. The area needed to adequately slow the flow was so large, with respect to the blower exit, that the gradual expansion would have been prohibitively long. For this reason, a splash-plate diffusion box design was employed to slow the mainstream air in a relatively short streamwise distance. This document will consistently refer to directions

as pitchwise, spanwise, and streamwise. The axis definition on Figure 3-1 graphically defines these directions with respect to the measurement planes.

The diffuser box, seen schematically in Figure 3-1, consisted of a large box, of uniform flow area, constructed of 2.54 cm medium density fiberboard (MDF). Immediately downstream of the blower inlet, the diffuser held a 2.54 cm MDF splash-plate, which directed the flow radially away from the center of the diffuser. The area around the splash-plate, which was suspended in the center of the diffuser box, was exactly twice the area of the blower exit. Upon moving around the splash-plate, the flow encountered a device best described as an inverse splash-plate. This object was simply a square orifice plate immediately downstream of the splash-plate. The open area in the center of the inverse splash-plate was exactly twice that of the area around the splash-plate—and four times that of the blower exit area. These area ratios were chosen to gradually allow the flow to expand to the full area of the diffuser before entering the thermal conditioning system. The diffuser box measured 1.5 m on a side for a total flow area of 2.34 m^2. This sizing corresponded to a 10:1 area ratio with the test section, which will be discussed with the contraction design. This splash-plate design incurred a large pressure drop when compared with the gradual diffuser described above, although the space saving aspect justified its use.

The mainstream thermal conditioning system was also located in the diffuser box. Because frictional pressure losses are a function of the square of the bulk velocity, it was advantageous to place any flow obstructions in the section of the loop with the lowest velocity. As explained, the diffuser box dramatically reduced the velocity of the flow. For this reason, a flow conditioning heat exchanger was placed in the diffuser box, downstream of the splash-plate network. The heat exchanger was donated to the VTExCCL by Super Radiator Coils in Richmond, Virginia. The heat exchanger was square and measured 1.4 m on a side. It was designed, by Super Radiator Coils, to heat or cool the air with a minimal friction loss. A data sheet with several dimensions and specifications relevant to the radiator coil can be found in Appendix B. Figure 3-1 shows a schematic of the coil as installed in the diffuser box. For the external effectiveness tests, the mainstream air had to be heated. A closed circulation loop provided the heat exchanger with the hot water needed to properly condition the mainstream flow. A 0.04

HP, TACO cast iron pump circulated hot water between the coil and a 12 kW American Standard hot water heater. The insulated hot water storage tank held 80 gallons of water which it heated with three 460-volt heating elements. The elements maintained their output with 82°C automatic thermostats. Figure 3-2 shows a schematic of the hot water circulation loop. If needed, the radiator coil could also be connected to a cold water source to cool the mainstream flow.

After the flow was sufficiently settled and thermally conditioned, it entered the contraction section of the mainstream loop. This feature was directly upstream of the test section. Its design was also critical for uniform flow conditions in the test section. The purpose of the contraction was to accelerate the flow to the desired mainstream velocity. As indicated by the name, this component employed an area reduction to achieve this acceleration. Along with a specified area contraction, care had to be taken to design this component to have as little friction loss as possible while maintaining the flow uniformity precisely engineered in the diffuser section.

A proven method of contraction design uses what is called an s-curve to ensure uniformity at the contraction exit. The s-curve takes its name from the shape of the resulting contraction. Its sides begin nearly straight in the flow direction, followed by a sharp turn towards the center of the flow area. Each side then gradually transitions back to being parallel with the flow direction, except with each side now closer to the centerline of the flow, resulting in an overall reduction in area. Our contraction, seen in Figure 3-3, uses an established s-curve that can be scaled to fit any given geometry [Lyman, 2000]. On its upstream side, the contraction was square. Each side measured 1.53 m to evenly match the diffuser box dimensions. The downstream side was rectangular, measuring 90 cm in the spanwise direction and 26 cm in the pitchwise direction. This evenly matched the dimensions of the downstream test section.

A fellow researcher at the VTExCCL, Erin Elder, designed the contraction using the s-curve method and computational fluid dynamic (CFD) predictions. Previous s-curve designs, however, assumed that the inlet and exit aspect ratios (width to height) were equal. For instance, if the inlet to the contraction was square, the exit was square as well. The inlet and exit aspect ratios on our contraction were not equal, complicating the design. The problem was solved by using two different s-curves: one for the horizontal

contraction and another for the vertical contraction. The horizontal contraction reduced the pitchwise width by 83%, while the vertical contraction reduced the spanwise height by 41%. The contractions specific geometry is presented in Appendix C. The contraction was constructed by a contracted metal worker of the Virginia Tech Physical Plant. He formed the curves out of 0.32 mm cold rolled steel. S-curves were formed in eight different sections, two to a side, and welded to form the three dimensional contraction. The weld beads inside of the contraction were then ground off, which created a smooth surface in contact with the mainstream air. Two 5.1 cm flanges were added to attach the contraction to the diffuser and test sections of the mainstream loop. The contraction length measured 1.4 m from inlet to exit in the streamwise direction. Several streamwise rows of reinforcing ribs around the outer perimeter were also added for rigidity. The contraction design was verified, also by Erin Elder, using CFD simulations done in Fluent, a commercial CFD solver. Figure 3-4 is a contour plot of the exit velocity predicted by Fluent, showing uniform flow conditions. Again, the contraction reduced the mainstream flow area by a factor of ten.

The next section encountered by the mainstream flow was the test section. However, there was a specific portion of the test section that deserves its own mention. Before encountering any of the downstream cooling features, mainstream air passed by a bleed slot intended to remove the cooler boundary layer air. The boundary layer tends to remain cooler than the mainstream because the walls of the wind tunnel remove heat from the adjacent air through conduction to the outside, ambient air. The boundary layer removal was achieved by creating a low static pressure region elsewhere in the mainstream loop that was used as a suction environment. The physics were straightforward. If the difference in static pressure between the bleed slot inlet and the suction pressure region was greater than the frictional losses incurred by the piping connecting the two regions, the mainstream boundary layer fluid was removed. The lowest static pressure in the mainstream loop was located just upstream of the blower inlet. Naturally, this position would be the ideal place to use as the low pressure region. However, in our situation, this region was physically quite far from the bleed slot. Connecting the two would have required a relatively long and complex piping network. The frictional losses in such a network prevented the slot from actually removing any of

the boundary layer. The next choice was to use another location as the suction region. Unfortunately, the closest area, the return duct directly above the test section, did not have a low enough static pressure to overcome the frictional losses of even the shorter pipe. The next step was to increase the pipe size. The pipe size increase helped, but even with 15.24 cm piping, the exhaust pressure was simply not low enough to drive the necessary flow. The only other available option was to artificially manufacture a low pressure region in the return duct. The creation of a low pressure region was completed by inserting a blockage into the duct to forcibly accelerate the return air, thereby lowering its static pressure. A schematic of the blockage can be seen in Figure 3-5. This blockage reduces the return duct area by 47%, creating a static pressure even lower than that existing at the blower inlet

A pressure difference measured across the bleed slot was used to determine if the bleed slot was adequately removing the boundary layer. Before continuing away from the bleed slot, the flow encountered a blunt edged foam section, used to ensure that streamlines were effectively split. Streamlines could either enter the bleed slot or curve inward and continue down the test section. This fact allowed a single measurement to determine if the bleed slot was removing the entire boundary layer. A differential pressure was measured across the bleed slot with the positive side of the transducer connected to a static pressure tap located upstream of the bleed slot and the negative side connected to a static pressure tap downstream of the slot. Figure 3-6 graphically presents each of the three possible situations regarding the boundary layer removal. If the transducer displayed a positive number, the bleed slot had not removed enough air since streamlines had curved into the passage. In such a case, the flow downstream would have then accelerated, the dynamic pressure would have increased, and the static pressure would have decreased. If the transducer displayed a negative number, the bleed slot would have removed more air than necessary, as even streamlines traveling straight—outside of the boundary layer—were being removed as well. This removal would result in fewer streamlines downstream of the slot, therefore less dynamic pressure and more static pressure. The ideal case was a reading of zero on the transducer, which was achieved within the transducer accuracy at test conditions.

As mentioned, the next element encountered by the flow was the test section. This section will discuss only the mainstream component of the test section, as the portion of the test section devoted to internal heat transfer coefficient measurement will be discussed in the next section. In terms of its mainstream flow interaction, the test section was a straight, rectangular duct section. Figure 3-1 is a schematic of the entire mainstream loop; the test section can be seen in the center of the schematic. Figure 3-7 is a closer view of the external test section and its interaction with the internal cooling feature. The right wall, with respect to the flow direction, was made out of 9.5 mm thick, low thermal conductivity foam. The foam used, FR6703 Last-a-Foam, was manufactured by General Plastics of Tacoma, Washington. The foam had a thermal conductivity of 0.022 W/m·K. A 2.54 cm MDF wall was used behind this foam wall wherever possible, both for insulation and support. In some locations, MDF could not be used due to the presence of the microcircuits on the opposite side of the wall. The opposite wall was made of 1.3 cm Lexan. The top of the test section was constructed of Lexan as well. The base was constructed of 2.54 cm MDF covered with a Formica laminate material. We used the Formica to cover several large bolt holes that attached the test section to its support structure. The test section measured 90 cm in height—spanwise; 26 cm in width—pitchwise; and 1.75 m in length—streamwise.

As mentioned, one side of the mainstream test section used low thermal conductivity foam to approximate an adiabatic boundary condition. For ease of manufacturing, this wall was constructed in three sections; a lead section before the cooling feature exits; a microcircuit section, to which the microcircuit was mounted; and a post microcircuit section present only to observe film effectiveness downstream of the cooling features. The lead section also contained the elliptical feature used to split the flow entering the boundary layer bleed slot from that entering the test section. A router bit with a 9.5 mm radius removed the corner from both pitchwise sides of the upstream edge of the lead foam section, creating a well-defined stagnation line to split the boundary layer flow. Revisit Figure 3-6 for a visual of the bleed slot ellipse. The lead section started at the boundary layer bleed slot and continued 46.3 cm downstream. The microcircuit section began immediately downstream of the lead section. Several design considerations dictated the lead length before the cooling feature exits. Our sponsors

envisioned future tests with several rows of cooling features. The adiabatic wall upstream of the test section needed enough length to accommodate these or any other upstream cooling configurations. A large upstream lead distance also allowed for greater boundary layer development and quantification.

For the current study, the source of the external film cooling flow was a staggered row of cooling slots. Figure 3-8 gives the overall layout of slot locations with respect to the boundary layer bleed slot and test section beginning. As mentioned above, the slots were placed a specific distance downstream of the test section entrance for several reasons. The distance between the boundary layer bleed slot and the center of the exit slot plane corresponded to the scaled distance from the stagnation point on a vane to the proposed location for microcircuit slot exits. In all, there were six film cooling slots staggered about the test section centerline and located 71.4 cm downstream of the boundary layer bleed slot. The slots themselves measured 6.35 cm in the width direction and 9.53 mm in breakout length, giving a 6.7:1 aspect ratio. A spanwise distance of 4.68 cm separated each slot from its adjacent slots. Staggered slots, the description provided above, referred to the location of each slot with respect to the centerline listed above. Some slots began, or had their upstream edge start, at the given centerline, while the adjacent slots would use that centerline as their ending measurement. The microcircuit section of the foam wall measured 48.7 cm in the streamwise direction. The final section of foam allowed a lengthy streamwise region to collect adiabatic effectiveness measurements. The distance from the slot location centerline to the end of the test section corresponded to 100 slot widths in order to characterize the film cooling benefit of the slot flow.

As noted, the adiabatic wall was constructed out of three sections of foam. To obtain good results, it was important to carefully mend the foam joints before collecting effectiveness data. The first joint, between the lead and microcircuit sections, was not located in a region where any effectiveness data would be taken. Therefore, preserving a smooth test surface became the only concern at this joint; thermally, the joint did not need to behave like the surrounding adiabatic foam. We filled the joint with Elmer's Wood Filler as it provided a solid joint and was easily applied, sanded, and painted. The wood filler did not, however, provide heat transfer characteristics similar to the foam.

For this reason, the filler could not be used on the joint between the microcircuit section and the downstream section. This downstream joint necessitated a bond created with material of equivalent heat transfer resistance as the adiabatic foam. An expanding foam material manufactured by the Stepan Company provided an end product with equivalent thermal conductivity that would form to the shape of the existing foam joint. The Stepan foam molded to the shape of the joint following a procedure established in Couch [2003]. In final preparation, foam surfaces were painted with flat black paint to increase the emissive properties of the foam, which aided imaging with the infra-red (IR) camera. The IR imaging process will be later in this section. Regular use of XO-19 Flat Black spray paint, made by X-O Rust, ensured a consistent adiabatic imaging surface [Couch, 2003].

The Lexan wall opposite the adiabatic test surface was very important as well. Not only did it enclose the external test section, it also housed the camera ports used to take IR images of the test surface. Figure 3-9 is a diagram of the opening used to image the adiabatic wall with the IR camera. Beginning 67 cm downstream of the test section start, the Lexan wall was open to the atmosphere. There were two adjoined rectangular openings. The first of the two began at the above dimension and extended 15.5 cm downstream; it was 56 cm wide in the spanwise direction. The second opening, although adjoined to the first, began at the downstream edge of the first opening, 82 cm downstream of the external test section start. This opening is 21 cm wide with respect the span, and extends 27.3 cm downstream. These openings allowed the IR camera to image the adiabatic surface, as the Lexan appeared opaque to IR wavelengths—this will be explained further in the following section. The opening described above allowed for nine separate IR images of the test surface, which were later stitched together in post-processing.

While this large opening allowed for many image locations, it left much to be desired in terms of sealing the test section from the atmosphere. Obviously, while one of the images was taken, the other image locations needed to be closed to the atmosphere. To solve this, we used a 13-piece set of custom fit blockage sections, specifically tailored to each of the nine IR image opening requirements. The blockage sections were made of the same material as the Lexan wall, and each had a 2.54 cm flange around its perimeter

used to attach the blockage to the fixed wall. All parts were bolted in place via threaded holes around the perimeter of the large opening. The parts fit together like a jigsaw puzzle, some parts interchanged and some performed multiple duties; Figure 3-10 details each of the nine imaging scenarios. Perhaps the most important part was the actual IR imaging piece. This piece was used in all nine imaging situations, as it actually contained the hole that the camera looked through. The piece bolted to the open frame, just the same as the rest, but contained a 10.2 cm hole in the center of it to allow the IR lens to image the wall. As previously mentioned, the Lexan was opaque to IR wavelengths. As noted in the previous section, the test section was 26 cm wide in the pitch wise direction. This presented a problem since the minimum focal distance of the IR camera was 30 cm. A simple solution was to back the camera several centimeters away from the wall. However, this ruined the carefully engineered sealing of the outer wall described above. A rigid cone spacer was the solution to both problems. A cone shaped lens case, made out of PVC, allowed the camera to stand off the correct distance, while still sealing the opening around the imaging port. Figure 3-11 is an image of the IR camera mounted on its stand with the cone lens case and imaging port in place.

Following the test section, the mainstream air entered a section of return duct whose only function was to return the air to the blower inlet as efficiently as possible. Again, Figure 3-1 is a schematic of the mainstream loop. An actual photo of the completed loop can be seen in Figure 3-12. We determined that routing the return duct above the test section was the most efficient use of available space. This, however, required an extensive support structure and careful planning to ensure that the flow would not encounter needless friction loss. Additionally, flow disturbances from the return ducting could not be allowed to propagate upstream into the test section. We placed a large, straight, empty duct just downstream of the test section, ensuring that any irregularities created in the first upward flow bend could not reach the test section. This leading duct was constructed to be wider than the test section. The change in width, when combined with a corresponding change in height that took place in the first upward bend, transformed the return duct to a square—for ease of manufacturing—while it maintained the flow area of test section.

The duct upstream of the upward bend was made entirely of 2.54 cm MDF. We also constructed a short transition section between the test section and duct to make the width change as efficient as possible. The transition section began at the test section and expanded at a 15° angle in the pitchwise direction to the predetermined return duct width. The sides and floor of this section were constructed out of the same MDF used for the test section and downstream duct. The top of this transition section, however, was constructed of the same 1.27 cm Lexan used on one of the test section walls to provide an easily removable access port into the upward turn lead duct. The transition section measured 71.3 cm in overall length. The upward turn duct, as mentioned, was wider than the test section. It measured 49.7 cm in width, but remained 90 cm in height. Its streamwise length was 2.2 m; when combined with the transition section, this distance corresponded to a lead distance of over 7 test section hydraulic diameters before the initial upward bend. This ducting can also be seen in Figure 3-1.

The first elbow encountered was used not only to turn the flow, but to transition the rectangular duct to a square cross section. To construct the sides of the bend we cut two curved sections of 2.54 cm MDF. The outside, downstream, curve swept through the 90° elbow with a radius of 75 cm. The inner radius measured 50 cm. This was the only irregular elbow in the mainstream loop; the remaining elbow radii measured 25 cm on the inner bends and 73.1 cm on the outer bends. Only the first upward elbow's sides were constructed of MDF, the remaining elbow sides were cut out of 63.5 mm hardboard. The curved sections of the elbows employed pre-curved 16 gauge stainless steel sections as the bend material. The stainless steel curves were anchored to 2.54 cm MDF flange evenly spaced along the edge of each radius. To help restrict heat loss, we covered the stainless steel bend material with 63.5 mm insulating foam.

The same hardboard used for the smaller elbow sides was used for the straight sections of return duct. We constructed these in 1.22 m flanged sections. The corners of the straight duct were reinforced and sealed with 5.08 cm aluminum L-bracket. The use of hardboard, over MDF, allowed a considerable cost and weight savings for the return duct and elbows. In total, the return duct employed four elbows, six standard 1.22 m straight sections, and two custom sized straight sections to transition back to the blower. Just upstream of the blower inlet, we placed a round orifice plate with a 2.54 cm flange

on the return duct. This allowed a flexible rubber attachment to the blower inlet, as previously mentioned.

External Mainstream Instrumentation. External adiabatic film effectiveness requires a detailed map of the temperature of the surface being studied. We measured the surface temperatures on our adiabatic wall using an IR camera. Thermocouples are necessary to calibrate images taken with the IR camera. The IR camera is excellent at measuring temperature gradients and relative temperature differences, but it cannot report the true magnitude of a surface's temperature without knowing some of the test environment parameters. For this reason, thermocouples in known locations on the adiabatic wall provide anchors to which an image can be calibrated. Since the thermocouple locations are known, we can locate and compare them to the temperatures recorded in the IR image. There are two parameters that the IR imaging software can adjust to match IR image results to known thermocouple readings; surface emissivity and background temperature. The changes in these two parameters adjust the surface temperature, T, according to the following relationship:

$$T = \sqrt[4]{\frac{1}{\varepsilon \cdot \sigma}\left[Q_{const} + (\varepsilon - 1) \cdot \sigma \cdot T_{bg}^4\right]} \tag{3.1}$$

where ε is the surface emissivity, σ is the Boltzman Constant, and T_{bg} is the temperature of the environment surrounding the surface. Q_{const} is the total radiation heat flux measured by the IR camera. The emissivity adjusts the range reported between two points while the background temperature scales the magnitude of all temperatures in the image. The anchoring thermocouples are placed in locations of both hot and cool temperatures in each image. High gradient areas are avoided since, in these regions, a small error in location can correspond to a large difference in temperature. The post-processing software also requires markers to orient the images; there are two marker locations in each image. The markers are made of small, 1.6 mm brass tubing pushed into the adiabatic foam. Figure 3-13 details the external thermocouple and marker locations on the test section wall.

Temperature and pressure measurements were also needed elsewhere in the mainstream loop. Thermocouples were used to quantify the mainstream flow temperature, the heat exchanger inlet and exit temperatures and the ambient atmospheric temperatures. Three upstream thermocouples, evenly spaced across the span of the test section entrance, characterized the bulk mainstream temperature for day to day testing.

Static pressure taps were used extensively in the mainstream circulation loop. We used them, in conjunction with thermocouple measurements, to specify mainstream flow-rates and ensure boundary layer removal. Pressure measurement usage and procedure will be explained in this sections discussion of the mainstream benchmarking process.

External Mainstream Data Acquisition Equipment and Procedure. Despite the best instrumentation, actual measurement would be impossible without some sort of data acquisition equipment. Even with the best data acquisition equipment, repeatable measurements would be impossible without an established data collection procedure. This section will discuss both. Both pressure transducers and thermocouples generate analog voltage signals proportional to their respectively experienced phenomena. These analog signals are captured by National Instruments SCXI-1100 data acquisition modules. These modules then pass the acquired analog signals to a SCXI-1000 chassis, which collects the voltage measurements and sends them to a 12-bit analog to digital conversion board in a computer. The A/D board digitizes the analog signals and allows them to be recorded and stored in digital form. National Instrument's Labview software is used to display and save pressure and temperature measurements. The Labview software's data acquisition settings are adjustable, for these experiments they are set to capture 1024 samples per scan and make 1024 scans per second [Couch, 2003].

As mentioned in the previous section, external surface temperatures were mapped with an IR camera, while a conventional digital camera collected internal surface temperatures from a TLC sheet.

Through careful planning, other's experience, and trial-and-error, data taking procedures were developed for both internal and external experiments conducted. As indicated in previous sections, adiabatic film effectiveness measurements were taken

after allowing the heated mainstream flow to come to steady state with cooling flows exiting the microcircuit slots. The slots, and film cooled regions downstream, were imaged with an IR camera; a ThermaCAM P20, made by FLIR Systems. The first step in the data taking process was to heat the mainstream flow. After starting the blower and activating the hot water circulation loops, the tunnel was allowed to heat for a minimum of two hours. This ensured that the tunnel had reached steady state with the surroundings. A change of less than 0.1°C in the average of the mainstream thermocouple readings over a half hour period defined steady state. Pressure measurements made upstream and downstream of the contraction, combined with ambient pressure and temperature measurements, quantified the mainstream velocity through the test section. A blower setting of 39 Hz resulted in a consistent test section velocity of 10.5 m/s. Most cases ran at this setting with two exceptions; the highest blowing ratio case ran at 36 Hz, and the lowest blowing ratio case ran at 59 Hz. The differing operational speeds resulted in test section velocities of 9.8 m/s and 15.8 m/s, respectively. The high blowing ratio case was adjusted to allow the coolant flow through the venturi tube to be measured without changing the diaphragm and recalibrating the pressure transducer. The low blowing ratio case was adjusted to increase the amount of coolant mass flow. At 10.5 m/s the coolant flow for the lowest blowing ratio case was so low that its magnitude was nearing the adjustment resolution of the flow control valve.

Once the mainstream characterization was complete, we determined the proper cooling flow rate based on the target mass flux ratio. Coolant flow rates were set by monitoring the pressure differential across a venturi tube, which will be discussed in detail in the next section. Static pressures at the microcircuit inlet were monitored to ensure uniform flow conditions. Microcircuit feed adjustment valves allowed adjustment of inlet static pressure to within 5% of the average inlet pressure. Another steady state waiting period followed successful inlet flow balancing; although not as long as the first. Generally, the flow achieved steady state within one half hour of inlet flow balancing. The steady state definition did not change, although the evaluation was based on surface thermocouples rather than mainstream thermocouples.

The imaging process could begin once the flow achieved a steady state. Prior to recording any data, the camera was positioned and prepared to take images. The camera

mounting device consisted of a short pedestal on a flat MDF base. Through the center of the pedestal, an aluminum rod with a camera mount could slide up and down. The rod was held in place vertically with a pin that fit through pre-drilled holes in the rod and both sides of the pedestal. Figure 3-14 shows a schematic of the IR camera mounting configuration. With the camera in position, temperature data acquisition was initiated in Labview. Eight IR images were then made of the adiabatic wall at the current camera location and the data acquisition was stopped. Labview did not log temperature data while the IR camera location moved. Once the camera was in position again, the images were downloaded onto the hard drive of the computer, sorted, and labeled along with their corresponding thermocouple log. With that completed, the next set of images was taken in the same manner until all nine image sets were gathered. It should be noted that the full nine-image set was only taken for the first few data sets. Once we determined that the method of balancing the inlet flows indeed resulted in periodic coolant flows on the external wall, image sets 1 and 2 were omitted. The process of calibrating and compiling the IR images will be discussed in the following chapter.

External Mainstream Benchmarking. Before any external test cases were run, temperature profiles were taken at several horizontal and vertical locations to fully capture the thermal environment and ensure the flow conditions were appropriate for data collection. Figure 3-15 is a plot of the horizontal temperature and velocity profiles taken upstream of the cooling slots. Figure 3-16 is a velocity profile taken vertically across the test section. Pressure measurements were needed to verify the mainstream velocity in the test section and to ensure the boundary layer bleed slot was removing the entire boundary layer flow—recall Figure 3-6. A host of pressure taps were installed in the mainstream diffuser, before the contraction, after the contraction, and across the boundary layer bleed slot. Static pressure taps sensed only the static portion of their pressure environment by sitting perpendicular to the flow field around them. Their installation configuration is shown in Figure 3-17, as documented in Couch [2003]. The overall total pressure of the system was measured with the static pressure tap located in the diffuser box, upstream of the heat exchanger. Obviously, there were total pressure losses throughout the mainstream loop, but the maximum total pressure reference was taken at this location.

Static pressure was an adequate indication of total pressure since the fluid was essentially at rest in the diffuser. The mainstream velocity was determined using two equations. The conservation of mass equation, given here:

$$\rho U A_{upstream} = \rho U A_{downstream} \tag{3.2}$$

guaranteed that the mass flow upstream of the contraction was equal to that downstream, in the test section. In this equation, ρ is the local density, U is the flow velocity, and A is the flow area. Since the contraction satisfied the conservation of mass constraint, velocity in the test section was solved for using Bernoulli's equation for a streamline, given here:

$$U_{TS} = \sqrt{\frac{2 \cdot \Delta P_{static}}{\rho_{\infty}} + U_{upstream}^2} \tag{3.3}$$

where ΔP_{static} is the measured static pressure difference across the contraction, ρ_{∞} is the density of the mainstream fluid and $U_{upstream}$ is the velocity in the diffuser—assumed to be zero. These pressure measurements were used to quantify the test section velocity during day-to-day experiments, but additional measurements were required to create the velocity profiles shown in Figures 3-15 and 3-16.

Experimentalists can get an idea of a flow's velocity profile using a pitot-static tube. Pitot-static tubes do not directly measure velocity, or even dynamic pressure. Rather, they deduce dynamic pressure, and thus velocity, by using the definition of total pressure, shown here:

$$P_{total} = P_{static} + P_{dynamic} \tag{3.4}$$

The probe has two ports, one open port that faces directly into the flow to be measured. This senses the total pressure, since the flow stagnates at the tip. The second port on the pitot-static probe is perpendicular to the first port and measures static pressure. When

connected to a pressure transducer, the resultant measure is the dynamic pressure of the flow. Then, by only knowing the density of the flow, the velocity can be resolved, since:

$$P_{dynamic} = \rho \frac{U^2}{2} \tag{3.5}$$

Where ρ is the density of the flow, and U is the desired velocity. Temperatures profiles are created by affixing a thermocouple to the pitot-static probe and taking simultaneous velocity and temperature measurements at each profile point.

A pitot-static probe was also used to quantify the boundary layer thickness in the test section. As discussed, the boundary layer was removed at the entrance to the test section. Of course, a new boundary layer immediately formed at that location and grew in the pitchwise direction as the mainstream flow progressed downstream. Two slot widths upstream of the cooling slots, the boundary layer was approximately 1.9 cm thick. Figure 3-18 is a detailed velocity profile near the adiabatic wall, showing the boundary layer just upstream of the slots. The boundary layer was measured with a pitot-static tube. Initally, the tube was placed on the wall, where the first velocity measurement was taken. We moved the probe away from the wall in even increments of 1 mm. When our measurements indicated little change between velocities sequentially further from the wall, we assumed the transition from boundary layer to mainstream flow was complete. Note that the probe has an outer radius that prevents measurement immediately adjacent to the wall. The first measurement is actually 1.5 mm away from the wall. The measurements shown in Figure 3-18 agree with predictions of a flat plate turbulent boundary layer, calculated according to [Bejan, 1995]:

$$\frac{\delta}{Z} = 0.37 \cdot Re^{-0.2} \tag{3.6}$$

where Z is the pitchwise distance away from the wall and δ is the turbulent boundary layer thickness.

Figure 3-19 is a plot of spanwise averaged adiabatic effectiveness for a blowing ratio of M = 0.30. Spanwise averaged data is averaged across the entire span of one periodic microcircuit, to include two staggered exit slots. Each line on Figure 3-19 indicates an independent test taken several days removed from the other two sets (an M = 0.28 case is added for comparison as well). Figure 3-19 shows repeatability within the measurement uncertainty, proving that our test method was independent of day to day variations in experimental conditions and providing further confidence in the test facility's benchmark.

Figure 3-20 shows a comparison between data taken from the top and bottom slots for a given blowing ratio. Effectiveness levels from the two slots match within the measurement uncertainty. The data in Figure 3-20 represents the effectiveness measurements along a straight line. The line originates at a point along the spanwise center of the downstream edge of the exit slot and extends downstream normal to the slot. Since the slots are actually staggered in the streamwise direction, the X/s scale is shifted for the downstream slots so that each line represents X/s measurements relative to each individual slot.

3.2 Internal Coolant Supply

The coolant supply system, although much smaller than the mainstream loop, was an integral portion of the wind tunnel for the type of experiments proposed. This system pulled coolant air from an outside compressed air source and slowed and evenly distributed it. The channels that made up the system then routed coolant through the microcircuit test piece, and exhausted it through the film cooling feature into the mainstream air loop. Figure 3-21 is a cross section of the microcircuit, showing the coolant flow path.

Internal Coolant System Design and Construction. The coolant system drew air from two outside compressed air sources. Figure 3-22 is a schematic of the coolant sources and their paths to the microcircuit inlets. The most often used source of

compressed air came from the Virginia Tech Physical Plant. The Physical Plant maintained a tank of compressed air at 551.6 kPa for general campus use. Compressed air lines ran from this tank to nearly every building on campus and the provided air is shared by laboratories, machine shops, and heating and air conditioning systems [Long, as documented in Couch, 2003]. The Virginia Tech Physical Plant compressed air tank provided enough air for all external effectiveness experiments; but it was an adequate supply for only half of the internal experiments. For the higher flow cases on the internal side, a second compressed air source was used. The second source was a compressor and holding tank located in the Aerospace and Ocean Engineering (AOE) Department of Randolph hall. The tank pressure was user controlled and usually set to 1379 kPa. This tank was used in conjunction with the Physical Plant air to achieve the required flow rates for internal testing. The AOE compressor did not maintain the tank at the user selected pressure. The tank supply pressure steadily dropped as testing took place, usually about 517 kPa per hour. Once the AOE supply pressure was too low to sustain the required flow rate, data acquisition was temporarily stopped and the AOE tanks were recharged back to the initial pressure [Edwards, as documented in Couch, 2003]. Air temperatures generally followed outside weather trends; colder days resulted in lower coolant temperatures, although actual temperatures were always very near ambient temperature. Both tanks were equipped with drying equipment to remove moisture present in the source air [Couch, 2003].

Initially, microcircuit coolant feeds were supplied to the coolant plenums by a compressed air hose. Hoses, however, are designed to transmit high static pressures; this was not an optimal design for the high air flow rates required for this study. The friction losses through such hoses are extremely large. Rather than try to increase the supply pressure, we decided to remove the air hose and replace it with 10.2 cm polyvinyl chloride (PVC) piping. This dramatically reduced the friction loss through the supply piping and allowed much higher microcircuit flow rates for the same compressed air supply pressure.

Once the coolant reached the wind tunnel, we quantified the mass flow rate with a venturi tube. The venturi allowed a mass flow measurement by providing a static pressure difference across a precise area change. Lambda Square, Incorporated,

manufactured the venturi tube used in these experiments. The venturi tube, a model CV-400, had a 10.2 cm inside diameter pipe size, and a 6.7 cm bore. The manufacturer recommended that straight, unobstructed pipe precede the venturi by at least five pipe diameters, and follow the venturi by at least two pipe diameters [Couch, 2003]. The venturi tube was placed in the center of a long straight section that easily accommodated these requirements. Appendix D contains the venturi calibration curve used to convert pressure differential to mass flow rate.

Upon leaving the venturi, coolant split into two paths; both of which supplied opposite sides of a large steel coolant plenum. This plenum served to manifold the coolant air evenly between the nine microcircuit inlet plenums. Coolant air was split into nine channels to provide the capability to simulate spanwise pressure gradients across the microcircuit inlets in future testing. The split air provided both sides of the steel plenum with equal flow rates and helped ensure that the downstream microcircuit plenums would be fed evenly. The steel plenum, known as the 'octopus' and shown in Figure 3-23, could not accommodate the large PVC pipe exiting the venturi [Radomsky, 2000]. Therefore, the piping was reduced to two 2.54 cm braided, high pressure hoses, which fed both sides of the octopus. The octopus, in turn, had eleven exit ports, each fitted with a 2.54 cm hose and adjustment valve. The adjustment valves served to ensure that the pressure drop through each parallel circuit leaving the octopus was equivalent; thus ensuring equivalent flow rates to each microcircuit inlet. Additionally, we wanted the capability to impose a spanwise pressure gradient on the microcircuit inlet feeds, better recreating actual engine conditions. This study used uniform inlet pressures, but future studies will impose the gradient. Adjustment valves were all 2.54 cm globe valves. In addition, all hoses leaving the octopus were cut to similar lengths, 106 cm, as an additional precaution against microcircuit inlet irregularities. As the microcircuit needed only nine inlet feeds, two of the octopus exits were left closed at all times. The nine hoses leaving the octopus led to a bank of fixed microcircuit inlet feed plenums. The plenum bank can be seen in Figure 3-24. Each plenum measured 29 cm by 41 cm and were each 6.5 cm in height. They served to again slow the air and ensure uniformity at the microcircuit inlet.

Leaving the plenums, air entered nine separate microcircuit feed channels that directed air into the microcircuit inlet bends. Figure 3-24 also shows the microcircuit feed channels mounted on the feed plenums. The channels were very small, matching the size of the inlet port of the microcircuit inlet bend. With respect to the flow, the channels measured 9.5 mm wide, 1.6 cm high and 22.5 cm long. This translated into an L/D_h ratio of 19 for the inlet channels which is long enough to consider the channel flows fully developed.

In the engine design, flow would enter the microcircuit inlet bend and immediately turn 90° to begin its journey around the pedestal features. Recreating this 90° bend was critical for obtaining useful results. The inlet channels were machined out of two separate pieces of Lexan. First, the Virginia Tech Physical Plant cut nine concave bends out of a 2.2 cm piece of Lexan with a radius of 1.9 cm. Then, they machined nine convex regions off of the corner of another sheet of the same material, this one only 1.3 cm thick, in the same spanwise locations as the nine concave sections. The convex regions had a radius of 9.5 mm. The pieces were then cemented together with the result being nine three-dimensional inlet channels that turn the flow 90° into the microcircuit. Figure 3-25 shows each of the inlet bend components separately and the finished product after they are cemented together. Each inlet measured 1.6 cm in the spanwise direction and 9.5 mm in the pitchwise direction. Each periodic microcircuit section had three inlets, the three microcircuit sections combined for the total of nine inlets described above. Microcircuit inlets were spaced evenly along the span of the test section; the center to center distance between inlets was 7.37 cm.

Figure 3-23 also shows a schematic of the microcircuit test section geometry from the inlet side. Although the actual microcircuit geometry will be discussed in detail in the following section of this chapter, a brief synopsis will be given here to orient the reader to the transition from cooling loop to mainstream loop. Upon exit of the microcircuit bend channels, the cooling air entered the main microcircuit channel. This chamber was not empty—rather, there were several rows of pin fin type features—but the feature geometry will not be discussed here. The bulk flow channel, think of the microcircuit channel with no features, measured 66.2 cm across in span. This dimension corresponded to the spanwise width of three microcircuits side by side. The actual test

section was quite a bit larger, 90 cm as mentioned in Section 3.1. The 90 cm dimension corresponded to the spanwise width of the three microcircuit array, plus the width of an additional half microcircuit on either end of the array to prevent edge effects in the external effectiveness tests. The bulk flow channel continued for 13.5 cm before exiting into the mainstream channel through six film cooling slots. The bulk flow channel was made of low thermal conductivity foam on the surface adjacent to the mainstream channel, the upper surface, and the lower surface. The outer surface of the channel was closed with a sheet of 1.6 mm thick cardstock paper. Adjacent to that, in the pitchwise direction, was a sheet of 9.5 mm thick anti-reflective glass, manufactured by American Computer Optics. The glass was held in place by two brackets attached to the microcircuit inlet bend plate with two 30.5 cm lengths of all-thread.

Microcircuit Test Section Specifics. Microcircuits have been mentioned several times in the previous sub-section, but their actual features and geometry have thus far defied mention. This section will discuss, in detail, the geometry of the internal heat transfer environment.

The cooling slots and corresponding adiabatic effectiveness measurements were only a part of the experiments completed in this study. The microcircuit passages that fed the slots were really the heart of the study, as they linked the internal cooling passages and external cooling slots. The general microcircuit geometry was discussed in the previous section. This section will discuss the specific shape and placement of the microcircuit features.

Previous sections have alluded to the pin fin shape of the microcircuit pedestal features. They are, indeed, pin-fin-like pedestal structures, although several of them have unique geometry intended to enhance their heat transfer augmentation. Often the geometry of the microcircuit can be complicated and confusing to explain, reference Figure 3-26, a negative of the microcircuit flow paths, often throughout the following description. The negative of the flow path is shown to highlight the periodic boundaries of the microcircuit. Figure 3-27 shows the microcircuit's flow path as it appears in the airfoil wall. Additionally, Table 3-1 is a comprehensive listing of all relevant microcircuit dimensions. As cooling flow entered the microcircuit—recall the coolant

entrance bends described in the previous section—it impinged on a row of oval shaped pin fins. The impingement pedestals were roughly oval shaped; the upstream-facing radius was larger than the downstream facing radius. Each microcircuit inlet had one of these roughly oval pedestals 1.7 cm downstream of it. The area between each inlet also contained a pedestal exactly like those in the impingement path. Each periodic microcircuit contained six of the roughly oval first row pedestals. The center to center distance between these pedestals was 3.7 cm in the spanwise direction. The centerline of the next row of pedestal features was 4.8 cm downstream of the microcircuit inlets. The features found at this location were cylindrical pin-fin pedestals. They were 1.3 cm in diameter and spaced 9.4 mm apart in the spanwise direction. Ten cylindrical pedestals made up the second row of features. The adjacent microcircuits shared half of a cylindrical pedestal at the microcircuit periodic boundary. See Figure 3-26 for further clarification. The center of the middle pedestal in the second row aligned with the spanwise center line of the microcircuit. The following row of features was identical to the second row, although staggered. The center of each feature in the third row aligned with the spanwise midpoint of the distance between pedestals in the second row. The third row also featured ten pedestals. The streamwise center of the third row was 6.7 cm downstream of the inlets.

Following the third row, any semblance of a standard pin fin array disappeared. Flow leaving the third row encountered two strangely shaped objects, termed the 'submarines' by their creators for their odd shape. From the view of flow leaving the third row, the submarines looked like a large, nearly flat blockage, directing flow up or down the span of the microcircuit. Again, Figure 3-26 will be helpful in visualizing the submarines. Flow leaving the third row in the center of the microcircuit saw a large blunt object doing the same thing, although with less extreme angles with respect to the streamwise direction—think of a large blunt arrow pointing upstream, flow either travels around one side or another. So, once flow was redirected, either by the submarines or the blunt arrow, it reached the metering area of the microcircuit. The submarines and arrows served to direct the flow into the channels leading up to the exit slots. As mentioned, the exit slots were staggered, so for a given periodic microcircuit section, the right slot—using the streamwise direction as forward—always had a shorter trip to the exit slot.

However, before the slot exit is described, the submarines have additional features that should be addressed. They did not simply split the flow without regard to what happened downstream of them. Their geometry attempted to control the expansion of the flow around the metering area with a thickening of the pedestal piece in the streamwise direction as the spanwise center of the slot was reached. The submarines, however, were not symmetric about the center of the slot. The streamwise thickening was much more gradual on the outward facing sides of the submarines. Eventually they reached the thickest point, an edge with a radius, the center of which corresponded to the spanwise center of the slot.

It can be helpful to think of each row of pedestal features as flow obstructions in an open channel. In this respect, each row has a corresponding dimensionless blockage ratio, the area obstructing the flow divided by the flow area of the channel if no pedestals existed. The first row has a blockage ratio of 0.52; second and third had equivalent blockage ratios, 0.57; and the fourth had a blockage ratio of 0.72. These ratios are noted on Figure 3-26 and in Table 3-1.

After the quick expansion around the edges of the submarine, flow exited the microcircuits through the film cooling slots. The exit slot bends were very similar to the inlet bends. The inner and outer radii were identical. In fact, the only difference between the two was the spanwise width of the exit slots. Slot exit bends spanned 6.4 cm, the same distance as previously mentioned.

All of the pedestal features were carved out of the same low thermal conductivity foam used in the adiabatic wall. As a template for the pedestal features, a negative of the microcircuit flow path was created out of hardened resin on a stereo lithography (SLA) machine by ProtoCAM in Northampton, Pennsylvania. Figure 3-28 shows the completed SLA part. The finished product from ProtoCAM was a three-dimensional inverse model of the microcircuit; a solid block of resin with holes where each microcircuit pedestal feature would fit. We used this SLA part as a template to size and place all of the pedestal features in the test section.

Although the exit slot bends shared similarities with the inlet bends, they were constructed in a different manner and out of a different material. Figure 3-29 is a graphic representation of the exit bend construction process. The exit slots were carved out of the

same foam as the adiabatic wall and pedestal features. To create the outer bends of the slots, two sections of foam—each 9.5 mm thick—were affixed together with epoxy (step 1). The upper piece of foam measured 12.7 streamwise centimeters and 6.4 spanwise centimeters. The lower piece was the same spanwise thickness but only 2.54 cm in the streamwise direction. They were aligned on their upstream edges. Once the epoxy was dry, a 1.9 cm radius was cut out of the material in the spanwise direction (step 2). The center of the radius began in the upstream corner of the lower piece and continued spanwise to the opposite upstream corner. The slots in the microcircuit section of the external wall were then widened by 6.4 mm to accommodate the small section not removed by the radius cut into the foam pieces. The inner radius did not require such an intense manufacturing process. The upstream corner of the slots on the microcircuit side were simply rounded off to the proper radius, 9.5 mm, by an aluminum tool specifically created for that purpose (step 3). The tool was a thin, flat piece of aluminum with a 1.9 cm hole drilled into it. The hole was cut into quarters, one of which was used to scrape away foam around the appropriate corners of the slots. The same process was used to create all six slot bends. The completed slot bends can be seen in Figure 3-30.

In general, the microcircuit test section can be thought of as a stack of several layers in the pitchwise direction, as shown in Figure 3-21. The first layer is the adiabatic foam wall—the other side of the wall used for external film cooling measurements. The second layer contains the microcircuit pedestal features and flow paths. The third layer is made up of a constant heat flux generator to be discussed in the following section. The fourth layer is the liquid crystal temperature measurement medium, also to be discussed in the following section. The fifth, and final, layer is the anti-reflective glass previously mentioned.

As mentioned, the adiabatic foam wall was a common boundary for both internal and external tests. The internal pedestal features were made of the same material and attached to the wall with epoxy. The SLA microcircuit pictured in Figure 3-28 was used to accurately place the features on the wall with respect to the inlet channels and exit slots. The next layer, the inconel heater, was placed over the center microcircuit section with the copper coating facing away from the microcircuit pedestal features. The heater was fixed to the pedestal features with silicone adhesive to prevent the heater from

moving and keep air from flowing over the top of the features. The thermochromic liquid crystal (TLC) sheets were placed directly on the copper coating of the inconel heater. The TLC sheets came from the factory with their own adhesive. Because the heater and TLC layers had a measurable thickness, the anti-reflective glass could not be placed directly on the microcircuit array. The glass failed to make contact with the pedestal features of the adjacent microcircuit arrays since the heater and TLC layers were in the way. To circumvent the problem, we placed a layer of thick card-stock paper between the pedestal features and the anti-reflective glass across the span of the microcircuit array, except over the center microcircuit. The card-stock paper is not shown in the schematic figure of the microcircuit test section, as it is in the same plane as the heater and TLC sheets. The junction between the card-stock paper and the heater/TLC sandwich was sealed with silicone as well. The anti-reflective glass was affixed to the card-stock and sealed with silicone.

The microcircuit layout described above was not the first attempt, however. Initially, the strip heater and liquid crystal were placed underneath the pedestal features. Ultimately the features caused shadows on the TLC sheets that were too intense to correct. The configuration was then changed to the one described above. Chapter 4 will describe the problems in greater detail.

Internal Coolant System Instrumentation. Internal heat transfer coefficient experiments used the same instrumentation suite as the external film effectiveness tests with one exception: surface temperatures were mapped using thermochromic liquid crystal (TLC) sheets rather than an IR camera. TLC solutions are available in a variety of forms, from paints to slurries and laminated sheets. Polyester sheets coated with a TLC solution offer the benefits of a temperature sensitive medium without the mess and uncertainty of mixing and applying a TLC slurry. The polyester sheets are of uniform thickness and can be purchased with adhesive already attached. TLC sheets use a chemical mixture that reflects light differently depending on its temperature. The liquid crystals used for this study are black below 30°C, they begin to turn red at this temperature. With increasing temperature they transition through the colors of the spectrum, and begin to turn blue at 35°C. The TLC sheets again turn black above 41°C

[Hallcrest, 2000]. The TLC sheets, part number R30C5W, are from Liquid Crystal Resources, LLC., formerly Hallcrest, Inc., of Glenview, IL.

To help understand why TLC sheets are helpful for this kind of research, a brief discussion of optics is necessary. As we know, visible light encompasses a certain bandwidth of the electromagnetic spectrum, namely any electromagnetic radiation with a wavelength of approximately 400 nm-700 nm. They human eye, or any man-made image capturing device, differentiates between wavelengths through the perception of different colors. In general, since most sources of electromagnetic radiation emit across a large bandwidth of the full spectrum—like the Sun or a light bulb—color really depends on how that light reflects off the surfaces that the eye sees. The liquid crystal changes its reflective properties with changing temperature. This affects the wavelength of reflected light perceived by the human eye—or camera—resulting in a change in color proportional to a change in temperature. To quantify temperatures using the liquid crystal a further breakdown of color is required. Specifically, any color can be completely described by three parameters; hue, saturation and intensity. The dominant wavelength of a specimen is described by the hue. Intensity refers to the overall brightness of the light, relating directly to the total sum of the spectral energy perceived by the sensor. Saturation is defined by the amount of white contained in the sample with respect to a pure specimen of its color. This description is a brief summary of an excellent, more comprehensive description given by Camci, et al. [1992]. Additionally, a pixel's hue can be determined from a standard red-green-blue (RGB) color map according to the following:

$$\mathrm{Hue}(\mathrm{R},\mathrm{G},\mathrm{B}) = \arctan\left(\frac{\sqrt{3}\cdot(\mathrm{G}-\mathrm{B})}{2\cdot(\mathrm{R}-\mathrm{G}-\mathrm{B})}\right) \tag{3.7}$$

where R, G and B are the corresponding red, green and blue values associated with each pixel's color and determined by the image processing software [Douglass, et al., 2003] .

Hue is the only property of interest to TLC users. The liquid crystals are designed to react linearly in hue with respect to temperature across a portion of their bandwidth—generally from red start to blue start. This facilitates calibration, which will be discussed

in greater detail in the following chapter. Therefore, if the experimenter has image processing capabilities that can distinguish between hues, they can distinguish temperatures as well. With minimal computation effort, a considerable cost savings over an IR imaging setup can be realized for the same measurement results. TLC sheets are relatively inexpensive and, compared to an IR camera, a conventional digital camera is extremely cost effective. Our TLC sheets are rated to be linear between 30°C and 35°C; although, they did not always react as expected. This problem, and the solution, will be discussed in the next chapter. All internal experiments use a Minolta DiMage S404 4.0 mega-pixel digital camera to capture liquid crystal images. These images become surface heat transfer coefficients through post processing that will be discussed in the following chapter as well.

One of the most important things to consider when working with TLC products was their illumination environment. A schematic of our lighting configuration can be seen in Figure 3-31. The liquid crystals were not auto-luminous, they required outside lighting to observe their color changing properties. In addition to the optics discussion, Camci's [1992] paper outlined several experiments that tested a liquid crystal's dependence on lighting environment. The net result was that the validity of a liquid crystal's calibration was independent of lighting angle or magnitude. However, calibrations could vary widely if illumination intensities or angles were changed during an experiment or between experiments using the same calibration. In short, a given calibration was only valid for the specified lighting angle and magnitude. Our experiments and calibrations were lit with two 100 Watt floodlights. One light was located 114.3 cm from the microcircuit at an angle 55° up in the spanwise direction from a pitchwise line through the center of the microcircuit. The second light was in the same spanwise plane as the microcircuit, but 67.3 cm away at an angle 47.5° upstream of the same pitchwise line through the center of the microcircuit. In addition to fixing these lights, the internal side of the test section was enclosed by a wooden roof and thick black curtain to remove any effects room lighting.

Part of the experimental setup that allowed resolution of heat transfer coefficients was the constant heat flux boundary condition. We achieved this boundary condition with a thin, custom-made inconel heater manufactured by the Electrofilm MFG.

Company in Valencia, California. The heater consisted of a serpentine inconel circuit encased in electrically non-conductive kapton. The serpentine paths bent and twisted around the prescribed geometry with a minimal gap between paths. The result was a circuit that, when carrying a current, heated with an even Watt density. To further balance the heat flux leaving the heater, a thin layer of copper was affixed to the top surface. Figure 3-32 shows the serpentine paths that made up the heating element. With respect to the internal test section, the heater was located between the TLC sheets and the microcircuit pedestal features. The heater was powered with a Hewlett-Packard 6024A DC Power Supply. Current from the power supply first passed through a 1 Ω precision resistor before entering the heater. The precision resistor provided a known impedance, across which an accurate voltage measurement was made. This translated to a measurement of power dissipated in the heater, and thus heat flux, with minimal experimental uncertainty. Actual collection of the voltage measurement will be discussed in the following chapter, although the wiring network can be seen in Figure 3-32.

Thermocouples played an important role in heat transfer coefficient mapping as well, although they were not nearly as pervasive as they were in external testing. Surface temperatures were not measured with thermocouples on the internal channel testing; but rather with the liquid crystals. Of course, the liquid crystal needed to be calibrated with thermocouples, just as the external images did. Although, calibration was completed only once, and before all testing began. As noted, calibration of the liquid crystals will be discussed in the following chapter. Thermocouples were used to measure the temperature of the coolant air. Temperatures were recorded in three coolant plenums, at the beginning of the three center microcircuit inlet bends and at four exit slot locations—two per slot. In addition, fourteen thermocouples were monitored at seven locations on both sides of the adiabatic foam wall. Internal thermocouple locations are documented in Figure 3-33. We took these measurements to quantify a conduction loss through the foam wall, although the loss turned out to be so small it was neglected. This, and another, conduction correction will be discussed in the following chapter.

In addition to thermocouples, the microcircuit channel was outfitted with a host of pressure taps installed in the foam wall. These taps were used to map the static pressure across several key measurement planes throughout the microcircuit channel. First,

pressure taps installed in the plane directly upstream of the first row of pedestals were used both to characterize the static pressure at this plane and to balance the microcircuit inlet flows. In all, this row contained seventeen static pressure taps, nine directly downstream of the inlets and eight between inlets, but still aligned with the other taps in the streamwise direction. The procedure used to balance the flows will be discussed in the following section. The next row of static pressure taps was located midway between the first and second pedestal rows. This row used eight taps to map the static pressure between these rows; four of the taps were located between first row pedestals, in a spanwise sense. The other four taps sat directly behind the first row pedestals upstream of them. The static pressure measurement plane between the second and third rows replicates the previous plane with eight taps; four taps behind pedestals and four taps between pedestals. However, these taps were in different spanwise locations than the upstream measurement plane. After the third pedestal row, before the submarines, nine static pressure taps were installed. Three taps each were devoted to the left and right submarines and the center divider; each had one tap in the center, one to the left of center, and one to the right of center. Downstream of the submarines, each slot exit channel had two pressure taps, for a total of twelve taps in that measurement plane. Figure 3-34 shows the pressure tap locations in the microcircuit.

Additionally, pressure taps on two feed plenums recorded microcircuit plenum feed total pressures. In all, 54 static pressure taps were monitored for the internal heat transfer tests. All pressure taps were fitted with vinyl tubing connected to a device called a Scanivalve. The Scanivalve had several pressure ports that could translate the pressure experienced in the vinyl tube to a central port attached to a pressure transducer. The pressure port transmitted to the pressure transducer was user selectable with a knob located on the front of the device. This allowed the measure of many pressure taps on one transducer without the constant removal and re-installation of pressure tubing.

All pressure measurements, with one exception, were taken on Setra and Omega differential pressure transducers of varying capacity. The one exception was the transducer employed to measure the pressure differential across the venturi tube. The line pressure in the venturi exceeded the capacity of the Setra and Omega transducers. Therefore, a Validyne DP-103 high line pressure transducer was purchased. This

transducer could accommodate a line pressure of up to 689 kPa. The Validyne transducer contained a removable diaphragm, unlike the Setra and Omega transducers, which have fixed differential ranges. The diaphragms purchased for our Validyne transducer were equipped to measure differential pressures of 34.9 Pa, 54.8 Pa, 221.7 Pa, and 871.8 Pa.

Internal Coolant System Data Acquisition Equipment and Procedure.

The internal channel data-taking procedure differed from the external procedure in several ways. To begin, the time from startup to steady state was considerably shorter. The heated area was orders of magnitude smaller for internal tests. Internal experiments typically reached steady state in less than 45 minutes. After recording ambient temperatures and pressures, the cooling flow required for the specified microcircuit Reynolds number was balanced in the same manner used for external experiments. At that point, the heater was activated and began to warm the microcircuit. The first heater setting of the experiment was somewhat arbitrary and based on past experience; it was chosen to activate the liquid crystals in the area with the lowest heat transfer coefficient. The power delivered to the heater was based on the resulting reaction of the liquid crystal. The reaction bandwidth of the liquid crystal was fixed between 30°-35°C so, for a given heat flux, only a portion of the surface reacted in the linear range of the TLC. Therefore, several images were required to completely map the entire microcircuit's surface temperature. Figure 3-35 is a theoretical plot of the surface temperature with respect to streamwise flow distance for several values of heat flux. The plot does not represent data take for this study, but the theoretical behavior of surface temperatures in a channel heated from one side. With the TLC bandwidth overlaid, the plot serves to illustrate the point described above. Figure 3-36 compares two images taken with different heat flux settings for the same Reynolds number. In general, six to eight image sets were required to fully characterize the heat transfer environment for each Reynolds number.

After selecting an initial heat flux setting, the system took about fifteen minutes to reach steady state. A set of twelve images was taken at each heat flux setting. To actually capture the image, a trigger mechanism was used to actuate the camera's shutter remotely. The lighting control switch was located out of the enclosure as well, allowing

completely remote imaging. Use of the lights was tightly controlled, as they induced a measurable amount of radiative heating when left on for longer than a few seconds. Fortunately, the camera's shutter operated quickly and, as long as they were not left on, the lights had no effect on the results. Figure 3-37 is a plot of the temperature time trace for an internal test. Lighting effects are evident, although the shutter cycle is completed by the time the lights raise the temperature by more than 0.01-0.02°C. The lights and camera shutter were actuated almost simultaneously, less than 1 second apart. The shutter was closed again less than one second after actuation. The lights were extinguished three or four seconds later to ensure adequate lighting for the image. After an image was taken, we waited at least one to two minutes before taking another image.

Before actually taking the images, Labview recorded two minutes of flow data to ensure the microcircuit flow rate had not fluctuated. During this time, the voltage across the precision resistor in series with the heater was also measured—recall Figure 3-33—to quantify the total power supplied to the microcircuit. Upon completion of the two minute flow data record, Labview was set to acquire temperature data. A total of 12 images were taken for each heat flux setting, with a minute waiting period between images. Once an image set was completed, the current supplied to the heater was increased, generally by an amount on the order of 0.25 Amps. The actual increase did not need to be consistent every time, the important factor was that the reacting area on the liquid crystal slightly overlapped the reactive area of the heat flux settings before and after it. This ensured complete mapping of the surface. Once several image sets were taken, the heater was powered down. The cooling air was left on to bring the microcircuit to room temperature before completing the experiment.

Coolant System Benchmarking. Before testing could begin, we needed to take a set of benchmark data that could easily compare to established data and correlations. A straight, semi-infinite channel was chosen for this step. Figure 3-38 is a diagram of the benchmark setup. This setup required several departures from the microcircuit setup described above. First, an independent feed plenum was constructed out of 1.3 cm Lexan. This was fed from two of the octopus plenum exits and led to an inlet bend similar to that of the microcircuit inlet bend. In fact, the benchmark inlet bend

construction consisted of exactly the same steps as those used for the microcircuit inlet bends. The only differences were their size and number. The benchmark inlet bend was much longer in the spanwise direction and only one was necessary. The benchmark channel was different in another aspect as well. As there were no external effectiveness tests required for the benchmarking study, the rear wall was constructed of MDF, instead of foam and the channel did not exit through a similar slot exit bend. The downstream portion of the channel simply exited to the atmosphere. The benchmark channel measured 16 cm wide in the spanwise direction, 21.7 cm long in the streamwise direction, and 6.3 mm in the pitchwise direction. This translated into an L/D_h ratio of 17 which was long enough to consider the flow fully developed.

Baseline data was taken using the liquid crystals and strip heater discussed in the instrumentation sub-section above. Each Reynolds number required six different heat flux settings to map the entire surface. The total heated area was 12.7 spanwise cm by 21.7 streamwise cm.

Straight channel heat transfer coefficients are well characterized in the literature. We compared our straight channel heat transfer coefficient results, normalized as Nusselt numbers, to data for fully developed flow in a straight, semi-infinite channel with a constant heat flux boundary and an adiabatic opposing wall [Kays et al., 1980]. The correlation was empirically derived as a function of Reynolds number (Re) and given as follows:

$$Nu_o = 0.0285 \cdot Re^{0.75} \tag{3.8}$$

Our straight channel results matched this correlation quite well. Figure 3-39 is a plot of spanwise averaged Nusselt number across the channel. The high initial Nusselt numbers are due to entrance effects. The exit spike is due to a small overhanging section at the channel exit where the channel no longer has a constant heat flux boundary. Figure 3-40 is a plot of equation 3.1. The VTExCCL data points in Figure 3-40 represent area averaged Nusselt numbers in the fully developed region of the channel. Turbulent duct flows are considered thermally and hydrodynamically fully developed in X/D_h distances of approximately 10 [Bejan, 1995].

As with the external experiments, the final step in establishing the internal portion of the test facility's benchmark was to establish experimental repeatability for internal tests. We did this by completing a single test two times on different occasions. We completed the 5262 experimental case twice. Figure 3-41 is a comparison of Spanwise averaged Nusselt number augmentation for two similar Reynolds numbers, showing agreement within the measurement uncertainty.

3.3 Experimental Uncertainty

An uncertainty analysis was performed on all of the data collected. Uncertainty was calculated for all of the variables mentioned above using the partial differential method described in Holman [1994].

Since there were many different types of data collected for this study, the relative uncertainty values will not be presented in the text. Table 3-2 will present uncertainty results for Nusselt number, Reynolds number, baseline Nusselt number, heat transfer augmentation, adiabatic effectiveness, friction factor, baseline friction factor, and friction augmentation. All of the uncertainties were calculated in the same manner. First, the formula for a given variable was written as detailed as possible. For instance, the formula for adiabatic effectiveness was written as follows:

$$\eta_{AW} = \frac{\frac{\eta_{o,\infty}(T_c) + T_\infty}{1+\eta_{o,\infty}} - T_{AW}}{\frac{\eta_{o,\infty}(T_c) + T_\infty}{1+\eta_{o,\infty}} - T_c} \tag{3.8}$$

Equation 3.8 is written in terms of measured parameters only. For example, the expression common to the numerator and denominator in Equation 3.8 is the formula used to correct the mainstream temperature measurements. The correction process will be discussed in Chapter 4. The point is that the formula is written such that every variable is a measurable quantity, there are no implicit calculations that are not shown.

Once the formula was put in a sufficiently detailed form, the partial derivative was taken with respect to each variable individually. Once the partial derivatives were completed, each was evaluated with representative quantities of each variable across the measurement range. For example, adiabatic effectiveness values ranged from zero to one across the measurement range. Subsequently, adiabatic effectiveness uncertainty was calculated for two conditions; adiabatic effectiveness levels of 0.9 and 0.2. The final partial derivatives were then multiplied by their respective measurement uncertainties. The total uncertainty of the variable was the square root of the sum of squares of each partial derivative multiplied by its measurement uncertainty. Using the above example for adiabatic effectiveness, the experimental uncertainty was calculated as follows:

$$u_{\eta_{AW}} = \sqrt{\left[\frac{\partial \eta_{AW}}{\partial T_c} \cdot u_{T_c}\right]^2 + \left[\frac{\partial \eta_{AW}}{\partial T_\infty} \cdot u_{T_\infty}\right]^2 + \left[\frac{\partial \eta_{AW}}{\partial \eta_{o,\infty}} \cdot u_{\eta_{o,\infty}}\right]^2 + \left[\frac{\partial \eta_{AW}}{\partial T_{AW}} \cdot u_{T_{AW}}\right]^2} \qquad (3.9)$$

As mentioned, there are too many variables and flow condition variations to list all experimental uncertainty results in the text. Table 3-2 lists the experimental uncertainties of the major quantities. Additionally, detailed uncertainty calculations can be found in Appendix E.

Table 3-1 Microcircuit Geometry

	Width (spanwise)	Height (pitchwise)	Length (streamwise)
Elliptical Pin Fins	1.5 d	0.75 d	1.2 d
Standard Pin Fins	d (9.5 mm)	0.75 d	d
Submarines	5.1 d	0.75 d	1.9 d
Inlet	1.25 d	0.75 d	
Inlet Spacing	5.8 d		
Exit slots	5 d	0.75 d	0.75 d
Between Exit Slots	3.7 d		
One Periodic Microcircuit	17.4 d	0.75 d	10.6 d
Three Microcircuit Array	52.2 d	0.75 d	10.6 d
Between Inlet/Row 1			0.84 d
Between Rows 1/2			0.78 d
Between Rows 2/3			0.51 d
Between Rows 3/4			0.65 d

	Flow Area Obstructed by Pedestal Features (%)
Row 1 (Elliptical Pin Fins)	52%
Row 2 (Standard Pin Fins)	57%
Row 3 (Standard Pin Fins)	57%
Row 4 (Submarines)	72%

Table 3-2 Experimental Uncertainty Results

Variable	Condition	Value	Uncertainty	% Uncertainty
Re	High Re	15127	641	4.2
	Low Re	5262	221	4.2
Nu	High Re, Low Local Nu	90.0	3.4	3.8
	High Re, High Local Nu	202.5	5.5	2.7
	Low Re, Low Local Nu	51.3	2.4	4.6
	Low Re, High Local Nu	102.6	1.6	1.6
η_{AW}	High η_{AW}	0.9	0.019	2.1
	Low η_{AW}	0.2	0.038	19.0
Nu_o	High Re	17.1	0.535	3.1
	Low Re	37.5	1.186	3.2
Nu/Nu_o	High Re, Low Local Aug	2.4	0.143	6.0
	High Re, High Local Aug	5.4	0.224	4.1
	Low Re, Low Local Aug	3.0	0.167	5.6
	Low Re, High Local Aug	6.0	0.211	3.5
f	High Re	2.4	0.179	7.5
	Low Re	3.0	0.229	7.7
f_o	High Re	2.9E-02	3.0E-04	1.1
	Low Re	3.7E-02	3.9E-04	1.1
f/f_o	High Re	83.6	6.41	7.7
	Low Re	80.0	6.17	7.7

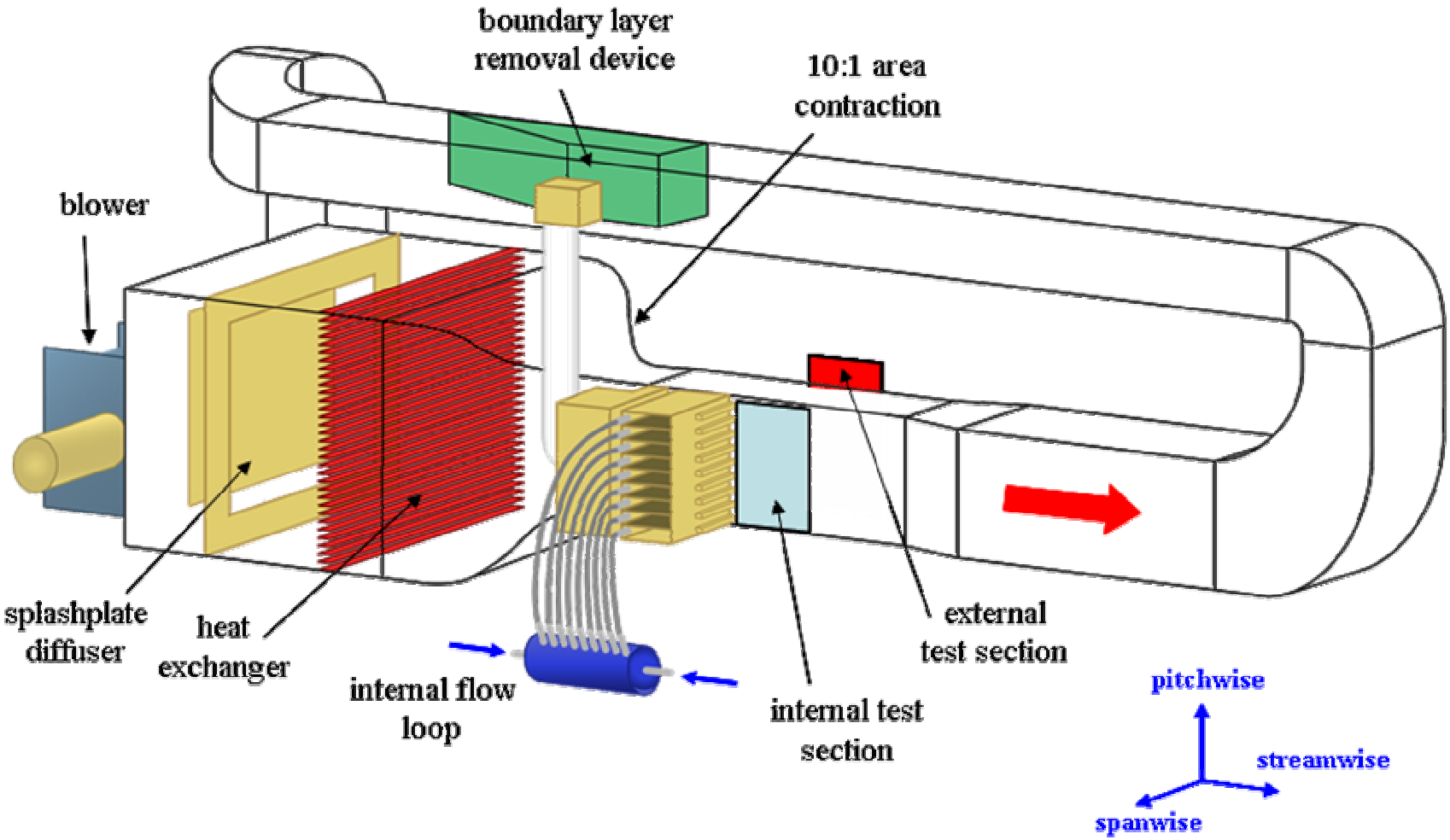

Figure 3-1 Flow path schematic.

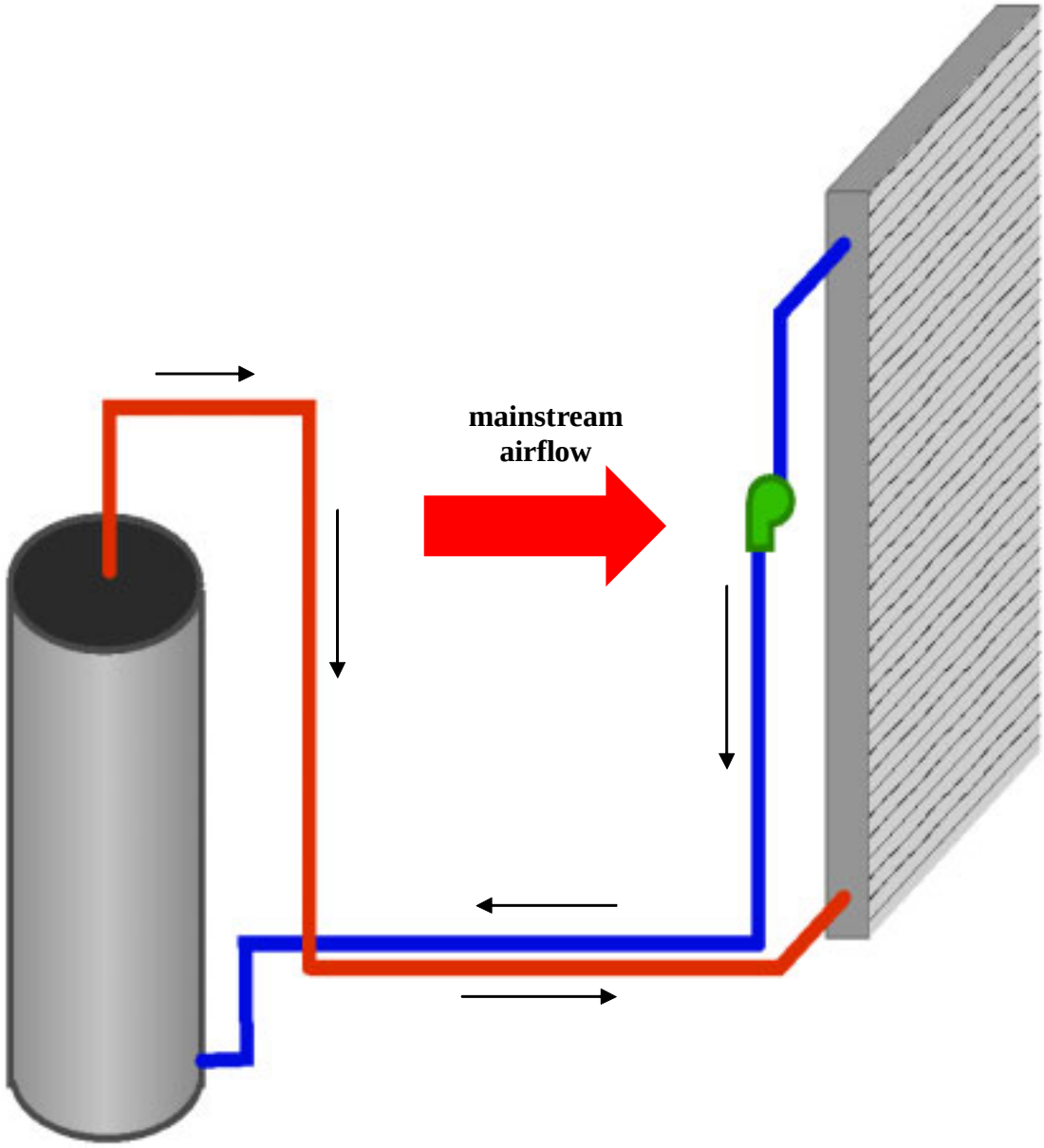

Figure 3-2 Heat exchanger circulation schematic showing the flowpath from the hot water heater to the coil. The pump is shown in green.

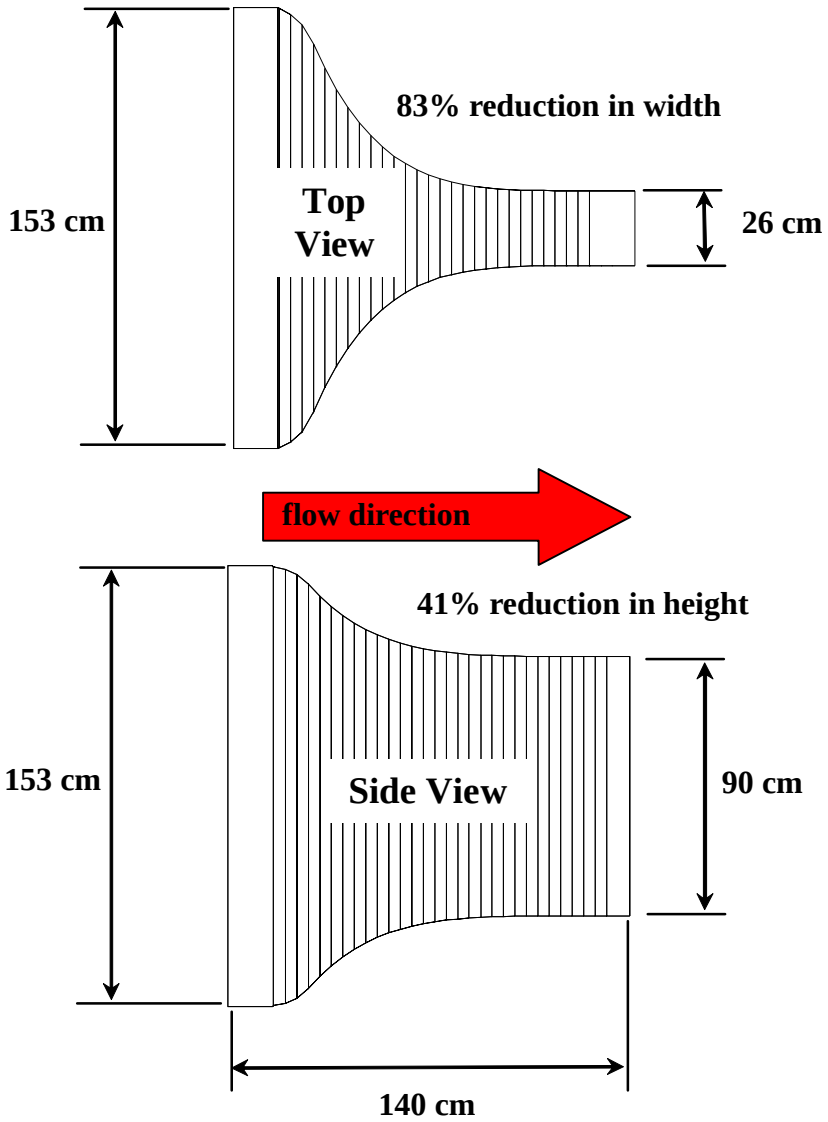

Figure 3-3 Schematic top and side views of the 10:1 area ratio contraction.

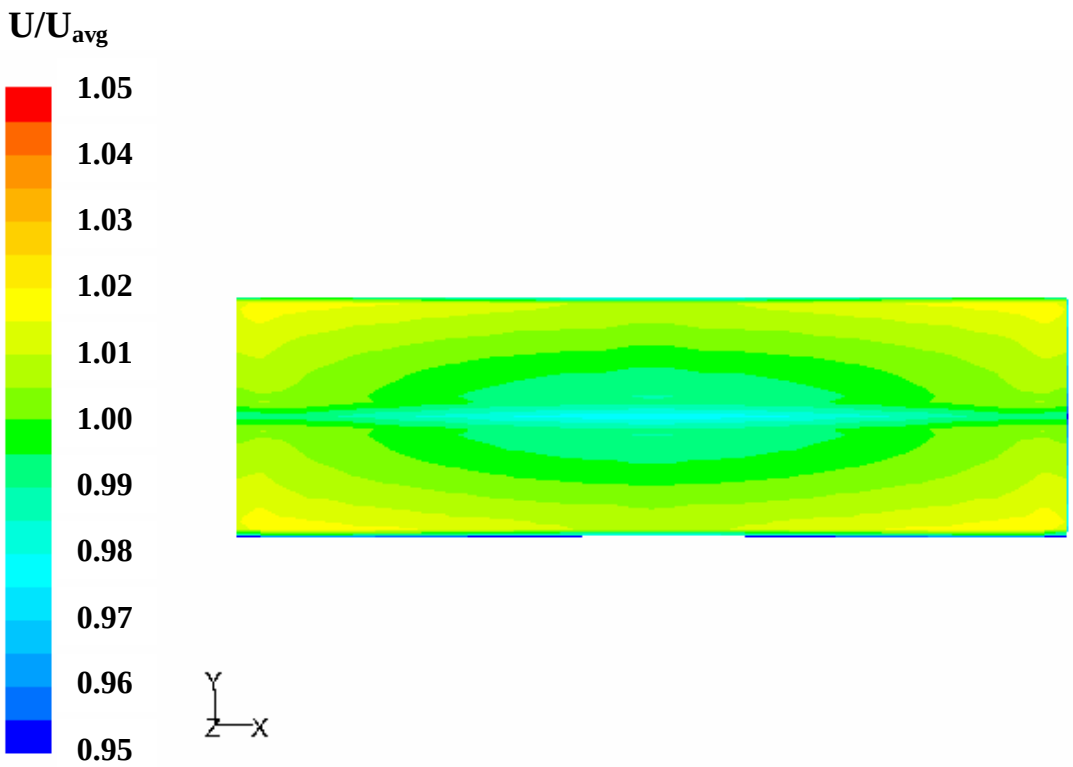

Figure 3-4 Contour plot of contraction exit velocity.

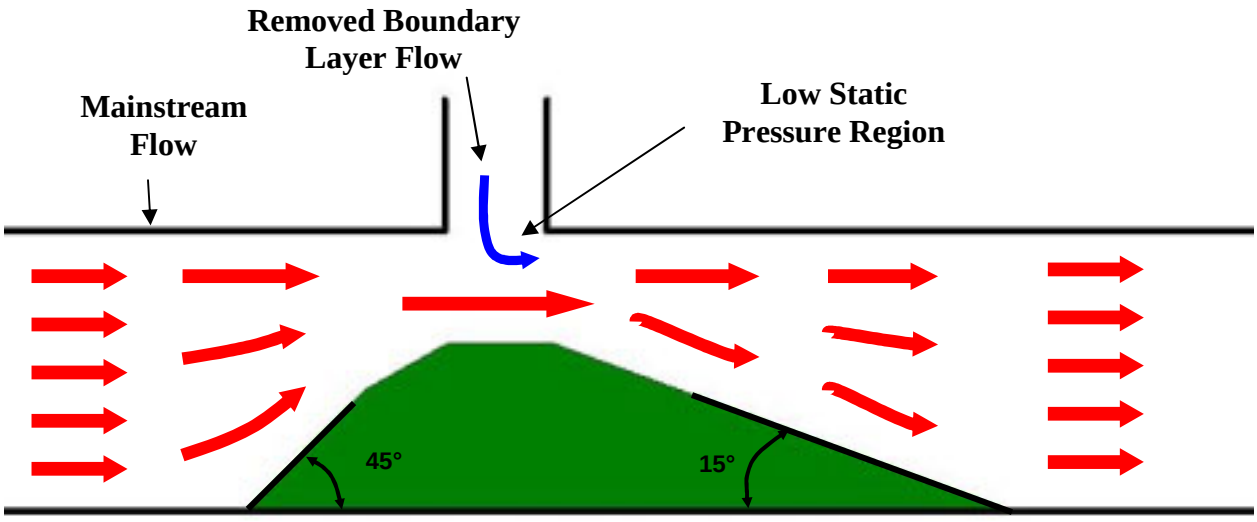

Figure 3-5 An area blockage in the return duct provides the suction required to remove the boundary layer in the test section.

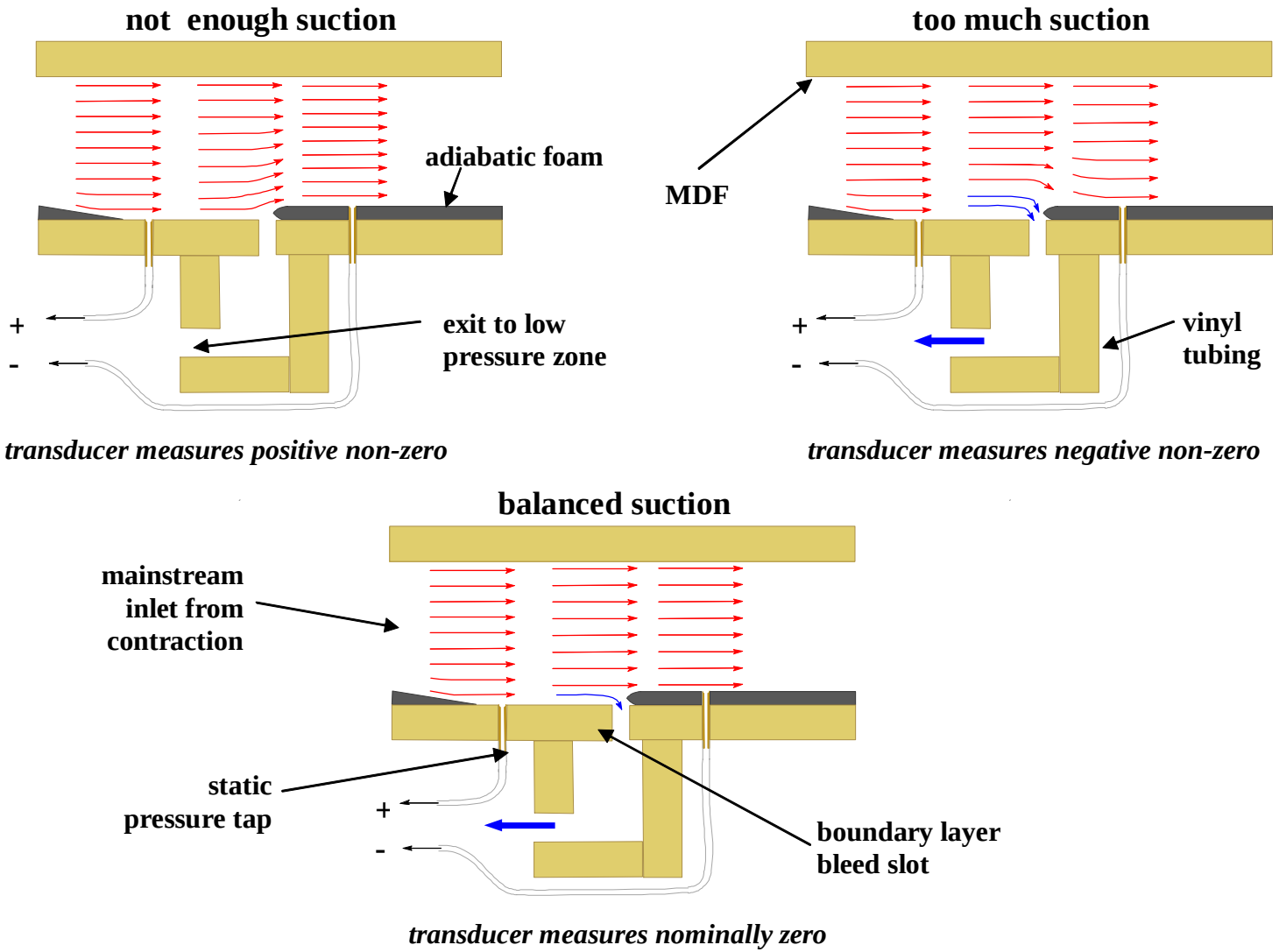

Figure 3-6 Boundary layer bleed slot situations

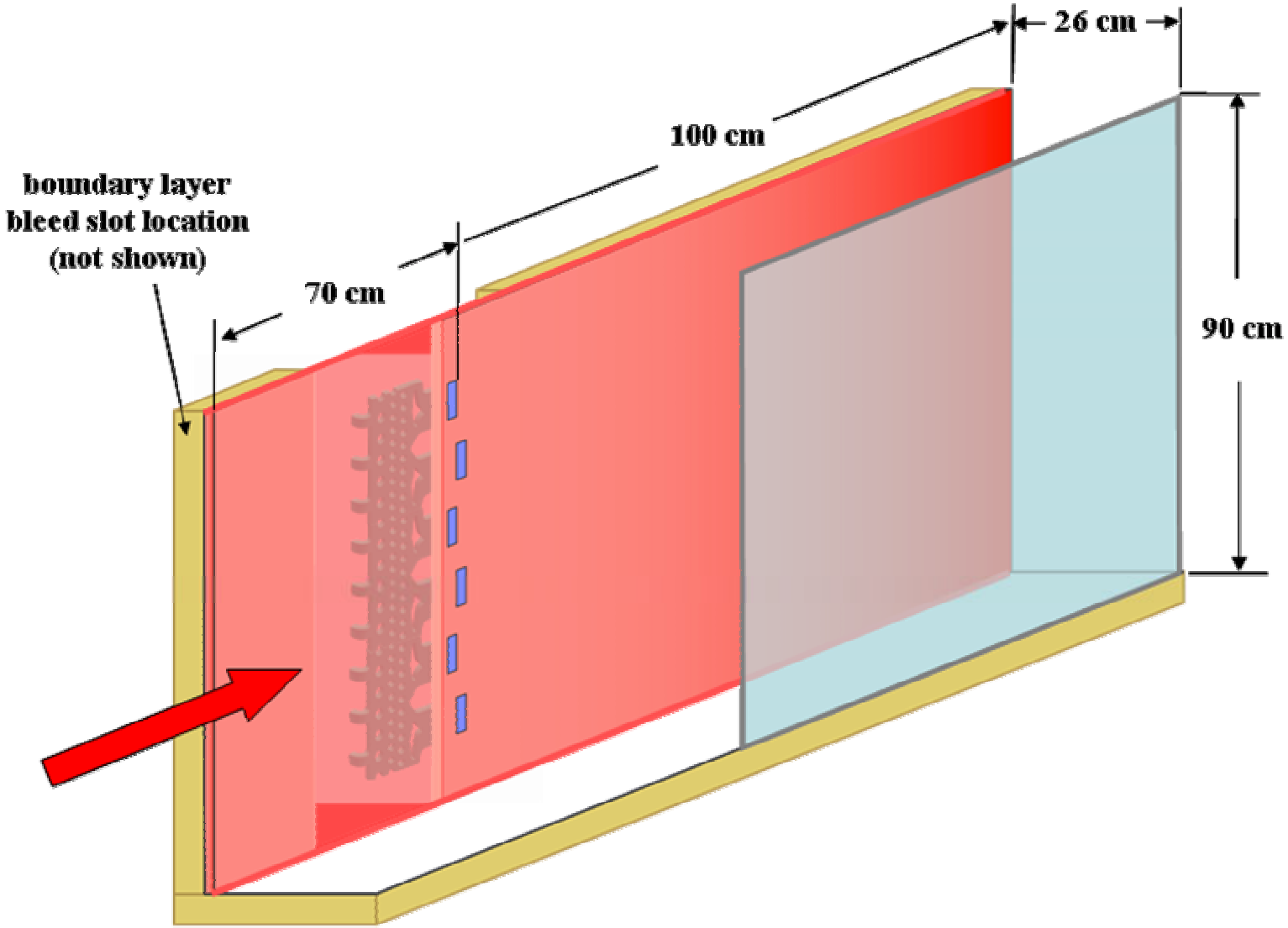

Figure 3-7 Mainstream test section close-up view. Half of the Lexan wall and the test section top are not shown for visibility. The adiabatic wall is shown in red, while the microcircuit slot exits are shown in blue. The microcircuit orientation can be seen through a semi-transparent section of the adiabatic wall.

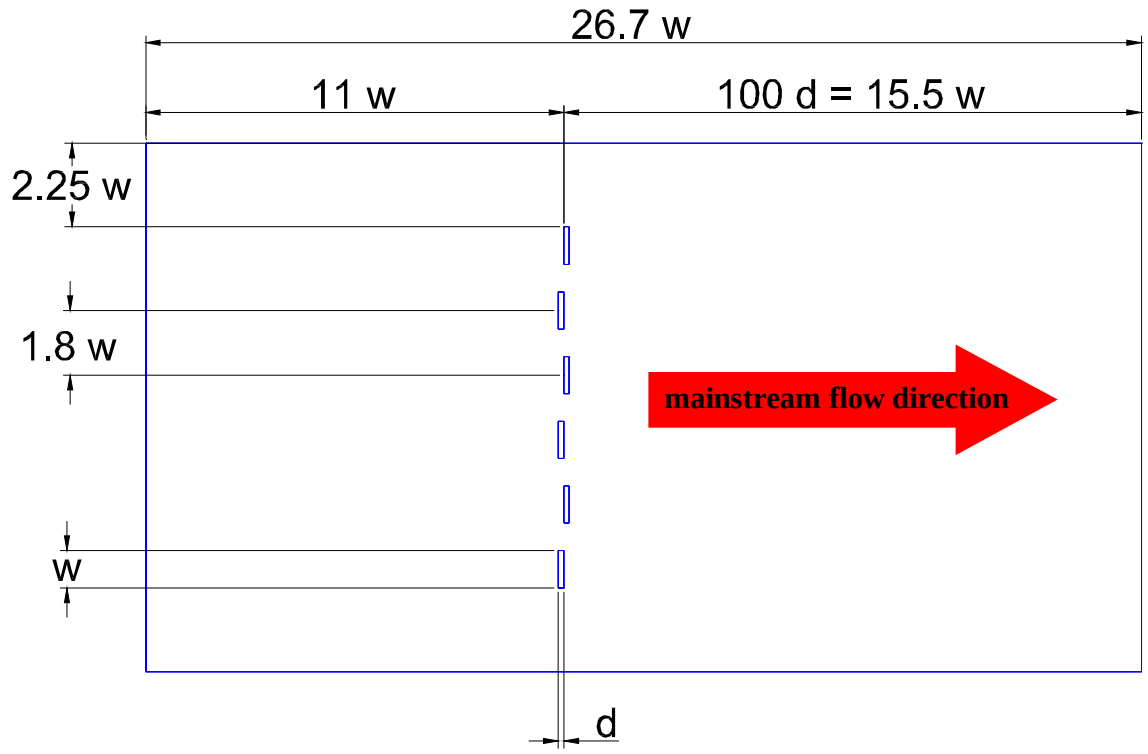

Figure 3-8 Slot locations on the external adiabatic wall. We allowed 100 slot widths (d) downstream of the slot locations to ensure we could measure the entire region benefited by the film cooling.

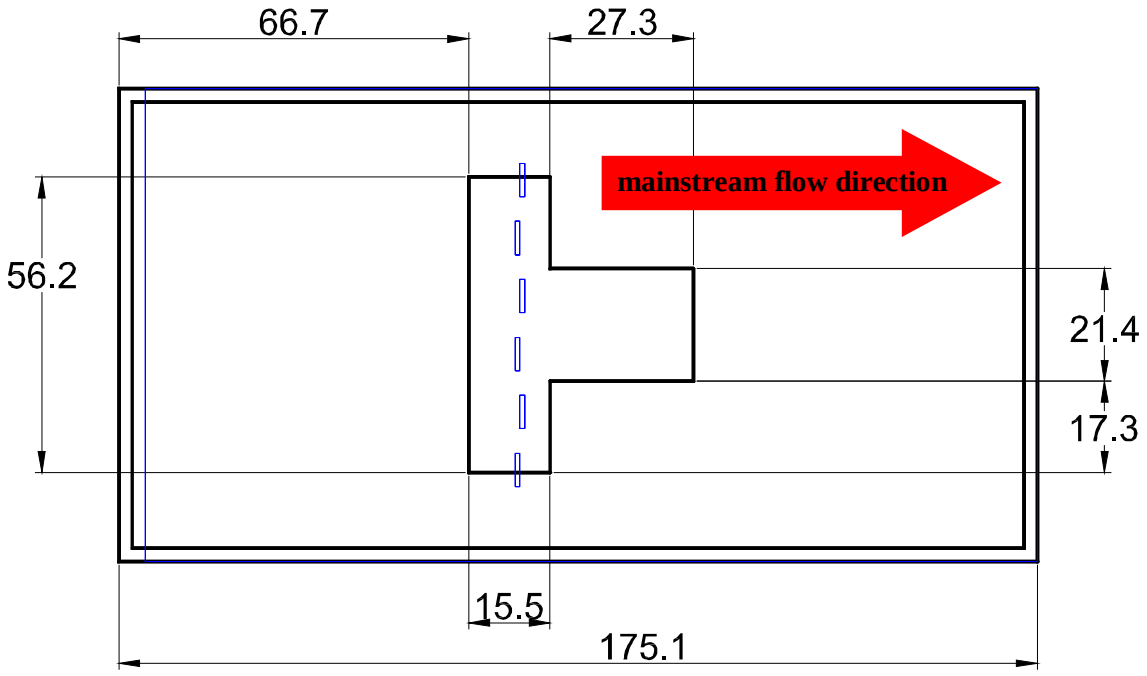

Figure 3-9 Imaging window in Lexan wall (external test section). All dimensions are in centimeters.

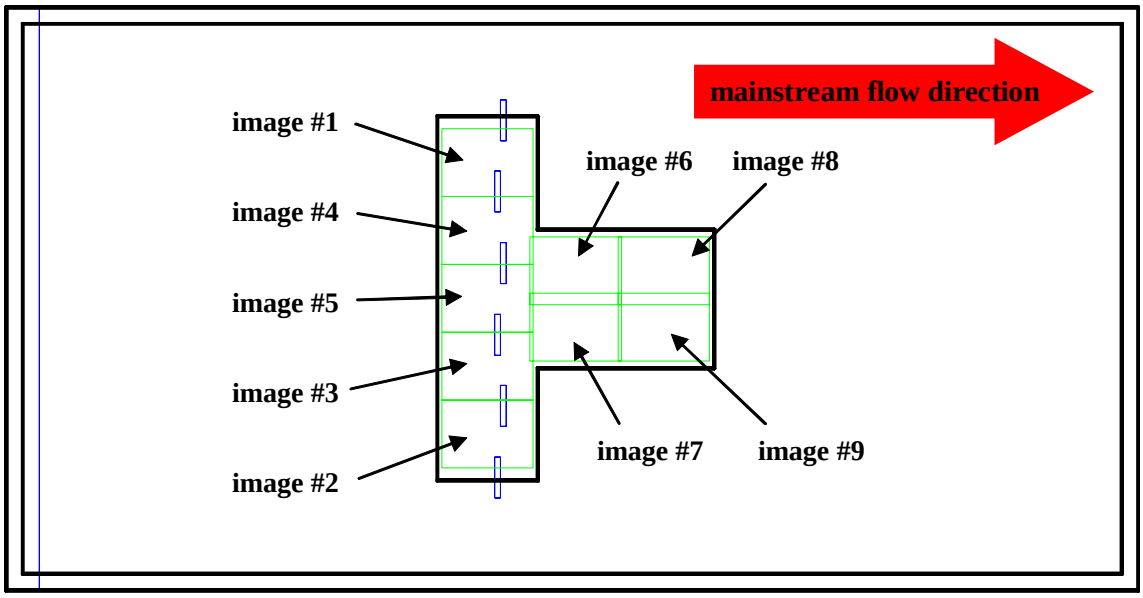

Figure 3-10 Detail of nine image scenarios. Slot locations and IR openings are shown for reference.

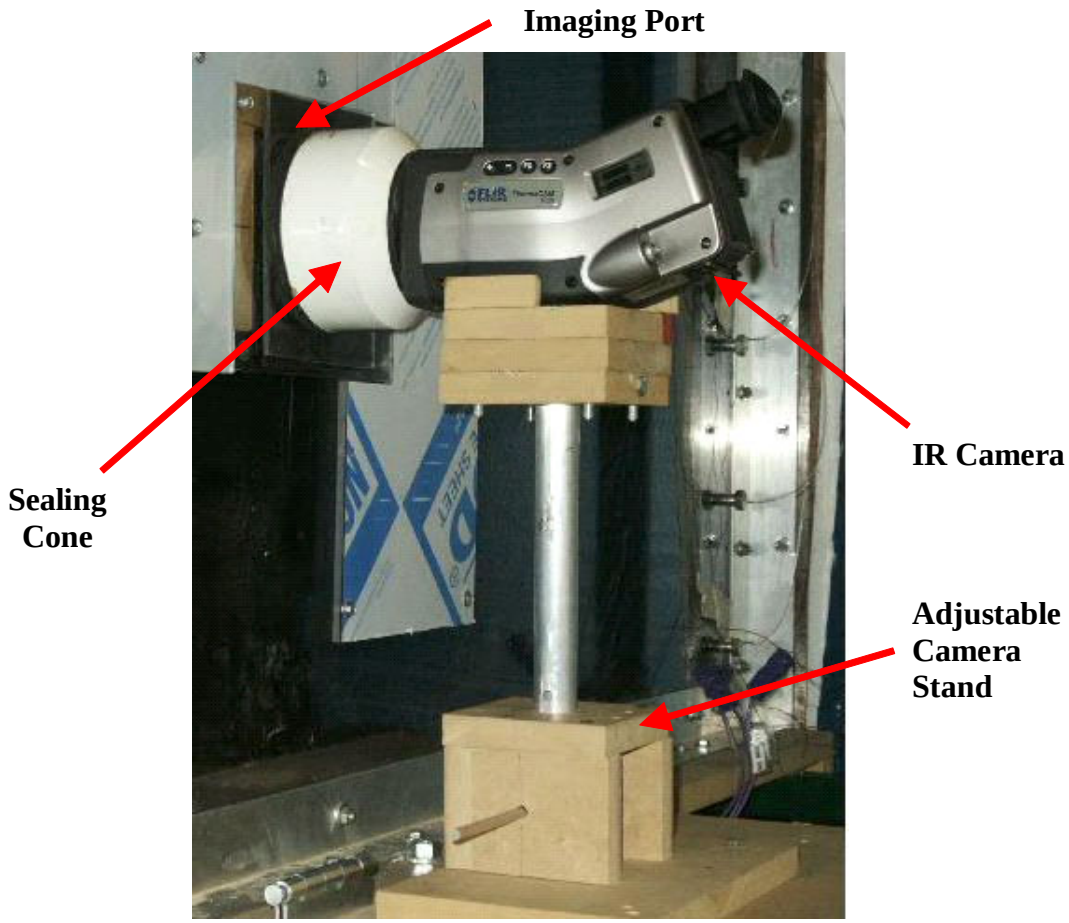

Figure 3-11 IR camera, as mounted on stand, with sealing cone and imaging port.

Figure 3-12 Photo of mainstream loop.

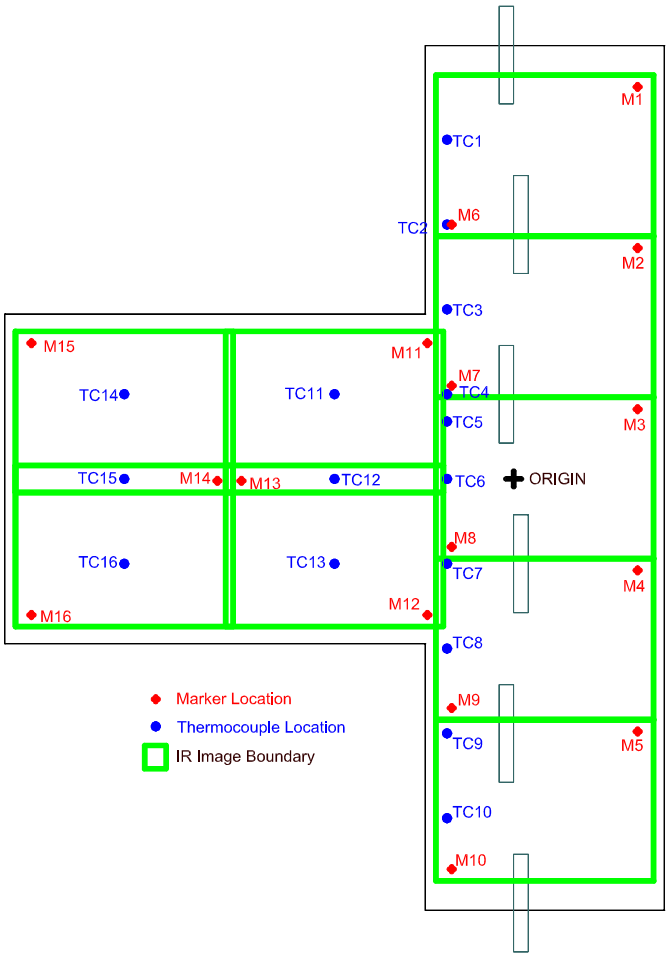

Figure 3-13 Thermocouple and marker locations on external wall.

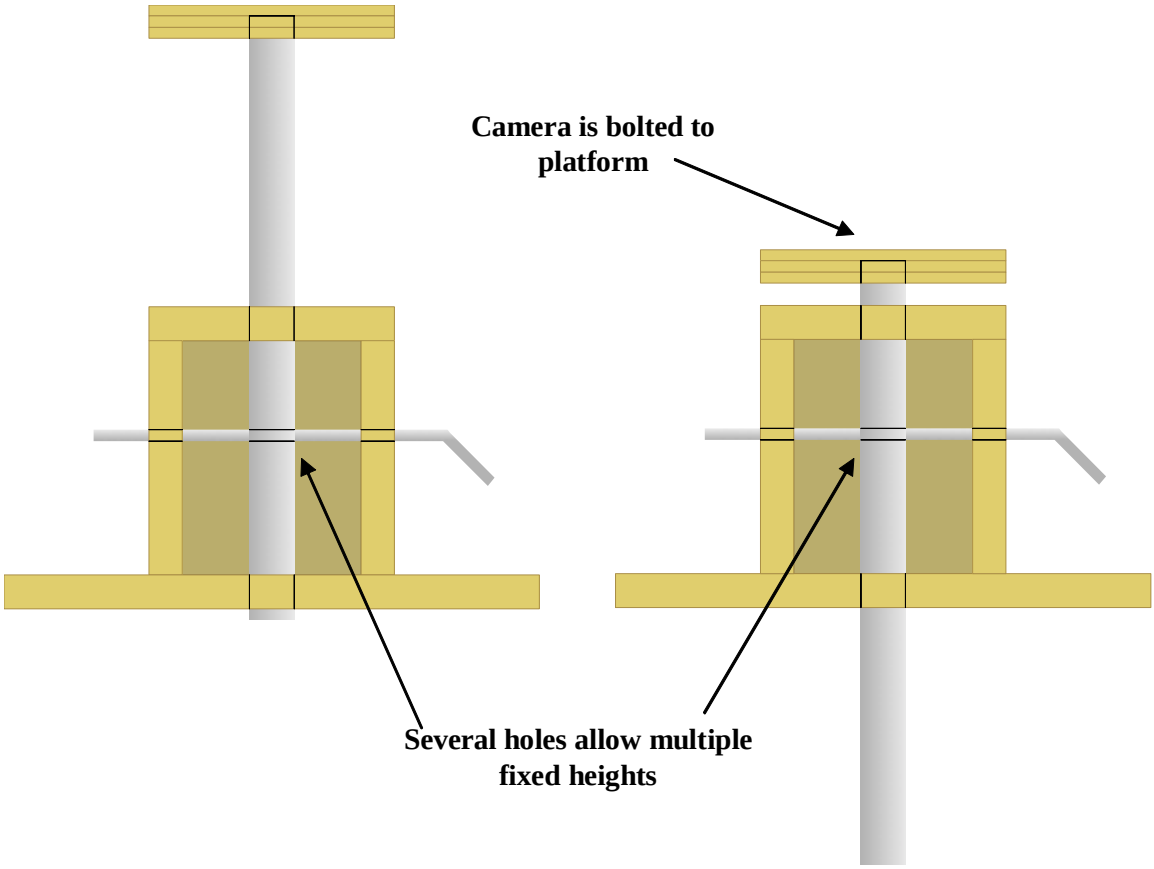

Figure 3-14 IR camera mounting apparatus. Camera height was adjusted by a pin through the traversing pole, it is depicted here in both high and low settings.

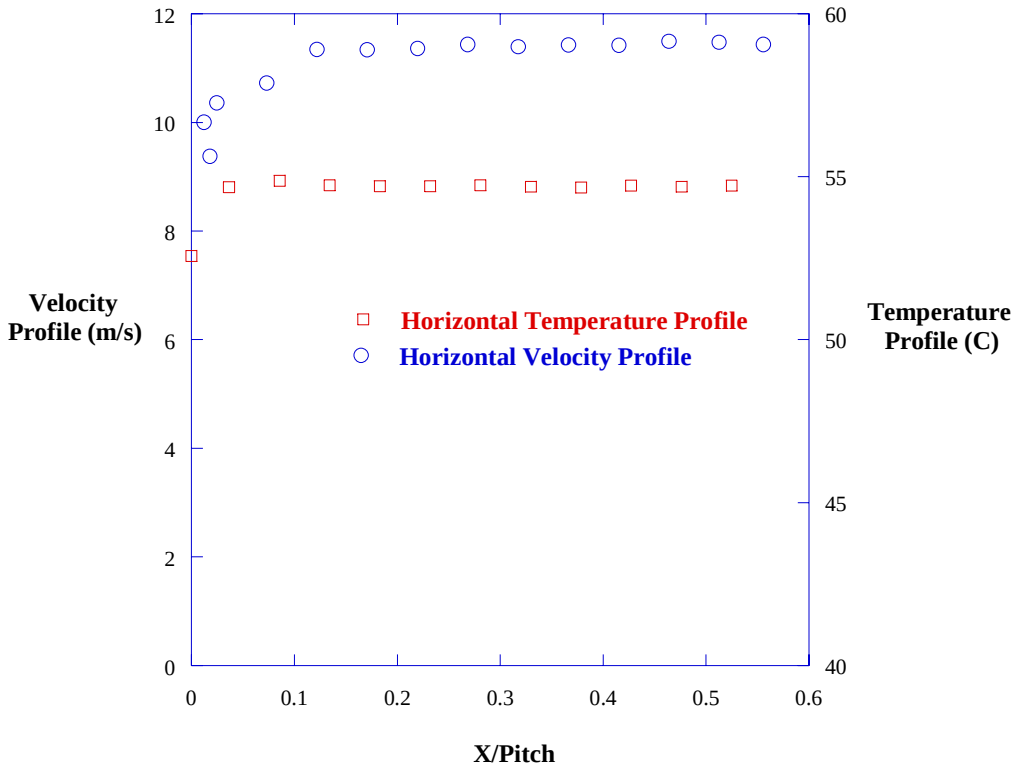

Figure 3-15 Horizontal velocity and temperature profiles.

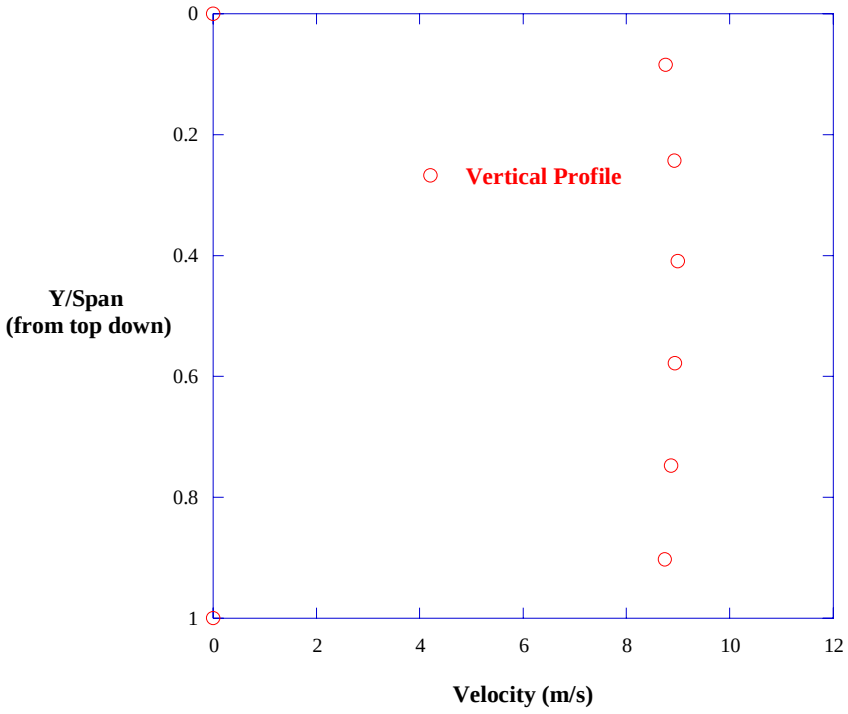

Figure 3-16 Vertical velocity profile.

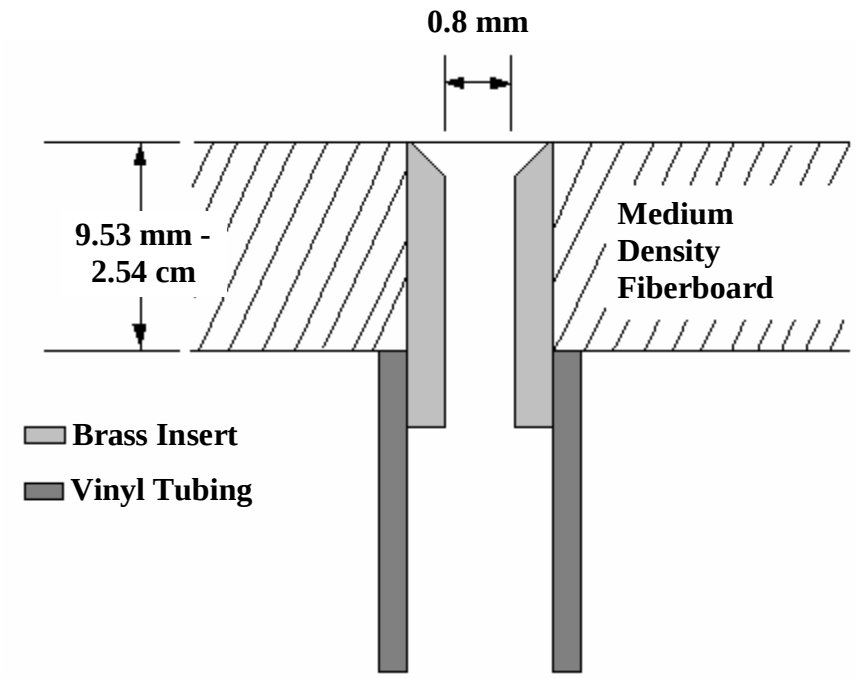

Figure 3-17 Pressure tap installation configuration for all pressure tap locations [Couch, 2003].

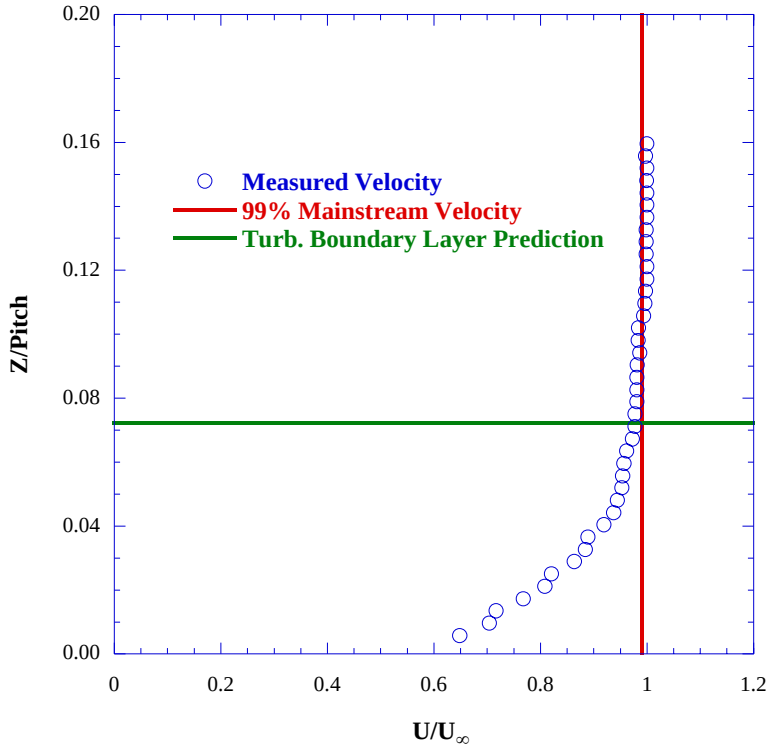

Figure 3-18 Horizontal velocity profile two slot widths upstream of the cooling slots. Measurements agree with flat plate turbulent boundary layer predictions.

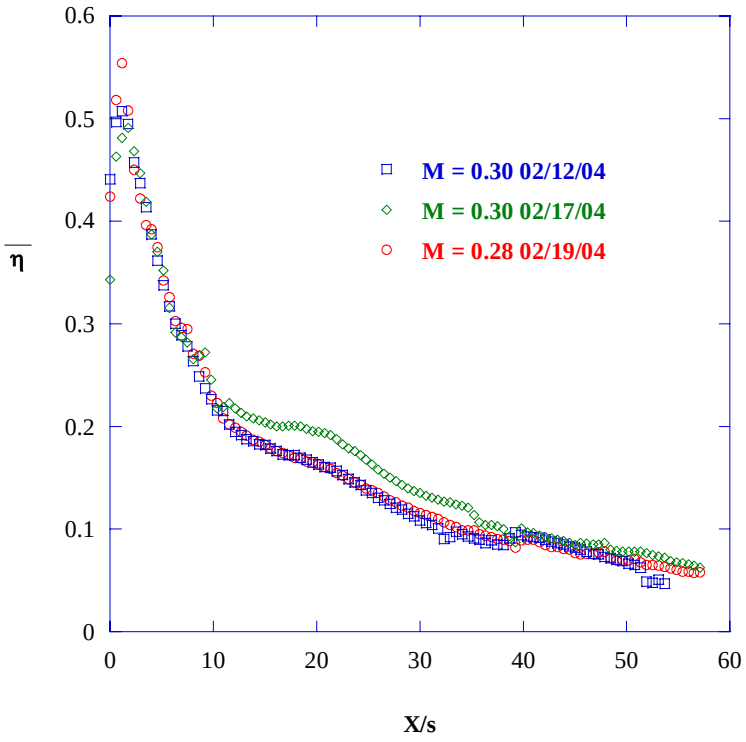

Figure 3-19 Three plots of effectiveness data taken on separate occasions. The agreement within the measurement uncertainty assures repeatability.

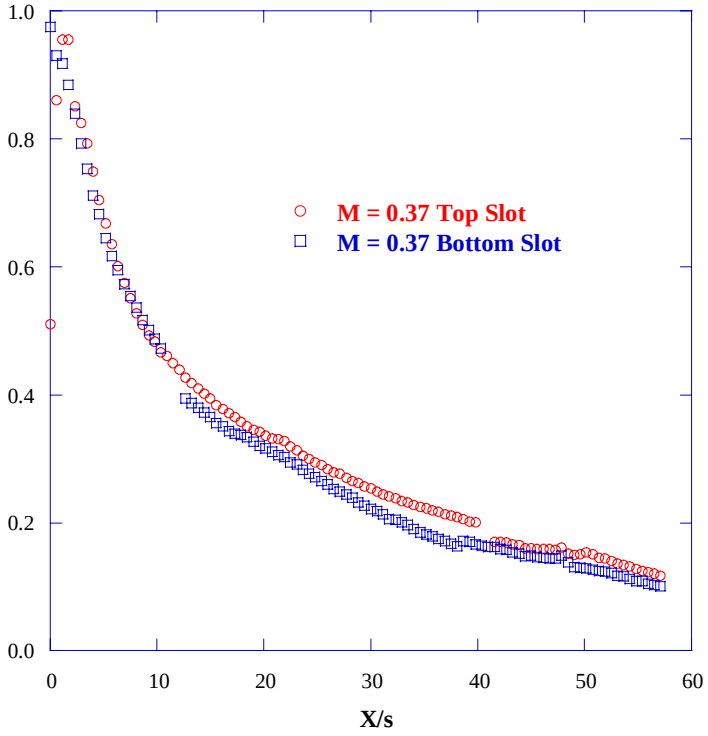

Figure 3-20 Centerline adiabatic effectiveness measurements corresponding to top and bottom slots. The agreement within the measurement uncertainty indicates our procedure to balance inlet flows was adequate.

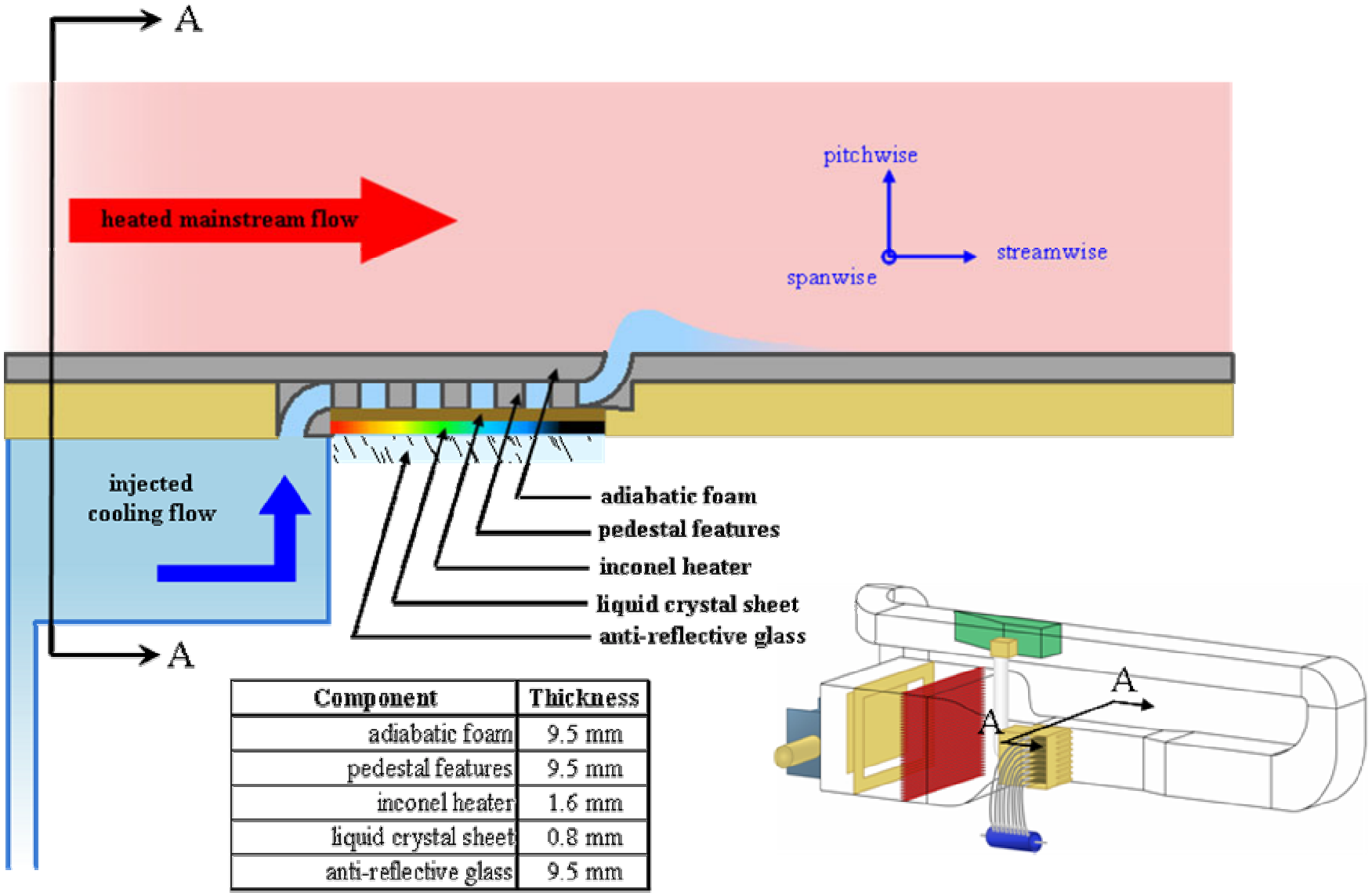

Component	Thickness
adiabatic foam	9.5 mm
pedestal features	9.5 mm
inconel heater	1.6 mm
liquid crystal sheet	0.8 mm
anti-reflective glass	9.5 mm

Figure 3-21 Cross-section schematic of test section.

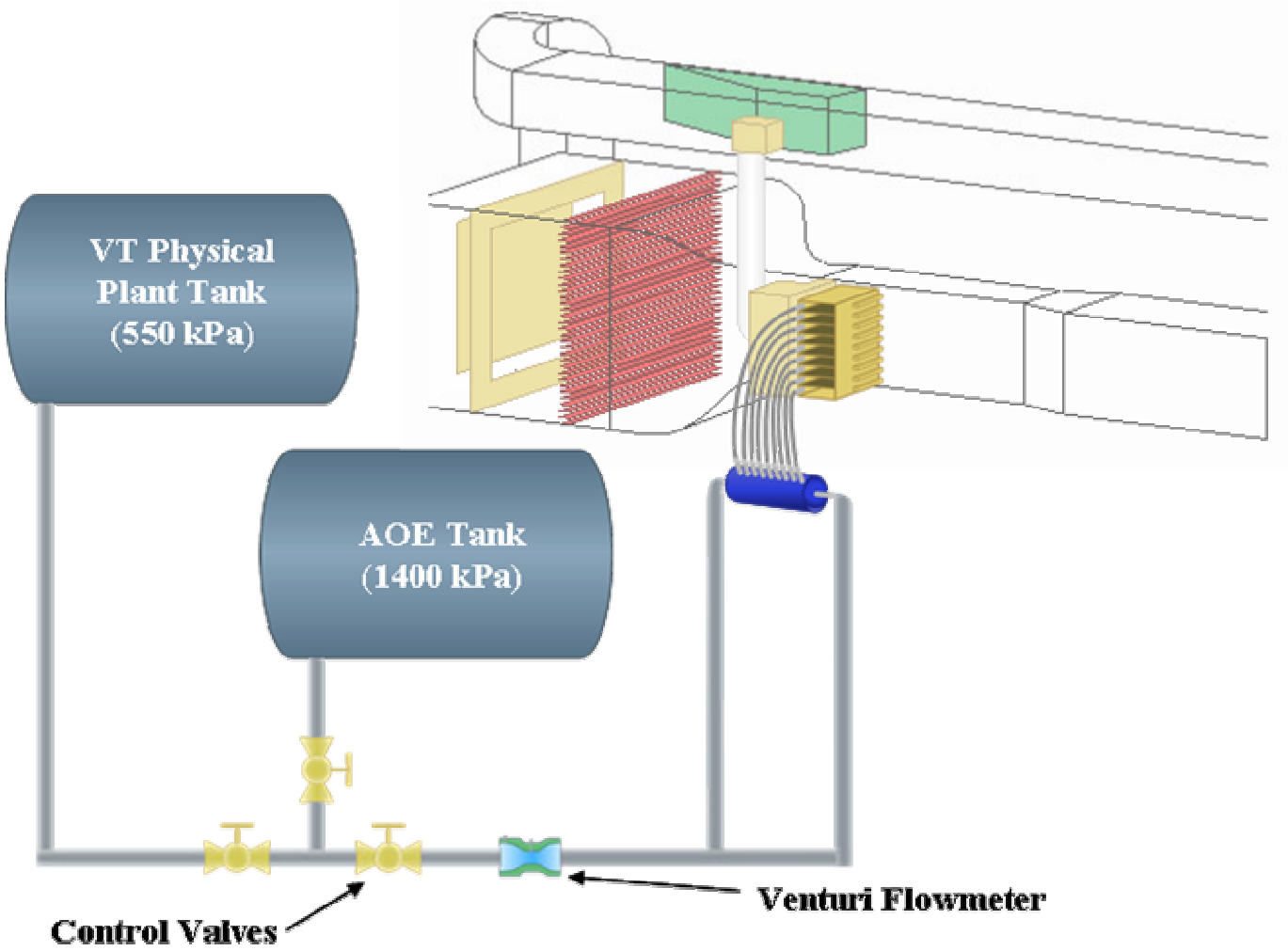

Figure 3-22 Schematic of coolant supplies and flow paths to the microcircuit inlets. The wind tunnel schematic is shown shaded for reference. Note, both compressed air tanks are located offsite.

Figure 3-23 "Octopus" microcircuit coolant flow plenum. Air enters through the tubing above and below, and exits through the nine valved exit hoses.

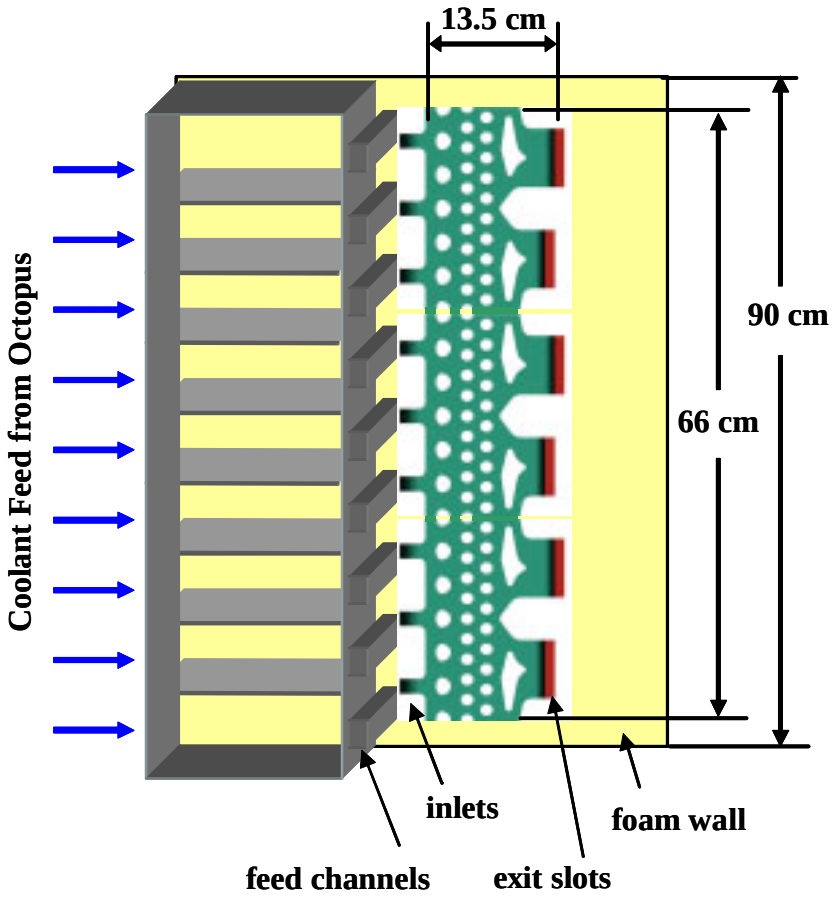

Figure 3-24 Diagram of the microcircuit feed plenums fed from the octopus [Elder, 2005].

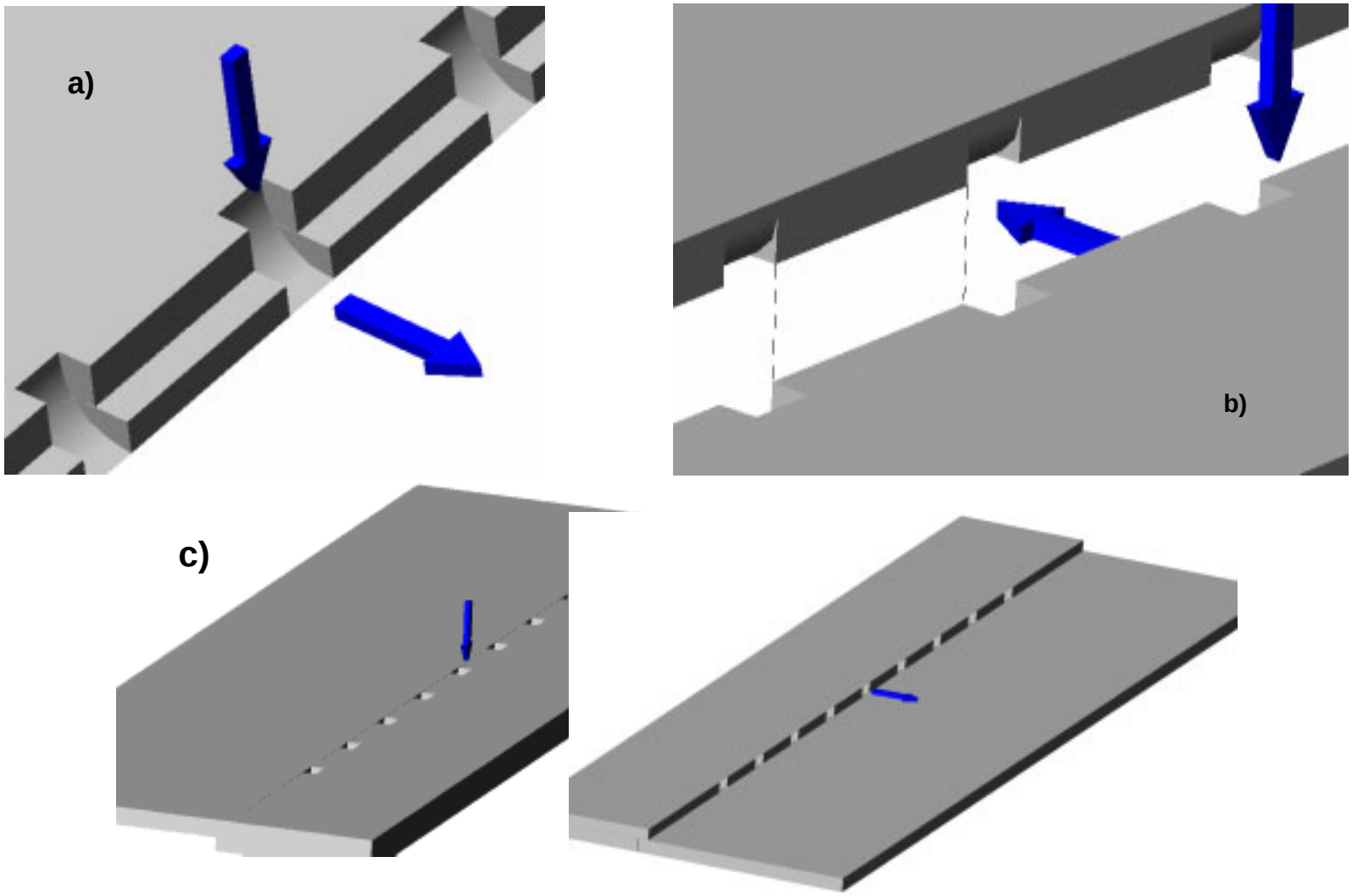

Figure 3-25 a) Concave inlet bend piece is shown, the coolant enters from the feed plenum and exits into the microcircuit b) Convex inlet bend piece, shown above the concave piece c) Completed inlet bend part from top (left) and bottom (right).

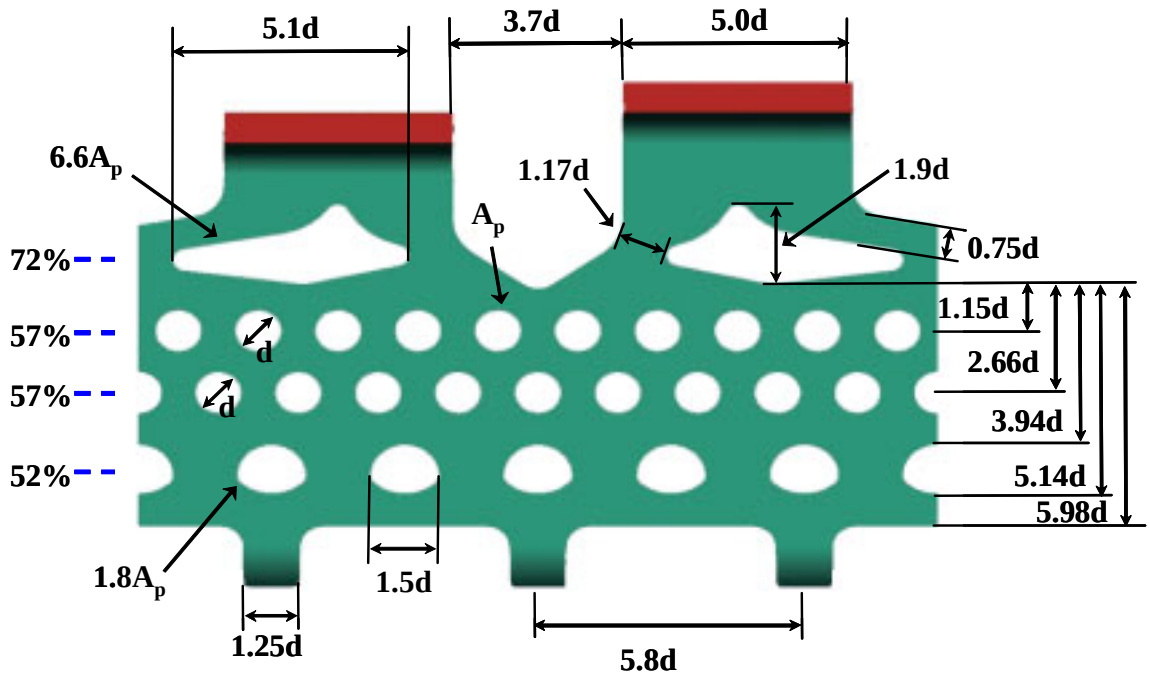

Figure 3-26 Negative view of microcircuit pedestal feature map. Solid green regions are the flow path.

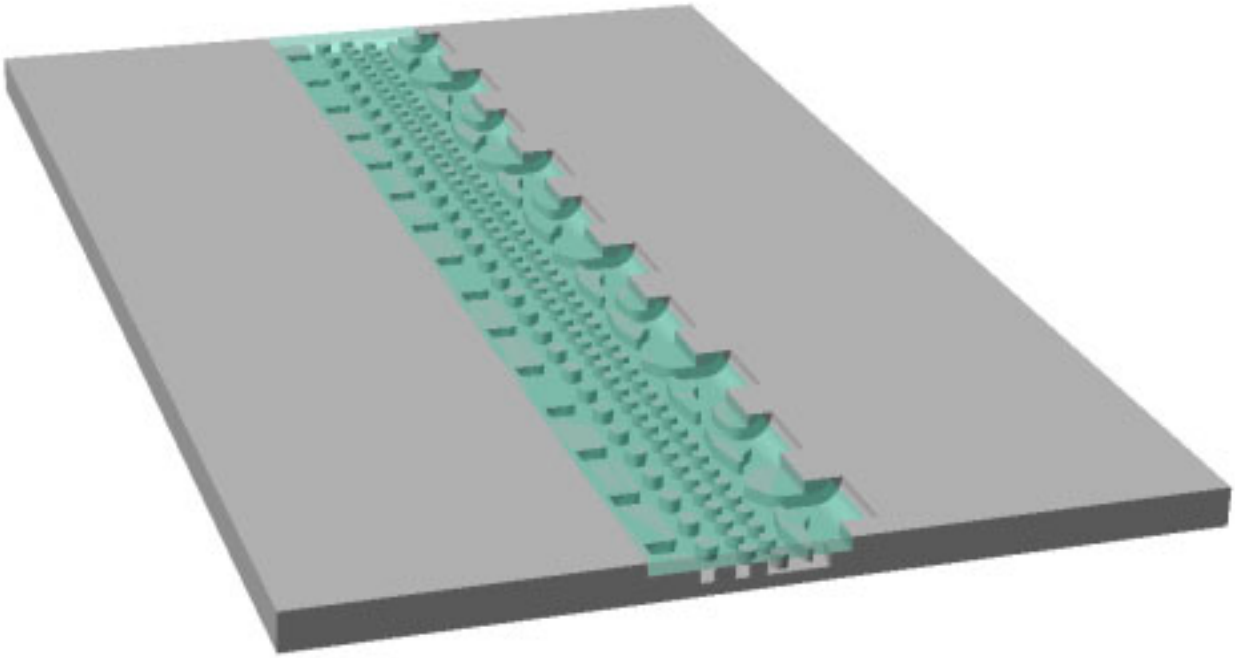

Figure 3-27 View of the microcircuit in an airfoil section. The airfoil wall above the flow path is green and semi-transparent to allow a view of the pedestal features below.

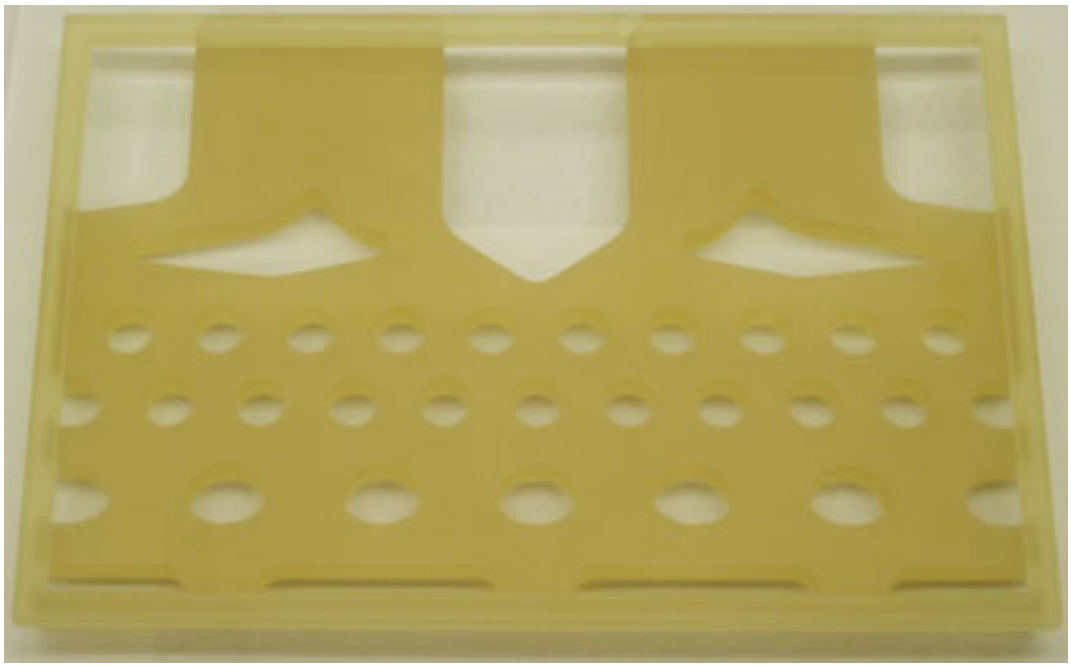

Figure 3-28 Completed SLA part used as template for microcircuit construction.

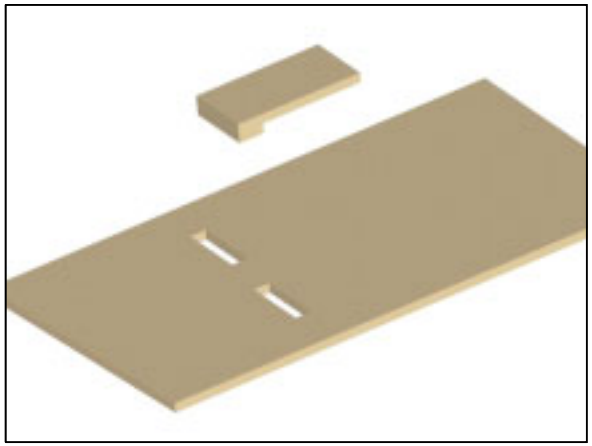

Step 1

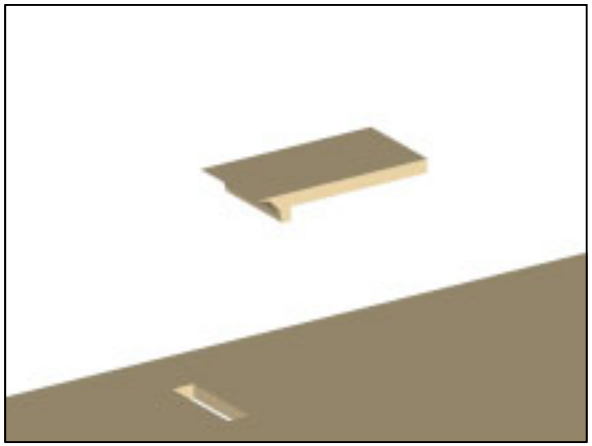

Step 2

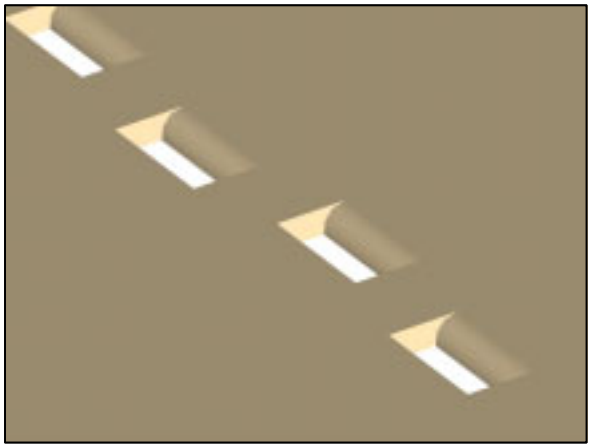

Step 3

Figure 3-29 Construction procedure for microcircuit exit slots, as detailed in Chapter 3, Section 2.

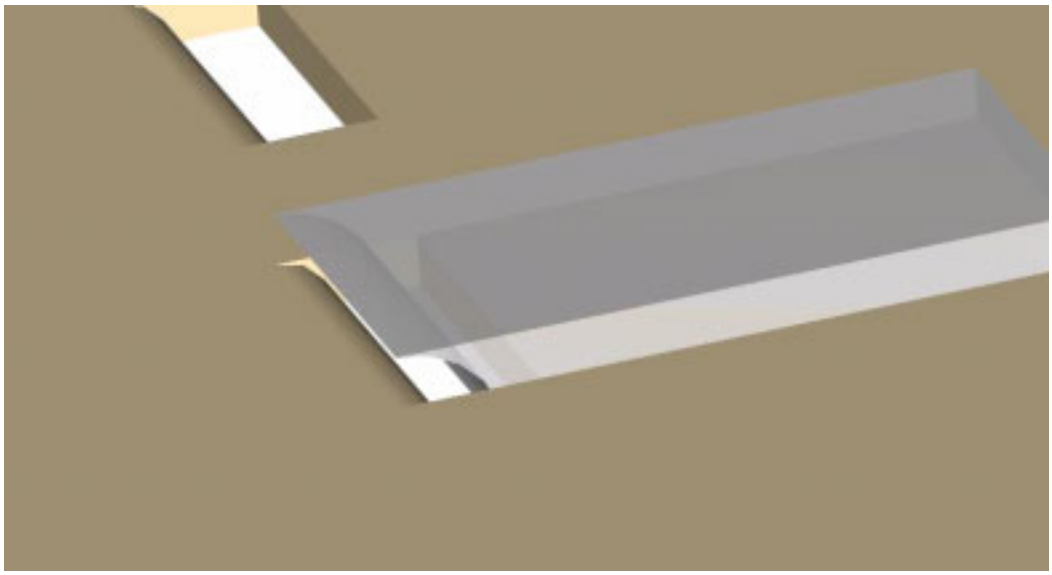

Figure 3-30 Completed slot bend. Note, the outer bend (step 2, above) is shown here semi-transparent to allow a view of the orientation within the slot.

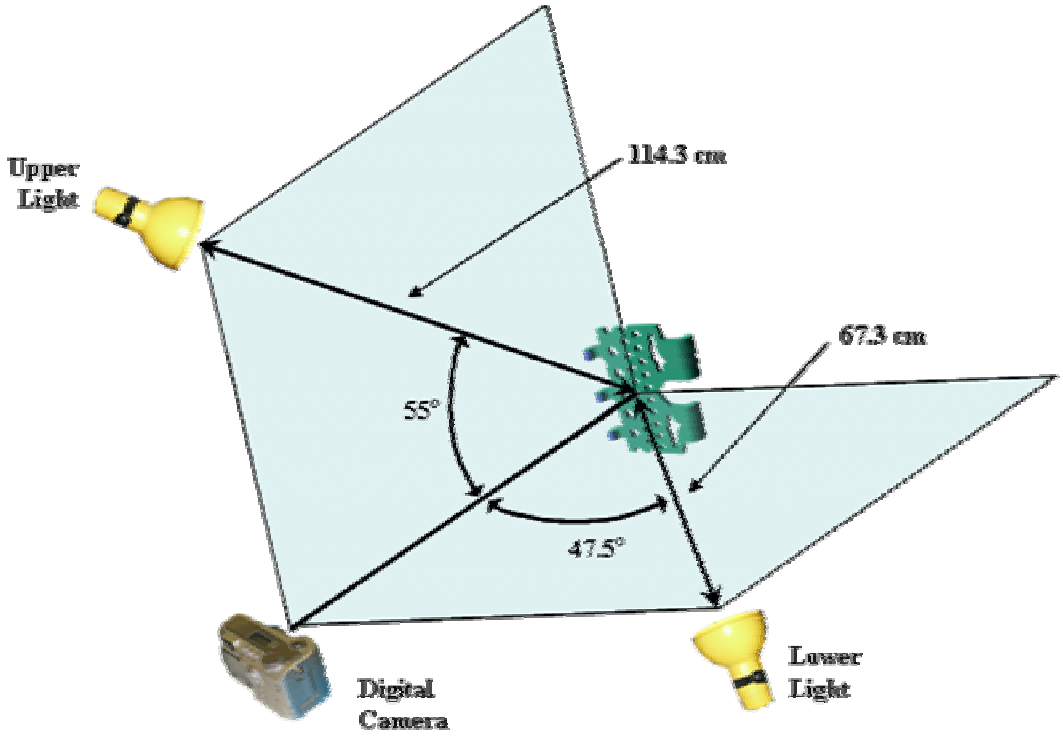

Figure 3-31 Microcircuit lighting arrangement.

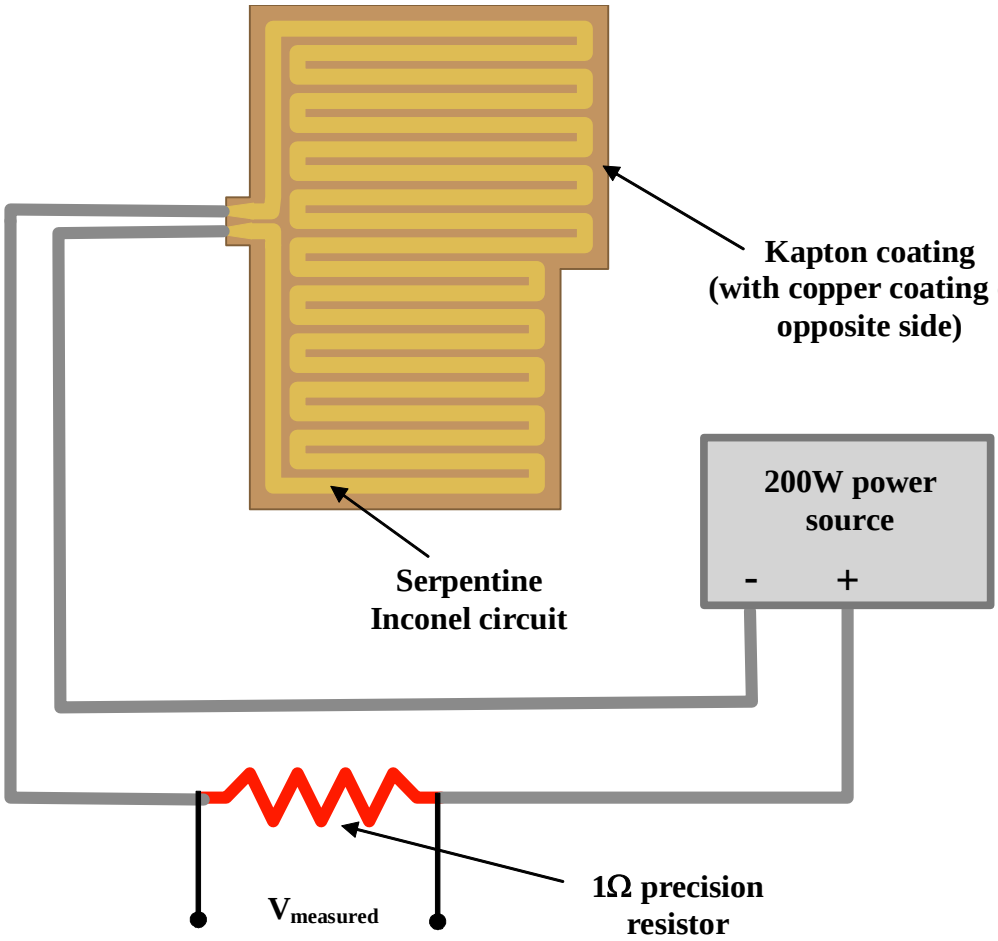

Figure 3-32 Surface heater wiring diagram and schematic.

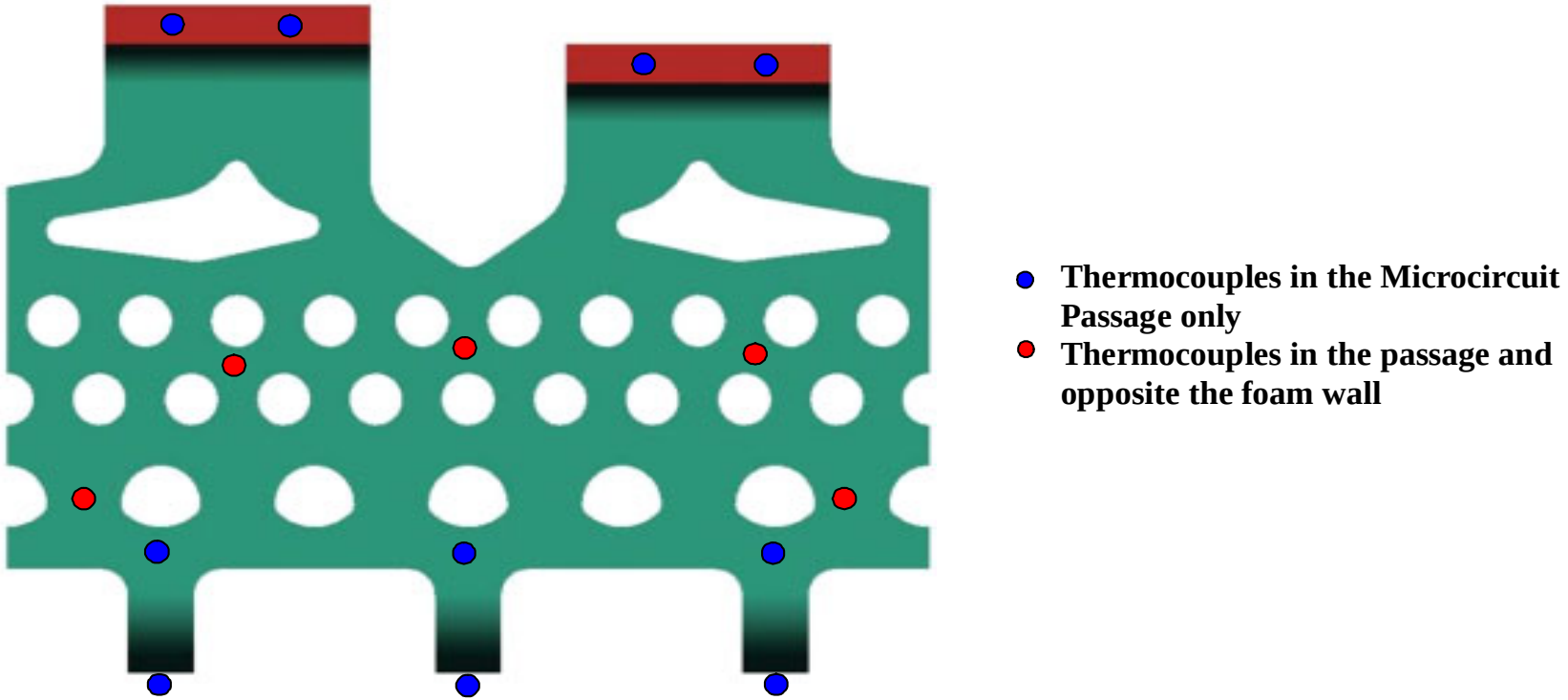

Figure 3-33 Thermocouple locations on the microcircuit surface (except where noted). Note, this view is a negative of the microcircuit, the airflow follows the solid green areas.

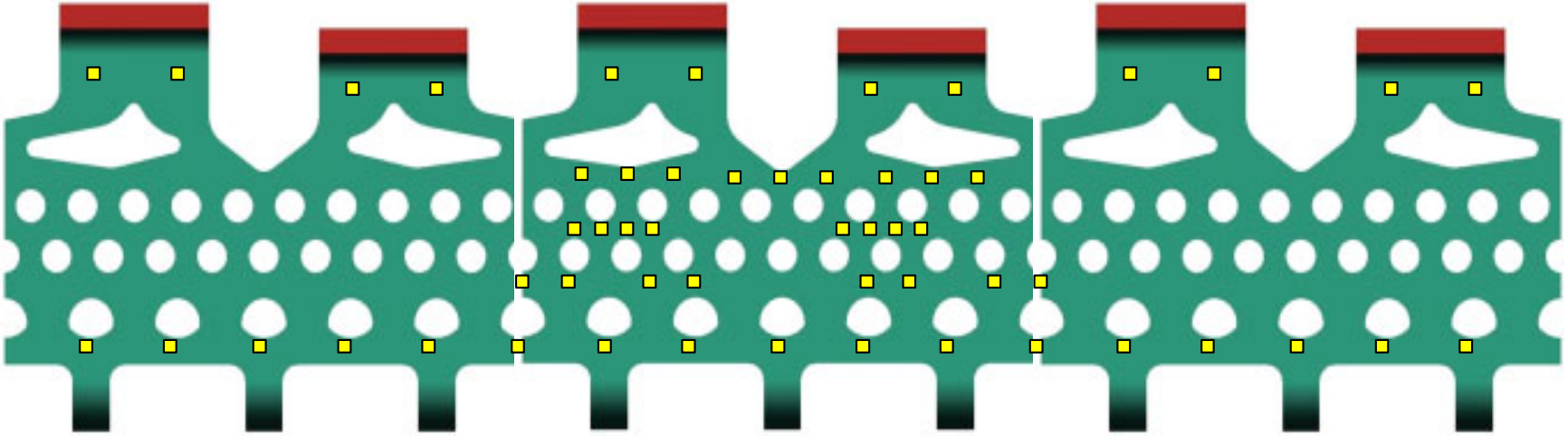

Figure 3-34 Microcircuit static pressure tap locations. Note, this view is a negative of the microcircuit, the airflow follows the solid green areas.

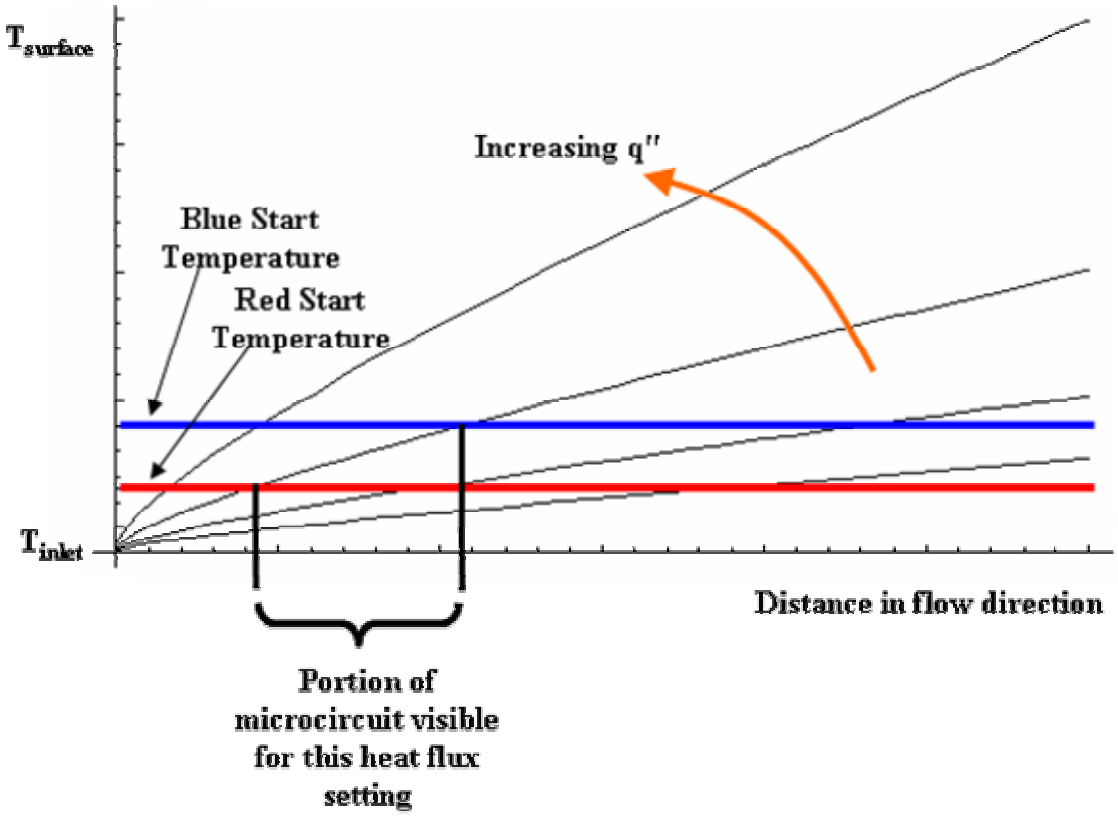

Figure 3-35 Plot of surface temperature vs. stream-wise flow distance for several values of heat flux.

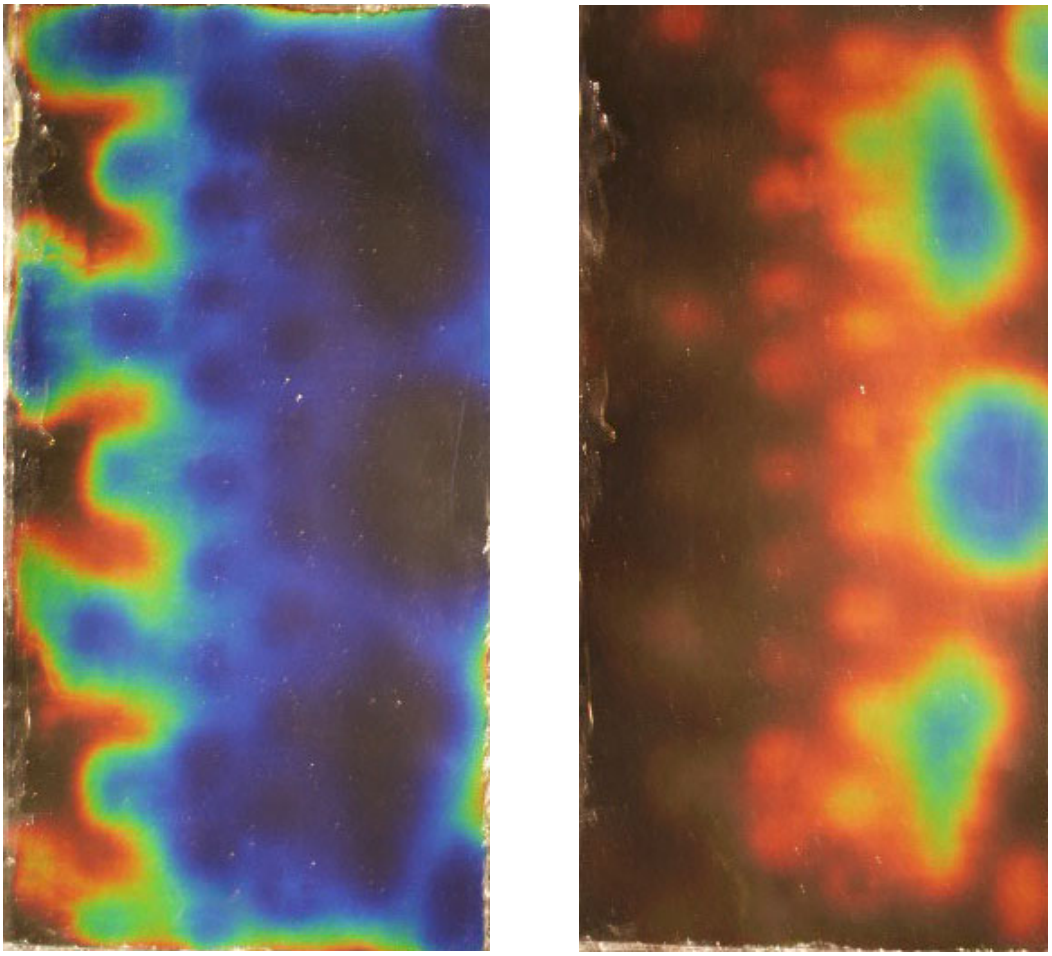

Figure 3-36 Image taken with a high heat flux (left) compared to one with low heat flux (right) for the same Reynolds number.

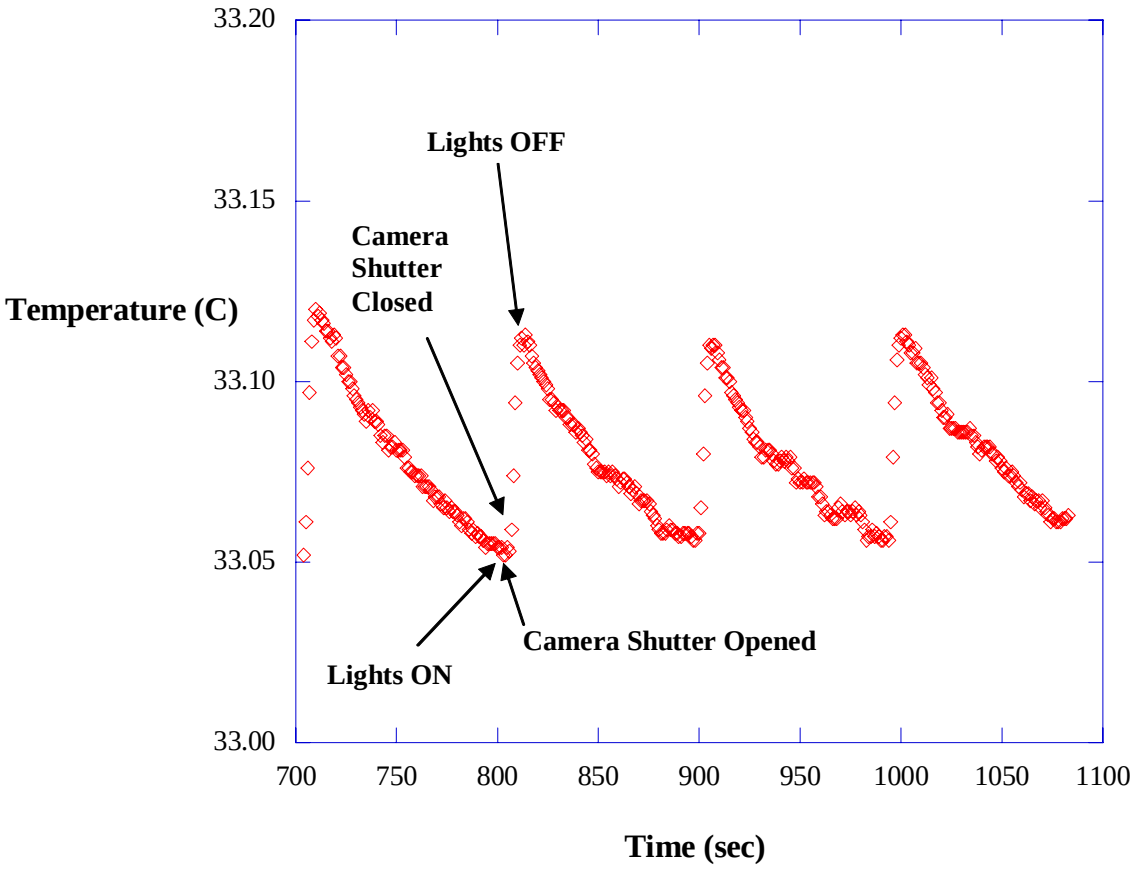

Figure 3-37 Internal surface temperature response to lighting irradiation.

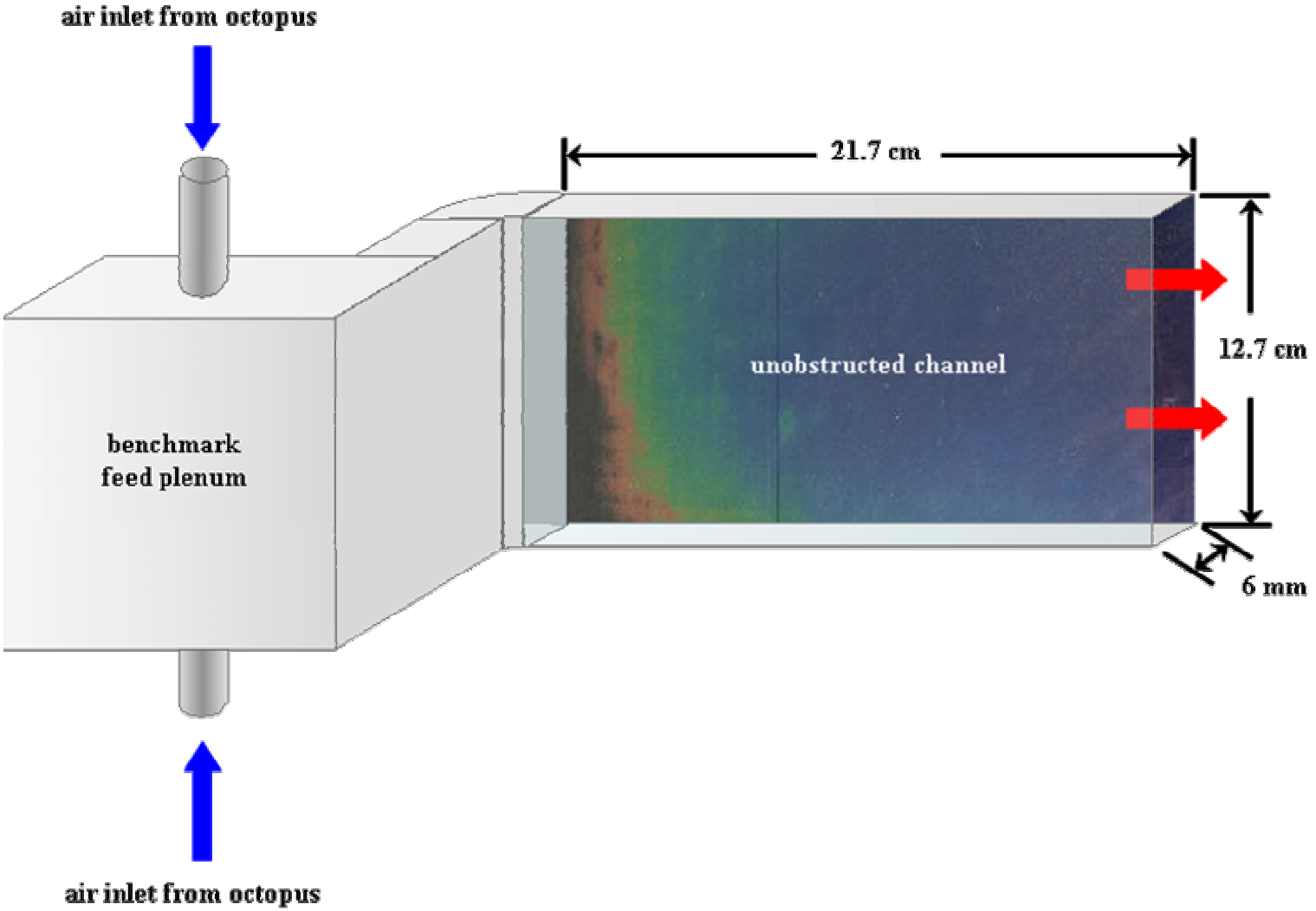

Figure 3-38 Experimental setup for baseline testing.

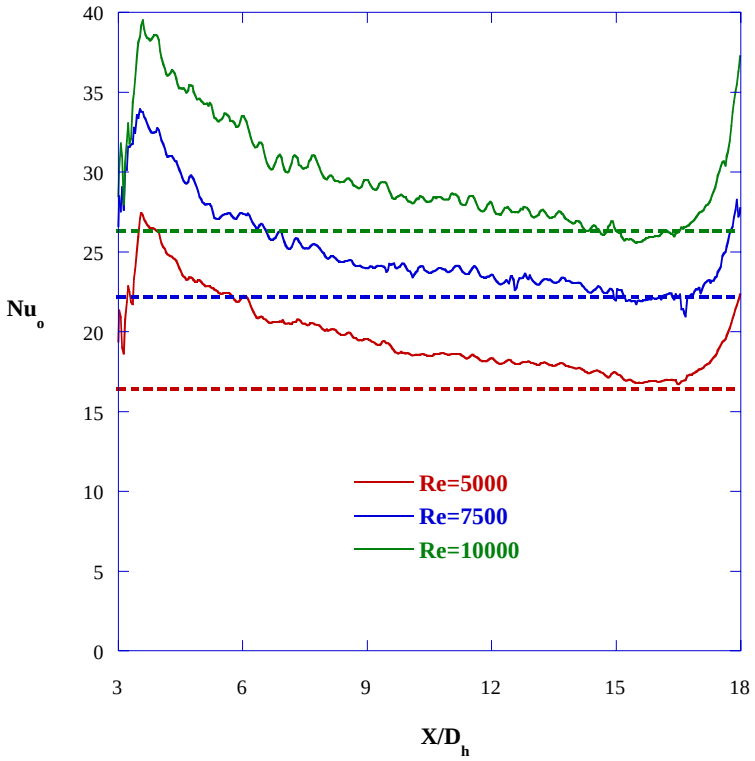

Figure 3-39 Unobstructed channel Nu versus X/D_h for three Re values. The large spikes are due to entrance and exit effects.

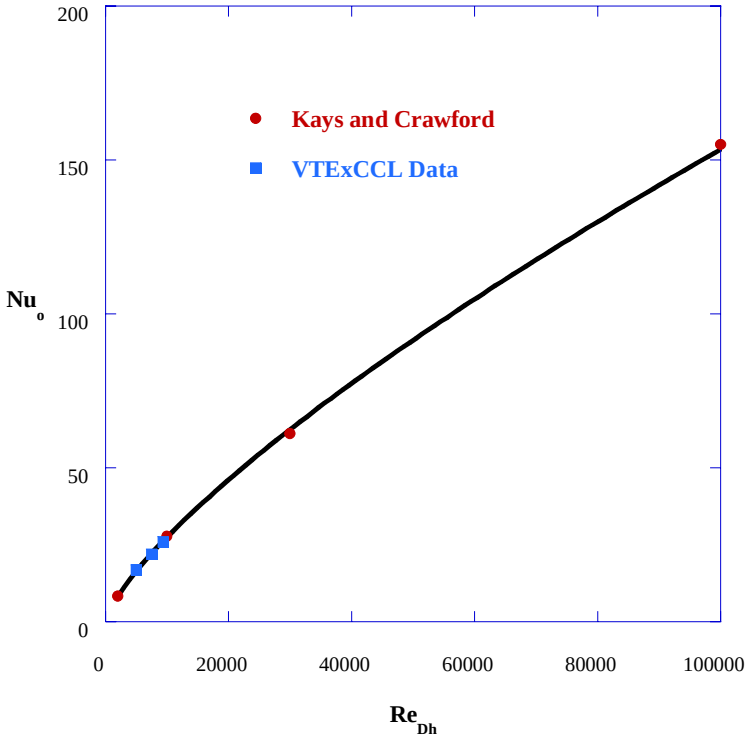

Figure 3-40 Unobstructed channel Nu as a function of Reynolds number. The line indicates the empirical fit used for this study

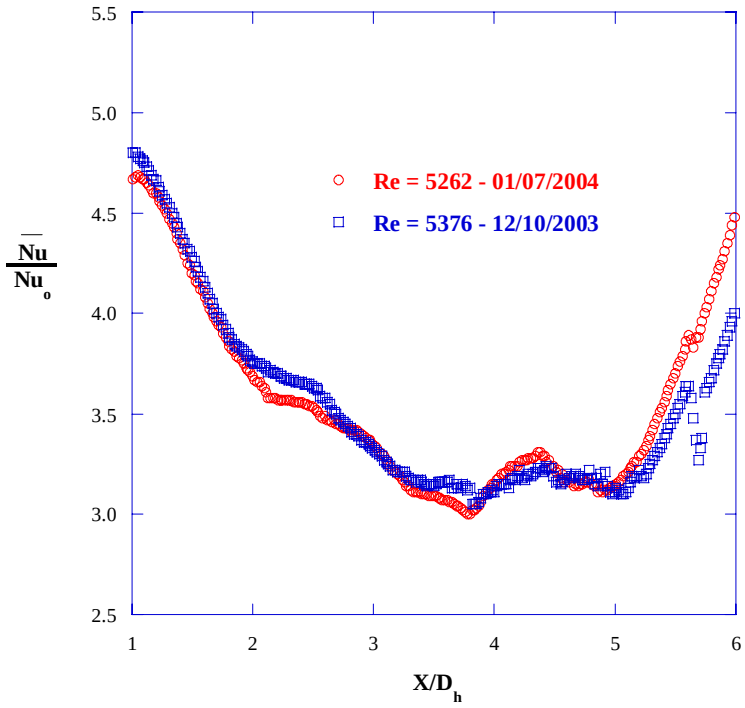

Figure 3-41 Spanwise averaged Nusselt number augmentation for two Reynolds numbers taken on separate days. The agreement within the measurement uncertainty indicates experimental repeatability.

Chapter 4

Data Reduction Methodology

This chapter discusses the logic, methods and equipment we used to analyze the raw data and find external effectiveness and heat transfer coefficient results. The methodology presented in this chapter employed several computer programs to crop, scale, and transform the raw data captured with the liquid crystals and infrared (IR) camera. In addition, Labview logged temperature and pressure data to accompany every IR camera or liquid crystal measurement. The first section of this chapter will discuss infrared image calibration using ThermaCAM Researcher [2002], the image processing software that complements the IR camera. Liquid crystal calibration will be the subject of the second section. Section 3.4 briefly mentioned the liquid crystal calibration process. The calibration process, including the failed first attempt and subsequent redesign, will be discussed in detail in Section 4.2. The third section will discuss the actual data reduction procedure using Matlab, Excel and Tecplot. The fourth section explains the test matrices for both external and internal testing, as well as for the straight channel benchmarking.

4.1 Infrared Image Calibration

Section 3.4 briefly discussed the calibration of the IR images. This section will describe the calibration procedure in detail. As mentioned, the calibration process required thermocouples to adjust the scale and magnitude of radiation measured by the IR camera. Upon completion of the data taking process, the thermocouple measurements were used to calibrate the IR images.

ThermaCAM Researcher [2002] was the calibration software provided with the IR camera. Images taken during the data acquisition procedure were loaded into this program and matched to the thermocouple readings logged during the imaging process.

Each individual image had at least two thermocouples located within its bounds. To tune the image, we found the pixel within the image that corresponded to a known thermocouple location and recorded the temperature measured by the IR camera. If that temperature was different than the thermocouple reading logged by Labview during the imaging process, we adjusted the background temperature—one of several adjustment variables—in the ThermaCAM program until the two readings agreed. Changes in background temperature caused an overall shift in magnitudes of the IR reported temperatures. For example, if two thermocouples measured 30°C and 32°C, respectively; a shift in background temperature may have resulted in measures of 31.5°C and 33.5°C, respectively. The difference between two measurement locations could not be changed with a background temperature shift alone. This is where a second variable, emissivity, became important. ThermaCAM users could adjust both parameters to force the surface temperatures to match the known thermocouple temperatures. The program adjusted surface temperature according to the following equation:

$$T = \sqrt[4]{\frac{1}{\varepsilon \cdot \sigma}\left[Q_{const} + (\varepsilon - 1) \cdot \sigma \cdot T_{bg}^4\right]} \tag{4.1}$$

where ε is the surface emissivity, σ is the Boltzman Constant, and T_{bg} is the temperature of the environment surrounding the surface. Q_{const} is the total radiation heat flux measured by the IR camera.

Often, a background temperature setting appropriate for one thermocouple location resulted in a mismatch for another thermocouple in the same image. Adjustment of another parameter of the image, emissivity, could solve this problem. Emissivity was the measure of the emitted radiation as a fraction of that emitted by a similar blackbody object [FLIR, 2002]. A surface's emissivity depended on the material, the surface viewing angle, the distance to the object, and the object's temperature. In the ThermaCAM program, the emissivity determined the range between a given set of temperature measurements. Recall, for the previous example the temperatures were 31.5°C and 33.5°C after the change in background temperature. A change in emissivity may have resulted in temperatures of 31°C and 34°C, respectively. However, since the

material, viewing angle, and distance to the wall were held constant; the emissivity was usually held constant for this study. Image emissivities would have only been adjusted if the background temperature tuning could not bring the IR measurements to within 1.0°C of the corresponding thermocouple measurements. Such a mismatch never occurred with the emissivity value used for this study, 0.94. Background temperatures, however, varied between images. Background temperatures varied from 61°C to 92°C, the average background temperature across all images was 72.5°C. Table 4-1 lists the background temperature and emissivity settings for all IR images.

Once we calibrated images to the logged thermocouple data, ThemaCAM exported them as Matlab matrices in preparation for the next data reduction step; image placement and orientation. As mentioned, one external data set consisted of nine separate image sets. The orientation of each image, and the eventual creation of a composite image, will be discussed in Section 4.3.

4.2 Liquid Crystal Calibration

This study used thermochromic liquid crystals to map surface temperatures, and ultimately heat transfer coefficients, inside the microcircuit passages. Section 3.4 briefly mentioned the temperature range of the liquid crystals. This range, however, still required a detailed calibration to determine the specific behavior of the liquid crystals within the testing environment. The TLC sheets, model R30C5W from Hallcrest, had to be calibrated for lighting and viewing angle exactly as they would be situated during the actual testing procedure; also called an *in-situ calibration*.

Camci, et al. [1992] detailed the importance of maintaining the viewing angle and illumination environment during the testing procedure. However, we immediately ran into a problem when considering the basic test setup. The light collector on the camera was essentially a single point in space, while the surface it viewed was a two dimensional plane. Figure 4-1 illustrates the discrepancy in viewing angles across the test piece. Clearly, the viewing angle to the top right corner of the microcircuit was quite different than the viewing angle to the bottom left corner. That thought experiment, along with the

paper written by Douglass et al. [2003], motivated us to perform the in-situ calibration. Further, the thought experiment proved that a single calibration curve was inadequate in describing the reaction of the entire liquid crystal surface. The digital camera created images by recording colors in matrices with thousands of elements, called pixels. The varied viewing angle from the camera to the TLC sheet guaranteed that numerous hue versus temperature calibrations were necessary since no two pixels had similar viewing and lighting environments. For this study, every pixel had a unique set of linear calibration curves associated with it. Development and examples of these calibration curves will be presented later in this section.

In order to accurately calibrate the TLC sheets, we needed a way to transform the constant heat flux boundary, provided by the inconel heater, into a constant temperature boundary. Affixing the liquid crystals and heater to a copper block 9.5 mm thick in the pitchwise direction accomplished this task. The block extended 22.9 cm in the spanwise direction and 12.5 cm in the streamwise direction. The high thermal conductivity of the copper assured that its surface temperature remained constant when the entire system reached steady state. The inconel heater provided heat to the copper block. The liquid crystals were affixed to the copper block in the same pitch-wise plane where they would be located for internal data collection; see Figure 4-2 for the calibration setup.

A grid of 15 thermocouples monitored temperature uniformity in the copper block. Prior to calibration, all thermocouples were immersed in an ice bath at 0°C to ensure none had a temperature bias. Any thermocouple reading more than 0.1°C above the ice bath temperature was discarded. Each thermocouple was positioned in a hole bored into the center of the copper and all thermocouples were cemented in place with Omega Bond. Omega Bond was a cement compound that had very low electrical conductivity but very high thermal conductivity. It would not restrict heat flow to the thermocouple beads, nor electrically corrupt the thermocouple signals by allowing them to touch the copper block.

To create a calibration curve, the copper block was heated to several different temperatures beyond and through the linear range of the liquid crystal. At each temperature setting, we allowed the system to come to steady state and took a set of twelve images. The twelve images taken at each temperature were averaged to lower the

overall experimental uncertainty of the measurements. A Matlab program extracted a hue value from each pixel of the averaged image sets and related that value to an average temperature logged by the copper thermocouples. The program created a hue versus temperature plot for each individual pixel location by comparing all of the measured hue values to the logged thermocouple measurements. Figure 4-3 is a sample hue versus temperature plot. The plot shown in Figure 4-3 was only valid for a single pixel. While a specific pixel's calibration was probably quite similar to the calibrations of the pixels immediately adjacent to it, computations were actually more simplistic when applied to every individual pixel separately. Temperature values calculated from hue varied from their corresponding thermocouple readings by 0.05°C, on average. Our image processing software, using standard 24-bit JPG images, could resolve hue in increments on the order of the round-off error of our data processing schemes, resulting in a negligible variation of temperature for a given hue measurement.

Ideally, the hue versus temperature plot created from the calibration data would have been linear across the intended measurement range. If that were the case, we could have applied a linear fit to the data and used that curve fit to resolve temperature from any subsequent hue measurements. However, the trend in Figure 4-3 is clearly non-linear. We solved this problem by fitting the data with two separate linear curve fits. Figure 4-4 is a plot of the same data as the previous figure, but with the linear regions shown. The first curve fit was applied from 32°C to 33.5°C, while the second fit was applied from 33.5°C to 35°C. Two linear approximations fit the data closely, keeping the experimental uncertainty of the liquid crystal measurements low. The fit lines were linear, and therefore in the form of:

$$T_w = \text{Hue} \cdot \text{Slope} + \text{Offset} \tag{4.2}$$

As mentioned, the slopes and offsets for each pixel's calibration varied across the measurement plane. The average slope and offset values of the lower linear fit were 9.7 and 31.7, respectively, with standard deviations of 0.6 and 0.1, respectively. The average slope and offset values for the upper linear fit were 4.7 and 32.6, respectively, with standard deviations of 0.1 and 0.03, respectively. If only one linear fit were applied to

the calibration data, the conversion from hue to temperature would have induced much greater uncertainty in the data. The mean variation between thermocouple readings and temperatures calculated from hue values increased when only one linear fit was applied to the data. The variation between thermocouple readings and calibrated liquid crystal temperatures was four times greater than the variation if two curves were used, 0.21°C instead of the 0.05°C reported above.

Each image contained over a quarter of a million pixels; cataloging a slope and intercept for each of these pixels would be nearly impossible without Matlab's matrix handling efficiency. The program stored each image set as a matrix of hue values. Hue matrices taken at different temperatures were then stacked atop one another; they formed a cube of data. The program then accessed each pixel location and created the calibration curves. It essentially removed the data from the cube one column at a time, making a hue versus temperature plot from each column and the logged thermocouple data [Knost, 2003]. Figure 4-5 is a graphic representation of the calibration process. The program then only needed to store four matrices of information; the slopes and offsets from each of the two linear curve fits, all stored in their corresponding pixel locations.

Once these calibration matrices were created, they could be applied, as a transformation matrix, to any hue matrix taken with the same viewing and illumination configuration. The hue matrix for a given data set was split into two matrices, one composed of hue values for which the first linear fit applied, and one composed of hue values for which the second linear fit applied. The process of applying the calibration, along with the rest of the data reduction, will be discussed in the following section.

The calibration described above was not the first attempt at liquid crystal calibration. The initial setup had the heater and liquid crystal underneath the microcircuit pedestal features. Because of the viewing angle problem described above, the pedestal features cast shadows across the TLC surface in the flow passages. Ideally, the shadows would not have affected the final results, since every pixel got its own calibration curve. In reality, however, some of the shadows were dark enough that very little light actually reached the liquid crystal. As explained in Section 3.4, we depended on incident light to illustrate the changes in the TLC sheet. The configuration described in the beginning of this section solved this problem and provided an added benefit as well. Figure 4-6 shows

the first calibration configuration; the shadows, and their effects, are evident. The second, and final, calibration configuration is shown in Figure 4-7. In addition to removing the damaging effects of shadows, the second configuration allowed us to see the temperature gradients underneath the pedestal features.

4.3 Data Reduction Procedure

In-house codes, created in Matlab, performed all data reduction processes. An existing code created a compiled image out of the raw IR images, while we developed a new code to create a composite image out of the liquid crystal data. Both procedures will be discussed in this section of Chapter 4.

Infrared Image Processing. External effectiveness contours were compiled with a graphical user interface (GUI) based Matlab routine. The program used several functions to import, average, locate, and transform each image. The end product was a composite of the nine images, stitched together at their boundaries. Figure 4-8 represents the program's output, based on the incoming data.

This text will give a brief overview of the program's workings, a meticulous explanation of the image transformation process can be found in Knost [2003]. The IR GUI program's first step was to average the images common to a set. As mentioned, several images were taken at each location to lower the experimental uncertainty of the temperature measurements. The program then loaded the images into a GUI where the user pinpointed the marker locations in each image. As mentioned in Section 3.4, each image contained two markers, intended to stand out from the surroundings. The global locations of these markers were known, referenced to a global origin across the entire test section. The GUI served to relate each global marker location to its local coordinates within the image, the user clicked on the marker location and the program recorded the coordinates. Once the GUI had the local image coordinates of each marker, it transformed each image to its global location and created a mosaic of the entire test area, as if taken in a single image.

The IR images provided a surface temperature map of the film cooled wall. Reducing this data to external adiabatic effectiveness required several more steps. Adiabatic effectiveness measured how well the injected flow film-cooled the vane wall. Adiabatic effectiveness is defined as follows:

$$\eta_{AW} = \frac{T_\infty - T_{AW}}{T_\infty - T_c} \tag{4.3}$$

T_∞ is the mainstream air temperature, T_{AW} is the adiabatic wall temperature measured by the IR camera, and T_c is the coolant temperature. Clearly, if the measured adiabatic wall temperature was equal to the mainstream temperature, the adiabatic effectiveness would equal zero. The coolant would have been completely ineffective in this case. Conversely, if the adiabatic wall temperatures were equal to the coolant temperature, the effectiveness would equal one; indicating perfect cooling.

Boundary layer theory predicts not only a slowing of fluid near an impermeable wall, but a cooling as well. Our experiments supported this theory, as wall temperatures measured upstream of the cooling slots were less than the bulk mainstream temperatures. This resulted in adiabatic effectiveness measurements of 0.125 upstream of the slots, on average, where no cooling benefit was expected. As outlined in Chapter 3, the thermal conditioning system was located nearly 2.5 m upstream of the exit slots. The long length of duct between the heat exchanger and the test section provided a considerable amount of surface area through which the hot flow could exchange energy with the surroundings.

In addition to the thermal boundary layer, the microcircuit underneath the foam upstream of the cooling slots tended to further cool the near wall fluid. The high convection coefficients in the microcircuit removed heat from the external boundary layer by conduction through the foam—the foam had very low thermal conductivity, but not low enough to prevent all heat loss. We needed to correct for these phenomena to ensure accurate results downstream of the cooling features. On average, the microcircuit's convective cooling lowered our wall temperature upstream of the slots by nearly 4°C.

To correct the data for the cooler flow upstream of the slots, we first took a set of adiabatic effectiveness data with no cooling flow. This ensured that any non-zero adiabatic effectiveness values upstream of the cooling slots were caused solely by the boundary layer cooling effect. We then took this upstream effectiveness value and corrected the mainstream flow temperature accordingly. The mainstream temperature correction was as follows:

$$T_{\infty,\text{corrected}} = \frac{\eta_{o,\infty}(T_c) + T_\infty}{1 + \eta_{o,\infty}} \tag{4.4}$$

where $\eta_{o,\infty}$ is the measured upstream effectiveness with no cooling flow—this value was experimentally determined to be 0.125. The experimentally determined upstream effectiveness is an area average of conditions recorded during three experiments run at elevated temperatures with no cooling flow. As in Equation 4.3, T_c is the coolant temperature and T_∞ is the measured mainstream temperature.

Figure 4-9 is a plot of spanwise averaged effectiveness for a blowing ratio of 0.30. Two of the lines in Figure 4-9 are data sets to which the above correction has been applied. The third data set is uncorrected. The correction results in a shift in average effectiveness.

Liquid Crystal Image Processing. The TLC image processing code was no more complicated than the IR image processing software. However, it will be explained here in greater detail than the IR image processing code, as it was created expressly for this study. As mentioned in Section 3.5, several image sets of the TLC surface were taken at each Reynolds number. The small bandwidth of the TLC sheets would not allow complete coverage with a single image—recall Figures 3-33 and 3-34. Six to eight images were required to map the entire microcircuit surface. Twelve images were taken at each heat flux setting; again, to lower the experimental uncertainty of temperatures measured by the liquid crystals. Since each Reynolds number data set is made up of eight different images, a code was developed to create a composite surface temperature

map out of the images taken at different heat flux settings. Once we had a composite surface temperature map, we could resolve heat transfer coefficients in the microcircuit.

The TLC image processing code began in similar fashion as the IR image processing code. The program averaged together the twelve images taken at each heat flux setting, resulting in a single representative matrix. All hue matrices were then multiplied by the appropriate slope matrices and added to the appropriate offset matrices, as described in Section 4.2. This transformation step left the program with a stack of matrices representing the temperatures recorded by the liquid crystal.

As previously mentioned, the liquid crystal sheets only reacted linearly over a small portion of their bandwidth. This meant that any data points in the temperature matrices outside the bandwidth were useless and discarded. This filtering process was complicated by the behavior of the liquid crystal well above the useable range. As mentioned, the TLC sheets began black. This was not a property of the liquid crystals themselves; they were colorless outside of their bandwidth. However, the TLC sheets were treated with black ink so users could easily distinguish actual TLC reactions from incident reflections. As they were heated, they transitioned to red and continued through the visible spectrum with increasing temperature. They ceased to react linearly when they became blue, and eventually returned to black—called the clearing point—when they were well above their reaction temperatures.

Blue pixels registered relatively high hue values, while black pixels exhibited the lowest hue values. Since the TLC sheets transitioned from blue to black after the clearing point, each pixel passed back through the continuum of hues as it heated past the clearing point. Figure 4-9 is the same calibration plot as Figure 4-4, except the transition back through the hue spectrum is shown. Keep in mind, the green line in Figure 4-9 does not represent actual data, but the theoretical behavior of the liquid crystal beyond the clearing point. The clearing point transition phenomenon resulted in small regions on the hue matrices that survived the filtering process despite not actually representing temperatures in the useable range. These anomalies usually occurred with the higher heat flux settings, as they were the hotter of the experimental cases. Figure 4-10 shows examples of this erroneous data compared to the actual image. Clearly, the regions that are beyond the

clearing point correspond to the misplaced temperature measurements. These regions were easily spotted and manually removed from the data.

Once the matrices were properly filtered, each was converted into a map of heat transfer coefficient. Heat transfer coefficient is defined as follows:

$$q''_{convection} = h\left(T_w - T_m\right) \tag{4.5}$$

where h is the heat transfer coefficient, $q''_{convection}$ represents the power supplied to the heater minus a conduction correction, T_m is the mean coolant air temperature at the microcircuit, and T_w is the surface temperature measured by the liquid crystals. The calculation of T_m and $q''_{convection}$ will be discussed next.

The conduction correction was made to ensure that the value used to solve for heat transfer coefficient accurately represented the actual heat flux imparted to the fluid via convective heat transfer. Recall, the heater was sandwiched between the microcircuit pedestal features and the anti-reflective glass. The heat flux could go two directions; through the glass via conduction, or into the cooling passages via convection. The adiabatic foam could also conduct heat, despite its low thermal conductivity.

We initially quantified the conduction heat flux through the pedestal features by determining the pedestal features' fin efficiency. Fin efficiency relates the actual heat transfer rate from a fin to the maximum heat transfer rate possible from the fin:

$$\eta_f = \frac{q_f}{q_{max}} \tag{4.6}$$

Fin efficiency was approximated using a correlation from Incropera and DeWitt [1996] that assumes a circular fin of uniform cross section with an adiabatic tip. The correlation is as follows:

$$\eta_f = \frac{\tanh \cdot \left(\sqrt{\frac{h \cdot p}{k_f \cdot A_c}} \right) \cdot L}{\left(\sqrt{\frac{h \cdot p}{k_f \cdot A_c}} \right) \cdot L} \tag{4.7}$$

where h is the convective heat transfer coefficient around the fin, p is the perimeter of the fin, k_f is the thermal conductivity of the fin, A_c is the fins' cross sectional area and L is the channel height. Despite the calculations, conduction loss through the pin fins was ultimately neglected, since it accounted for less than 0.5% of the total heat flux, on average.

Referring back to the conduction correction, surface temperatures inside the glass were known. The liquid crystals reported temperatures at that interface. The temperature outside the glass was measured with a thermocouple. Since the thermal conductivity and thickness of the glass were known, and a reasonable estimate of the natural convective heat transfer coefficient of the still air outside the glass was also known, we could formulate a conduction correction. The conduction correction was calculated with the following equation:

$$q''_{conduction} = \frac{\left(T_w - T_{surr}\right)}{\frac{1}{h_{freeconv}} + \frac{t_{glass}}{k_{glass}}} \tag{4.8}$$

where k_{glass} is the thermal conductivity of the glass, T_w is the temperature measured by the liquid crystals, T_{surr} is the measured ambient temperature, $h_{freeconv}$ is an assumed 5 W/m^2K for relatively still air, and t_{glass} is the thickness of the glass, 9.5 mm. Conduction corrections were typically 5.0% of the total heat flux, and decreased with increasing Reynolds number. The internal image processing code was written to perform an individual conduction correction for each pixel of the image. The conduction correction was subtracted from the total heat flux to obtain the convection heat flux:

$$q''_{convection} = \frac{Q_{total}}{A_{heater}} - q''_{conduction} \tag{4.9}$$

where Q_{total} is the measured wattage provided to the strip heater, A_{heater} is the area of the heater, 0.03 m^2. Q_{total} ranged from 12 to 60 W, depending on the portion of the microcircuit being imaged. Q_{total} was determined using Ohm's Law. The resistance of the heater and current flow through the heater allowed us to calculate the power provided to the heater. We solved for the electrical current by measuring the voltage across a precision resistor, recall Figure 3-29.

While solving for heat transfer coefficients, another problem was encountered. The coolant exit temperatures measured with single point thermocouple measurements could not adequately measure the mean exit temperature of a flow with an unknown temperature profile. Energy balances were completed according to the following:

$$q''_{convection} = \dot{m}_c C_p \left(T_{inlet} - T_{exit}\right) \tag{4.10}$$

where $\dot{m}_c$ is the coolant mass flow rate of the heated microcircuit, C_p is the specific heat of air, T_{inlet} is the measured mean inlet temperature to the microcircuit, and T_{exit} is the measured mean exit temperature at the microcircuit slot exits. The calculated convective heat flux on the left side of Equation 4.10 matched to within 20% when we used the exit thermocouple measurements. Rather than leave the energy unbalanced, the exit temperatures were treated as the unknown in Equation 4.10 and solved for directly. This forced an energy balance with the known heat flux, mass flow, and specific heat quantities. We had considerable confidence in the inlet temperature measurements since they were taken in several places, including in the microcircuit feed plenums, where there were no thermal gradients.

By knowing the inlet temperatures and $q''_{convection}$ from Equation 4.9, we could then solve for heat transfer coefficients. Since the bulk flow temperature in the microcircuit increased from inlet to outlet, a matrix of fluid temperatures with a gradient was created. By knowing the measured microcircuit inlet temperatures, T_{in}, and the calculated

microcircuit exit temperatures, T_{exit}, we could determine the mean fluid temperature, T_m, at any streamwise location in the microcircuit. T_m was calculated according to the following equation:

$$T_m = \frac{T_{exit} - T_{inlet}}{X} + T_{inlet} \tag{4.11}$$

where X is the distance downstream of the microcircuit inlets of the location of interest.

The fluid temperature matrix began at the inlet temperature and increased linearly in the flow direction, with the last columns equivalent to the calculated exit temperatures. With this matrix created, heat transfer coefficients were resolved with Equation 4.5.

Once the internal matrices were converted to heat transfer coefficient, they could be compiled into one composite image of the microcircuit test piece. Since the heat flux boundary conditions changed for each image set, the temperatures at each heat flux were not comparable to the other temperature measurements. As mentioned, the liquid crystals only responded across a fixed temperature bandwidth. Since each image was taken with different heat flux values, but the resultant temperatures were within the same range as all the respective heat flux settings, each image had to be normalized before they could be combined into a single, composite image. Converting to heat transfer coefficient normalized the results by their boundary conditions, namely the convective heat flux. This put each image set on a similar scale, and allowed them to be combined.

Using the data cube analogy again, individual pixel columns were removed from the image stack and analyzed. If a given column contained one non-zero value—meaning that was the only image that had a valid temperature result at that pixel—the heat transfer coefficient value was passed to the waiting composite matrix. If there were multiple non-zero values in the column—indicating overlap at that particular pixel—the values were averaged and passed to the composite matrix. The end result was a composite heat transfer coefficient map of the microcircuit test piece. Figure 4-11 relates the TLC imaging processing software output to the raw data input required.

To normalize the results, heat transfer coefficients were converted into Nusselt numbers. Nusselt number is defined by:

$$Nu = \frac{h \cdot D_h}{k} \tag{4.12}$$

where h is the heat transfer coefficient value for a single pixel; D_h is the hydraulic diameter of the channel, 1.9E-2 m; and k is the thermal conductivity of the coolant air based on the mean temperature in the microcircuit, nominally 0.026 W/mK. Since our tunnel did not match engine temperatures or pressures, dimensionless results—like Nusselt numbers—were the most useful form of data for our sponsors.

Since all heat transfer results were ultimately matched to unobstructed straight channel results, the Nusselt numbers were further normalized. The final heat transfer results were reported as heat transfer augmentation which is the measured Nusselt numbers divided by the Nusselt number for an unobstructed channel flow. The correlation we used for unobstructed channel flow was interpolated from data reported in Kays and Crawford [1980] and is as follows:

$$Nu_o = 0.0285 \cdot Re^{0.75} \tag{4.13}$$

The data that we curve fit to come up with this correlation was taken with a constant heat flux boundary on one side of the channel, and all other walls were adiabatic. Reporting results as augmentation provided an easily recognizable baseline, whereby augmentation greater than one was good, and augmentation less than one was poor. Heat transfer results will be discussed in the following chapter.

Microcircuit tests included pressure measurements to study the increased pressure drop caused by the pedestal features. Just as with the heat transfer study, we compared the microcircuit pressure loss to that of a straight channel. Straight channel pressure drop was reported as a dimensionless friction factor. As is the case with most dimensionless values, this allowed comparison with other studies that did not share the precise geometry of the microcircuit or baseline channel. Friction factor can be defined two ways, either

by a D'arcy friction factor or a Fanning friction factor. D'arcy friction factor is four times greater than Fanning friction factor. This study used D'arcy friction factor for all calculations. It is defined as follows:

$$f_o = 0.316 \cdot Re^{-0.25} \tag{4.14}$$

This is known as the Blasius correlation, and represents the turbulent friction factor in a smooth pipe or channel [Munson, et al., 1998].

The friction factor in the microcircuit was not as easy to define. Normally the D'arcy friction factor is defined by:

$$f = \left(\frac{\Delta P_{MC}}{\rho_{bulk}} + \frac{U_{bulk}^2 - U_{out}^2}{2} \right) \cdot \frac{D_h}{X} \cdot \frac{2}{U^2} \tag{4.15}$$

where, ΔP_{MC} is the static pressure drop across the microcircuit—shown in Figure 4-12, ρ_{bulk} is the mean microcircuit density, U_{bulk} is the unobstructed velocity at the inlet plane, U_{out} is the velocity at the slot exit plane, D_h is the microcircuit hydraulic diameter, X is the stream-wise length of the microcircuit, and U is the normalizing velocity. Compressibility effects were neglected, as the Mach number in the microcircuit never reached above 0.17.

An interesting component of the friction factor definition was the normalizing velocity, U. In a straight channel or pipe, it was simply the average velocity of the flow. The microcircuit, however, was hardly a straight channel. There were several candidate regions where the normalizing velocity could be defined. The bulk flow at the inlet was a choice, but it did not necessarily represent the flow between the pedestal features. The velocity in the channels leading up to the exit slots was also considered, as was the velocity at the metering area. We analyzed our data according to two methods to compare to two different existing data sets. Existing data taken by Chyu [1990] used U_{max} as the normalizing velocity for the friction factor through the pedestal features, yet used U_{bulk} in the Reynolds number definition of the straight channel friction factor. U_{max} was the velocity between pedestal features inside the microcircuit, or any pin fin array.

Additionally, Chyu's data used the D'arcy friction factor definition to define his channel friction factors, but the Fanning definition to define his baseline friction factor. We put our data in Chyu's form for comparison purposes, but decided a consistent friction factor definition was a more appropriate method for friction augmentation calculations. The comparison to Chyu's data can be found in Chapter 5.

We decided to use the D'arcy friction factor definition to calculate both our baseline and microcircuit friction factors. The normalizing velocity in the microcircuit friction factor calculation was U_{max}, the velocity between pedestal features. This definition allowed a direct comparison to a pin fin prediction code provided by our sponsors, as their definition also used D'arcy friction factors and U_{max} as the normalizing velocity. Friction factor results and comparisons to predictions will be discussed in Chapter 5.

Finally, as well as reporting friction and heat transfer augmentation, results were also reported as an efficiency index. Efficiency index is defined as:

$$\text{Efficiency Index} = \frac{Nu/Nu_o}{f/f_o} \tag{4.16}$$

Efficiency Index related the beneficial heat transfer increase gained by the microcircuit to the detrimental friction factor increase incurred by the microcircuit. Efficiency index comparisons were very helpful in determining the overall worth of a microcircuit design, although we needed to be extremely careful when making comparisons. If the normalizing velocity used in the friction factor definition was different between the two data sets, comparison would be unfounded.

4.4 Test Matrices

This section will describe the selection of test cases for both internal and external tests. In total, five cases matching mass and momentum flux ratios were run on the external side of the test facility. Four different Reynolds number tests were run for

internal tests. The benchmark tests matched the literature at three different Reynolds numbers.

External adiabatic effectiveness tests matched engine conditions by simulating realistic mass and momentum flux ratios. Mass flux ratio is defined as follows:

$$M = \frac{\rho_j U_j}{\rho_\infty U_\infty} \tag{4.17}$$

where ρ_j is the coolant jet density, U_j is the coolant jet velocity, ρ_∞ is the mainstream density, and U_∞ is the mainstream velocity. Momentum flux ratio is defined slightly differently:

$$I = \frac{\rho_j U_j^2}{\rho_\infty U_\infty^2} \tag{4.18}$$

All of the variable definitions are the same as for mass flux ratio, but the velocities are squared to represent momentum flux as opposed to mass flux. Both, however, are meant to relate the amount and force of coolant exiting the film cooling feature to that of the discharge environment.

Since velocities were important terms in the definition of mass and momentum flux ratio, the flow area used to define the velocity was also an important consideration. We defined our mass and momentum flux ratios using the slot exit velocity. Our sponsors defined the ratios using the velocity in the metering area of the microcircuit. The metering area is the smallest flow area in the microcircuit. This resulted in a scaling factor of 2.60 for mass flux ratio and 6.76 for momentum flux ratio. VTExCCL ratios were multiplied by the scaling factors to arrive at our sponsor's ratios. We ran three cases that matched mass flux ratios and two cases that matched momentum flux ratios with our sponsor's data. Mass flux cases were matched at 0.37, 0.50 and 1.00. Momentum flux cases were matched by running mass flux ratios of 0.28 and 0.71. Table 4-2 lists the five blowing ratio cases and their Pratt & Whitney equivalents. Additionally,

Table 4-2 lists the Reynolds number in the microcircuit that corresponds to the mass flow rate set to achieve each blowing ratio.

Heat transfer coefficient experiments were carried out at four engine realistic Reynolds numbers. Our sponsors provided us with a range of Reynolds numbers and we chose four representative cases within that range. Experiments were planned at four Reynolds numbers; 5,000, 7,500, 10,000 and 15,000. These were nominal, target values. Actual experimental Reynolds numbers were 5,262, 6,945, 10,496, and 15,127. Table 4-3 lists the internal test matrix. Table 4-3 also lists the mass flux and momentum flux ratios that would have been achieved if the mainstream tunnel had been running at 10 m/s during internal testing. Table 4-4 lists the Reynolds numbers tested for the benchmark experiments.

Table 4-1 IR Image Calibration Settings

Mass Flux Ratio	Variable	Image number								
		1	2	3	4	5	6	7	8	9
0.28	T_{bg}	n/a	n/a	70	77	92	81	84	87	89
	ε	0.94	0.94	0.94	0.94	0.94	0.94	0.94	0.94	0.94
0.30	T_{bg}	n/a	n/a	66	66	65	67	66	66	71
	ε	0.94	0.94	0.94	0.94	0.94	0.94	0.94	0.94	0.94
0.37	T_{bg}	n/a	n/a	70	68	70	66	67	73	76
	ε	0.94	0.94	0.94	0.94	0.94	0.94	0.94	0.94	0.94
0.50	T_{bg}	n/a	n/a	75	72	72	75	68	75	80
	ε	0.94	0.94	0.94	0.94	0.94	0.94	0.94	0.94	0.94
0.71	T_{bg}	n/a	n/a	65	80	66	73.5	61	67.5	66
	ε	0.94	0.94	0.94	0.94	0.94	0.94	0.94	0.94	0.94
1.00	T_{bg}	n/a	n/a	65	80	68	75	73	74	78
	ε	0.94	0.94	0.94	0.94	0.94	0.94	0.94	0.94	0.94

Table 4-2 External Adiabatic Effectiveness Test Matrix

M_{VT}	M_{PW}	I_{VT}	I_{PW}	Corresponding Microcircuit Re
0.28	0.73	0.07	0.47	2540
0.37	0.96	0.12	0.81	2350
0.50	1.30	0.23	1.56	3170
0.71	1.85	0.46	3.12	4500
1.00	2.60	0.90	6.10	5900

M = Mass Flux Ratio $M_{PW} = 2.6 \cdot M_{VT}$ I = Momentum Flux Ratio $I_{PW} = 2.6^2 \cdot I_{VT}$

Table 4-3 Internal Heat Transfer Coefficient Test Matrix

Unobstructed Reynolds Number	Baseline Nusselt Number	Microcircuit Mass Flowrate (kg/sec)	Blowing Ratio	Momentum Flux Ratio
5262	17	0.032	0.83	0.62
6945	21	0.042	1.09	1.09
10496	29	0.063	1.64	2.44
15127	38	0.091	2.39	5.20

Table 4-4 Unobstructed Channel Baseline Test Matrix

Channel Reynolds Number	Baseline Nusselt Number
5000	16
7500	22
10000	28

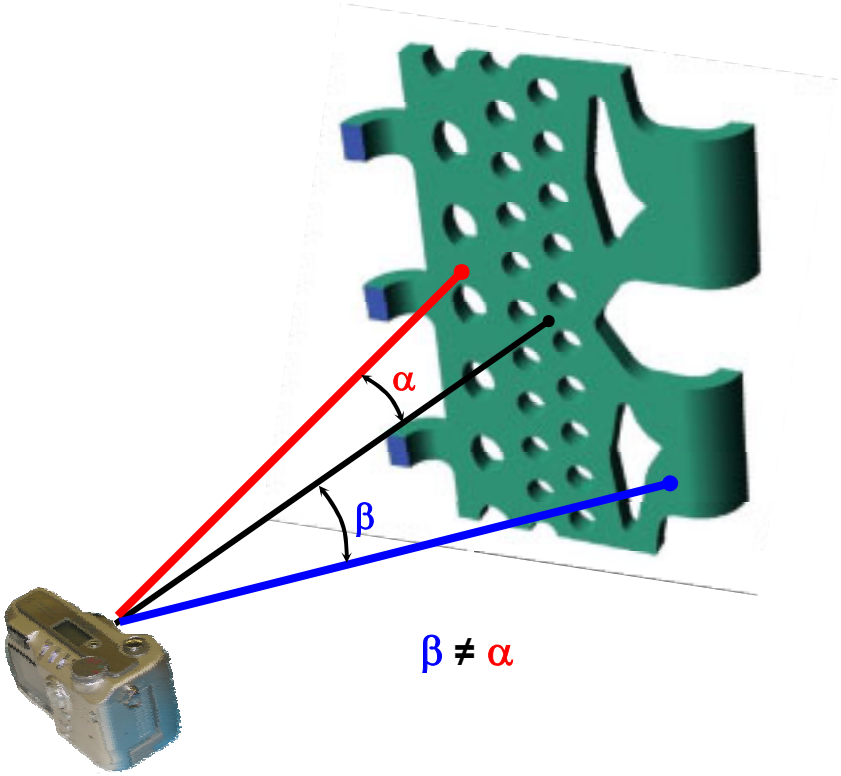

Figure 4-1 Varying viewing angle from camera perspective. The differing angles demanded an in-situ calibration and many calibration curves.

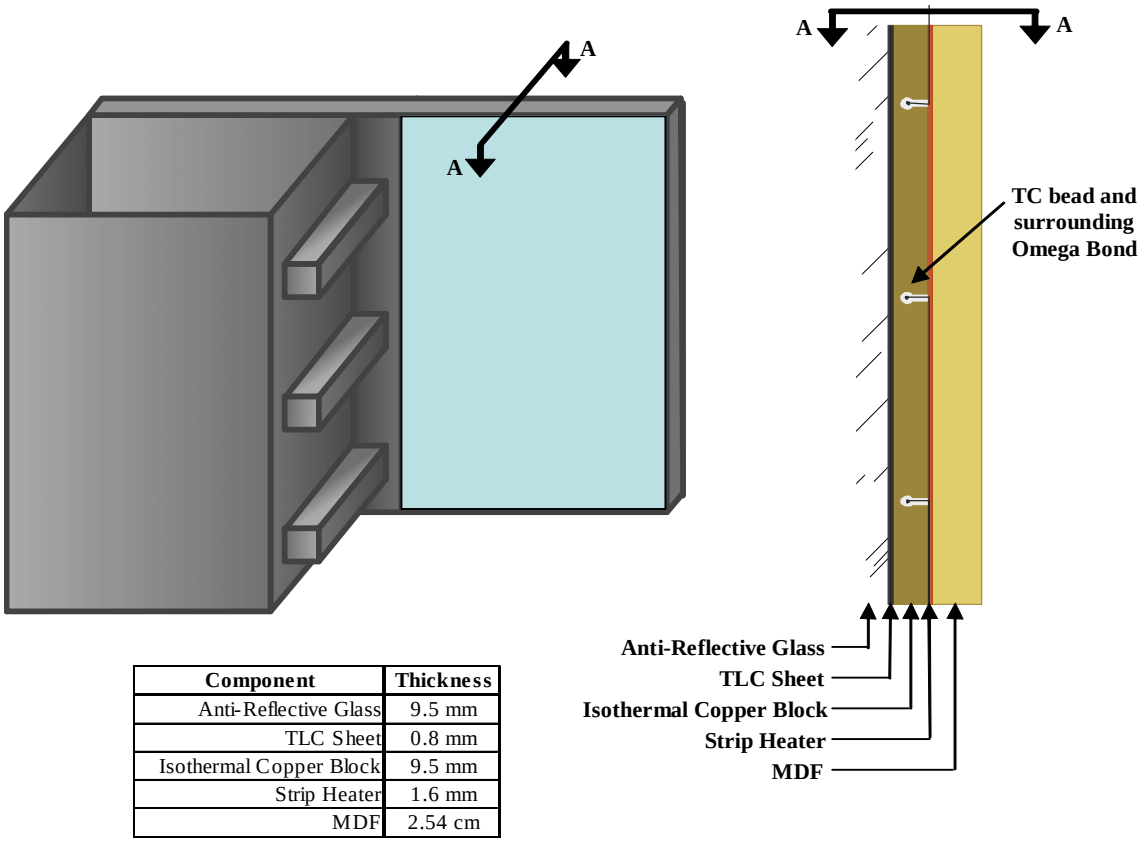

Component	Thickness
Anti-Reflective Glass	9.5 mm
TLC Sheet	0.8 mm
Isothermal Copper Block	9.5 mm
Strip Heater	1.6 mm
MDF	2.54 cm

Figure 4-2 TLC calibration setup. The copper block transforms the constant heat flux boundary into a constant temperature boundary, indicated here by the uniform reaction of the liquid crystal

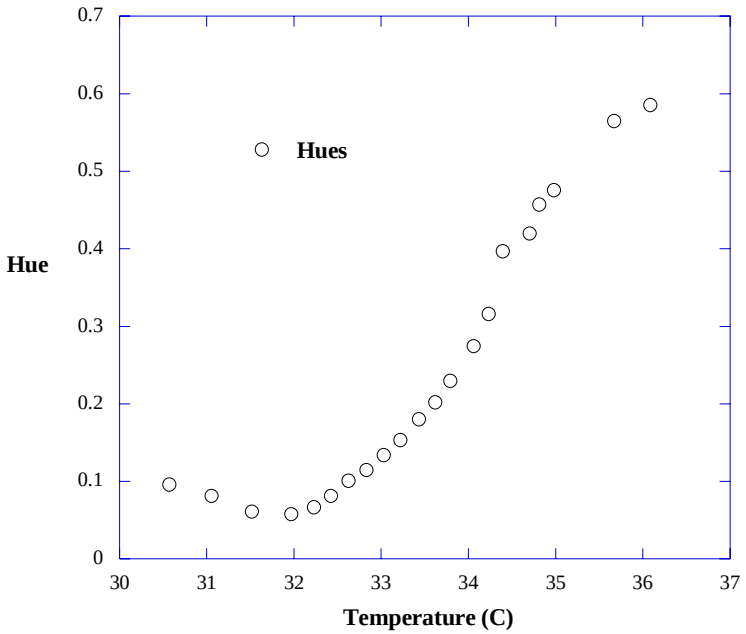

Figure 4-3 Sample plot of hue versus temperature. Note, the liquid crystal is supposed to react linearly from 30° C to 35° C.

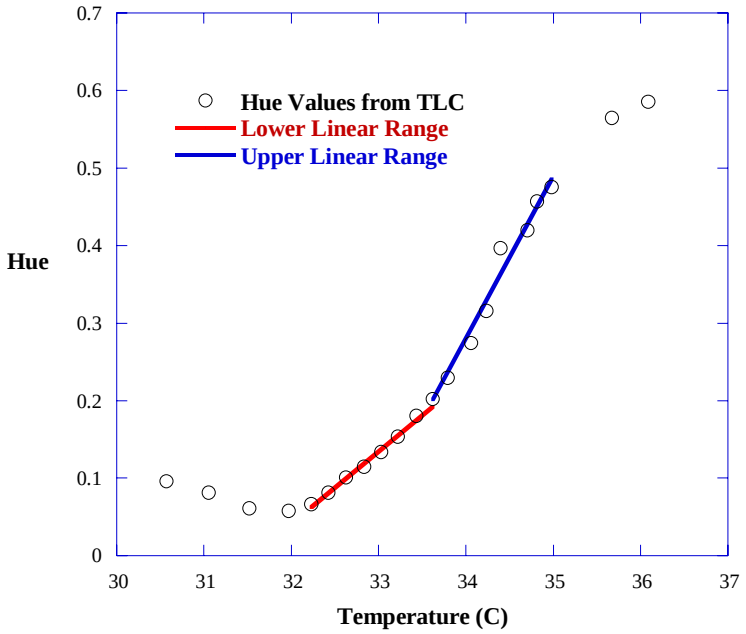

Figure 4-4 Hue versus temperature plot for sample pixel location. The dual linear curve fits are plotted as well.

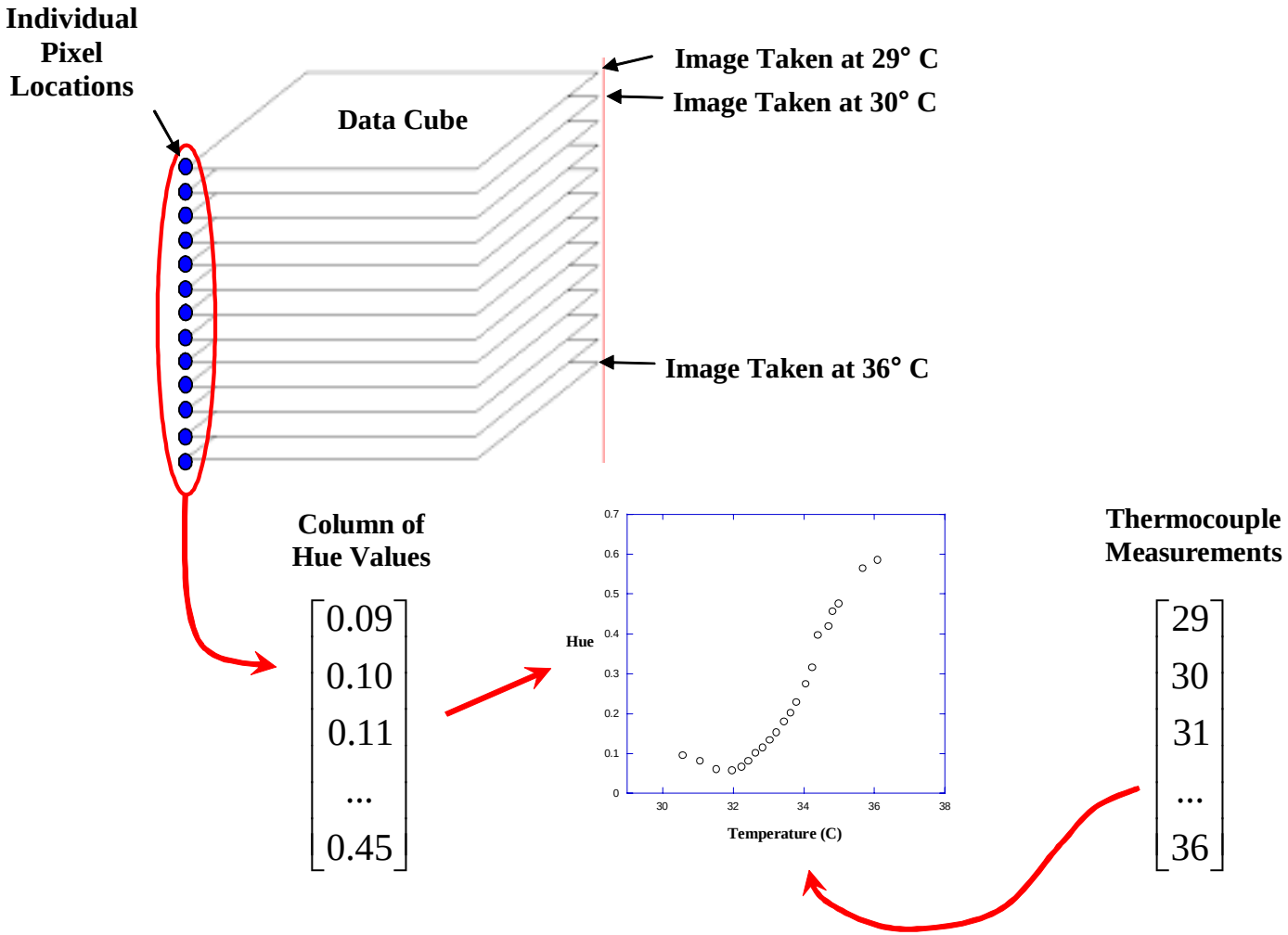

Figure 4-5 Graphic representation of TLC calibration process.

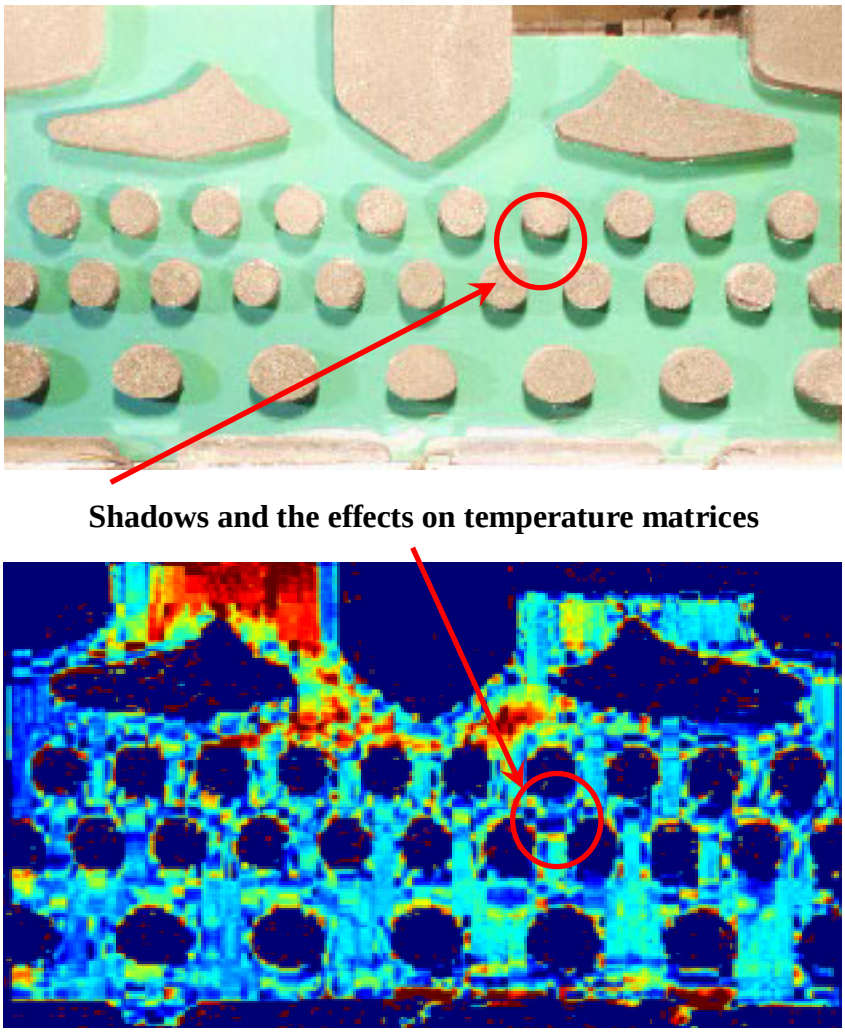

Figure 4-6 Original calibration setup. The viewing angle changes from the camera to the microcircuit (see Figure 4-1) cause disruptive shadows between pedestal features.

Variation due to shadows mitigated

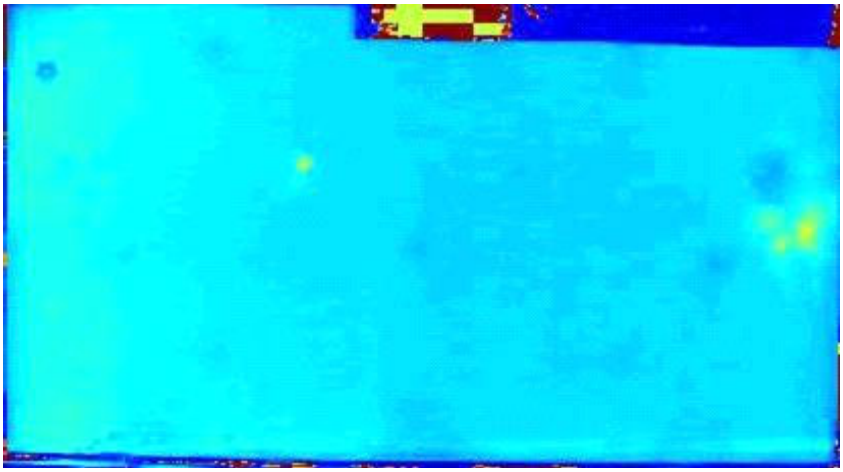

Figure 4-7 Final calibration setup. Since pedestal features were underneath the liquid crystals, shadow variation was eliminated.

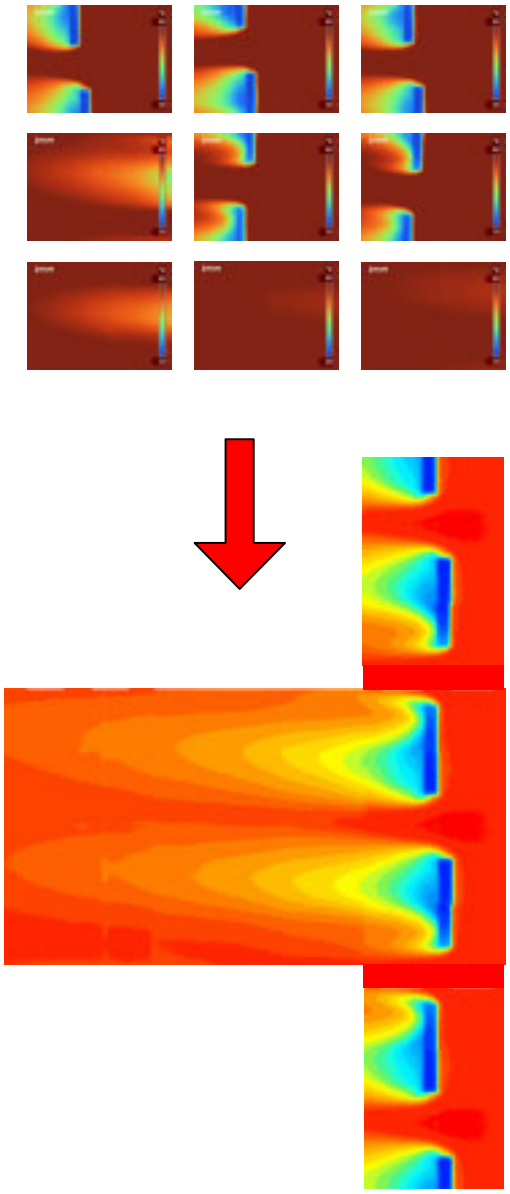

Figure 4-8 Individual IR Images and resulting IR image mosaic. Note, only the middle two slots were used to determine results, the upper and lower slots were present for flow balancing.

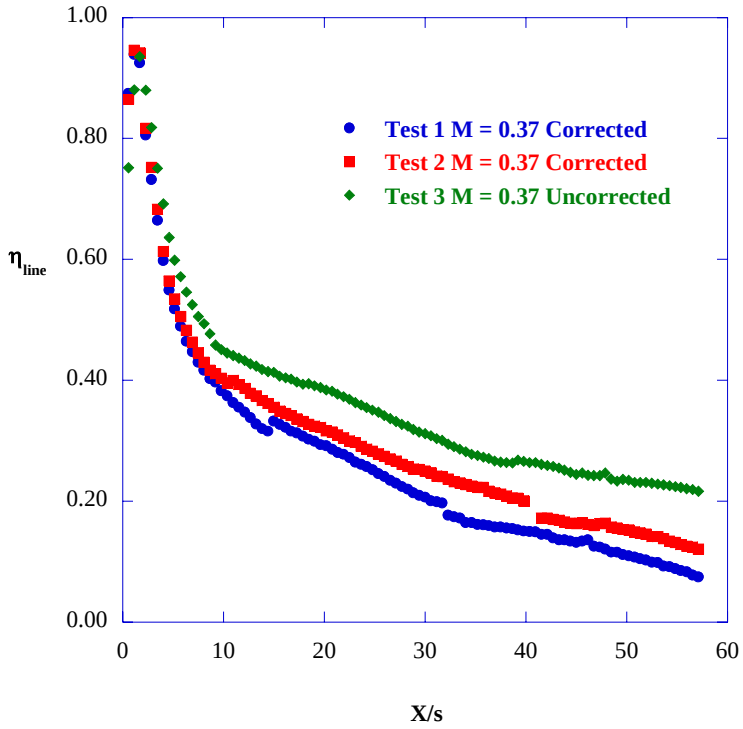

Figure 4-9 Corrected adiabatic effectiveness measurements.

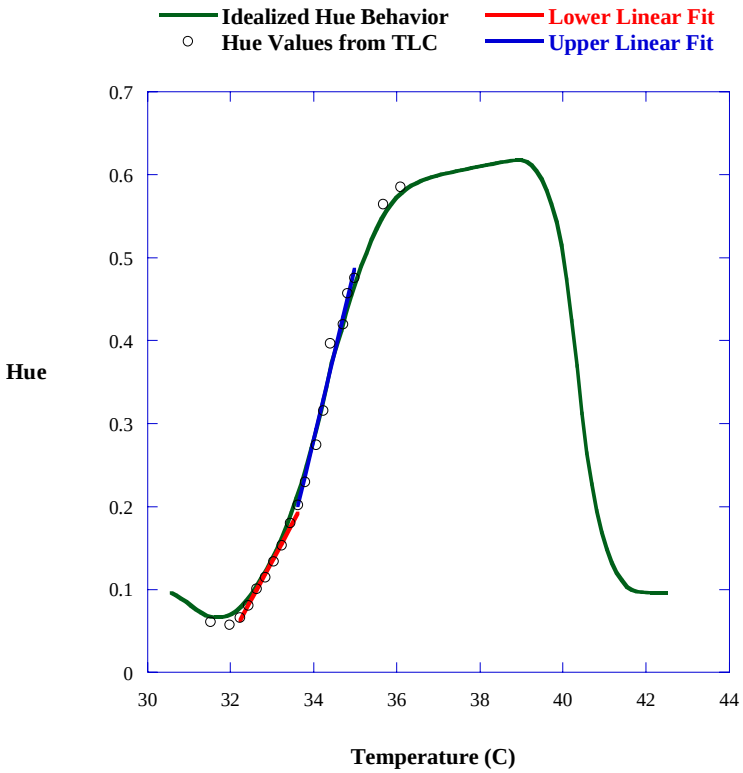

Figure 4-10 Hue versus temperature plot with idealized TLC behavior. The green line does not represent data, but the observed transition from blue to black

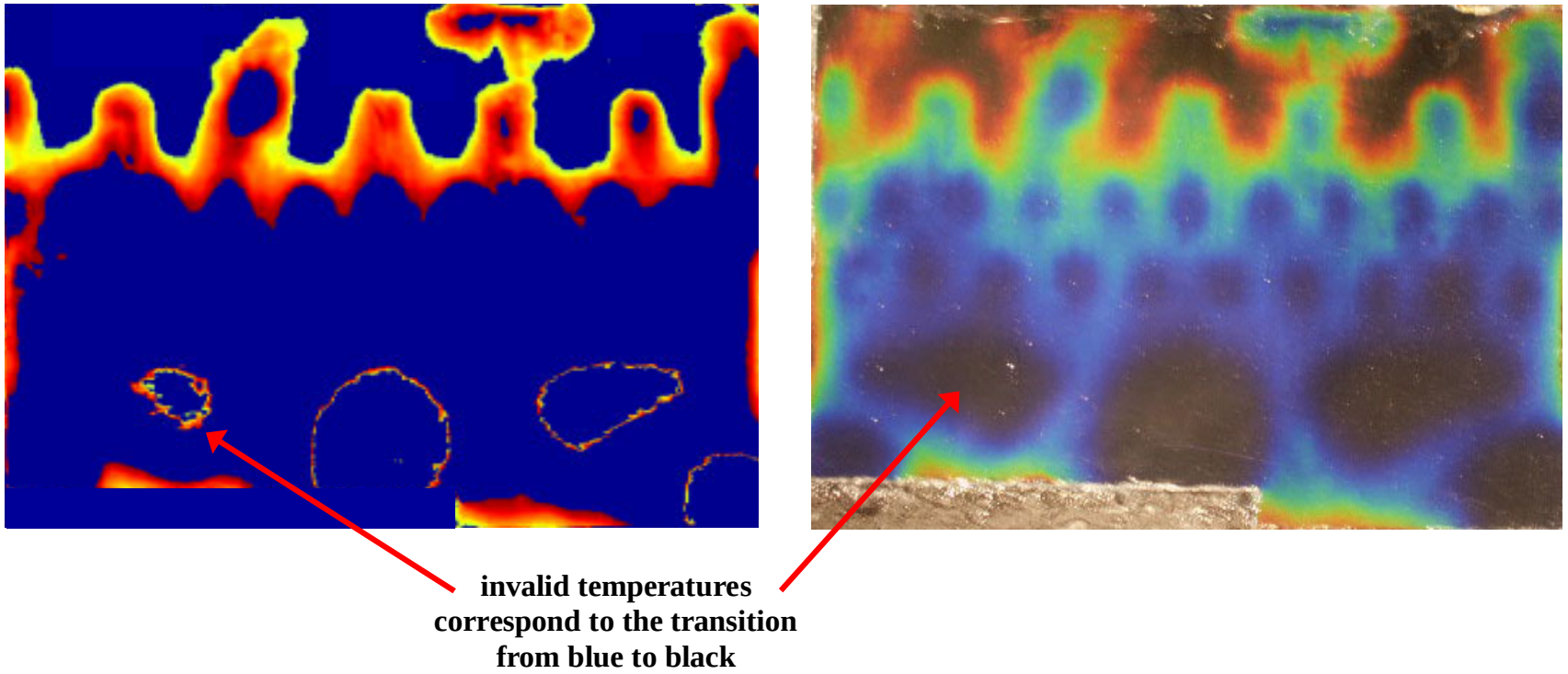

Figure 4-11 Comparison of temperature map (left) to corresponding hot image (right). Regions with hues in the blue-black transition range result in temperature data points that appear to fall within the TLC bandwidth, although they clearly do not.

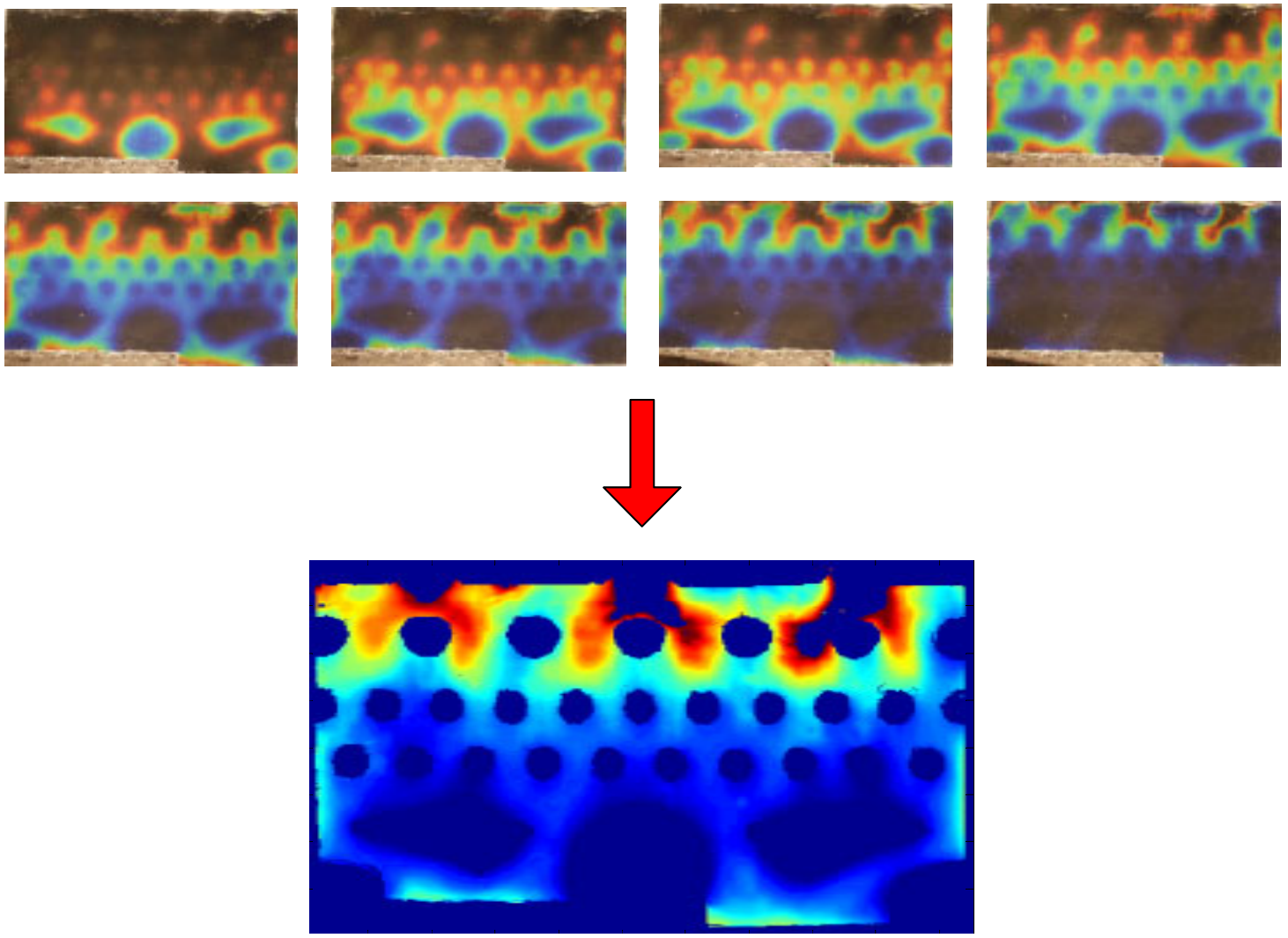

Figure 4-12 Individual TLC temperature maps and resulting composite heat transfer coefficient map.

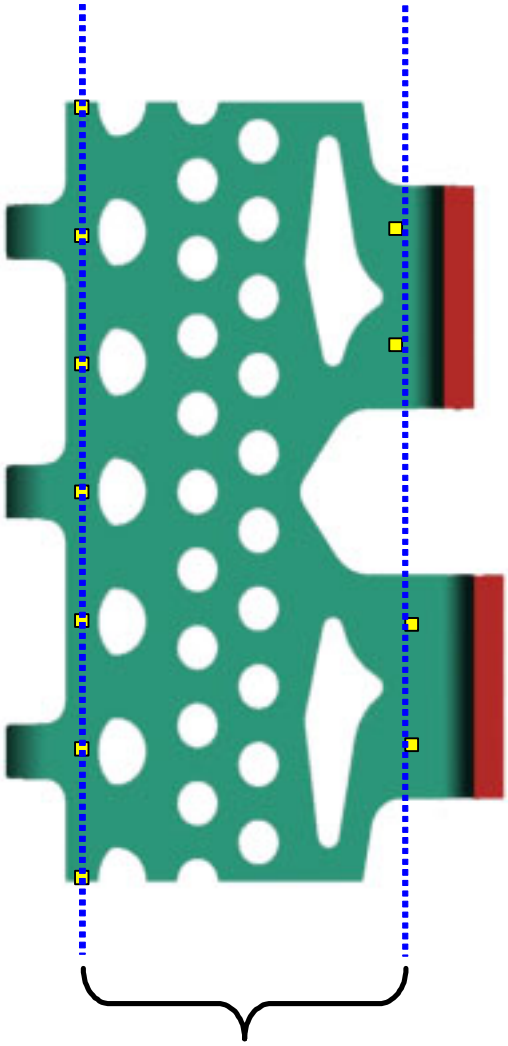

Figure 4-13 Static pressure measurement across the microcircuit. Discrete pressure tap measurements in inlet and exit planes were averaged and subtracted to achieve an overall pressure loss.

Chapter 5
External Film Cooling and Internal Heat Transfer Measurements

This chapter presents the results of the experiments described in Chapters 3 and 4. As mentioned, external film effectiveness experiments were completed at five different values of mass flux ratio (blowing ratio), which varied according to engine conditions. External results will be presented in terms of the variable η, adiabatic effectiveness. Internal heat transfer coefficient experiments were completed at four different engine specific Reynolds numbers. Internal results will be presented as heat transfer augmentation relative to an unobstructed fully-developed channel flow.

This study was commissioned with three major goals in mind. First, our sponsors wanted to determine if the microcircuit features, shown in Figure 5-1, have a measurable effect on the distribution of the film cooling flow exiting through the microcircuit exit slots. Second, in order to determine how much the features could affect the film flow, we also evaluated the cooling performance to compare to the literature. Third, we characterized the internal heat transfer and friction environments in the microcircuit. As with heat transfer augmentation, friction factor augmentation is measured relative to the friction factor of an unobstructed fully-developed channel flow.

We found that the microcircuit features affect the external film in a definite, repeatable manner. The details of these effects and the external adiabatic film effectiveness results will be presented in the first section of this chapter. External effectiveness results will include a discussion of each blowing ratio and comparisons to results of similar geometry. The second section will discuss internal heat transfer coefficients for each of the four tested Reynolds numbers with an emphasis on comparisons to published data for several different internal cooling schemes. The second section also discusses friction factor augmentation in the microcircuit.

5.1 External Film Effectiveness Results

The cooling benefit of the external film was evaluated at five different blowing ratios (M) corresponding to conditions found in the actual engine. To begin, this section will discuss the contours of adiabatic effectiveness for each blowing ratio, including the effects of the microcircuit pedestal features. Following the contour discussion, spanwise and area averaged data will be discussed. Finally, external adiabatic effectiveness results will be compared to three published data sets.

Figure 5-2 is a collection of adiabatic effectiveness contour plots. The contours are plotted from 0 to 1, with divisions of 0.05. Blue regions indicate a cooled wall, closer to the coolant temperature. Red regions indicate a hot wall, closer to the mainstream temperature. The test case with the lowest blowing ratio was M = 0.28. It is the upper left contour in Figure 5-2. The M = 0.28 experimental case was performed to match the momentum flux ratio (I = 0.07) of another slot film cooling experiment done at Virginia Tech [Smith et al., 2004]. Table 5-1 details our external test matrix and its relation to the test matrix of Smith et al. [2004]. Comparisons to that work will be presented later in the section

Upon first glance, the non-uniform flow exiting the slot stands out among the contours. The internal convective cooling scheme has definite, detrimental effects on the external film cooling flow leaving the microcircuit's exit slots. The non-uniformity is caused by uneven flow around the submarine pedestal features at the metering area. The coolant film exiting the microcircuit slots is asymmetric about the centerline of the cooling slot. Flow out of the slots is highly skewed back toward the spanwise center of the microcircuit.

The metering area of an irregular channel is the smallest flow area encountered by the bulk flow. Since, by definition, all of the flow passes through the metering area of a channel, slight variations can have dramatic effects on the flow structure in the channel. This is especially the case when the metering area is a specified plane in an irregularly spaced channel, like the microcircuit. The smallest area that the entire microcircuit mass flow passes through is marked by a plane through the submarine pedestal features. The

flow area is reduced significantly, forcing the flow to accelerate around the submarines and increasing the local heat transfer coefficients.

In the current microcircuit design, however, the areas on either side of each submarine are not equal. This serves to create a mismatch in pressure drop across the two sides of the metering area. Figure 5-1 illustrates the metering area described. As we know, pressure loss is a function of the square of the flow velocity. Since one side of the metering area is larger than the other, one side can accommodate a larger mass-flow for a given pressure loss. The flow automatically adjusts itself to equalize the pressure loss across the two sides of the metering area, resulting in a higher mass-flow on the side of the submarine closer to the microcircuit spanwise centerline.

Subsequent to this imbalance, the film exiting the microcircuit slots is uneven and skewed in the same direction. Substituting symmetric pedestal features for the submarines in the current microcircuit will help alleviate the non-uniformity seen in the cooling film. Symmetry upstream of the slot exit channels will help ensure uniform flow through the exit slots and spread the adiabatic effectiveness contours evenly across the external wall.

An interesting consequence of the uneven cooling flow is the shift in the region starved for coolant downstream of the slot exits with changing blowing ratio. As is evident in the external adiabatic effectiveness contours, the lower blowing ratios have a large region starved for flow downstream of the slots. Steadily increasing blowing ratios result in this starved region shifting away from the spanwise center of the microcircuits, toward the outer edges of the slots. This shift is caused by the increase in mass flow through the microcircuit. As the flow is increased, the flow around the inside edge of the submarine increases as well. The greater flow can fill the slot exit channel better than the lower flow rates, moving the starved region away from the spanwise center of the microcircuit.

The asymmetric effectiveness distributions are a function of the local changes in blowing ratio across the slot. We know that the flow is uneven as it approaches the slot exits. Therefore, if we were to examine a differential section of the slot area and evaluate the local blowing ratio at that location, it would certainly vary, as the flow upstream is non-uniform. The total mass flow divided by the total area is the average blowing ratio

across the slot, but the local changes would most certainly result in differing adiabatic effectiveness downstream of the slots. With regard to the current study, the flow is absent in a specific location for the lowest blowing ratio, indicating the possibility of a local blowing ratio even lower than the overall average slot blowing ratio. However, that same location is adequately cooled at a higher blowing ratio. It is possible that the overall increase in coolant has resulted in a local blowing ratio that better cools that specific location on the wall. Since it is evident that the microcircuit features affect the external film flow, the magnitude of the cooling benefit must be evaluated as well.

Coolant exits the slot and cools the near-slot region quite well. Recall, Figure 1-1 stated that a drop in metal temperature of just 14°C would increase the component's life by a factor of two. The adiabatic effectiveness level of $\eta = 0.8$ in the near-slot region for the M = 0.28 case corresponds to a temperature drop on the order of 175°C, using the temperatures quoted in Figure 1-1. While this sounds like a tremendous success for the design, we must consider the fact that this is a very small portion of the airfoil surface. The exceptional cooling near the slot is at the expense of poor cooling downstream. The airfoil would be better served by spreading the exceptional cooling between the slots, where no coolant is present.

The M = 0.28 test case sets the stage for several trends that will be observed throughout the external effectiveness results. First, coolant is able to cool the near-slot region, the area immediately downstream of the slots, so effectively because it stays completely attached to the wall. The coolant exits the slots with so little momentum that it cannot penetrate very far into the mainstream channel (in the pitchwise direction). Higher blowing ratios will show a general decrease in near-slot effectiveness because of the tendency for the higher momentum coolant jets to separate from the wall upon exiting the slot. Figure 5-3 is a graphic representation of the three accepted modes of coolant jet behavior: attached, detached-reattached, and detached. The M = 0.28 blowing ratio is most likely completely within the attached regime described in Figure 5-3.

The next blowing ratio shown in Figure 5-2, M = 0.37, shows similarly high near-slot effectiveness levels and greater downstream effectiveness when compared to the M = 0.28 case. The increased mass flux from M = 0.28 to M = 0.37 results in a slight downstream extension of the highly cooled region near the slot. This spreading is due to

the combination of two factors. The increased mass flux provides more coolant to the wall, but the increase in momentum flux is not enough to cause the jet to detach from the wall. Downstream effectiveness levels are also greater than the M = 0.28 case, as is to be expected with the increased coolant flow.

The M = 0.50 blowing ratio, shown in Figure 5-2, shows the first signs of jet detachment. The exceptional cooling in the near-slot region diminishes from the previous blowing ratio, undoubtedly due to the separation of the jet from the wall just downstream of the coolant slot. Since the downstream effectiveness levels for the M = 0.50 blowing ratio are not drastically lower than those measured in the M = 0.37 case, we can assume that the jet indeed reattaches. This follows the progression through the regimes noted in Figure 5-3.

The near-slot region continues its decrease in effectiveness for the M = 0.71 blowing ratio, the shown in Figure 5-2. The M = 0.71 case, like the M = 0.50 case, shows decreased effectiveness levels in the near-slot region, also due to the separation of the jet from the wall. In addition to the penalty incurred by the mainstream mixing, the higher momentum flux ratio pushes the re-attachment region further downstream. Interestingly, the downstream cooling effectiveness levels for the M = 0.71 blowing ratio are comparable to those measured in the M = 0.50 test case.

The M = 1.0 blowing ratio reinforced the effects seen in the previous blowing ratios, as seen in the bottom contour of Figure 5-2. The near-slot effectiveness levels are decreased from the lower blowing ratios, as the coolant jet is most certainly separated from the wall. Interestingly, the near-slot effectiveness distribution is markedly different for the M = 1.0 blowing ratio. The first three blowing ratios have a similar effectiveness distribution in the near slot region. The M = 0.71 case near-slot region starts to deviate from the pattern, and the M = 1.0 blowing ratio looks completely different. As discussed in the first section, this change is due to the internal features of the microcircuit. The downstream effectiveness levels of the M = 1.0 blowing ratio are lower than measured for the M = 0.71 blowing ratio. The increased mixing with the hot mainstream hampers the coolant flow's ability to protect the wall from the hot mainstream. The downstream effectiveness levels are high enough that the coolant jets are probably not completely detached from the wall. Most likely the jets re-attach, but only after considerable

mainstream mixing. The M = 1.0 blowing ratio is beyond the optimum blowing ratio, as the increased coolant mass flow does not provide additional cooling benefit.

A convenient way to compare the cooling benefits provided by different blowing ratios is to compare their spanwise averaged effectiveness levels. Figure 5-4 is a plot of the spanwise averaged effectiveness levels for all blowing ratios. Note, the abscissa in Figure 5-4 is the quantity X/s. The quantity X represents the streamwise distance from the slot exit plane to any downstream measurement. The quantity s is described by the following:

$$s = \frac{d \cdot w}{P} \tag{5.1}$$

where d is the streamwise slot length at the coolant feature breakout, w is the spanwise slot width at the breakout, and P is the sum of the slot width and the distance between two adjacent slots. Figure 5-5 is a schematic of the geometric parameters described above. Normalizing the streamwise distance by X/s removes the data's dependence on the cooling feature geometry and allows comparisons to a wider field of published data. For streamwise averaged effectiveness plots, X/s measurements begin at the downstream edge of the downstream slot.

In addition to spanwise averaged effectiveness, this chapter will discuss effectiveness measurements along a straight line. The line originates at a point along the spanwise center of the downstream edge of the exit slot and extends downstream normal to the slot. Since the slots are actually staggered in the streamwise direction, the X/s scale is shifted for the downstream slots so that each line represents X/s measurements relative to each individual slot. Figure 5-5 explains this geometry as well. This document will often switch between data of the type just described and spanwise averaged data, as described in the previous paragraph. For clarity, spanwise averaged data will always be referred to as such, while data along the streamwise slot centerlines will be called centerline effectiveness. The variable for spanwise averaged adiabatic effectiveness is $\bar{\eta}$, while the variable for centerline adiabatic effectiveness is η_{cl}.

Notice, the maximum coolant levels on Figure 5-4 are considerably lower than those observed in the contours of Figure 5-2. This is because the area over which the spanwise average is calculated contains both cooled and un-cooled sections of the adiabatic wall. Figure 5-6 is a depiction of the spanwise averaging process. By knowing the slot width and the distance between slots, we can calculate a theoretical maximum spanwise average effectiveness level across the slots. The theoretical maximum is calculated by assuming the effectiveness levels in the slot are equal to unity, while the levels between slots are equal to zero. Then the theoretical maximum is determined by performing a weighted average across the span between slots according to the following:

$$\eta_{max} = \frac{\eta_{slot} \cdot w + \eta_{between} \cdot 0.74w}{P} = \frac{1 \cdot w + 0 \cdot 0.74w}{w + 0.74w} = \frac{1}{1.74} = 0.575 \qquad (5.2)$$

Appropriately, none of the data presented in Figure 5-4 exceed the theoretical maximum spanwise average value. Again, the slot geometry is presented in Figure 5-5.

A close examination of Figure 5-4 confirms the trends observed when comparing the contour plots of each blowing ratio. The M = 0.28 blowing ratio exhibits the highest near-slot effectiveness levels, and the lowest downstream effectiveness levels. Increasing the blowing ratio to 0.37 results in a dramatic improvement in downstream cooling without any significant sacrifice in near-slot cooling. Starting at X/s of approximately 12, the M = 0.37 blowing ratio clearly outperforms the M = 0.28 case.

The M = 0.50 blowing ratio results in a spanwise averaged plot very similar to that of the M = 0.37 blowing ratio. This is discouraging, as the increased coolant flow is not providing any added benefit. Both near-slot averages and downstream averages are very similar to those found in the M = 0.37 case. As mentioned, the M = 0.50 blowing ratio is beginning to show the effects of mainstream penetration. The core coolant flow penetrates far enough to begin mixing with the mainstream before providing coolant to the wall. This mixing raises the temperature of the core coolant jet, thereby decreasing the cooling potential of the flow.

The M = 0.71 blowing ratio exhibits some interesting behavior. There are two competing trends that account for the changes between the M = 0.71 case and the lower

blowing ratios. First, the increased momentum flux results in a larger separation region just downstream of the slot exits. The separation region causes the decrease in near-slot effectiveness seen in Figure 5-4. Conversely, downstream effectiveness levels are slightly higher for the M = 0.71 case than for any of the lower blowing ratios. Despite the increased mainstream interaction, the increased coolant still performs slightly better after re-attaching. The better performance can be attributed to the fact that there is simply more cool fluid, even after mixing with the hot mainstream, available to cool the wall.

The M = 1.0 case exhibits the worst cooling performance despite injecting more coolant than any other blowing ratio examined by this study. The near-slot effectiveness levels are significantly lower for the M = 1.0 case than for all of the lower blowing ratios. The downstream effectiveness levels are decreased as well, although they are still higher than those measured for the M = 0.28 case. Despite significant mixing with the hot mainstream, the coolant jet still provides some cooling benefit after re-attaching downstream. Since the downstream effectiveness levels are still somewhat similar to the levels measured for the lower blowing ratios, it is unlikely that the M = 1.0 coolant jet is completely detached.

A good method of comparing data taken at different blowing ratios is to change the dependent variable with which we plot each spanwise averaged effectiveness curve. A higher blowing ratio exhausts more coolant into the mainstream flow. One would expect the increased cooling to reach further downstream, although we know that other factors can limit the ability the coolant's ability to cool downstream. Comparing to a lower blowing ratio over the same downstream distance does not adequately account for the increased cooling potential offered by the greater coolant flow rate. A comparison can be made by normalizing the dependent variable by the amount of coolant injected. Using an abscissa of X/Ms normalizes test cases by the amount of cooling [Wieghardt, 1946]. Theoretically, any blowing ratio that uses the full potential of its coolant mass flow will collapse to a single curve. Figure 5-7 is a plot of the same data used for all previous spanwise averaged plots, but using X/Ms as the independent variable. The first two blowing ratios nearly collapse to a single curve, indicating that they cool as best they can for the amount of cooling provided. The M = 0.50 case is slightly removed from the

first two blowing ratios. This indicates that the cooling performance of the M = 0.50 case does not measure up to its full potential. Penetrating further into the hot mainstream channel has had an adverse effect on the cooling capability of the flow. This adverse effect is even more prevalent in the M = 0.71 and M = 1.0 cases. Clearly, the added coolant exhausted through the slots to reach the higher blowing ratios is wasted, especially in the final two cases. Cooling benefits from increased slot flow are nominal or nonexistent at blowing ratios above M = 0.50.

Figure 5-8 is also a plot of spanwise averaged effectiveness versus X/Ms. However, included are curve fits to equations used by our sponsors to predict effectiveness levels based on X/Ms. The data and curve fits shown in Figure 5-8 are for the completely attached blowing ratios only. Figure 5-9 is a separate plot for the blowing ratios that detach from the wall compared to one of the curve fits used for the attached regimes. The curve fits are in the following form:

$$\bar{\eta} = \frac{1}{\frac{P}{w} + C_1\left(\frac{X}{Ms}\right)^{C_2}} \tag{5.3}$$

where P is the spanwise distance from one slot to the same location on the adjacent slot, w is the spanwise slot width, X/Ms retains its definition, and C_1 and C_2 are constants based on the coefficients of power curve fits of the experimental effectiveness data for a given blowing ratio. Table 5-2 lists the constants determined for each blowing ratio. Data for all blowing ratios was curve fit, although only cases within the attached regime are presented in Figure 5-8.

To gage the overall benefit of the coolant flow, the spanwise averaged adiabatic effectiveness data can be averaged in the streamwise direction as well, creating an area averaged effectiveness value, $\bar{\bar{\eta}}$, for each blowing ratio. Figure 5-10 is a plot of area averaged effectiveness versus blowing ratio. The streamwise portion of the area averaging is done from the downstream edge of the downstream slot, X/s = 0, and continues to the end of the collected data, X/s = 60. At engine scale, the current study's

area averages are calculated over a region that would cover only four of the capital letters on this page.

Area averaged effectiveness is helpful in discerning large changes in adiabatic effectiveness between blowing ratios. However, care must be taken when using them as a tool for evaluation of a blowing ratio's overall worth. Area averaged effectiveness completely washes out the detail of both overcooled and under-cooled regions. There is the distinct possibility that a blowing ratio with higher area averaged effectiveness could have gradients or hot-spots that are more severe than a case with lower area averaged effectiveness.

Figure 5-12 shows that the area averaged effectiveness peaks at M = 0.37. The increase in area averaged effectiveness from M = 0.28 to M = 0.37 is due to the increased coolant flow within the attached regime. Clearly, more coolant has a positive cooling effect as long as the jet remains attached to the wall. Comparing M = 0.37 to the higher blowing ratios, results match those found by the spanwise averaged plots. The increased coolant decreases the effectiveness levels in the near slot region and provides nominal, if any, cooling benefit in the downstream region. Again, this is due to increased mainstream mixing at the higher blowing ratios. Interestingly, while the coolant jet starts to separate from the wall somewhere between M = 0.37 and M = 0.50, the detrimental effects of mainstream interaction must peak somewhere between M = 0.50 and M = 1.0. The area averaged effectiveness drop from M = 0.37 to M = 0.50 can be attributed to the jet separation, but the downstream effectiveness levels do not decrease until M = 1.0. Since we know that the jet is already separated at that blowing ratio, the decrease in the downstream levels must be due to the increased mixing with the mainstream. Therefore, the detrimental mixing phenomenon must overcome the increased mass flux somewhere between the M = 0.50 and M = 1.0 blowing ratios.

Many researchers do film cooling studies, as they have the potential to significantly cool turbine parts. In fact, turbine durability engineers consider film cooling the first line of defense for a turbine component. The many studies published every year provide researchers with an abundance of data with which they can compare their results. This study will compare the discreet film cooling slots that we tested with three published studies. The first comparison will be made to effectiveness data taken with film cooling

holes. Our data will also be compared to a study that uses a long continuous slot, instead of the discreet staggered slots we used. In addition, our effectiveness results will be compared to another set of experimental data taken here at Virginia Tech. The other set of Virginia Tech data, taken by Smith et al. [2004], uses the same slot geometry with no microcircuit features upstream of the exit slots.

Drost et al. [1997] tested two film cooling configurations, one of which will be compared to our data. The study used a transient liquid crystal technique to resolve adiabatic effectiveness downstream of a row of 14 film cooling holes on a flat plate. The film cooling holes were inclined 35° from the horizontal, in the streamwise direction. The spanwise averaged effectiveness (called laterally averaged effectiveness in that paper) was calculated by averaging effectiveness data downstream of the five holes in the center of the row. Holes measured 1.8 mm in diameter, resulting in a breakout streamwise width of 3.1 mm. Experiments were performed at blowing ratios of 0.30, 0.50, 0.70 and 1.0, allowing direct comparison to our study. Experiments were performed at several turbulent intensities and Mach numbers, but the ones to which we will compare were performed with a turbulent intensity of 1% and a Mach number of 0.3. All experiments had a density ratio of 1.6.

Figure 5-11 is a plot of spanwise averaged adiabatic effectiveness for four blowing ratios. The current study is plotted, as well as data taken from Drost et al. [1997], whose data had to be adjusted to fit our axes. Drost et al. [1997] plotted spanwise averaged effectiveness versus X/d, where d was the hole diameter. As mentioned, our data is plotted versus X/s. The variable s is calculated for the Drost et al. [1997] data according to Equation 5.1, the numerator being the area of the hole's metering area. As defined in Equation 5.1, X/s represents the distance downstream of the cooling feature in slot widths. The formula for s normalizes all cooling geometries so that they represent continuous cooling slot, since the hole area is divided by the spanwise spacing of the holes [Soechting and L'Ecuyer, 1985]. The literature considers the normalization for comparison between slots and holes a special case. Therefore s picks up a subscript e, s_e, to denote the equivalent slot width specified by the normalization. The magnitudes of the cooling benefits do not match within our experimental uncertainty, but the trends observed between blowing ratios are similar with one exception. The M = 1.0 case in the

published data exhibits downstream cooling comparable to the published M = 0.70 case. Data from the current study shows a greater decrease in effectiveness at the highest blowing ratio. All blowing ratios from the current study show lower effectiveness levels than that of Drost et al. [1997] throughout the downstream measurement range. Undoubtedly, this decrease in effectiveness is due to the slot exit angle. The Drost et al. [1997] study had holes that were inclined downstream, as indicated. This reduced jet separation, especially at higher blowing ratios, since the coolant exited the holes with streamlines already pointing downstream. In the current study, slots exit normal to the flow, theoretically resulting in coolant blow-off at much earlier blowing ratios.

Figure 5-12 is another comparison of data from the current study to that of a published experiment. Data for this comparison was taken from Liburdy et al. [1997]. Liburdy et al. [1997] used a continuous cooling slot, rather than discreet cooling features. The experiments were performed using a transient liquid crystal method to resolve adiabatic effectiveness on a flat plate. The cooing slot was inclined 35° from the horizontal, in the streamwise direction. Spanwise averaged effectiveness was calculated by averaging over a 3 cm section in the spanwise center of the cooling slot. The actual slot was 5 mm long and 200 mm wide. The slot inclination resulted in a coolant jet breakout width of 8.7 mm. The experiments for the study were conducted with varying turbulent intensities and a density ratio of 1.55.

The adiabatic effectiveness levels measured by Liburdy et al. [1997], seen in Figure 5-12, are considerably higher than those found for the current study. There are two main reasons for the discrepancies. First, Liburdy et al. [1997] used a continuous slot. Our study conducts spanwise averaging over a region that contains both cooled and uncooled portions of the measurement surface, corresponding to one periodic microcircuit. Nearly 43% of the spanwise averaging distance in the current study represents regions that do not have a cooling feature upstream of them. Naturally, this resulted in lower spanwise averaged effectiveness levels, since the comparison study averaged data that was entirely cooled. Using the current study's centerline effectiveness data makes for a better comparison. This comparison is made in Figure 5-13. Additionally, the comparison study used an inclined slot. As previously mentioned, the inclination of the slot allows the coolant to stay near the wall, even at higher mass flux

ratios. This reasoning accounts for the change in trends between blowing ratios as well. Liburdy et al. [1997] shows increasing effectiveness with increasing blowing ratio. This is to be expected, as the higher blowing ratios provide more coolant without the corresponding coolant separation penalty observed in the current study. Recall, the current study's effectiveness values peaked at a lower blowing ratio and began to show decreased overall effectiveness at the higher blowing ratios. The difference caused by the initial separation of the current study's data can be seen in both Figures 5-12 and 5-13.

The data from the current study was also compared to curve fits and data taken from a concurrent study done at Virginia Tech. The data to be compared was gathered by Smith et al. [2004] in the Virginia Tech AOE Department's transient blow-down tunnel. Smith et al. [2004] collected effectiveness data using a single row of heat flux sensors along the centerline of a slot geometrically similar to the current study. Figure 5-14 is a plot of the centerline effectiveness values of Smith et al. [2004] data compared to the centerline effectiveness for the current study, both at a blowing ratio of $M = 0.37$. Smith et al. [2004] data was not taken with any microcircuit pedestal features in the cooling passages upstream of the slots, so the adiabatic effectiveness pattern on the flat plate did not match those found during the current study. As a consequence, the centerline effectiveness values in Figure 5-14 do not represent a direct comparison, as the Smith et al. [2004] effectiveness distribution was symmetric about the slot's span. Table 5-1 outlines the test matrices for the current study compared to Smith et al. [2004].

5.2 Internal Heat Transfer Coefficient Results

Our sponsors commissioned this study to gage the overall internal heat transfer benefit that the microcircuit cooling features could provide over a given set of engine specific Reynolds numbers. As mentioned in Chapter 4, experiments were conducted for Reynolds numbers between 5,200 and 15,000. This section will discuss heat transfer and friction factors for each experimental Reynolds number. As with the previous section, contour plots will be discussed first, followed by spanwise and area averaged plots.

Friction factor augmentation will be discussed after the heat transfer results are presented. Comparisons with published data will follow the friction factor results.

The sponsors of this project requested that the experimental validation of the microcircuit array take place over a range of engine specific Reynolds numbers. Originally, this range was specified to be 5,000 – 10,000, based on the hydraulic diameter in the open channel of the microcircuit, as if no pedestal features were present. Based on this range, we chose our test cases to be, nominally, Reynolds numbers of 5,000, 7,500, and 10,000. As experiments progressed, we made improvements that allowed higher Reynolds number testing as well. Our sponsors expressed interest in the higher Reynolds numbers, so we added the 15,000 test case. As mentioned, these Reynolds numbers were nominal, target values. Reynolds numbers were variable and difficult to trim to exact values.

Figure 5-15 is a collection of internal heat transfer augmentation contour plots. The contours are plotted from 1.5 to 6.5. As mentioned in Chapter 4, heat transfer augmentation refers to the increase in heat transfer (and later friction factor) in the microcircuit when compared to the baseline heat transfer results of a straight, unobstructed channel with similar boundary conditions. Recall Equations 4.13 and 4.14 for the definitions of baseline Nusselt number and baseline friction factor:

$$Nu_o = 0.0285 \cdot Re^{0.75} \tag{4.13}$$

$$f_o = 0.316 \cdot Re^{-0.25} \tag{4.14}$$

Table 5-3 documents the baseline Nusselt numbers and friction factors used to determine heat transfer augmentation levels at each Reynolds number. Contours of actual experimental Nusselt numbers (not augmentation) can be found in Appendix F.

The actual Reynolds number in the first experimental case was 5,262. The upper left contour in Figure 5-15 is a plot of heat transfer augmentation for the first microcircuit test case, Re = 5,262. As expected, the areas of highest augmentation occur around the first row of pedestal features downstream of the microcircuit inlets. Impingement cooling in this region provides so much heat transfer that the standard heat flux settings for our experiments did not provide enough heat to cause the liquid crystals to react. That is the cause for the missing data just upstream of the impingement regions (data

shown in black). We did, for one study, evaluate the heat transfer coefficients as far into the impingement region as possible, the Re = 6,945 case, which will be discussed next. Otherwise we did not resolve heat transfer coefficients well into the impingement region to avoid operating the thin strip heater at its maximum capability for long periods of time. Heat transfer augmentations in the impingement region were very high, nearing 5. Recall, heat transfer augmentation is the factor by which the microcircuit exceeds a straight, unobstructed channel's heat transfer performance.

Even downstream of the impingement region, the Re = 5,262 contour of Figure 5-15 shows good augmentation through the second and third rows of features, both standard pin fins. Interestingly, the pedestal features upstream of the submarine features do not have as high of augmentation levels as similar features adjacent to them. Clearly, the effects of such a large blockage propagate well upstream. The contours are lower around the pin fins that are directly upstream of the submarines. The regions of highest augmentation in the second and third rows are between the pedestal features, where the flow is accelerated around the pin fins.

Downstream of the standard pin fins, the flow encounters the submarines and flow divider. As noted above, the submarines are wide and block a significant portion of the flow area. The center divider, which splits flow in the center of the microcircuit between the two slot exits, is not nearly as blunt of a separator as the submarines. The center divider doesn't impede the central microcircuit flow as much as the submarines. Therefore, the upstream flow in the center of the microcircuit is not slowed as severely. Subsequently, augmentation levels in the center of the microcircuit are higher than on the sides.

Overall augmentation, however, makes a local recovery in the flow plane around the submarines. The flow is accelerated around the submarines and central divider and, therefore, increases the heat transfer in these regions. High values of augmentation downstream of the submarines are due to the slot bends at the microcircuit exits. Interestingly, the highest augmentation near the slot exits is in the corner of the slots. Since the slot channels are of uniform geometry, the higher augmentation must be the result of higher flow on the sides of the channel. The flow non-uniformities exiting the

slot have direct implications on the external film and is responsible for the adiabatic effectiveness unbalance discussed in Section 5.1.

The upper right plot in Figure 5-15 is the contour for the Re = 6,945 case. As expected, augmentation patterns for this flow setting are similar to those seen in the Re = 5,262 case. One of the first noticeable changes, with respect to the previous contour plot, is the higher augmentation around the impingement regions. As mentioned, we chose to resolve the high impingement augmentations near the inlets for this flow setting. Augmentations of 6 and higher were recorded in the impingement region.

The augmentation patterns of the standard pin fin rows observed in the Re = 5,262 case are repeated in the Re = 6,945 case. The pedestals located upstream of the submarines have lower augmentation levels than those adjacent. The local recovery in augmentation around the submarines is evident on the Re = 6,945 contour as well. The Re = 6,945 contours also show the exit flow imbalance. Effectiveness levels on the inner side of the slot exit channels are higher than the outer side, just as with the Re = 5,262 case. Overall, augmentation levels for the Re = 6,945 case are decreased from the Re = 5,262 experimental case.

The lower left contour in Figure 5-15 is the data taken for the Re = 10,496 case. Again, the impingement region reports high augmentation levels that decrease as the flow enters the standard pin fin arrays. Regarding augmentation distributions throughout the microcircuit, the Re = 10,496 case follows the patterns established in both the Re = 5,262 and Re = 6,945 cases. Additionally, the Re = 10,496 case shows an overall decrease in effectiveness levels throughout the microcircuit.

The Re = 15,127 experimental case does not deviate from the trends established in the lower Reynolds number cases, as seen in the lower right contour of Figure 5-15. The augmentation distributions for the Re = 15,127 case are identical to those observed in the other Reynolds number cases. Accordingly, the overall augmentation levels decrease for the Re = 15,127 case as well. Our theory for this trend of decreasing overall augmentation levels has to do with the turbulence levels in the microcircuit at different Reynolds numbers. The low Reynolds numbers are close to the point at which flow naturally transitions from laminar flow to turbulent flow. Clearly, the pedestal features promote turbulence. Possibly, the pedestals promote enough turbulence at the lower

Reynolds numbers to make heat transfer augmentation higher than at the higher Reynolds numbers. After all, we are measuring *augmentation* of heat transfer. The baseline Nusselt number applied to a given data set is consistent with a level of turbulence occurring at the Reynolds number used to calculate that baseline.

Just as external effectiveness measurements of different blowing ratios were compared with spanwise averaged plots, internal heat transfer augmentation results were averaged across the span of one periodic microcircuit. Figure 5-16 is a plot of spanwise averaged effectiveness for all tested Reynolds numbers. The data is plotted versus the variable X/D_h, where X is the streamwise distance downstream of the microcircuit inlets and D_h is the hydraulic diameter of the microcircuit channel with no obstructions. The $X/D_h = 0$ location is defined as the location where the 90° inlet bends are tangent with the microcircuit walls. Because of the missing data around the impingement regions, and specifically the differing regions of missing data between Reynolds numbers, impingement regions are not included in the spanwise averaged curves. Data is presented starting at $X/D_h = 1.7$, which is the streamwise location of the downstream edge of the elliptical pedestal features. Additionally, Nusselt numbers were resolved underneath the pedestal features as well. However, this data was neglected in the current study since the pedestal features were constructed of low conductivity foam. It was assumed that the fin efficiency of the foam features was near zero and therefore did not transfer heat to the microcircuit flow.

Figure 5-16 confirms many of the trends observed by comparing contour plots of augmentation data. The most evident trend is the overall decrease in augmentation with increasing Reynolds number. All curves begin high, as expected due to both the impingement region and the thermal entry region. All Reynolds numbers exhibit a steady decrease in spanwise averaged augmentation through the rows of standard pin fins. Interestingly, all cases also exhibit a local augmentation recovery around $X/D_h = 4$, which corresponds to the streamwise location where the flow accelerates around the submarine pedestal features on its way into the slot exit channels. The increased augmentation values are a function of two variables. First, the velocity of the flow increases as the flow area contracts around the submarine features. As discussed, this acceleration increases the local Reynolds number thereby increases the local heat transfer coefficient. Second,

since the flow area is much smaller, the area over which the averaging takes place is smaller as well, giving the high augmentation regions around the submarines a higher weight in the spanwise average at that location.

The large increases in augmentation seen at the microcircuit exits are due to the exit effects of the curved slot exits. The jump in the spanwise averaged plots at approximately $X/D_h = 5.75$ correspond to the location where the averaging routine switches from averaging across both slot channels to only averaging across the span of the longer slot channel.

Our sponsors, Pratt & Whitney, created a computational simulation, called PinFin, to approximate the heat transfer and friction augmentation of a standard pin fin array [Cunha, 2004]. The program predicted fully developed heat transfer augmentation levels for user entered pin fin geometries. The results of the program compared quite well to our experimental data, considering the assumptions the program makes. The program does not include provisions for the impingement regions, the complicated geometry of the microcircuit, or any thermal entry region effects. The dashed lines on Figure 5-16 represent the PinFin predicted heat transfer augmentation levels for each Reynolds number with geometry comparable to the standard pin fins in the center of the microcircuit.

In another parallel with the external adiabatic effectiveness analysis, the augmentation data is also averaged in the streamwise direction to obtain area averaged augmentation values for each experimental Reynolds number. Figure 5-17 is plot of area averaged heat transfer augmentation versus Reynolds number. Both the experimental measurements and PinFin predictions are shown on Figure 5-17. Area averaging takes place across the entire microcircuit span and extends from $X/D_h = 1.7$ to $X/D_h = 6$ in the streamwise direction, where the flow encounters the exit slot bends. Like the spanwise averages, the impingement regions are not included in the area averaged augmentation calculations. As expected, area averaged augmentation drops with increasing Reynolds number.

In addition to examining heat transfer augmentation, this study also investigates the increase in pressure loss across the microcircuit. The pedestal features represent flow blockages that increase the total pressure losses though the microcircuit. We report these

losses as friction factor augmentation, defined in Section 4.3. Baseline friction factors at each Reynolds number are documented in Table 5-3.

Pratt & Whitney's PinFin code defines friction augmentation differently. Their analysis centers around a variable they called Friction Multiplier, F_M. Friction Multiplier is defined as follows:

$$F_M = \frac{\left(\frac{\Delta P_{static}}{4} \cdot \frac{2}{\rho \cdot U_{max}^2} \cdot \frac{X}{s_p}\right)\left(\frac{D_h}{X}\right)\left(\frac{1}{1 - d/s_n}\right)^2}{f_o} \tag{5.4}$$

where ΔP_{static} is the static pressure loss across the microcircuit as defined in Figure 4-13, ρ is the mean microcircuit density, U_{max} is the velocity between pedestal features, X is the streamwise flow length, D_h is the channel hydraulic diameter, d is the pin fin diameter, s_p is the streamwise pin fin spacing, s_n is the pitchwise pin fin spacing, and f_o is the baseline friction factor. The analysis leading to Friction Multiplier is documented in Appendix G. Just as PinFin's analysis for heat transfer differs from our experimental data, the friction factor predictions differ from our experimental values as well. Again, the program is an approximation for a fully developed flow through a standard pin fin array only. The program does not account for the high pressure loss of the inlet impingement regions, nor does it have provisions for the submarines or the separate slot exits. Figure 5-18 is a plot of friction multiplier versus Reynolds number, for both PinFin predictions and our experiments. The agreement is as good as can be expected for regimes with such differing geometry, as is the case between the microcircuit and standard pin fin array. Despite the apparent variations at different Reynolds numbers, the data is nearly Reynolds number independent when the experimental uncertainty is taken into account. Recall from Table 3-2, friction factor augmentation uncertainty is nearly 8%.

Recall, Equation 4.16 defined Efficiency Index, a variable that relates the beneficial heat transfer augmentation with the detrimental effects of the friction factor augmentation. Figure 5-19 is a plot of Efficiency Index versus Reynolds number for the current study. Note, for this plot friction augmentation is defined as stated in Chapter 4,

not as defined for Friction Multiplier. Figure 5-19 shows a general decrease in Efficiency Index with increasing Reynolds number.

There are countless studies regarding internal heat transfer augmentation, although none have the specific geometry used in this study. Additionally, most have not taken place so close to the airfoil skin. This study will compare results with published studies that are comparable in geometry and flow conditions. Results will be compared to a ribbed channel study, a dimpled surface study, and a pin fin study.

We compared our results to a ribbed channel study completed by Han et al. [1992]. Han et al. [1992] compared heat transfer and friction augmentation results for numerous ribbed channel configurations. The Reynolds numbers tested in that study ranged from 14,000 to 88,000. To fairly compare results, the current study will only compare to the Han et al. [1992] Re = 14,000 data. Additionally, Han et al. [1992] compared eight different specific rib geometries. This study will only compare to four of the most traditional configurations; continuous ribs perpendicular to the flow (a), parallel broken ribs perpendicular to the flow (b), parallel broken ribs 45° from the flow direction (c), and parallel broken ribs 60° from the flow direction (d). Figure 5-20 is a plot of heat transfer augmentation versus X/D_h. The ribbed channel configurations cannot match the augmentation provided by the impingement regions of the microcircuit, but their repetitive design allows higher augmentation levels downstream.

Han et al. [1992] reports friction augmentation in the range of 6-8 for the 14,000 Reynolds number. This is a tenth of the friction augmentation measured by the current study. However, it must be noted that the rib height to hydraulic diameter ratio for Han et al. [1992] was quite small, 0.0625. The majority of the channel flow had no interaction with the ribbed features at all, causing less friction loss. All of the coolant flow in the current study encountered a pedestal feature at one point or another. The net result of the comparison is that the ribbed channels can maintain high heat transfer augmentation levels with relatively little frictional penalty. However, the true cost is in space. The current study's channels are designed to work in conjunction with ribbed channels, not to replace them.

The current study was also compared to a heat transfer and friction augmentation study completed for a dimpled channel cooling configuration. Dimpled channels can

provide heat transfer augmentation by inducing complicated flow structures in the coolant flow, as noted by Bunker et al. [2003]. Figure 5-21 is a reproduction of the Bunker et al. [2003] data regarding heat transfer augmentation as a function of friction factor augmentation. The other sets of comparison data are shown in Figure 5-21 as well. Of the data presented in Bunker et al. [2003], three were chosen for comparison. The three sets represent configurations with different dimple densities and/or different dimple-depth to tube-diameter ratios. Dimple density is represented in Bunker et al. [2003] with the variable f, while dimple-depth to tube-diameter ratio is represented with d/D. The Nusselt numbers and friction factors reproduced from Bunker et al. [2003] in 5-21 represent only fully developed data. Bunker et al. [2003] did not analyze the entry region of the dimpled channel test configuration. As with the ribbed channel comparison, the friction penalty is not nearly as high in the dimpled channels. However, this is to be expected, since there are no flow blockages. Clearly, however, the channels are not capable of producing the high augmentation that the microcircuit creates. Additionally, the beneficial impingement region found in our microcircuit design is absent. One advantage for the dimpled channel configuration is manufacturability. Again, space considerations for the configuration tested by Bunker et al. [2003] would not work well for application near the airfoil skin. It would be impractical to place these circular channels near the airfoil's outer surface, as their cross section would place only a small fraction of the tube diameter adjacent to the heat source. However, if the dimpled channels could be adapted to a semi-infinite, rectangular application, they may be of use near the airfoil skin.

The pin fin study chosen for comparison evaluates both inline and staggered arrays of filleted and straight pin fins between Reynolds numbers of 5,000 and 30,000. The study, Chyu [1990], presents results that can most aptly compare to the results of the current study. The pin fin diameter, channel hydraulic diameter, and pin fin spacing are all similar to the current study. However, there were differences between the studies. Chyu [1990] had a section of open duct upstream of the pin fin array to allow the flow to become fully developed. Additionally, the coolant inlet was spread across the entire array, there were no impingement regions.

Specifically, this study will compare to the Chyu [1990] straight cylinder, staggered array data, as the experimental setup for that data best fits our experimental setup. Figure 5-22 shows the spanwise averaged Nusselt numbers for the comparison study and the current study. As with the previous comparison, the data taken by Chyu [1990] was fully developed. That accounts for the differences at each study's inlet plane. The spanwise averaged augmentation starts to tend toward similar values as they flow passes through the standard pin fin rows. However, similarities cease when the flow through the microcircuit encounters the submarine pedestal features. However, the Chyu [1990] study does find that the trends between Reynolds numbers are similar to those observed by the current study. Efficiency Index, shown in Figure 5-23, shows the data for the Chyu [1990] study as well. The current study compares closest in geometry to the third design, which represents a staggered array of cylindrical pin fins without fillets at the pin-wall junctions. As expected, our data for Efficiency Index matches closest for this case as well. Note that the data reproduced from Chyu [1990] in Figure 5-23 has been adjusted to match the method of friction factor analysis used by this study. Chyu [1990] defined friction factor by the D'arcy friction factor definition and normalized by a Fanning friction factor baseline. However, the Chyu [1990] data based friction factor on the maximum velocity in the duct, between the pin fins. Therefore, the data from the current study has been analyzed as such for comparison.

To compare the overall benefit of all of the studies, Figure 5-24 is a plot of area averaged heat transfer augmentation versus Reynolds number for four studies; the current study, Pratt & Whitney's PinFin program, Bunker et al. [2003], and Chyu [1990]. Data from the Han et al. [1992] study was not included in Figure 5-24 as the comparison data was only taken at a single Reynolds number. Clearly, the microcircuit design is able to augment heat transfer the best of the three studies, but there is a penalty paid in friction loss.

Table 5-1 External Effectiveness Test Matrix as Compared to Smith et al. [2004]

M	DR, Smith et al. [2004]	VR, Smith et al. [2004]	I, Smith et al. [2004]	DR, current study	VR, current study	I, current study
0.28				1.1	0.24	0.066
0.30	2.0	0.15	0.045			
0.37	2.0	0.19	0.068	1.1	0.33	0.121
0.50	2.0	0.25	0.125	1.1	0.45	0.225
0.71				1.1	0.64	0.451
1.0	2.0	0.50	0.500	1.1	0.90	0.891

Notes: DR = Density Ratio, VR = Velocity Ratio, yellow highlighted cases were chosen to match momentum flux ratio

Table 5-2 Film Cooling Durability Curve Fit Constant Coefficients

M	C_1	C_2	P	w
0.28	0.12	0.90	4.31	2.5
0.37	0.14	0.82	4.31	2.5
0.50	0.21	0.77	4.31	2.5
0.71	0.32	0.69	4.31	2.5
1.0	0.57	0.65	4.31	2.5

Table 5-3 Baseline Summary for Internal Augmentation Calculations

Re	Nu_o	f_o
5262	17.1	3.71E-02
6945	21.1	3.46E-02
10496	28.7	3.12E-02
15127	37.7	2.85E-02

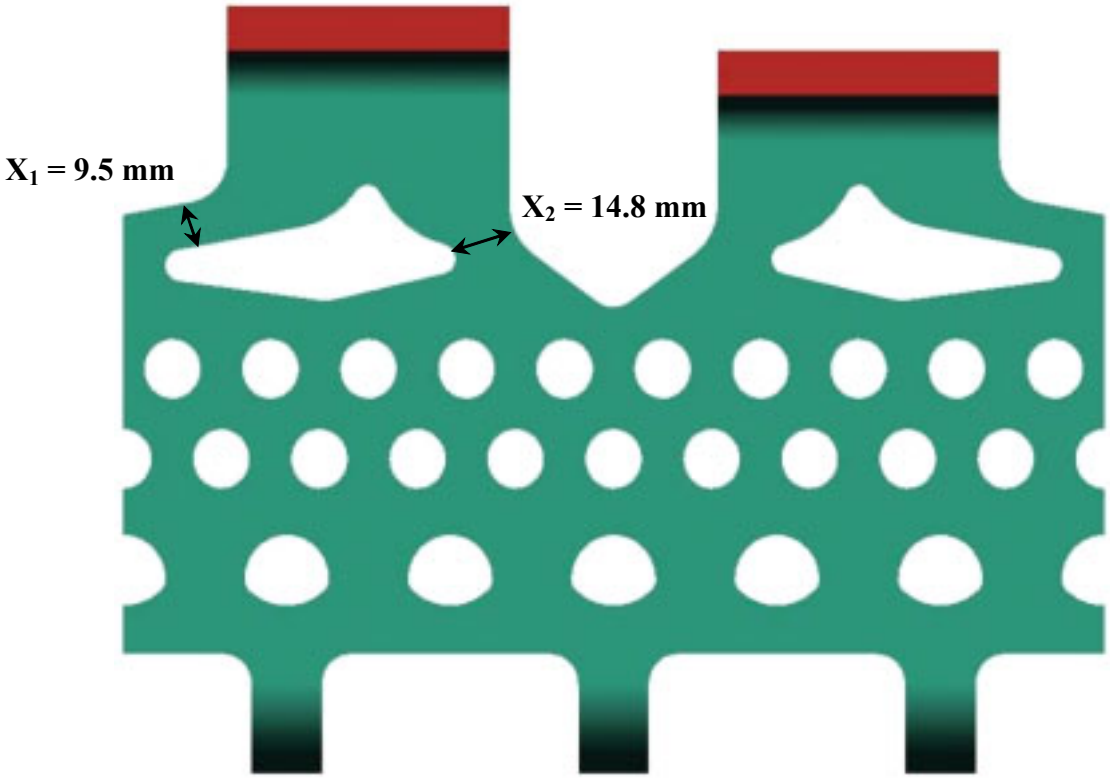

Figure 5-1 Metering areas in the microcircuit channels. Distances are at experimental scale (25X engine scale).

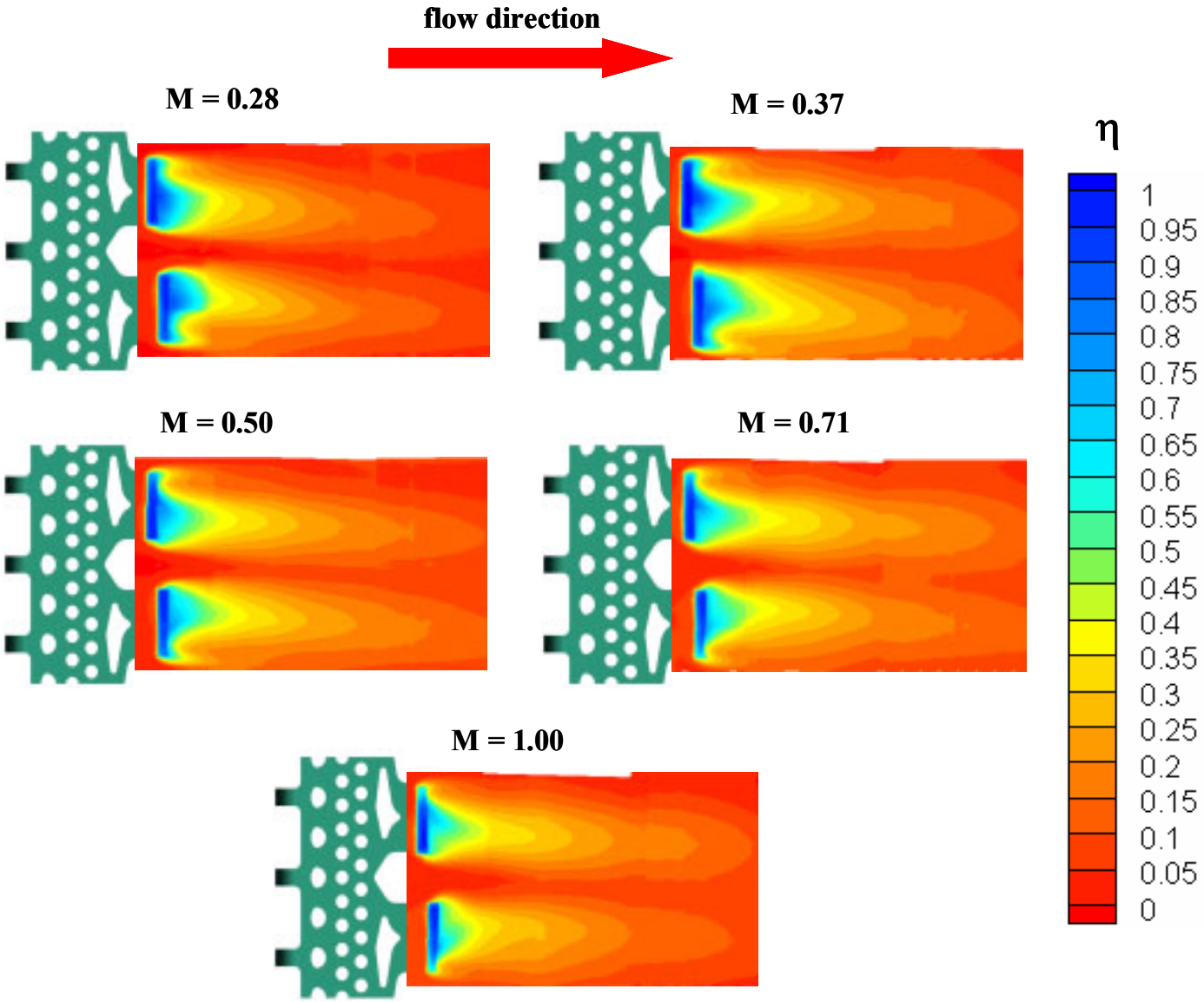

Figure 5-2 Contour plots of all five external adiabatic effectiveness cases.

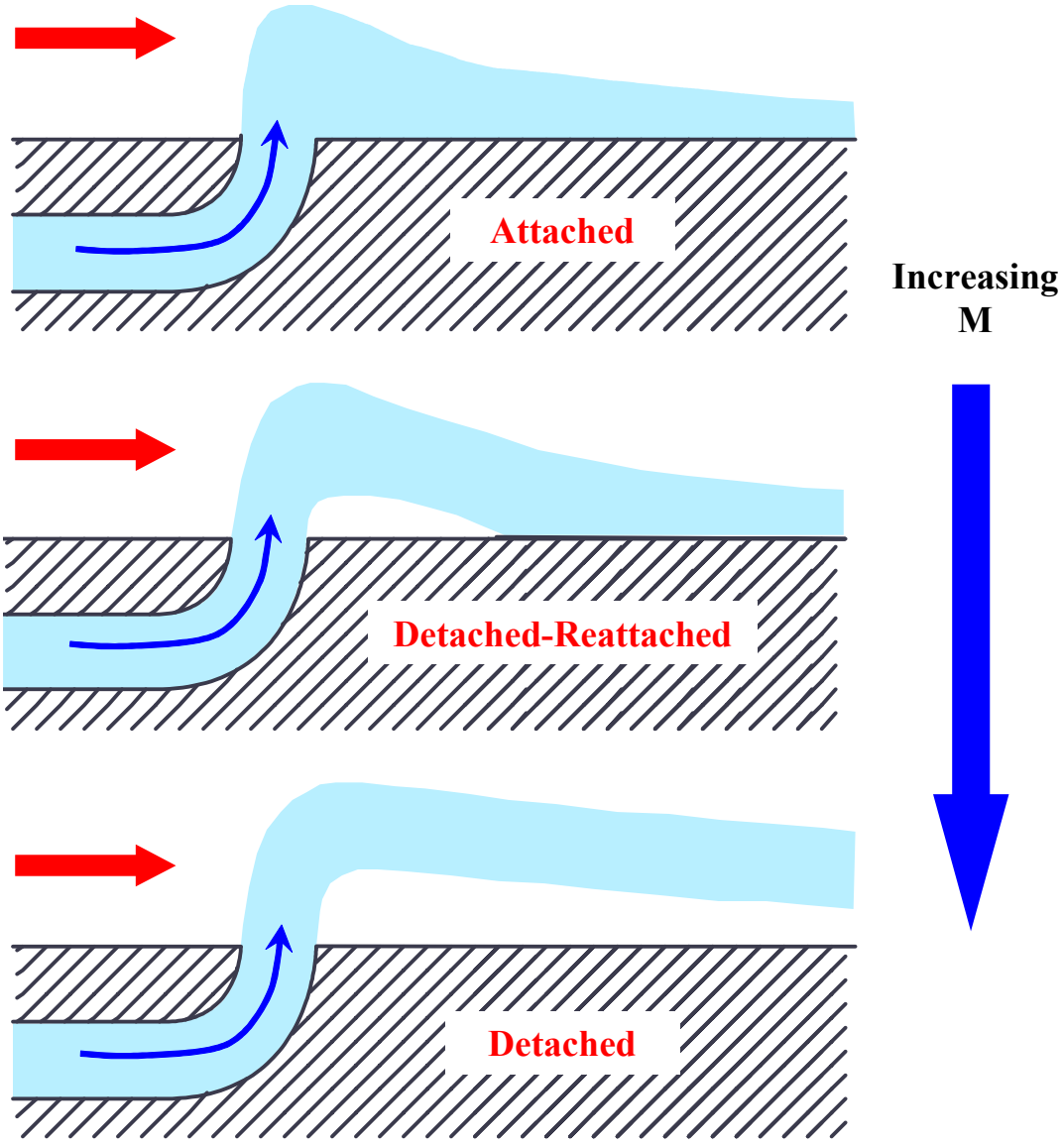

Figure 5-3 Three regimes of jet behavior upon cooling feature exit.

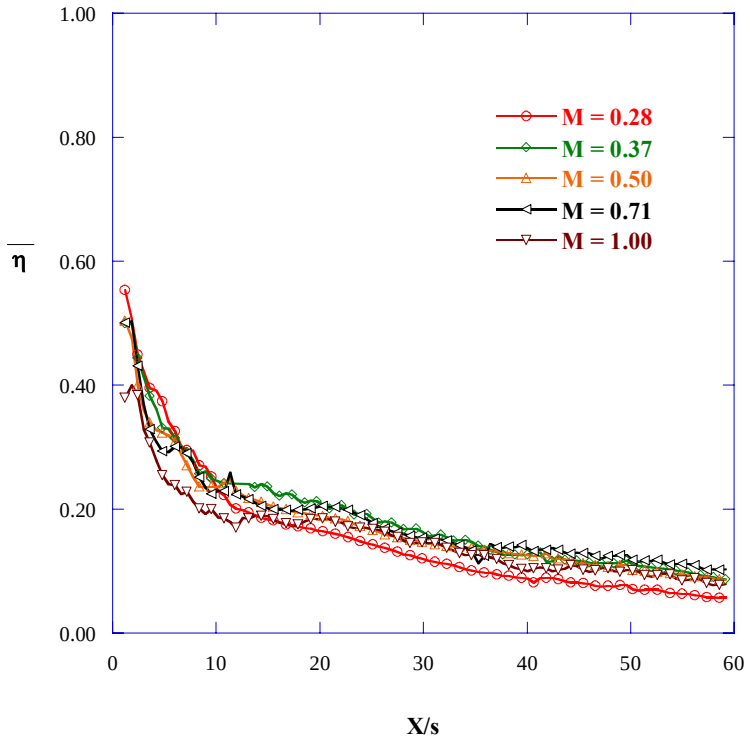

Figure 5-4 Spanwise averaged effectiveness versus X/s for all blowing ratios.

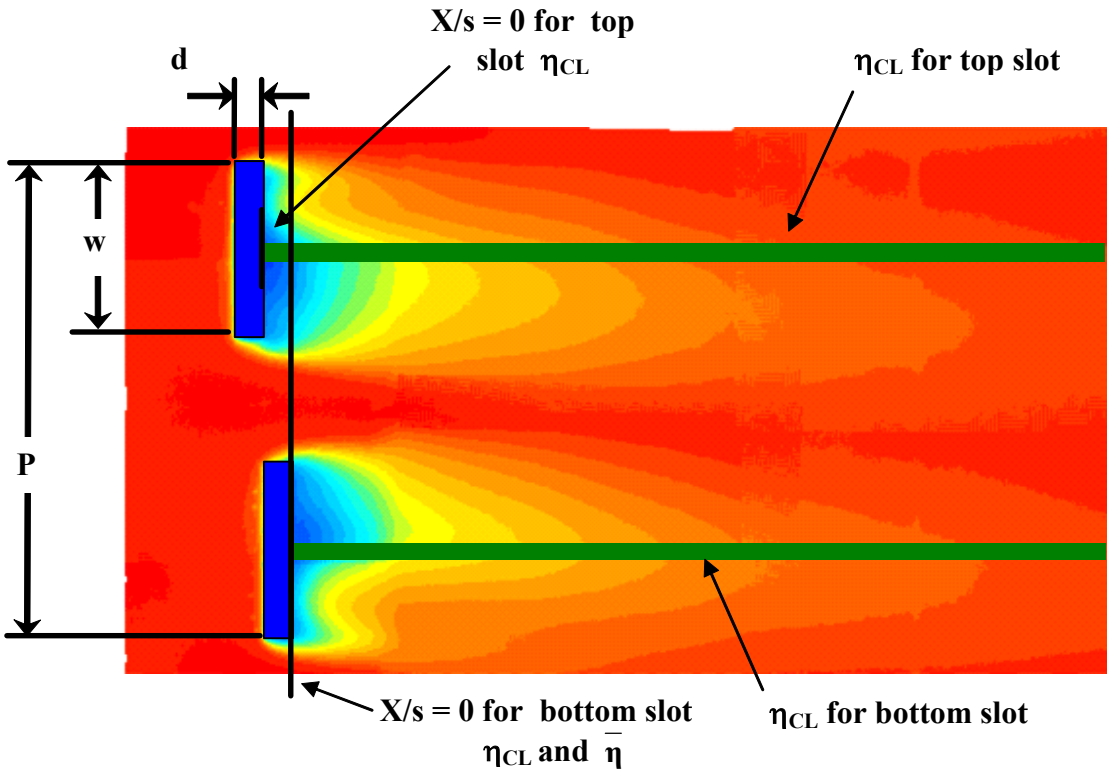

Figure 5-5 Schematic of slot region geometry and geometric parameters.

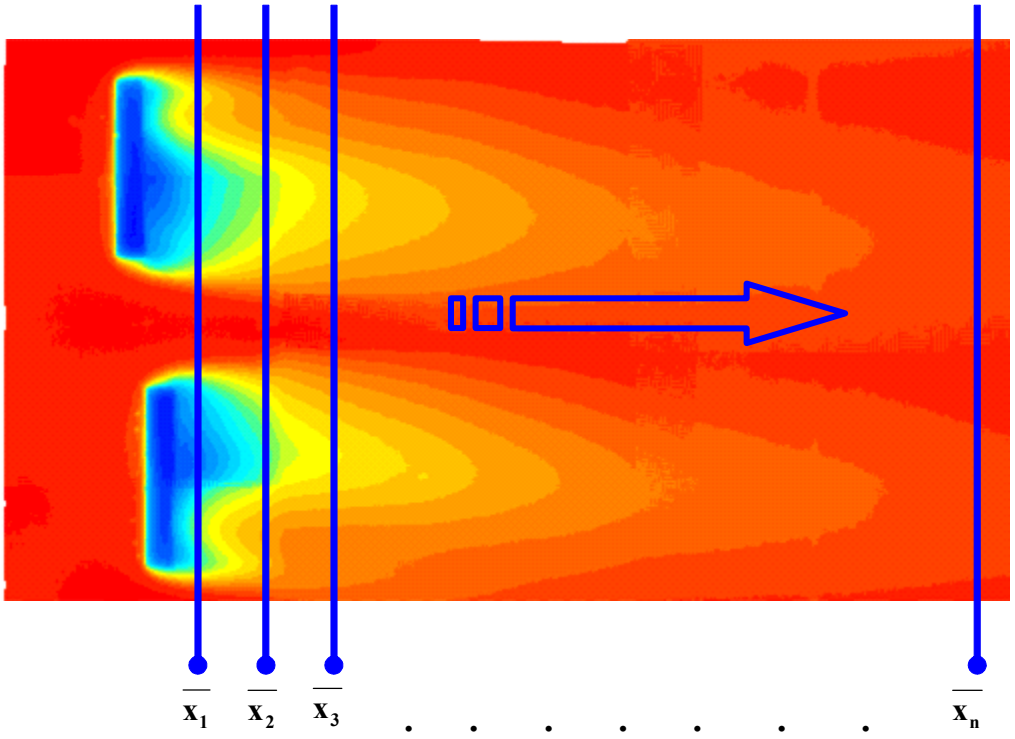

Figure 5-6 Schematic of spanwise averaging process.

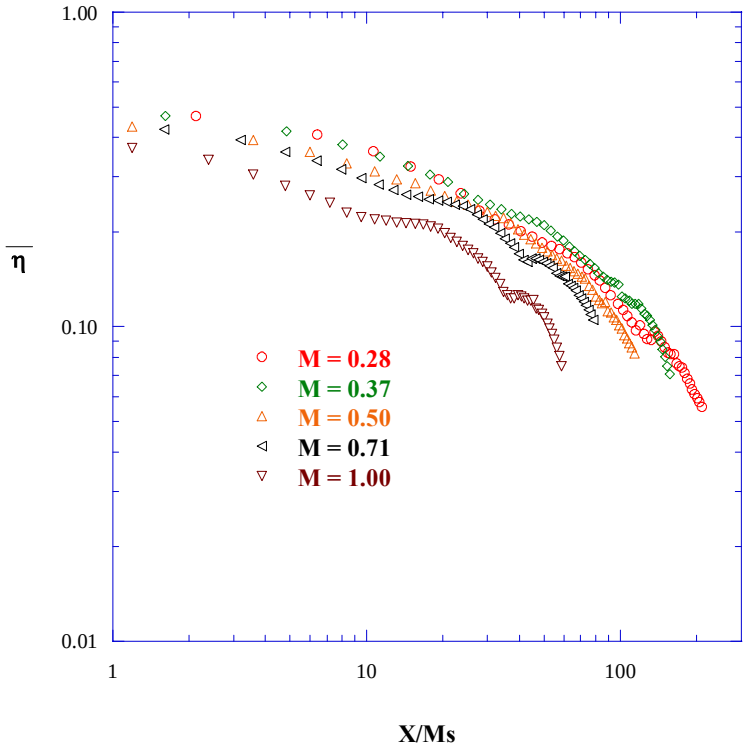

Figure 5-7 Spanwise averaged effectiveness for all blowing ratios versus X/Ms. The two lower blowing ratios nearly collapse to a single curve, indicating they cool to their maximum potential.

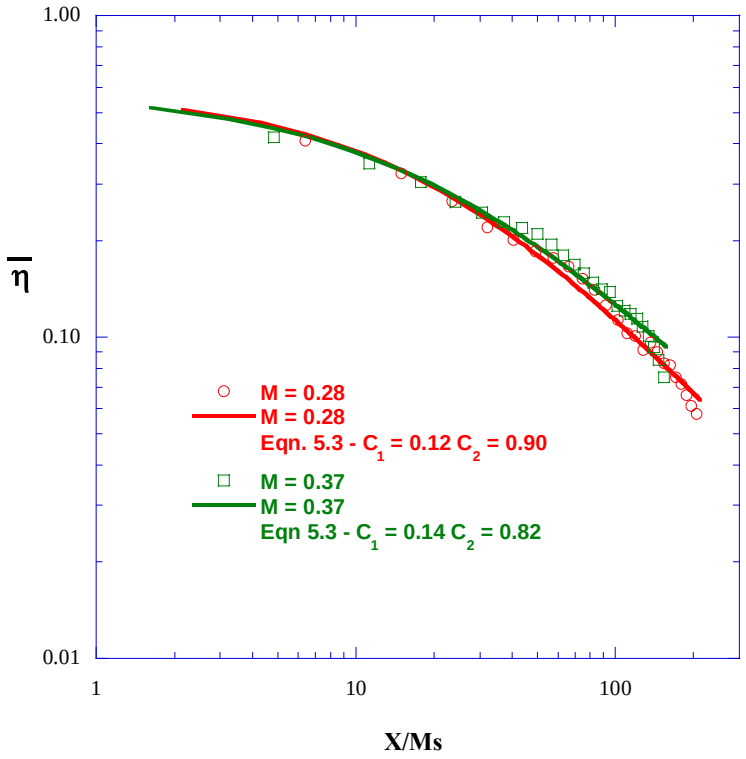

Figure 5-8 Spanwise averaged effectiveness versus X/Ms for attached blowing ratios. showing curve fits. Curve fits provided by Pratt & Whitney [Cunha, 2004]

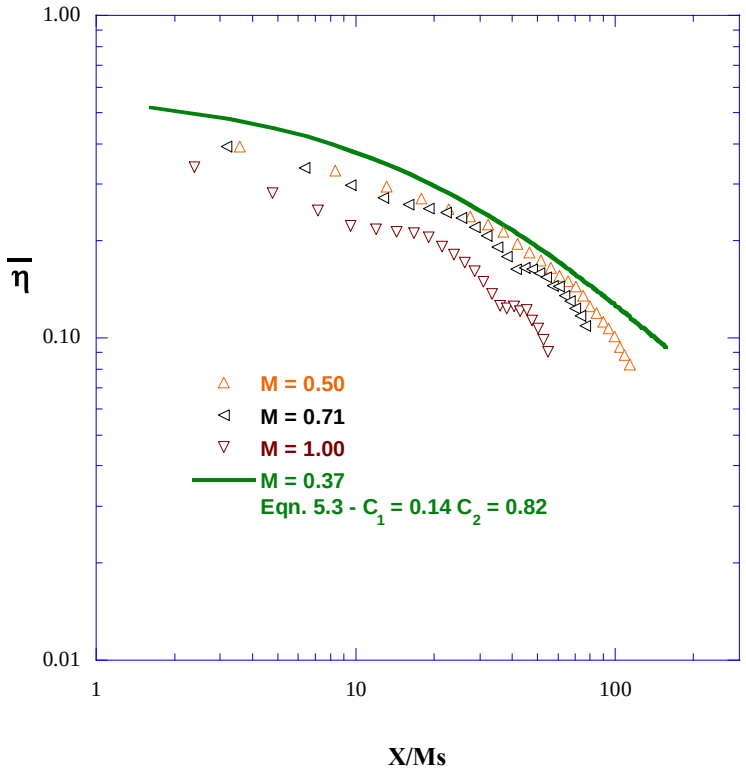

Figure 5-9 Spanwise averaged effectiveness for versus X/Ms for detached blowing ratios showing curve fit for M = 0.37. Curve fit courtesy of Pratt & Whitney [Cunha, 2004].

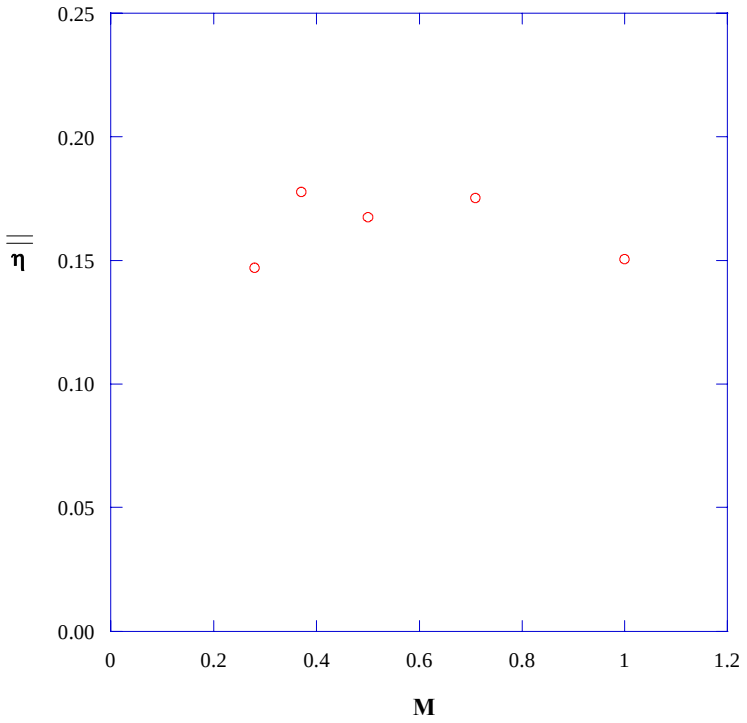

Figure 5-10 Area averaged effectiveness versus blowing ratio. The M = 0.37 blowing ratio provides the best area averaged cooling and does not separate from the wall. Area averaging takes place from X/s = 0 at the downstream edge of the downstream slot to X/s = 60 and across the span of one periodic microcircuit.

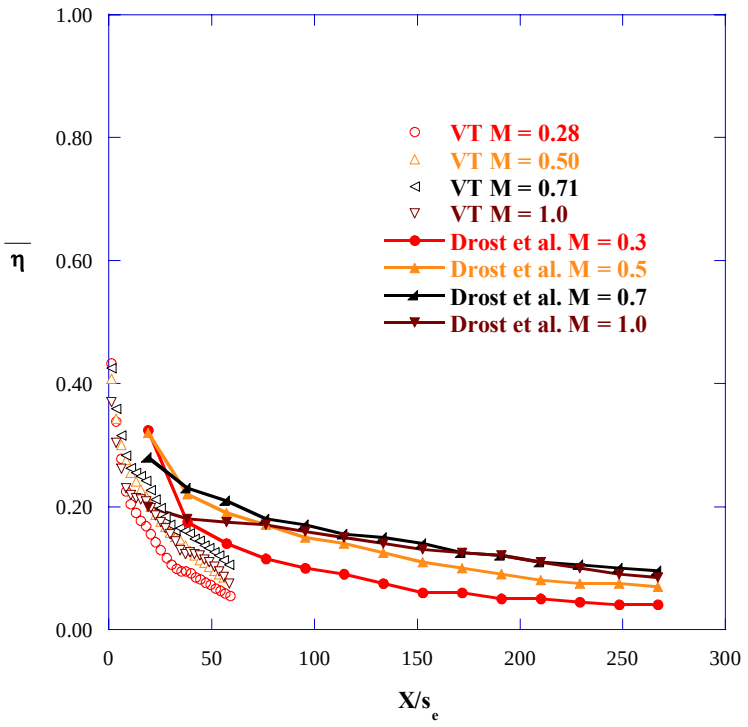

Figure 5-11 Spanwise averaged effectiveness compared to Drost et al. [1997]. While the cooling magnitudes between the current study and Drost et al. [1997] do not match, the trends between blowing ratios do, except for the M = 1.0 cases. Drost et al. [1997] data for the highest blowing ratio cools the downstream region better since the cooling holes are inclined in the streamwise direction.

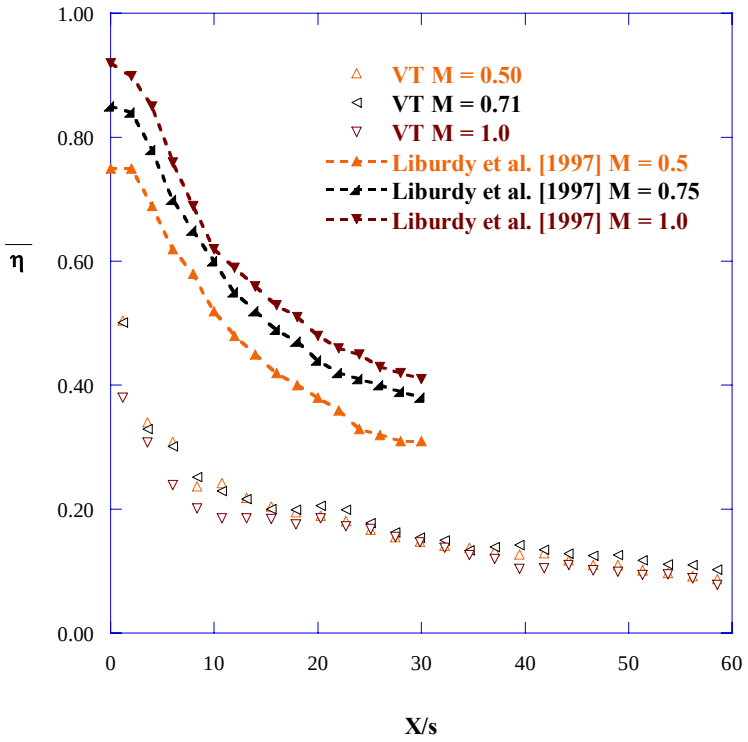

Figure 5-12 Spanwise averaged effectiveness compared to Liburdy et al. [1997]. Streamwise averaged data from the current study does not compare well to data from Liburdy et al. [1997] because the current study uses 2-D staggered slots as opposed to a continuous inclined slot.

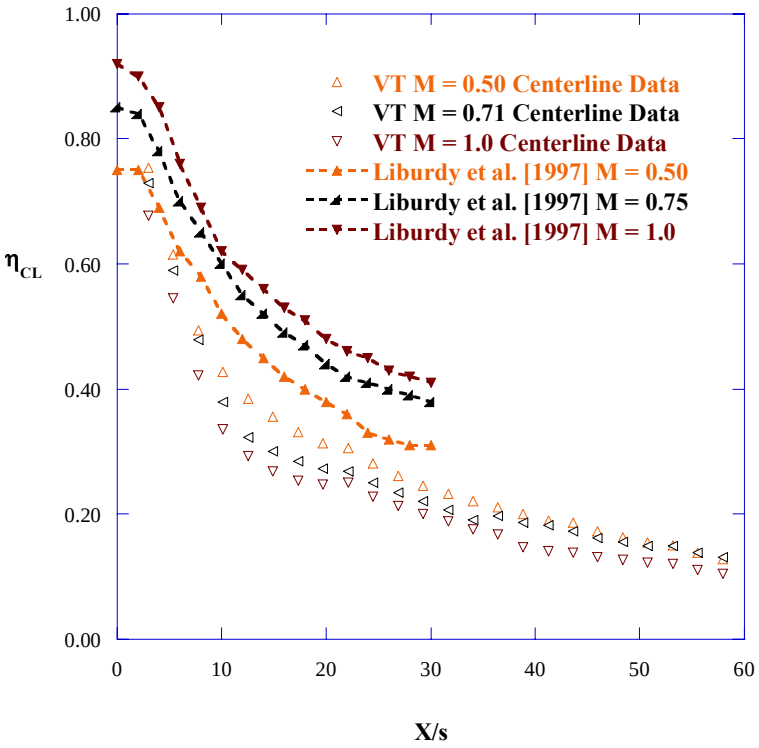

Figure 5-13 Centerline effectiveness compared to Liburdy et al. [1997]. Centerline effectiveness better compares to Liburdy et al. [1997] data since the effects of averaging uncooled regions are removed.

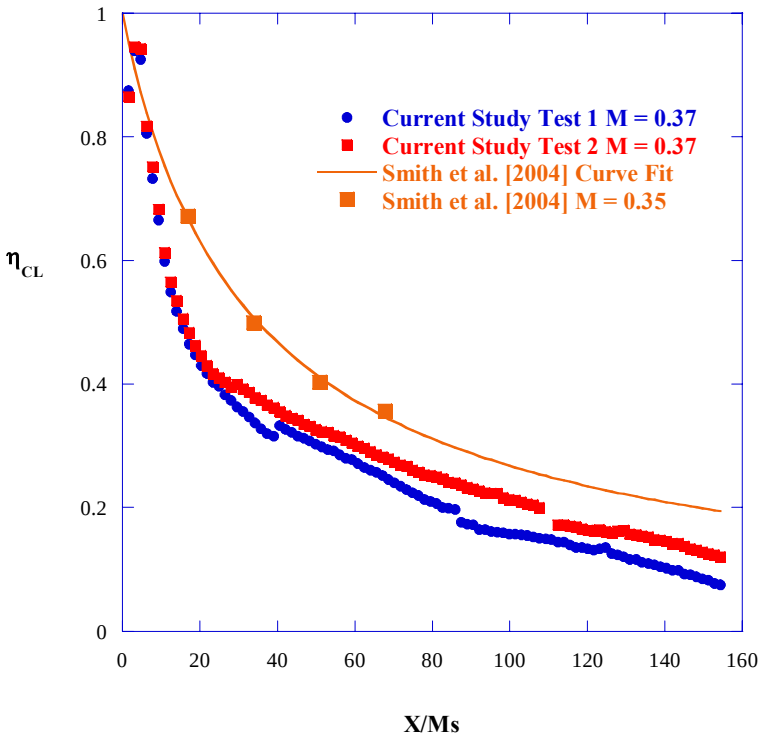

Figure 5-14 Centerline effectiveness compared to Smith et al. [2004]. The slot geometry tested by Smith et al. [2004] is identical to the current study except there are no microcircuit features upstream of the cooling slot exits.

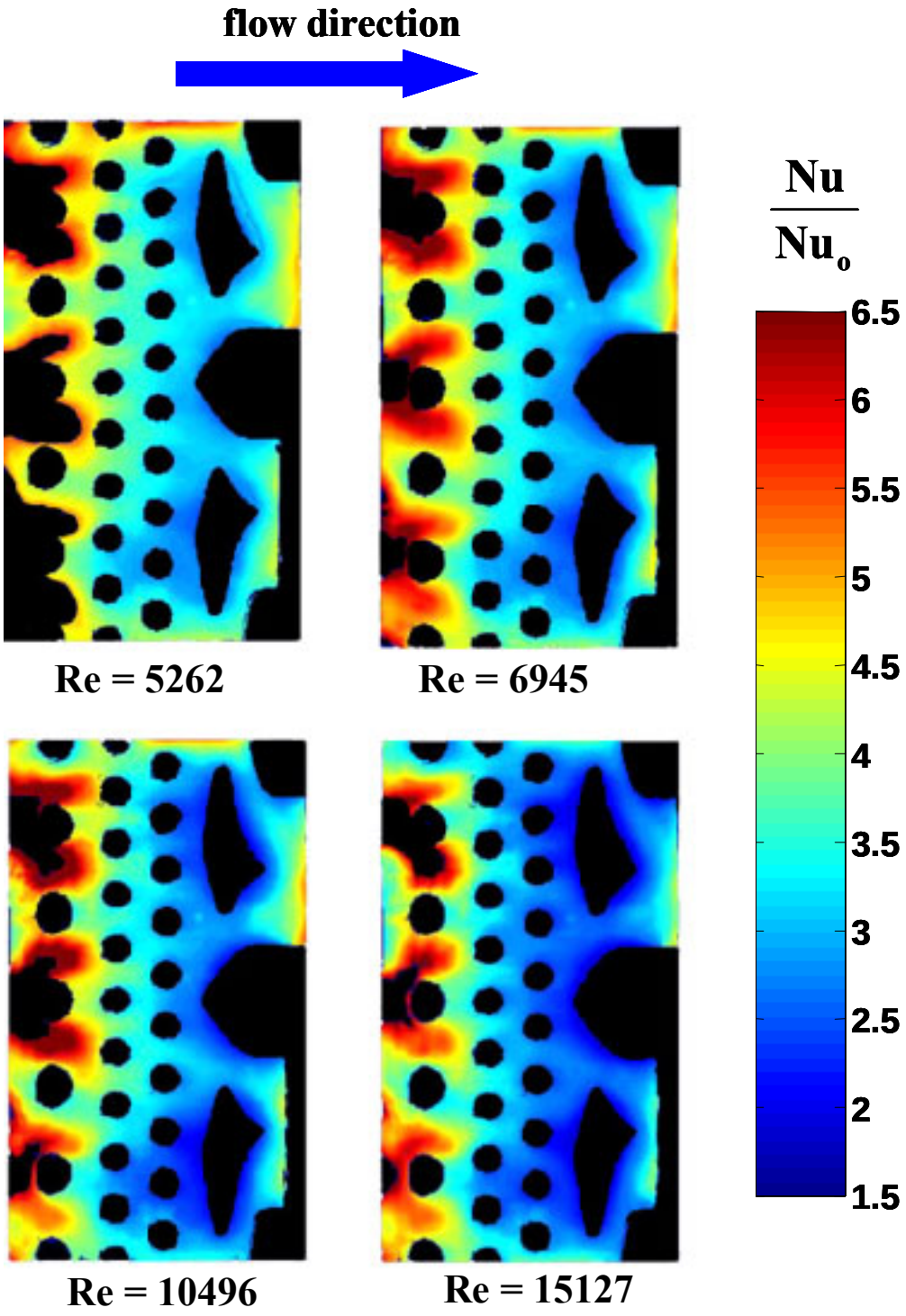

Figure 5-15 Heat transfer augmentation contours for the four tested Reynolds numbers. Black regions indicate the absence of data, either due to the presence of a pedestal feature or the inability to resolve the high heat transfer coefficients in the impingement region

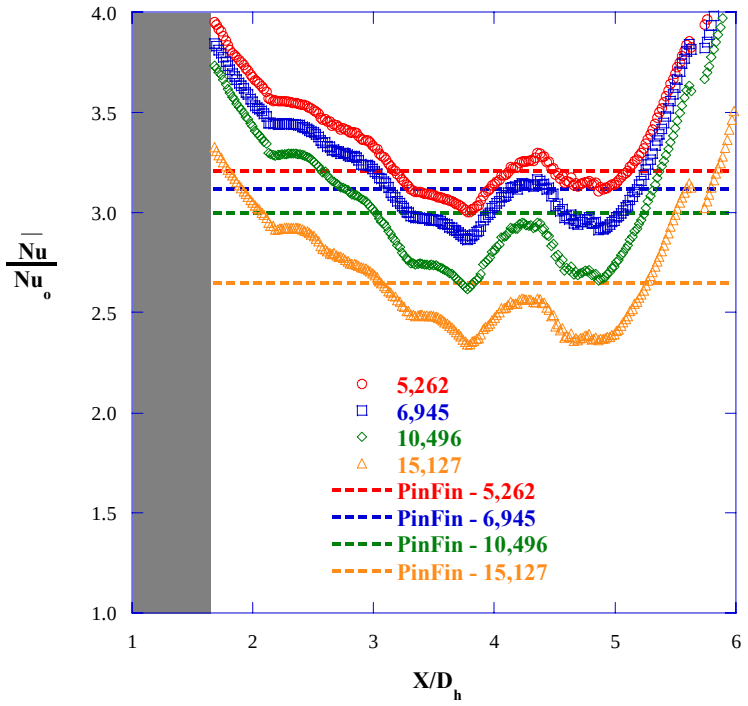

Figure 5-16 Spanwise averaged heat transfer augmentation for all Reynolds numbers. The gray strip indicates the impingement region, where spanwise averaging did not take place. The dashed lines indicate PinFin predictions.

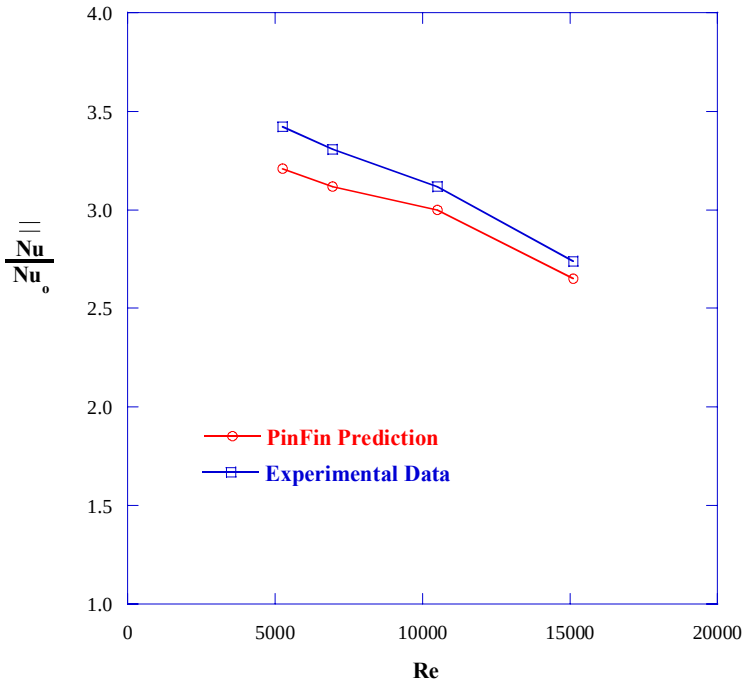

Figure 5-17 Area averaged heat transfer augmentation versus Reynolds number. Augmentation decreases with increasing Reynolds number. PinFin predictions are shown as well.

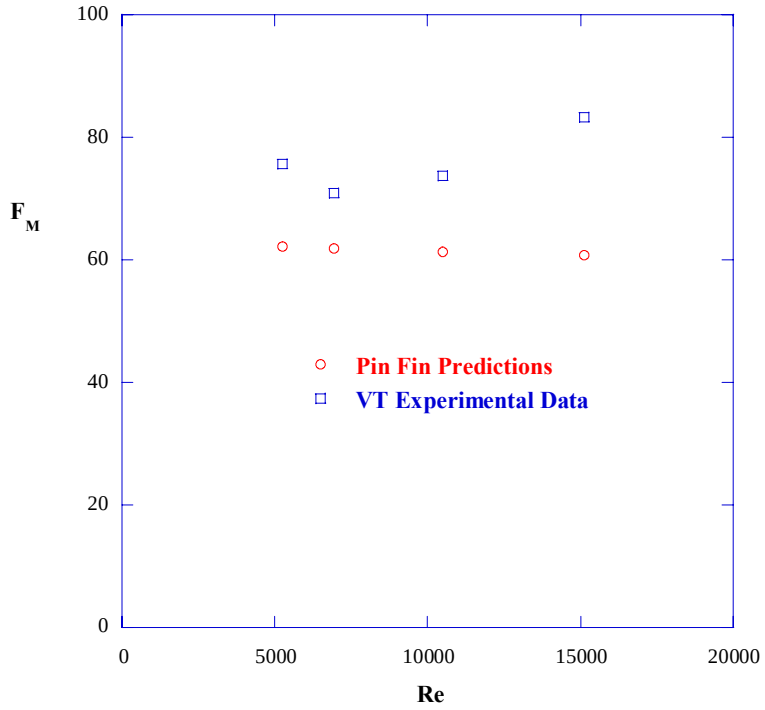

Figure 5-18 Experimentally measured Friction Multiplier compared to predictions from PinFin. Given the geometric differences between the models, the data agrees quite well. When uncertainties are accounted for, the experimental data is Reynolds number independent.

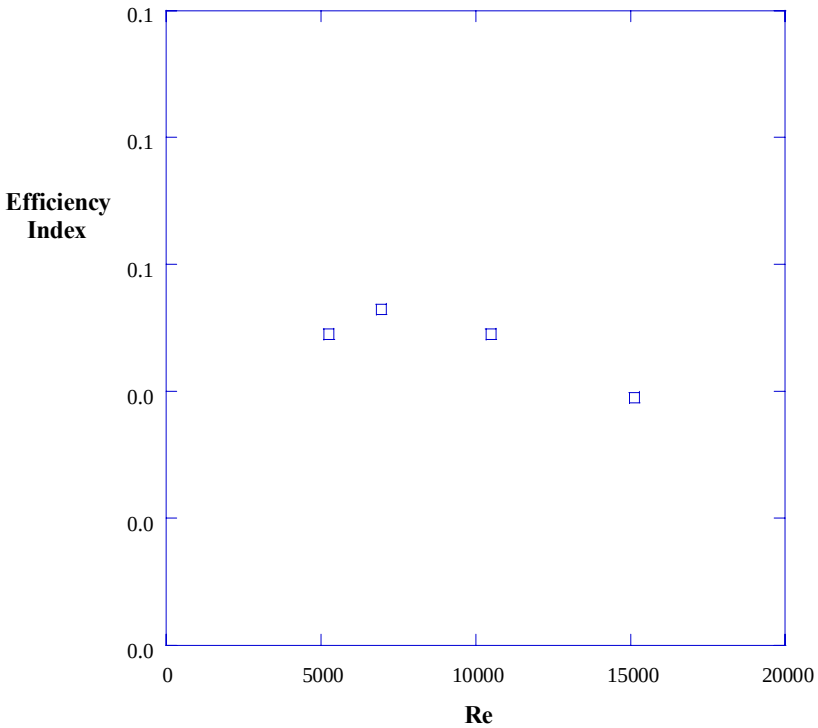

Figure 5-19 Efficiency Index for current study. Friction factor is based on bulk velocity in the microcircuit.

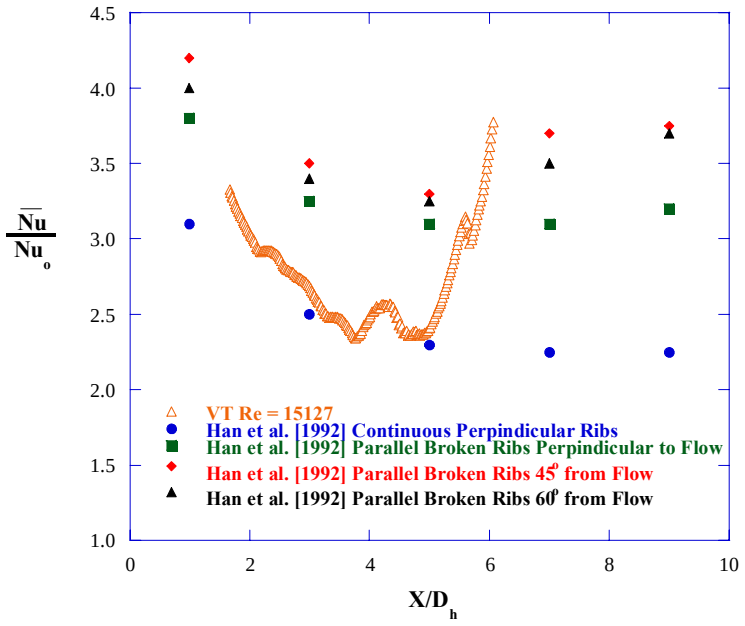

Figure 5-20 Spanwise averaged heat transfer augmentation compared to Han et al., [1992]. Data from the current study includes the impingement region since the data presented by Han et al. [1992] includes a thermal entry region.

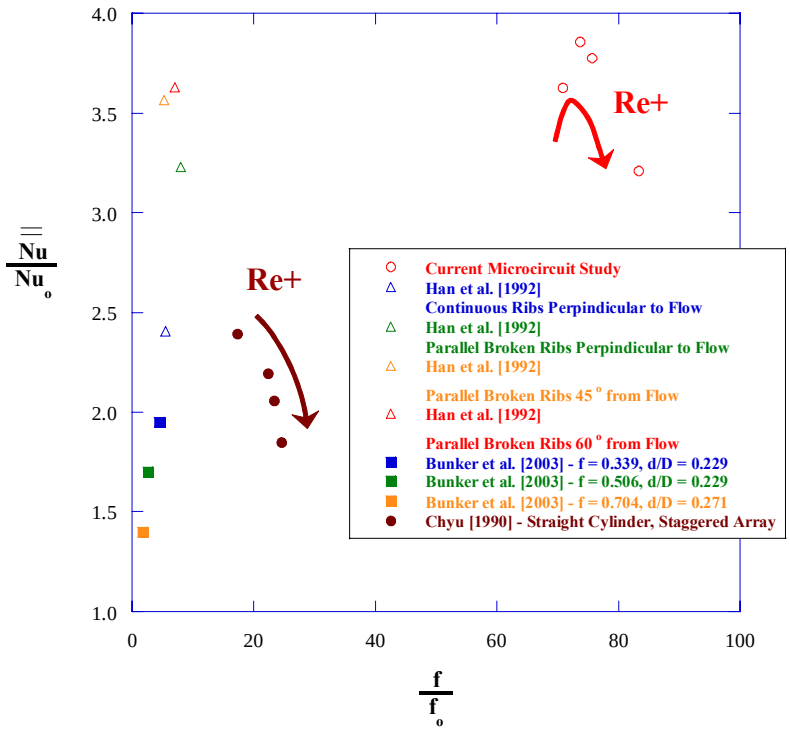

Figure 5-21 Heat transfer augmentation versus friction factor augmentation for four different studies. All friction factors are based on bulk velocity in the respective channels. Data from Chyu [1990] and the current study represent a single configuration at multiple Reynolds numbers. Data from the other two studies, Han et al. [1992] and Bunker et al. [2003], represent different configurations at single Reynolds numbers. Clearly, the microcircuit design provides the highest heat transfer augmentation, but also incurs the largest friction penalty.

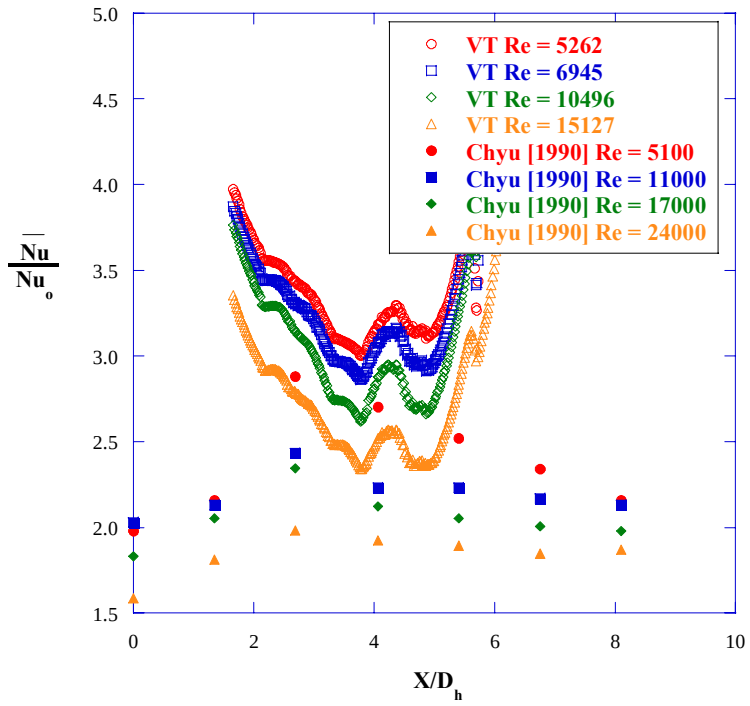

Figure 5-22 Spanwise averaged heat transfer augmentation compared to Chyu [1990].

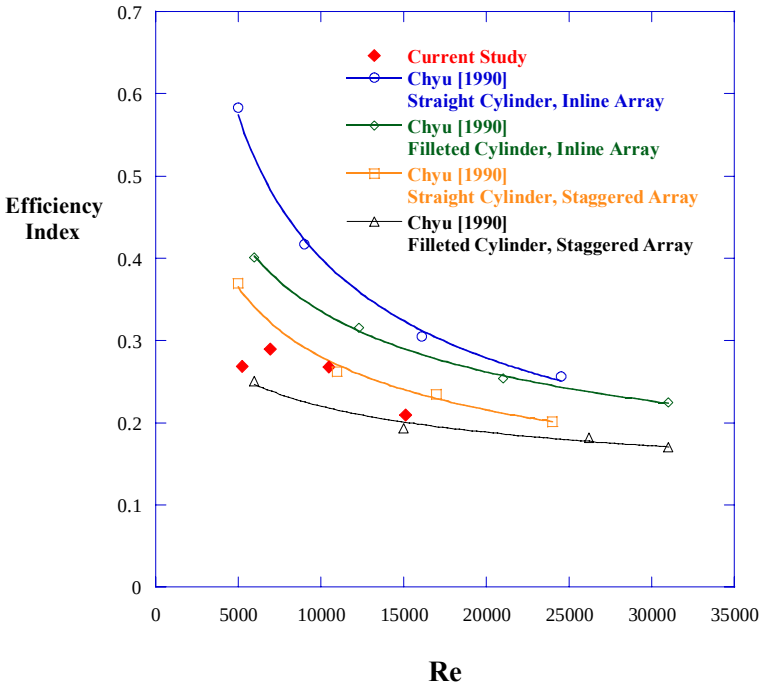

Figure 5-23 Efficiency Index compared to Chyu [1990]. Note, measured friction factors are based on maximum channel velocity and baseline friction factors are defined as D'arcy friction factors. Friction data from Chyu [1990] was adjusted to allow direct comparison to the current study.

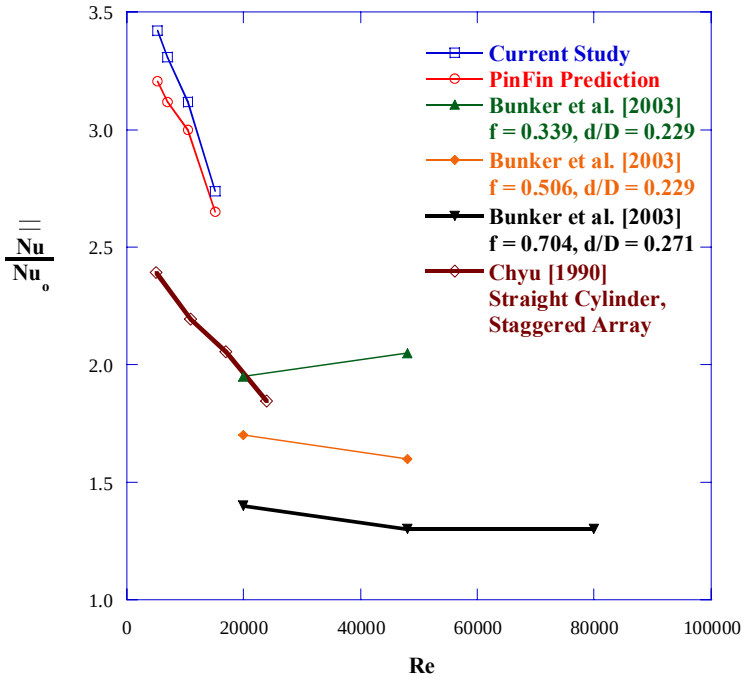

Figure 5-24 Area averaged heat transfer augmentation for six different cooling schemes. All but one of the Bunker et al. [2003] configurations show decreasing area averaged augmentation with increasing Reynolds number.

Chapter 6
Conclusions

This study has reviewed the investigation of a microcircuit cooling feature designed for use in the mainbody skin of a turbine airfoil. Specifically, the study resolved internal heat transfer coefficients and external adiabatic film effectiveness results. In addition to evaluating the magnitude of the microcircuit's cooling performance, this study outlines the interaction between the two individual cooling schemes. There are few papers that even remotely match the geometry for either the internal or external tests completed in this study, and no papers that match both simultaneously. There have been several microcircuit publications, but none with this specific microcircuit geometry. An entirely new test facility was constructed to provide access to the dual measurement planes required by this study. We calibrated the new facility and performed baseline testing to match the literature. This chapter will briefly summarize the results discussed in the previous chapter and draw conclusions in the first section. The following, and final, section will make recommendations for future testing.

6.1 Overview of Results

This section will summarize the experimental results of this study. External adiabatic effectiveness conclusions will be discussed first, followed by internal heat transfer augmentation conclusions.

External testing showed that the microcircuit slot exits were most certainly affected by the internal pedestal arrangement. Adiabatic effectiveness distributions were consistently skewed toward one side of the slot. The observed non-uniformity was consistent across all five of the tested mass flux ratios. All of the blowing ratios showed extensive cooling in the near slot region, with coolant performance degrading with downstream distance. Based upon area averaged effectiveness results, the M = 0.37

blowing ratio outperformed both higher and lower coolant blowing ratios. The peaked performance was attributed to minimal coolant lift-off for this blowing ratio.

Based upon spanwise averaged adiabatic effectiveness plotted versus X/Ms, the detrimental effects of severe coolant liftoff were observed in blowing ratios as low as M = 0.50. This was low when compared to the literature, but expected due to the normal injection angle of the coolant slots relative to slots with inclined injection configurations. Perhaps an inclined slot would have better served both aerodynamic and durability needs. Less coolant interaction with the mainstream would result in fewer aerodynamic losses around the airfoil, lower heat transfer coefficients in the vicinity of the airfoil wall, and higher levels of adiabatic effectiveness downstream of the coolant slots.

The flow split around the final set of pedestal features within the microcircuit was uneven and resulted in skewed distributions of adiabatic effectiveness on the external wall. The non-uniform distribution was due to mismatched flow areas around the final pedestal features. The flow area around the outer side of the large, irregular pedestal features (submarines) was smaller than the flow area around the inner side of the features. The area mismatch allowed more flow to travel around the inner side of the feature, thus crowding the flow to one side of the microcircuit exit slots. The uneven flow resulted in the non-uniform effectiveness distributions.

The heat transfer augmentation observed in the microcircuit was exceptional. Impingement regions near the microcircuit inlets achieved Nusselt numbers 6.5 times those observed in an unobstructed straight channel. Downstream of the impingement region, the microcircuit augmentation levels remained near 3. Microcircuit testing took place at four engine representative Reynolds numbers. Heat transfer augmentation slightly decreased with increasing Reynolds number.

Experiments showed large augmentations in frictional losses across the microcircuit. Friction factors were augmented by factors as high as 80. This indicated that the microcircuit incurred 80 times the frictional losses of an unobstructed channel. While these results sound extremely high, they were only nominally worse than standard pin fin arrays. Efficiency Index values (heat transfer augmentation divided by the friction augmentation) calculated for the current geometry compared to published pin fin studies.

6.2 Recommendations for Future Testing

There are several different avenues that future research could follow. The test facility created for this study is extremely versatile and could conceivably test any microcircuit configuration imaginable. Results suggest that the microcircuit exit flow is sensitive to the metering area of the flow passages upstream of the slot exits. A change in the 'submarine' pedestal features could split the flow evenly and create a more uniform slot exit flow. This would be beneficial to the external film flow, which is considered the first line of defense in protection of the blade.

In addition to changing the internal features of the microcircuit, the actual slot exit may merit attention as well. First, before any changes are made, I would suggest a detailed flow-field study of the slot exit jets. A solid understanding of the temperature and flow profiles leaving the slot will give a better picture of the lift-off phenomenon. Once that aspect is fully characterized, I would suggest varying the injection angle of the slot exits. It seems that a normal injection angle does not maximize the adiabatic effectiveness levels downstream. Additionally, the area downstream of the slot exit locations could accommodate additions to the test facility that could resolve NHFR on the wall. A NHFR study would help fully characterize the microcircuit performance as situated in a blade.

It would be interesting to test a larger segment of the airfoil as well. The test section constructed could accommodate several microcircuits in the streamwise direction. Depending on the intended streamwise spacing of the microcircuits, current adiabatic effectiveness levels may be exhausted before reaching the next streamwise set of microcircuits. A study with realistic microcircuit spacing would further help optimize design parameters such as coolant injection angle, blowing ratio, and microcircuit placing.

References

Armstrong, J., D. Winstanley, 1988, "A Review of Staggered Array Pin Fin Heat Transfer for Turbine Cooling Applications," *Journal of Turbomachinery*, **vol. 110**, pg. 94-103.

Bejan, A., 1995, "Convection Heat Transfer," 2nd Edition, New York, New York, John Wiley and Sons, Inc.

Boyle, R.J., 1984, "Heat Transfer in Serpentine Passages with Turbulence Promoters," ASME Paper No. 84-HT-24.

Brown, A., R. Mandjikas, J.M. Mudyiwa, 1980, "Blade Trailing Edge Heat Transfer," ASME Paper No. 80-GT-45.

Bunker, R.S., K.F. Donnellan, 2003, "Heat Transfer and Friction Factors for Flows Inside Circular Tubes with Concavity Surfaces." ASME Paper No. GT2003-38053.

Burggraf, F., 1970, "Experimental Heat Transfer and Pressure Drop with Two-Dimensional Turbulence Promoter Applied to Two Opposite Walls of a Square Tube," *Augmentation of Convective Heat and Mass Transfer*, New York, ASME, pg. 70-79.

Camci, C., K. Kim, 1992, "A New Hue Capturing Technique for the Quantitative Interpretation of Liquid Crystal Images Used in Convective Heat Transfer Studies", *Journal of Turbomachinery*, **vol. 114**, pg. 765-775.

Christophel, J.E, K.A. Thole, F.J. Cunha, 2003d, "Using a Microcircuit Design for Cooling the Tip of a Turbine Blade—Part 2: Internal and External Heat Transfer Measurements," submitted to the *Journal of Turbomachinery*.

Cunha, F.J., 2004, “PinFin,” Matlab Code for Pin Fin Array Analysis.

Cunha, F.J., 2004, Turbine Durability, Pratt & Whitney, personal correspondence.

Chyu, M.K., 1990, "Heat Transfer and Pressure Drop for Short Pin-Fin Arrays with Pin-Endwall Fillet," *Journal of Turbomachinery*, **vol. 112**, pg. 926-932.

Chyu, M.K., Y.C. Hsing, T.I.-P. Shih, V. Natarajan, 1999, "Heat Transfer Contributions of Pins and Endwall in Pin-Fin Arrays: Effects of Thermal Boundary Condition Modeling," *Journal of Turbomachinery*, **vol. 121**, pg. 257-263.

Chyu, M.K., Y.C. Hsing, V. Natarajan, 1998, "Convective Heat Transfer of Cubic Fin Arrays in a Narrow Channel," *Journal of Turbomachinery*, **vol. 120**, pg. 362-367.

Couch, E.L., 2003, "Measurements of Cooling Effectiveness Along the Tip of a Turbine Blade," Master's Thesis, Department of Mechanical Engineering, Virginia Polytechnic Institute and State University.

Douglass, C.J., J.S. Kapat, E. Divo, A.J. Kassab, 2003, "Steady Thermochromic Liquid Crystal Technique for Study of Conjugate heat Transfer Problems," ASME Paper No, GT2003-38587.

Drost, U., A. Bölcs, A. Hoffs, 1997, "Utilization of the Transient Liquid Crystal Technique for Film Cooling Effectiveness and Heat Transfer Investigations on a Flat Plate and a Turbine Airfoil," ASME Paper No. 97-GT-26.

Edwards, Steve, 2002, Electronics Engineer at Aerospace Engineering Electronics Shop, Personal correspondance, as documented in Couch [2003].

Elder, E., 2005 Master's Thesis, Department of Mechanical Engineering, Virginia Polytechnic Institute and State University.

Goldstein, 1971, “Film Cooling,” *Advances in Heat Transfer*, **vol. 7**, pg. 321-379.

Goldstein, R.E., E. Eckert, F. Burggraf, 1974, " Effects of Hole Geometry and Density on Three-Dimensional Film Cooling," *International Journal of Heat and Mass Transfer*, **vol. 17**, pg. 595-607.

Hall W.B., 1962, "Heat Transfer in Channels Having Rough and Smooth Surfaces," Journal of Mechanical Engineering Science, **vol. 4**, pg. 287-291.

Han J.C., Y.S. Kim, S.C. Lau, 1985, "Effects of Pin Configuration and Entrance Length on Local Endwall Heat/Mass Transfer in a Pin Fin Channel," ASME Paper No. 85-WA/HT-62.

Han, J.C., 1984, "Heat Transfer and Friction in Channels with Two Opposite Rib-Roughened Walls," *Journal of Heat Transfer*, **vol. 106**, pg. 774-781.

Han, J.C., S. Dutta, S. Ekkad, 2000, Gas Turbine Heat Transfer and Cooling Technology," New York, New York, Taylor & Francis.

Han, J.C., Y.M. Zhang, 1992, "High Performance Heat Transfer Ducts with Parallel Broken and V-Shaped Broken Ribs," *International Journal of Heat and Mass Transfer*, **vol. 35 no. 2**, pg. 513-523

Hohlfeld, E.M., 2003, "Film Cooling Predictions Along the Tip and Platform of a Turbine Blade," Master's Thesis, Department of Mechanical Engineering, Virginia Polytechnic Institute and State University.

Holman J.P., 1994, "Experimental Methods for Engineers," 6th Edition, New York, New York, McGraw-Hill, Inc.

Incropera F.P., D.P. DeWitt, 1996, "Fundamentals of Heat and Mass Transfer," 4th Edition, New York, New York, John Wiley and Sons, Inc.

Kays, W.M., M.E. Crawford, 1980, "Convective Heat and Mass Transfer," New York, New York, McGraw-Hill.

Knost, D., "Film Cooling Predictions and Measurements of Film-Cooling on the Endwall of a First Stage Vane," Master's Thesis, Department of Mechanical Engineering, Virginia Polytechnic Institute and State University.

Liburdy, J.A., J.P. Farmer, D.J. Seager, 1997, "The Effect of Shaping Inclined Slots on Film Cooling Effectiveness and Heat Transfer Coefficient," ASME Paper No. 97-GT-339.

Long, John, 2002, Buildings and Ground Supervisor at Virginia Tech Physical Plant Department, Personal correspondance, as documented in Couch [2003].

Lyman, A.C., 2000, "Spatially Resolved Heat Transfer Studies in Louvered Fins for Compact Heat Exchangers," Master's Thesis, Department of Mechanical Engineering, Virginia Polytechnic Institute and State University.

Mahmood, G.I., M.L. Hill, D.L. Nelson, P.M. Ligrani, H.-K. Moon, G. Glezer, 2001, "Local Heat Transfer and Flow Structure on and Above a Dimpled Surface in a Channel," *Journal of Turbomachinery*, **vol. 123**, pg. 115-123.

Metzger, D.E., R.A. Berry, J.P. Bronson, 1982a, "Developing Heat Transfer in Rectangular Ducts With Staggered Arrays of Short Pin Fins," *Journal of Heat Transfer,* **vol. 104**, pg 700-706.

Metzger, D.E., R.P. Vedula, 1987, "Heat Transfer in Triangular Channels with Angled Roughness Ribs on Two Walls," *Exp. Heat Transfer*, **vol. 1**, pg. 31-44.

Metzger, D.E., R.T. Baltzer, D.I. Takeuchi, P.A. Kuenstler, 1972, "Heat Transfer to Film Cooled Combustion Liners," ASME Paper No. 72-WA/HT-32.

Metzger, D.E., S.W. Haley, 1982b, "Heat Transfer Experiments and Flow Visualization for Arrays of Short Pin Fins," ASME Paper No. 82-GT-138.

Metzger, D.E., W.B. Shepard, S.W. Haley, 1986, "Row Resolved Heat Transfer Variations in Pin-Fin Arrays Including Effects of Non-Uniform Arrays and Flow Convergence," ASME Paper No. 86-GT-132.

Munson B.R., D.F. Young, T.H. Okishi, 2002, "Fundamentals of Fluid Mechanics," 4th Edition, New York, New York, John Wiley and Sons, Inc.

Papell, S.S., 1960, "TN D-299," *NASA Tech. Note*.

Radomsky, R.W., Jr., 2000, "High Freestream Turbulence Studies on a Scaled-Up Stator Vane," Doctor of Philosophy Dissertation, Department of Mechanical Engineering, University of Wisconsin-Madison.

Ranson, W.W., 2004, "Adiabatic Effectiveness Measuremtents of Leakage Flows Near the Hub Region of Gas Turbine Engines," Master's Thesis, Department of Mechanical Engineering, Virginia Polytechnic Institute and State University.

Rhee, D.H, Y.S. Lee, H.H. Cho, 2002, "Film Cooling Effectiveness and Heat Transfer of Rectangular-Shaped Film Cooling Holes," ASME Paper No. GT-2002-30168.

Scesa, S., 1954, Doctor of Philosophy Thesis, University of California.

Sen, B., D.L. Schmidt, D.G. Bogard, "Film Cooling with Compound Angle Holes: Heat Transfer," *Journal of Turbomachinery*, **vol. 118**, pg. 800-806.

Smith, A. C., Hatchett, J. H., Nix, A. C., Ng, W. F., and Thole, K. A., "Effectiveness of Normal and Angled Slot Cooling," submitted to *Journal of Turbomachinery*, ASME Paper No. GT2004-53248.

Soechting, F.O., L'Ecuyer, M.R, 1985, "A Model for Correlating Flat Plate Film Cooling Effectiveness for Rows of Round Holes," *AGARD Propulsion & Energetics Panel*, pg. 19-1-19-12.

Taslim, M.E., S.D. Spring, 1987, "Friction Factors and Heat Transfer Coefficients in Turbulated Cooling Passages of Different Aspect Ratios, Part I: Experimental Results," *23rd AIAA/ASME/SAE/ASEE Joint Propulsion Conference*, San Diego, Paper No. AIAA-87-2009.

ThermaCAM P20 Operator's Manual, June 2002, FLIR Systems, Revision A.

Thole, K.A, G.A. Zess, 2001, "Computational Design and Experimental Evaluation of Using a Leading Edge Fillet on a Gas Turbine Vane," ASME Paper No. 2001-GT-404.

Thole, K.A., M. Gritsch, A. Shulz, S. Wittig, 1996b, "Transonic Film-Cooling Investigations: Effects of Hole Shapes and Orientations," ASME Paper No. 96-GT-222.

VanFossen, G.J., Jr., R.J. Simoneau, 1984, "Effect of Location in an Array on Heat Transfer to a Short Cylinder in Crossflow," *Journal of Heat Transfer*, **vol. 106**, pg. 42-48.

Wieghardt, K., 1946, "Hot Air Discharge for De-icing," *AAF Translation F-Ts 919-Re, August 1946, Wright Field*. Original in Deutsche Luftfahrtforschung: Über das Ausblasen von Warmluft für Enteiser, Forschungsberict Nr. 1900, Zentrale für Wissenschaftliches Berichtswesen, 1943.

Wittig, S., G. Bittlinger, A. Shulz, 1994, "Film Cooling Effectiveness and Heat Transfer Coefficients for Slot Injection at High Blowing Ratios," ASME Paper No. 94-GT-182

Wittig, S., J. Dittmar, A. Shulz, 2002, "Assessment of Various Film Cooling Configurations Including Shaped and Compound Angle Holes Based on Large Scale Experiments," ASME Paper No. GT-2002-30176.

Zukauskas, A., 1972, "Heat Transfer from Tubes in Crossflow," *Advances in Heat Transfer*, **vol. 8**, pg. 93-160.

Appendix A: Test Facility Scaling Study

As mentioned in Chapter 3, to correctly size the test facility, an appropriate microcircuit scale was first necessary. The facilities design, size and component selection all depended heavily on the selected scale of the microcircuit test piece. There were several dimensions critical to the scaling analysis. Microcircuit channel height, and the corresponding metal wall thickness, was the most important variable considered by the scaling study.

The channel height dictated the wall thickness and microcircuit footprint area. If the scale were too large, the area required to accommodate a periodic, three microcircuit array would result in an excessively large external test section. The external test section could not be so large that readily available blowers could not push enough air to achieve the required velocities. If the scale were too small, the wall thickness would be too thin to allow the adiabatic assumption used for the low thermal conductivity material that made up the walls.

Ultimately, a scale of 25X resulted in reasonable mainstream sizing while still allowing the adiabatic assumption. Table A-1 is a summary of the major variables and results of the scaling study for the three best potential scales. Eight possible scales were examined.

Table A-1 Test Facility Scaling Study

Scale	P&W		VTExCCL - Internal			VTExCCL - External			
	Engine	16.66667	15	25	35	15	25	35	x
Mass Flux Ratio - M	**0.4**	**0.4**	**0.6151**	**0.3690**	**0.2636**	**1.00**	**1.00**	**1.00**	
Cooling Slot Width - d	0.0381	0.635	0.572	0.953	1.334	0.572	0.953	1.334	cm
Vane Wall Thickness - t	0.0381	0.635	0.572	0.953	1.334	0.572	0.953	1.334	cm
Slot Length - w	0.2540	4.233	3.810	6.350	8.890	3.810	6.350	8.890	cm
Channel Height - h	0.0381	0.635	0.572	0.953	1.334	0.572	0.953	1.334	cm
Total Test Section Height - Spanwise	0.00	60.00	50.00	90.00	120.00	50.00	90.00	120.00	cm
MC Length Streamwise	1.09	18.17	16.35	27.25	38.15	16.35	27.25	38.15	cm
Streamwise Slot Lead Distance	2.86	47.63	42.86	71.44	100.01	42.86	71.44	100.01	cm
Post Slot Effectiveness Region - Streamwise	3.81	63.50	57.15	95.25	133.35	57.15	95.25	133.35	cm
Total Test Section Length - Streamwise	6.67	111.13	100.01	166.69	233.36	100.01	166.69	233.36	cm
(Pratt and Whitney) $Re_{channel}$	15000	15000	15000	15000	15000	15000	15000	15000	
Average Channel Velocity - $U_{channel}$	595.13	35.71	39.68	23.81	17.00	64.51	64.51	64.51	m/sec
Total Microcircuit Array Mass Flowrate	0.00061	0.01012	0.00936	0.01560	0.02184	0.01522	0.04228	0.08287	kg/sec
Single Slot Area - A_s	0.00000	0.00027	0.00022	0.00060	0.00119	0.00022	0.00060	0.00119	m^2
Average Single Slot Velocity- U_{ss}	**86.89**	**5.21**	**5.95**	**3.57**	**2.55**	**9.68**	**9.68**	**9.68**	**m/sec**
Average Mainstream Velocity - U_m	**224.49**	**13.47**	**10.00**	**10.00**	**10.00**	**10.00**	**10.00**	**10.00**	**m/sec**
Mainstream Depth - D	0.0100	0.1700	0.1500	0.2600	0.3600	0.1500	0.2600	0.3600	m
Mainstream Height - H	0.0120	0.2005	0.5000	0.9000	1.2000	0.5000	0.9000	1.2000	m
Mainstream Flow Area - A_m	0.0001	0.0341	0.0750	0.2340	0.4320	0.0750	0.2340	0.4320	m^2
Mainstream Volume Flowrate - Q_m	**57**	**973**	**1589**	**4958**	**9153**	**1589**	**4958**	**9153**	**cfm**
% BL height to Mainstrem depth	**0.23**	**0.22**	**0.25**	**0.21**	**0.20**	**0.25**	**0.21**	**0.20**	**%**
Total Pressure Losses - P_{loss}	804023.40	933.73	536.45	477.32	476.46	537.21	478.04	477.35	Pa
Total Pressure Losses - P_{loss}	3227.99	3.75	2.15	1.92	1.91	2.16	1.92	1.92	in H_2O
Adjusted blower sizing P_{loss}	**3938.15**	**4.57**	**2.63**	**2.34**	**2.33**	**2.63**	**2.34**	**2.34**	**in H_2O**
Required MC Plenum Total Pressure	**4415.28**	**8.02**	**20.00**	**8.10**	**4.88**	**49.95**	**17.74**	**17.74**	**in H_2O**

Appendix B: Mainstream Component Datasheets

DIRECT DRIVE RATING TABLES
for 100% wheel widths

CFM and BHP at Static Pressure Shown • Ratings at 70°F., .075 Density, Sea Level

MODEL NO.	RPM	WHEEL TYPE	1" SP CFM	1" SP BHP	2" SP CFM	2" SP BHP	3" SP CFM	3" SP BHP	4" SP CFM	4" SP BHP	5" SP CFM	5" SP BHP	6" SP CFM	6" SP BHP
SQAF-180	1150	HDAF	2300■	.49										
		SQAF	2794■	.67										
	1750	HDAF	4353■	1.47	3720■	1.67	2986■	1.74						
		SQAF	5161	2.19	4466	2.31	3776	2.42						
	3500	HDAF	9618	10.36	9310	10.81	9002	11.26	8707	11.75	8413	12.24	8119	12.73
		SQAF	11277	16.40	10965	16.79	10653	17.18	10322	17.50	9973	17.74	9623	17.98
SQAF-200	1150	HDAF	3260■	.74										
		SQAF	3900■	1.03										
	1750	HDAF	5855	2.26	5201	2.56	4429	2.72						
		SQAF	6935	3.42	6173	3.58	5426	3.75	4656	3.85				
	3500	HDAF	12726	16.25	12389	16.84	12051	17.44	11717	18.04	11396	18.69	11074	19.34
SQAF-220	1150	HDAF	4874	1.28										
		SQAF	6275	2.15	4994	2.22								
	1750	HDAF	8487	3.95	7681	4.39	6811	4.72	5844	4.87				
		SQAF	10461	7.14	9786	7.51	9037	7.71	8170	7.77	7259	7.83		
SQAF-240	1150	HDAF	6803■	2.00										
		SQAF	8658	3.45	7320	3.58								
	1750	HDAF	11509	6.24	10637	6.88	9715	7.38	8739	7.77	7634	7.90		
		SQAF	14138	11.45	13433	12.07	12612	12.34	11750	12.55	10783	12.63	9775	12.71
SQAF-270	1150	HDAF	10921	4.17	9508	4.62								
		SQAF	12632	5.60	11289	6.09	9626	6.16						
	1750	HDAF	17833	13.68	16919	14.45	15960	15.18	15013	15.88	14151	16.49	13226	17.03
		SQAF	20343	18.61	19492	19.46	18623	20.25	17739	20.99	16805	21.61	15632	21.68
SQAF-300	1150	HDAF	15354	6.90	13734	7.55	12269	8.11						
		SQAF	17573	9.23	16098	9.92	14395	10.32	12345	10.32				
	1750	HDAF	24700	22.87	23685	23.96	22646	25.01	21575	25.99	20535	26.94	19577	27.78
		SQAF	27985	30.99	27041	32.15	26097	33.31	25118	34.32	24137	35.33	23138	36.29

MODEL NO.	RPM	WHEEL TYPE	7" SP CFM	7" SP BHP	8" SP CFM	8" SP BHP	9" SP CFM	9" SP BHP	10" SP CFM	10" SP BHP	11" SP CFM	11" SP BHP	12" SP CFM	12" SP BHP
SQAF-180	3500	HDAF	7787	13.06	7440	13.33	7093	13.60	6728	13.75	6356	13.85	5973	13.93
		SQAF	9273	18.22	8933	18.48	8593	18.74	8253	19.00	7904	19.18	7552	19.34
SQAF-200	3500	HDAF	10752	20.00	10403	20.50	10023	20.85	9642	21.21	9262	21.56	8858	21.72
SQAF-240	1750	SQAF	8228	12.35										
SQAF-270	1750	HDAF	11463	16.56										
		SQAF	14430	21.69	13164	21.59	10874	19.99						
SQAF-300	1750	HDAF	18619	28.63	17012	28.50	12653	24.71						
		SQAF	21837	36.38	20536	36.47	19154	36.38	17751	36.25	15052	33.77		

MODEL NO.	RPM	WHEEL TYPE	13" SP CFM	13" SP BHP	14" SP CFM	14" SP BHP	15" SP CFM	15" SP BHP	16" SP CFM	16" SP BHP
SQAF-180	3500	HDAF	5529	13.88						
		SQAF	7199	19.49	6821	19.56	6414	19.54	6007	19.51
SQAF-200	3500	HDAF	8451	21.86	8043	21.99	7576	21.97	7089	21.91

■ See page 17 for minimum motor frame sizes regardless of BHP.

Performance shown is for installation type B-Free inlet, Ducted outlet.
Performance ratings do not include the effects of appurtenances in the airstream.

Tinted ratings are with Class III wheels.
All other ratings are with Class II wheels.

Figure B-1 Performance table for mainstream blower, a SQAF-180 with a HDAF Wheel.

Super Radiator Coils

Dry Water Coil
Copyright (c) 2003
by Super Radiator Coils

Customer:	Virginia Tech	Date:	8/5/2003
Job Ref.:	Air Heating	By:	Jeff Spaeth
Job Item:		Record:	

Dry Water Coil	**Units (Eng.)**	
AirSide:		
Air Flow	Lb/Hr Dry Air	18576
Required Capacity	BTUH	12300
Entering Air Temp.	°F	165.83
Required Air Temp.	°F	167
Airside Pressure	PSIA	14.696

Tubeside:		
Fluid ID		WATER
Fluid Flow Rate	GPM	16.39
Entering Fluid Temp.	°F	180

Coil Selection:		
Model Number		35x35-4R-12/120
Die Surface		1/2 - 1-1/4 x 1.083 Stag.(Corr-#16)
Die Number & Location		16 (All Plants)
Face Area	Ft^2	20.25 4.5ftx4.5ft
Face Velocity	Ft/Min.	244
Number of Circuits		14
Tube Velocity	Ft/Sec.	2
Configuration		Thermal Counterflow
Tube Material		CU
Tube Wall Thickness	In.	0.016
Fin Material		AL
Fin Thickness	In.	0.0055
Header Diam.	In.	1.125

Capacity:		
Rating	BTUH	239,611
Leaving Air Temp.	°F	149.2
Leaving Fluid Temp.	°F	150.1
Fluid Press. Drop	Ft. H2O	4.4
Air Friction	In. H2O	0.26

Figure B-2 Radiator coil specifications, quoted by Jeff Spaeth of Super Radiator Coils.

Appendix C: Specific Contraction Geometry

The contraction used to accelerate the mainstream flow upstream of the test section was designed with a specific curve optimized for minimal pressure loss and engineered for uniform flow at its exit. The overall geometry was given in Chapter 3. This appendix documents the contraction's specific dimensions along its streamwise distance. Table C-1 gives the specific measurements of the contraction, while Figure C-1 illustrates the relevant measurements. Distances from the flow centerline to the walls are quoted in terms of distance along the contraction's curve, not in even increments along the centerline. This was done so any attempts at recreation will use adequately sized sheet metal, as the final curve distances (S_v and S_h) convey the sizes of the sheet metal before bending.

Table C-1 Contraction Dimensions

Vertical Contraction		Horizontal Contraction	
S_v (cm)	Y_v (cm)	S_h (cm)	Z_h (cm)
0.0	76.5	0.0	76.5
2.5	76.5	2.5	76.5
5.1	76.5	5.1	76.5
7.6	76.5	7.6	76.5
8.9	76.5	8.9	76.5
10.2	76.5	10.2	76.4
11.4	76.4	11.4	76.4
12.7	76.4	12.7	76.3
14.0	76.3	14.0	76.1
15.3	76.2	15.2	75.9
16.6	76.1	16.5	75.6
17.9	75.8	17.8	75.2
19.3	75.6	19.1	74.6
20.8	75.2	20.4	73.9
22.3	74.8	21.8	73.0
24.0	74.2	23.2	71.8
26.0	73.5	24.6	70.4
28.1	72.6	26.2	68.6
30.7	71.5	27.8	66.4
33.6	70.2	29.7	63.8
36.7	68.8	31.6	61.0
39.7	67.5	33.4	58.3
42.5	66.2	35.2	55.7
45.3	65.0	37.0	53.3
48.0	63.8	38.7	50.9
50.5	62.7	40.4	48.7
53.0	61.7	42.0	46.6
55.4	60.6	43.6	44.5
57.7	59.7	45.2	42.6
59.9	58.8	46.8	40.8
62.1	57.9	48.3	39.1
64.2	57.1	49.8	37.4
66.2	56.3	51.3	35.8
68.1	55.6	52.8	34.4
70.0	54.9	54.2	33.0
71.9	54.2	55.7	31.6
73.6	53.6	57.1	30.4
75.4	53.0	58.5	29.2
77.1	52.5	59.9	28.1
78.7	51.9	61.2	27.0
80.3	51.4	62.6	26.0
81.9	51.0	64.0	25.1
83.5	50.5	65.3	24.2
85.0	50.1	66.6	23.3
86.5	49.7	68.0	22.6
88.0	49.4	69.3	21.8
89.4	49.0	70.6	21.1
90.8	48.7	71.9	20.5
92.2	48.4	73.2	19.9
93.6	48.1	74.5	19.3
96.4	47.6	77.1	18.3
99.0	47.2	79.7	17.4
101.7	46.8	82.3	16.7
104.3	46.5	84.8	16.0
106.9	46.2	87.4	15.5
109.5	46.0	89.9	15.0
112.1	45.8	92.5	14.6
114.6	45.6	95.0	14.3
117.2	45.5	97.6	14.0
119.7	45.4	100.1	13.8
122.3	45.3	102.6	13.6
124.8	45.2	105.2	13.4
127.4	45.2	107.7	13.3
129.9	45.1	110.3	13.2
132.5	45.1	112.8	13.2
135.0	45.1	115.3	13.1
137.5	45.0	117.9	13.1
140.1	45.0	120.4	13.0
142.6	45.0	123.0	13.0
145.2	45.0	125.5	13.0
147.7	45.0	128.0	13.0
150.2	45.0	130.6	13.0
152.8	45.0	133.1	13.0
155.3	45.0	135.7	13.0
157.9	45.0	138.2	13.0
160.4	45.0	140.7	13.0
162.9	45.0	143.3	13.0
165.5	45.0	145.8	13.0
168.0	45.0	148.4	13.0

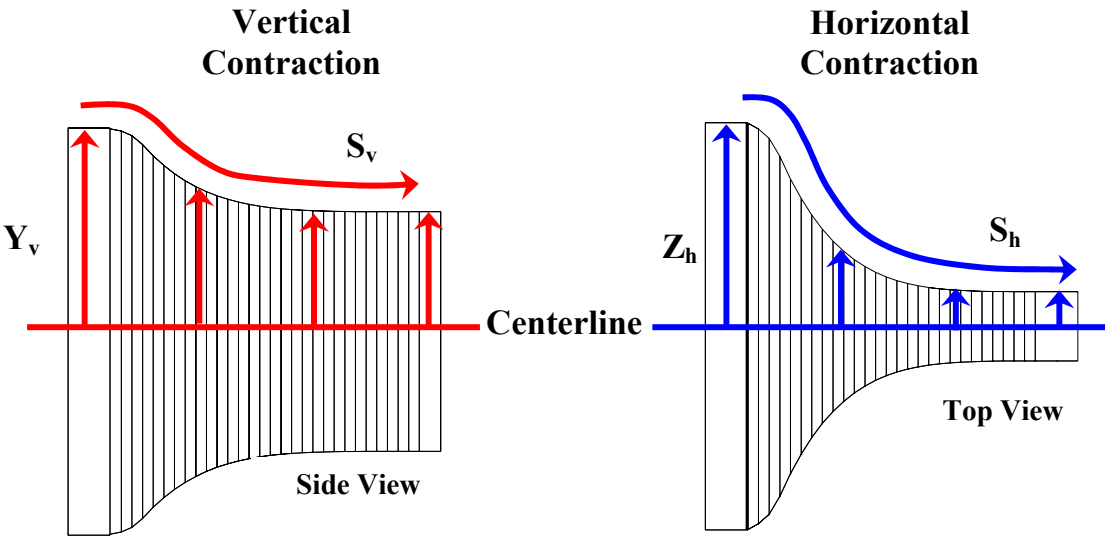

Figure C-1 Contraction dimension specifics

Appendix D: Venturi Flow-Meter Calibration Curve

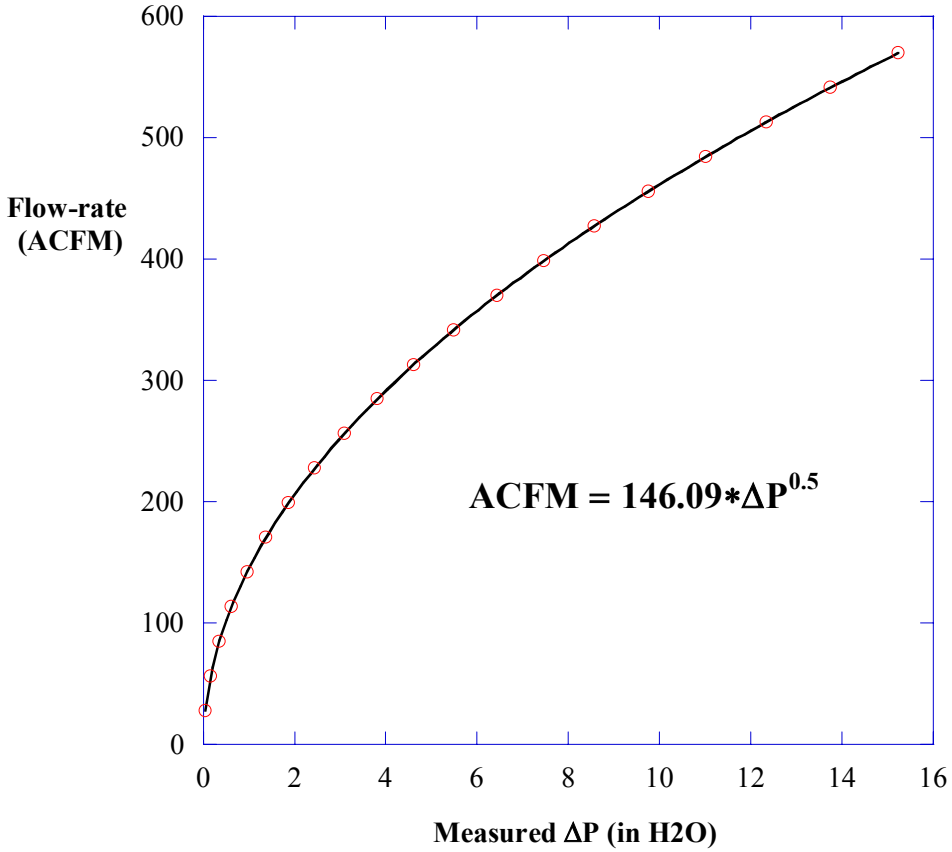

Figure D-1: Venturi flow-flow meter calibration curve. Note, this curve accounts for a average error of 6% found when this venturi was benchmarked versus a Laminar Flow Element.

Appendix E: Experimental Uncertainty Calculations

This appendix presents the uncertainty analysis for η, Nu, and f.

Uncertainty for Adiabatic Effectiveness, η

$$\eta = \frac{T_\infty - T_{AW}}{T_\infty - T_c} = \frac{\left[\frac{\eta_{o,\infty} \cdot T_c + T_\infty}{1+\eta_{o,\infty}} - T_{AW}\right]}{\left[\frac{\eta_{o,\infty} \cdot T_c + T_\infty}{1+\eta_{o,\infty}} - T_c\right]}$$

$$u_\eta = \sqrt{\left(\frac{\partial \eta}{\partial \eta_{o,\infty}} \cdot u_{\eta_{o,\infty}}\right)^2 + \left(\frac{\partial \eta}{\partial T_c} \cdot u_{T_c}\right)^2 + \left(\frac{\partial \eta}{\partial T_{AW}} \cdot u_{T_{AW}}\right)^2 + \left(\frac{\partial \eta}{\partial T_\infty} \cdot u_{T_\infty}\right)^2}$$

High Value of η

Variable	Value	Precision Uncertainty (°C)	Bias Uncertainty (°C)	Total Uncertainty
η	0.90	–	–	0.019 (2.1%)
T_{AW}	29.9	0.080	0.33	0.34
T_∞	59	–	–	0.2
T_c	27	–	–	0.2
$\eta_{o,\infty}$	0.125	–	–	0.05

Low Value of η

Variable	Value	Precision Uncertainty (°C)	Bias Uncertainty (°C)	Total Uncertainty
η	0.20	–	–	0.038 (18.9%)
T_{AW}	49.8	0.080	0.33	0.34
T_∞	50.7	–	–	0.2
T_c	27.9	–	–	0.2
$\eta_{o,\infty}$	0.125	–	–	0.05

Uncertainty for Nusselt Number

$$Nu = \frac{h \cdot D_h}{k} = \frac{q_{convection} \cdot D_h}{(T_{wall} - T_m) \cdot k} = \frac{(q_{total} - q_{conduction}) \cdot D_h}{(T_{wall} - T_m) \cdot k} = \frac{\left(\frac{V^2 \cdot R_h}{R_r^2 \cdot A_h} - \frac{T_{wall} - T_{amb}}{\frac{1}{h_{free}} + \frac{t_{glass}}{k_{glass}}} \right) \cdot D_h}{(T_{wall} - T_m) \cdot k}$$

$$u_{Nu} = \sqrt{\left(\frac{\partial Nu}{\partial V} \cdot u_V \right)^2 + \left(\frac{\partial Nu}{\partial R_h} \cdot u_{R_h} \right)^2 + \left(\frac{\partial Nu}{\partial R_r} \cdot u_{R_r} \right)^2 + \left(\frac{\partial Nu}{\partial A_h} \cdot u_{A_h} \right)^2 + \left(\frac{\partial Nu}{\partial T_{wall}} \cdot u_{T_{wall}} \right)^2 + \ldots \ldots + \left(\frac{\partial Nu}{\partial T_{amb}} \cdot u_{T_{amb}} \right)^2 + \left(\frac{\partial Nu}{\partial T_m} \cdot u_{T_m} \right)^2 + \left(\frac{\partial Nu}{\partial D_h} \cdot u_{D_h} \right)^2}$$

High Re, Low Local Nu

Variable	Value	Precision Uncertainty (°C)	Bias Uncertainty (°C)	Total Uncertainty
Nu	90	–	–	3.44 (3.8%)
V	4.1	–	–	0.01
R_h	1.13			0.01
R_r	1	–	–	0.01
A_h	0.027	–	–	3.E-05
T_{wall}	32	0.080	0.33	0.34
T_{amb}	24.7	–	–	0.2
T_m	24.7	–	–	0.2
D_h	0.02	–	–	3.E-05

High Re, High Local Nu

Variable	Value	Precision Uncertainty (°C)	Bias Uncertainty (°C)	Total Uncertainty
Nu	202.5	–	–	5.45 (2.7%)
V	7.3	–	–	0.01
R_h	1.13			0.01
R_r	1	–	–	0.01
A_h	0.027	–	–	3.E-05
T_{wall}	36	0.080	0.33	0.34
T_{amb}	24.7	–	–	0.2
T_m	24	–	–	0.2
D_h	0.02	–	–	3.E-05

Low Re, Low Local Nu

Variable	Value	Precision Uncertainty (°C)	Bias Uncertainty (°C)	Total Uncertainty
Nu	51.3	–	–	2.36 (4.6%)
V	3.4	–	–	0.01
R_h	1.13			0.01
R_r	1	–	–	0.01
A_h	0.027	–	–	3.E-05
T_{wall}	33	0.080	0.33	0.34
T_{amb}	24.7	–	–	0.2
T_m	24	–	–	0.2
D_h	0.02	–	–	3.E-05

Low Re, Low Local Nu

Variable	Value	Precision Uncertainty (°C)	Bias Uncertainty (°C)	Total Uncertainty
Nu	102.6	–	–	1.64 (1.6%)
V	4.0	–	–	0.01
R_h	1.13			0.01
R_r	1	–	–	0.01
A_h	0.027	–	–	3.E-05
T_{wall}	36	0.080	0.33	0.34
T_{amb}	24.7	–	–	0.2
T_m	24.7	–	–	0.2
D_h	0.02	–	–	3.E-05

Uncertainty for Friction Factor

$$f = \left(\frac{\Delta P_{static}}{\rho_{bulk}} + \frac{U_{bulk}^2 - U_{out}^2}{2} \right) \cdot \left(\frac{D_h}{X} \right) \cdot \left(\frac{2}{U_{bulk}^2} \right)$$

$$u_f = \sqrt{\left(\frac{\partial f}{\partial \Delta P_{static}} \cdot u_{\Delta P_{static}} \right)^2 + \left(\frac{\partial f}{\partial \rho_{bulk}} \cdot u_{\rho_{bulk}} \right)^2 + \left(\frac{\partial f}{\partial U_{bulk}} \cdot u_{U_{bulk}} \right)^2 + \ldots \ldots + \left(\frac{\partial f}{\partial U_{out}} \cdot u_{U_{out}} \right)^2 + \left(\frac{\partial f}{\partial D_h} \cdot u_{D_h} \right)^2 + \left(\frac{\partial f}{\partial X} \cdot u_x \right)^2}$$

High Value of f

Variable	Value	Precision Uncertainty (°C)	Bias Uncertainty (°C)	Total Uncertainty
f	2.96	–	–	0.229 (7.7%)
ΔP_{static} (Pa)	1.96	–	–	11
ρ_{bulk} (kg/m^3)	1.104			6.0E-03
U_{bulk} (m/s)	4.6	–	–	0.52
U_{out} (m/s)	8.0	–	–	0.52
D_h (m)	1.91E-02	0.080	0.33	1.2E-04
X (m)	1.07E-01	–	–	2.5E-04

Low Value of f

Variable	Value	Precision Uncertainty (°C)	Bias Uncertainty (°C)	Total Uncertainty
f	2.38	–	–	0.181 (7.6%)
ΔP_{static} (Pa)	1471.0	–	–	11
ρ_{bulk} (kg/m^3)	1.115			6.0E-03
U_{bulk} (m/s)	13.1	–	–	0.52
U_{out} (m/s)	22.9	–	–	0.52
D_h (m)	1.91E-02	0.080	0.33	1.2E-04
X (m)	1.07E-01	–	–	2.5E-04

Appendix F: Experimental Nusselt Number Contours

Nusselt number augmentation contours were presented in Chapter 5, this Appendix presents the contours of Nusselt number before they were normalized by the baseline Nusselt number at each Reynolds number.

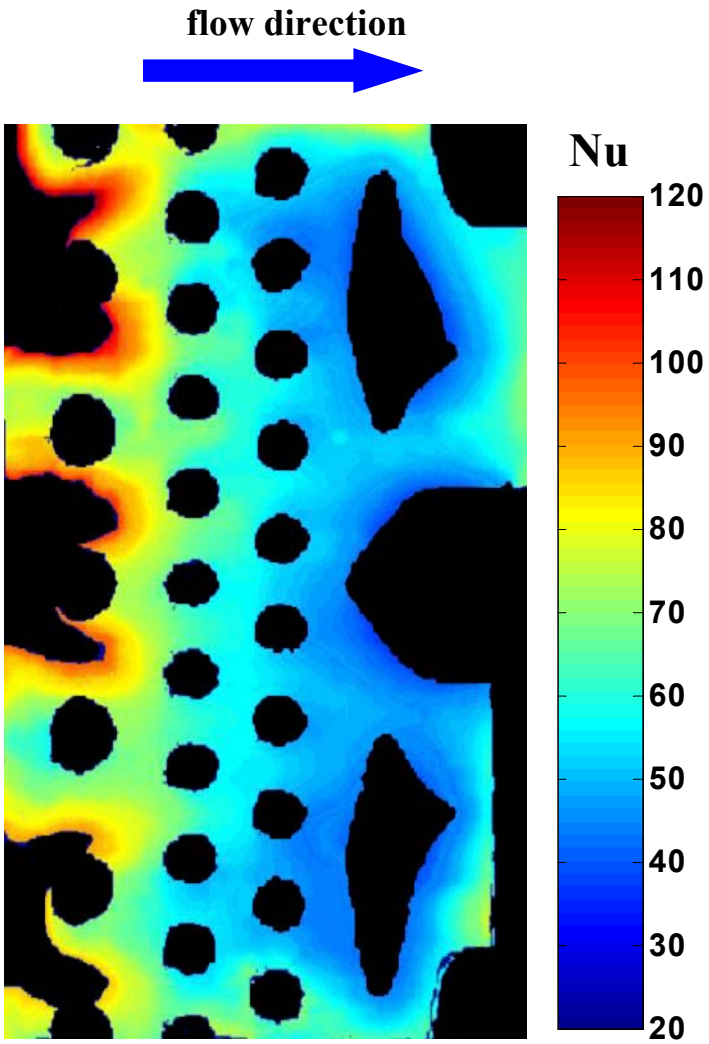

Figure F-1 Experimental Nusselt number contours for Re = 5262. Black regions indicate the absence of data, either due to the presence of a pedestal feature or the inability to resolve the high heat transfer coefficients in the impingement region

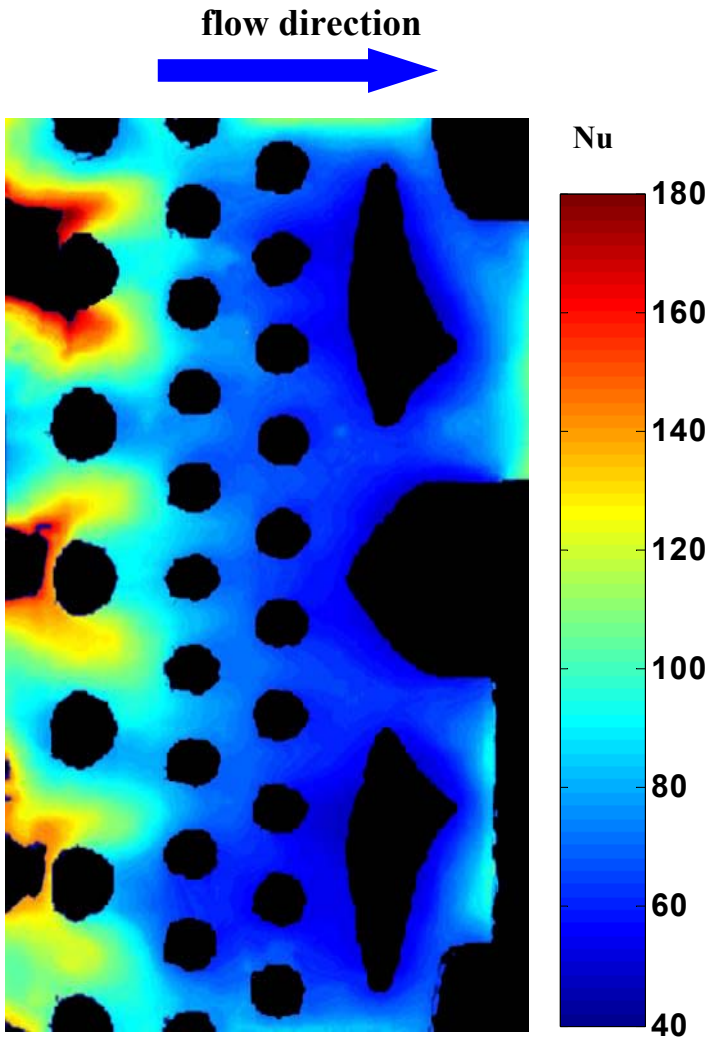

Figure F-2 Experimental Nusselt number contours for Re = 6945. Black regions indicate the absence of data, either due to the presence of a pedestal feature or the inability to resolve the high heat transfer coefficients in the impingement region.

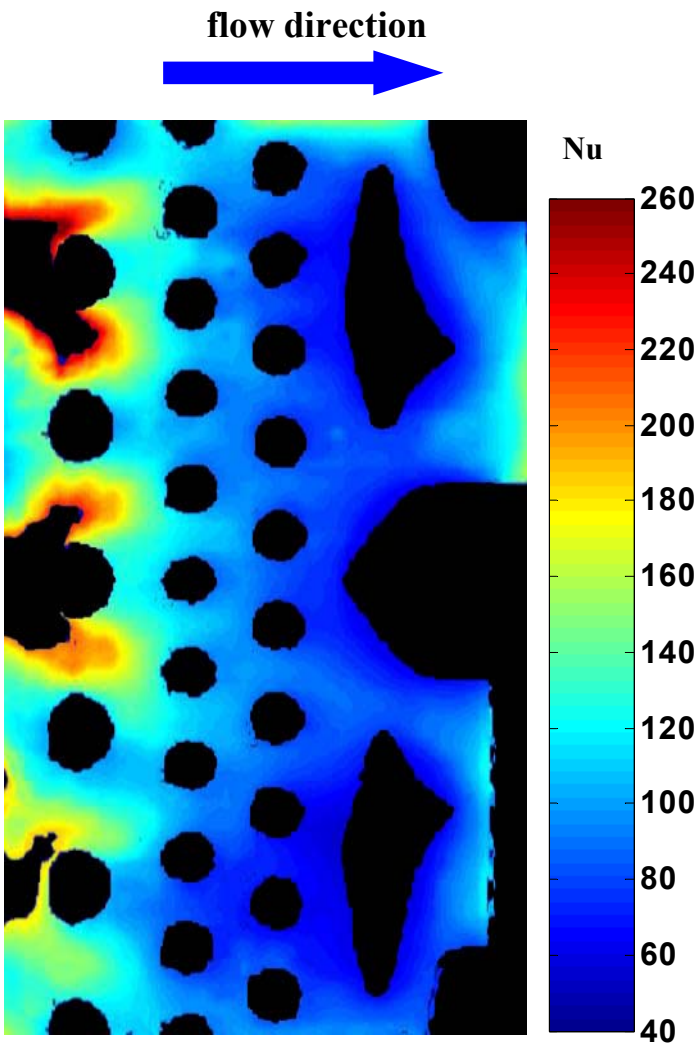

Figure F-3 Experimental Nusselt number contours for Re = 10496. Black regions indicate the absence of data, either due to the presence of a pedestal feature or the inability to resolve the high heat transfer coefficients in the impingement region.

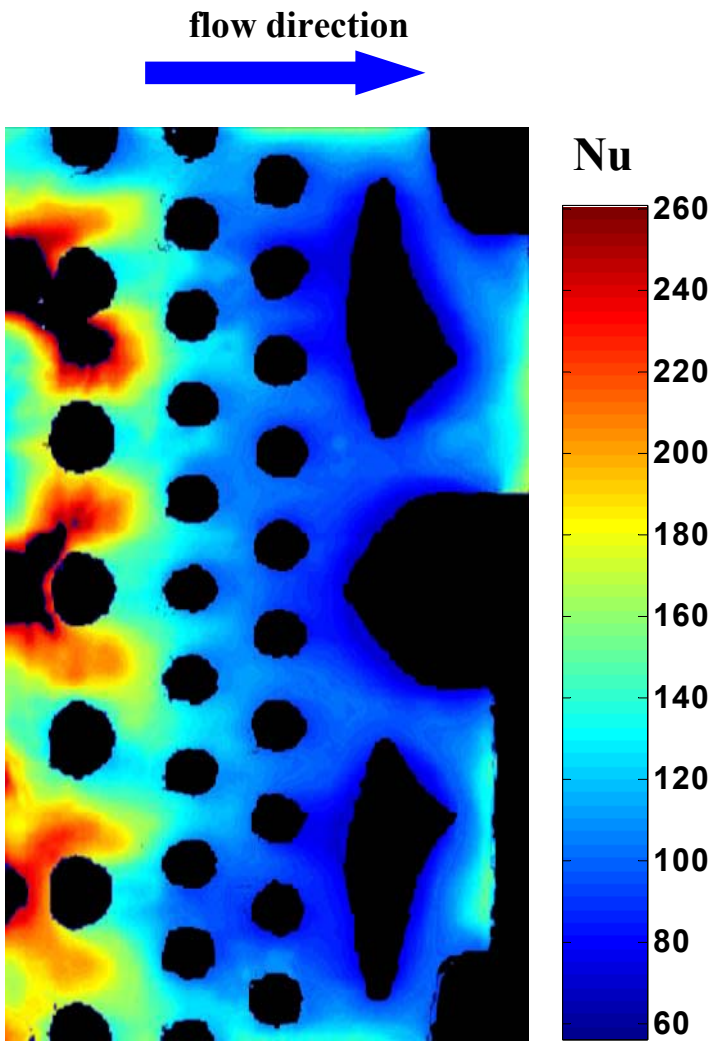

Figure F-4 Experimental Nusselt number contours for Re = 15127. Black regions indicate the absence of data, either due to the presence of a pedestal feature or the inability to resolve the high heat transfer coefficients in the impingement region.

Appendix G: Friction Multiplier Derivation

The following is a description of PinFin's friction calculation development. PinFin and the following derivation were provided by Cunha [2004].

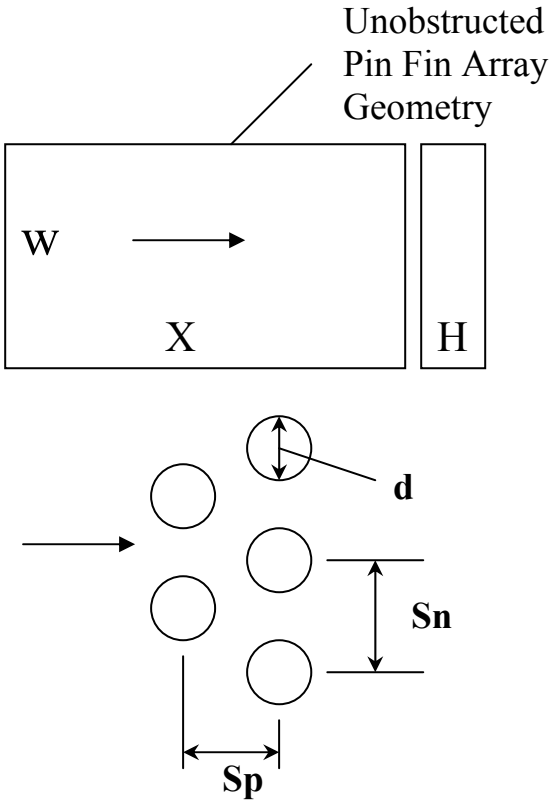

$$A_{min} = (W - N_T d)H \qquad U_{max} = U_{bulk}\frac{A_{bulk}}{A_{min}} \qquad Re_d = \frac{\rho d U_{max}}{\mu}$$

$$F\_per\_row = C_1 C_2 \frac{d}{H} + F_{pin}$$

$$\text{where}: C_1 = \frac{2.132}{Re_d},\ C_2 = \frac{1}{(4\frac{Sn}{d} - 1)},\ F_{pin} = \frac{0.872}{Re_d^{0.278}}$$

$$\Delta P_{per\_row} = 4F\_per\_row\left(\frac{\rho U_{max}^2}{2g}\right);\ \Delta P = N_L \Delta P_{per\_row}$$

$$F_M = \frac{(4F\_per\_row\ N_L)\left(\frac{X}{D_h}\right)\left(\frac{W}{W - N_T d}\right)}{f_o} \quad \text{where} \quad f_o = 0.316 \cdot Re^{-0.25}$$

and for the microcircuit array used in the current study:

$$F\_per\_row = \frac{\Delta P_{static}}{4_{rows}}\left(\frac{2}{\rho \cdot U_{max}^2}\right)$$

$$F_M = \frac{\left(\frac{\Delta P_{static}}{4} \cdot \frac{2}{\rho \cdot U_{max}^2} \cdot \frac{X}{s_p}\right)\left(\frac{D_h}{X}\right)\left(\frac{1}{1 - d/s_n}\right)^2}{f_o}$$

Jeffrey N. Prausa

Jeff Prausa was born in Baker City, Oregon in November of 1979 to Rick and Robin Prausa. Rick is a Senior Executive in the United States Forest Service and Robin is the Chief Financial Officer/General Manager of a large government contractor. Shortly after birth, Jeff moved to Rhinelander Wisconsin, where he lived for five years. After Wisconsin, Jeff moved to Albuquerque, New Mexico where he spent another five formative years in the high country of the American Southwest. In 1989, his father's job moved the family once again, this time to the bustling outskirts of the metropolis centered on our nation's capital. Jeff spent 9 years living in Northern Virginia, before leaving to attend the Virginia Military Institute.

Jeff spent the customary four years working towards an undergraduate degree in Mechanical Engineering at VMI. While there he served in several military and academic leadership positions. He graduated second in his class with a 3.9 GPA, first in Mechanical Engineering. While at VMI, Jeff's parents relocated yet again, this time to the open expanse and big sky of Great Falls, Montana. Jeff spent several weeks per year hiking the Rocky Mountain Front and snowboarding the fine powder of the eastern slope of the Rocky Mountains.

Upon completion of VMI, Jeff enrolled in the Mechanical Engineering Graduate Program at the Virginia Polytechnic Institute and State University in Blacksburg Virginia. There he spent one semester as a Graduate Teaching Assistant and three more as a Graduate Research assistant under Dr. Karen A. Thole. Upon completion of his Master's degree, Jeff accepted a job with aircraft engine manufacturer Pratt & Whitney. Subsequently, he and his wife, Tricia, relocated to Jupiter, Florida, where they currently live.

Jeff and Tricia have two dogs, Eddie and Kayla, both mixed lab derivatives of some sort. With their close proximity to the Atlantic, Jeff and Tricia have taken up surfing, snorkeling, parasailing, jet-skiing, scuba diving and long distance ocean swimming.